LIBRA-SP, A Light Ion Fusion Power Reactor Design Study Utilizing a Self-Pinched Mode of Ion Propagation – Report for the Period Ending June 30, 1995

B. Badger, D. Bruggink, P. Cousseau, R.L. Engelstad, Y.M. Lee, H.Y. Khater, G.L. Kulcinski, J.J. MacFarlane, E.A. Mogahed, G.A. Moses, R.R. Peterson, M.E. Sawan, I.N. Sviatoslavsky, P. Wang, L.J. Wittenberg, C.L. Olson, R.E. Olson

June 1995

UWFDM-982

FUSION TECHNOLOGY INSTITUTE

UNIVERSITY OF WISCONSIN

MADISON WISCONSIN

LIBRA-SP

A Light Ion Fusion Power Reactor Design Study Utilizing a Self-Pinched Mode of Ion Propagation

Report for the Period Ending
June 30, 1995
Performed Under Sandia National Laboratory Contract #AI-7232

B. Badger, D. Bruggink, P. Cousseau, R. L. Engelstad, Y-M. Lee,
H. Y. Khater, G. L. Kulcinski, J. J. MacFarlane, E. A. Mogahed,
G. A. Moses, R. R. Peterson, M. E. Sawan,
I. N. Sviatoslavsky, P. Wang, L. J. Wittenberg

Fusion Technology Institute
Nuclear Engineering and Engineering Physics Department
University of Wisconsin-Madison
Madison, Wisconsin 53706

C. L. Olson and R. E. Olson

Sandia National Laboratory
Albuquerque, NM 87185

June 1995

UWFDM-982

Contents

1. Executive Summary

LIBRA-SP is a 1000 MWe light ion beam power reactor design study which utilizes a self-pinched mode for propagating the ions from the ion-diode to the target. This feature distinguishes it from the earlier studies LIBRA and LIBRA-LiTE. There are several other improvements that have been implemented which are described in this report.

The reactor is driven by 7.2 MJ of 30 MeV Li ions (on target), of which 1.2 MJ is in the pre-pulse, and 6 MJ in the main pulse. The transport efficiency is 90% and there are 24 beams in the reactor. The ions are transported to the target in a self-pinched mode where the net electrical current of the beams provides the azimuthal magnetic fields that confine the ions to the channels. For the beam to have a net current, most of the ion current must be neutralized by electrons coming from the target chamber gas, where the electrons move with the beam ions. Guide tubes are used to aim the beams at the target and for this reason, these tubes must be precisely aimed. The guide tubes confine the beam with image charges and will accommodate some large radius bends.

A novel scheme of first wall protection for ion beam driven inertial confinement fusion reactors is used. Earlier versions of LIBRA reactors used flexible woven SiC or steel tubes. The current version uses rigid HT-9 ferritic steel tubes called PERIT (perforated rigid tubes) units. These tubes are equipped with tiny nozzles on either side which spray vertical fans of liquid metal, overlapping each other such that the first two rows of tubes are completely shadowed from the target emanations. The target generated x-rays accelerate the LiPb spray through the rapid vaporization of the surface facing the target. Simulations of the behavior of the spray with the BUCKY computer code show that the spray remains intact and is still at liquid density when it hits the PERIT units producing a peak pressure on the PERITs of several GPa, and a total impulsive loading of 72 Pa-s. The spray that is vaporized by the x-rays blows into the center of the target chamber intercepting the target debris ions. The first row of tubes in the blanket carries the brunt of the radial impulsive load, which is applied at the reactor repetition rate of 3.88 Hz.

A code has been developed for determining the transient and steady state response of the tubes containing the liquid metal, driven by sequential pulses for specific boundary conditions. Maximum steady state deflections and bending stresses as a function of the rep-rate are calculated and used to optimize the length of the PERIT units for avoiding resonant conditions. The cylindrical portion of the chamber is covered by a blanket of rigid steel tubes at a packing fraction of 50%. Only the front two rows of tubes are equipped with the spray nozzles. These tubes are at a radius of 4 m and the radius of the reflector, which is the vacuum boundary, is 5.2 m. The reflector is made of HT-9 ferritic steel, and is 50 cm thick with a 10% fraction of LiPb coolant. In the vertical direction the front tubes are divided into two banks, each 5.3 m long. Manifolds feed the tubes at the top and at the midplane. The rear tubes are continuous from the top to the bottom and are manifolded only at the top. All the liquid metal ends up in a pool on the bottom and is fed through a perforated plate to steam generators located in the base of the reactor. After going through the steam generator the LiPb goes to a T_2 recovery system, in which a vacuum disengaging technique is used to extract the T_2. An overpressure of $10^2 - 10^3$ Pa of D_2 is needed for efficient T_2 extraction and this is done by infusing D_2 at a pressure of 10^3 Pa just upstream of the vacuum disengager. In the vacuum disengager, the LiPb is converted to 100 μm diameter droplets and then free-fall a distance of 3.5 m while being subjected to vacuum pumping. Only 30% of the mass flow rate of the LiPb goes through the vacuum disengager during which time, 68% of the D_2 and T_2 is extracted in the 0.5 s free-fall. This maintains the T_2 partial pressure in the LiPb at 10^{-7} Pa and thus keeps T_2 diffusion in the steam generator to 40 Ci/d. The total T_2 inventory in the LiPb is only 2 g.

Three dimensional neutronics has been performed for the diodes including a neutron trap located in the shield plug behind each diode. The analysis has shown that the diode casing as well as the cathode and anode feed bus-bars are lifetime reactor components. The lifetime of the magnet coils in the cathode depends on the type of insulators used. If ceramic insulators are used, then the coils too will be lifetime components. If, however, organic insulators will be used, the coils will have to be replaced once in the 30 full power year life

of the reactor. We also note that if the beam tubes are tapered, such that no neutrons are incident on their walls, then even organically insulated coils may be lifetime components. The neutron trap itself sustains damage slightly higher than the design limit, but since it is not a highly stressed structural component, it may survive the reactor lifetime.

The total direct costs are 1772 M$ (1995) and the total capital costs 3227 M$ (1995). The cost of electricity (COE) using a target cost of 18¢, 8% interest on capital and an availability of 75% is 56.4 mills/kWh. This somewhat higher cost than in LIBRA-LiTE is due to a more recent way for computing indirect costs which is more in line with current practices. This COE is still very competitive when compared to other inertial or magnetic fusion reactor systems.

2. Introduction

The LIBRA (Light Ion Beam ReActor) series of studies have evolved into the premier commercial inertial confinement light ion beam driven reactor studies in the world. The critical issue in these studies is the beam transport to the target. In the current study, beam transport is via a self-pinched mode in which the net electrical current of the beam provides the azimuthal magnetic fields that confine the ions to the channels. The evolution of this study, LIBRA-SP (Self-Pinched), was the subject of a paper presented at the Eleventh Topical Meeting on the Technology of Fusion Energy held in New Orleans, LA, June 19-23, 1994. Further, an abstract has been submitted to the 16th IEEE/NPSS Symposium on Fusion Engineering which will be held in Champaign, Illinois, on September 30-October 5, 1995. Both the paper and the abstract are included in the Appendix. Additional background for the concept was also given at the Technical Meeting on Drivers for Inertial Fusion Energy sponsored by the IAEA in Paris, November 14-18, 1994 and the description of LIBRA-SP will be published by the IAEA.

The statement of work (SOW) for the period ending June 30, 1995, under Sandia Contract #AI-7232, is as follows:

A. Continued examination of first wall vaporization by x-rays.
B. Examine the mechanical vibrations induced in the first wall tubes (PERITs) including the effect of fatigue on the lifetime of the tubes.
C. Determine target heating during injection.
D. Three-dimensional neutronics of blanket, shield and diode.
E. Continue activation and safety analysis.
F. Perform economic analysis.
G. Write an end of period report.

Each of these elements of the SOW have been addressed. Task A has been addressed in Section 5.4.1, Task B in Section 5.4.2, Task C in Section 4.6, Task D in Sections 5.5 and 6.2, Task E in Sections 7.2 and Task F in Section 8. An updated parameter list is given in Section 9.

3. Ion Beam Generation and Transport

3.1. Two-Stage Ion Diode

As in all earlier versions of LIBRA, a magnetically insulated extraction ion diode is used to accelerate the driver ions. Earlier versions used single stage diodes. Since the conclusion of LIBRA-LiTE, considerable experimental [1,2] and theoretical [3] progress has been made on multi-stage diodes, showing them to couple diode energy to the ions more efficiently and to reduce beam divergence. A multi-stage diode accelerates ions across more than one gap by having more than one virtual cathode; a single stage diode has one cathode and one gap.

A schematic picture of the LIBRA-SP 2-stage diode concept is shown in Fig. 3.1.1. The picture is only schematic and is not necessarily to scale. Two sets of insulating magnets are shown; the central cone and an outer ring. These define the magnetic fields in the cathode region. There are clearly other magnets in the anode region and elsewhere, which are not shown. The central cone of magnets defines the inner radius of the anode source plasma, R_i. The focal length of the diode, F, is controlled by the shape of the anode, the magnets and the degree of neutralization of the beam ions. The cathode tips are held to potentials V_1 and V_2, relative to the potential of the diode. The gap widths of the two stages are d_1 and d_2.

The outer radius of the anode plasma, R_o, is an important parameter for the self-pinched transport. R_o is determined by the required anode area, A_a and R_i. R_i must be large enough to contain all of the magnetic field coils, power feeds and cooling within the inner cone. The required particle current I_d and the current density J_d determine A_a. J_d is the space-charge limited current density J_{scl} times an enhancement factor K_e, which accounts for the fact that the ions are emitted from a volume of plasma and not from an infinitely thin surface. To avoid a high beam microdivergence θ_μ, K_e should be no more than 5. J_{scl} is a function of d_1 and V_1,

$$J_{scl} = 0.715 \frac{V_1^{3/2} q_1}{A d_1^2} \,. \tag{3.1}$$

$V_1/(V_2 - V_1)$ is thought to affect θ_μ, though in a way that is not yet clear. For the current work, we assume that $V_1 = 0.5 V_2$. It is important that θ_μ be as low as possible because

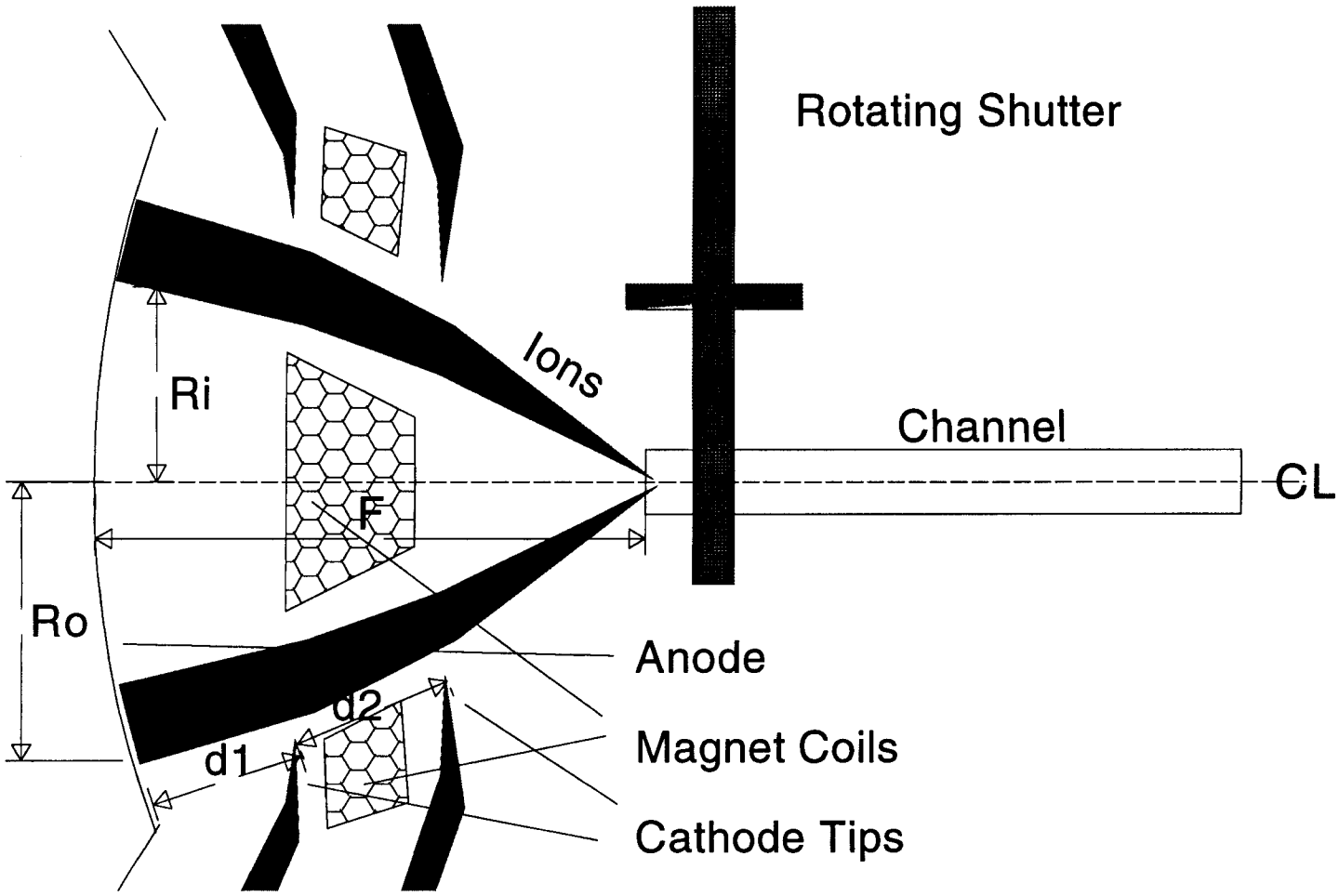

Figure 3.1.1. Schematic picture of LIBRA-SP two stage diode.

it determines the focal spot size that affects the self-pinched transport. The magnets must supply an applied magnetic field at twice the critical field to avoid the shorting of either gap by the cathode electrons before ions are accelerated, B_{crit},

$$B_{crit} = 0.34\frac{(V^2 + V)^{1/2}}{d} \text{ tesla}\,, \tag{3.2}$$

with V in MV and d in cm. A separate B_{crit} will exist for each gap. These will define the coils.

The focal spot radius r_f is determined by F, θ_μ, and scattering. The effects of scattering and microdivergence add in quadrature,

$$r_f^2 = F(\theta_\mu^2 + \theta_{scat}^2). \tag{3.3}$$

θ_{scat} is the growth in microdivergence caused by scattering. The SCATBALL computer code has been used to calculate r_f with the scattering explicitly calculated and we have found that, for the assumed chamber gas densities, scattering does not have an important impact on the spot size. The focal spot size and R_o/F determine the self-pinched transport parameters.

3.2. Self-Pinched Transport

In the LIBRA-SP concept, the ion beams are transported to the target in the self-pinched mode. The net electrical current of the beams provides the azimuthal magnetic fields that confine the ions to the channels. The required net electrical current is

$$I_{net} = 0.5\left(\frac{R_o}{r_f}\right)^2 \theta_\mu^2 I_A. \tag{3.4}$$

I_A is the Alfvén current,

$$I_A = \beta\gamma\frac{A}{q}\frac{m_p c^3}{e}. \tag{3.5}$$

β and γ are the normal relativistic parameters, A is the beam ion atomic mass, e is the electronic charge, c is the speed of light, and m_p is the mass of a proton. For the beam to have a current of I_{net}, most of the ion current must be neutralized by electrons ionized from the target chamber gas. The electrons move with the beam ions, neutralizing most of the

ion current. The current neutralization fraction is

$$f_m = 1 - \left(\frac{I_{net}}{I_{beam}} \right) . \tag{3.6}$$

The degree of neutralization achieved can only be calculated with a full 2-D electromagnetic particle-in-cell computer simulation.

The guiding of a self-pinched beam to the target is one open question. Lasers could be used to pre-ionize a path to the target. The increased conductivity might lead to propagation along a preferred direction. Another option, the method chosen for LIBRA-SP, uses guide tubes that aim the beams at the target. It is thought that the beams will propagate in a straight line without any pre-ionizing by a laser. The beams must be aimed precisely. The guide tubes confine the beam with image charges and will allow some large radius bends. Neither of these methods has been studied in any detail.

In a self-pinched beam the neutralization is created by the head of the beam. Azimuthal magnetic fields are created in the head of the beams and are frozen in when the conductivity is sufficiently high. The head of the beam is not itself fully confined and is continually eroded, leading to an energy loss per unit transport length. This is not related to any energy loss per ion, but is a loss of ions. From a discussion with Dale Welch of Mission Research Corporation in Albuquerque, NM, a 30 MeV fully stripped 50 kA net current beam would lose 1 ns of beam per 400 cm of transport. We have scaled an energy loss law from this,

$$\epsilon = E_{pulse} \frac{1\,\text{ns}}{\tau} \frac{L_{beam}}{400\,\text{cm}} \frac{I_{net}}{50\,\text{kA}}. \tag{3.7}$$

This is only one component to the efficiency. Each ion may lose energy from axial fields and scattering.

3.3. Ion Beam Parameters

The concepts described in the previous two sections have been used to create consistent designs for the diodes and transport systems. The overall parameters, which serve as the system requirements, are shown in Table 3.3.1. The target requires 7.2 MJ in a 40 ns pre-pulse and a 20 ns main pulse. The main pulse is time-of-flight bunched by a factor

Table 3.3.1. LIBRA-SP General Ion Beam Parameters

Parameter	Unit	Main	Pre-Pulse
Ion species		Lithium	Lithium
Ion energy	MeV	30	30
Energy on target	MJ	6.0	1.2
Total transport efficiency	%	90	90
Energy leaving diodes	MJ	6.67	1.33
Number of beams		12	12
Pulse width at diodes	ns	40	40
Pulse width at target	ns	20	40
Power at diodes	TW	167	33
Power at target	TW	300	30
Particle current at diodes	MA	5.56	1.11
Particle current at target	MA	10	1

of 2. The ions must be roughly 30 MeV lithium ions. The peak total power must be 330 TW. These parameters have been used in designing the diodes, whose parameters are shown in Table 3.3.2. Both the main and pre-pulse diodes accelerate the lithium ions to 30 MeV in 2 stages; we assume that the charge state in both stages is 1, and that the stages have equal voltages. The diode parameters determine the self-pinched transport parameters, shown in Table 3.3.3.

3.4. Ion Diode Engineering

The diode design shown in Fig. 3.1.1 demonstates the diode concept, but gives limited information on the actual structural design, which is needed for other analysis, including neutron transport and activation. We have based the mechanical design of the two-staged ion diode on the parameters given in Table 3.3.2 and the mechanical design of the light ion Target Development Facility (TDF) single-staged diode [4]. The geometrical model used for radiological dose calculations in the TDF is shown in Fig. 3.4.1. The TDF diode is powered by a coaxial feed with a negative inner conductor, so crossover conductors are needed to power the outer cathode tip. The LIBRA-SP diode is shown in Fig. 3.4.2. This diode is powered with a coaxial feed with a positive inner conductor. Crossover conductors are

Table 3.3.2. LIBRA-SP Diode Parameters

Parameter	Unit	Main	Pre-Pulse
Current/diode	kA	463	92.6
Voltage Drop 1 V_1	MV	15	15
Voltage Drop 2 V_2	MV	30	30
Physical Gap 1 d_1	cm	2	2
Physical Gap 1 d_2	cm	2	2
Enhancement factor K_e		5	5
Inner anode radius R_i	cm	10	10
Microdivergence θ_μ	mrad	4	4
Focal length F	cm	150	150
J_{scl}	kA/cm^2	0.3	0.3
J_d	kA/cm^2	1.5	1.5
Anode area A_a	cm^2	309	62
Outer anode radius R_o	cm	14.1	10.9
Focal spot radius r_f	cm	0.6	0.6
R/F		0.094	0.073
B_{crit} for Gap 1	T	2.63	2.63
B_{crit} for Gap 2	T	2.63	2.63
B_{appl} for Gap 1	T	5.27	5.27
B_{appl} for Gap 2	T	5.27	5.27

Table 3.3.3. LIBRA-SP Self-Pinched Transport Parameters

Parameter	Unit	Main	Pre-Pulse
Transport length L	cm	800	800
γ		1.005	1.005
β		0.096	0.096
Charge state		3	3
Alfvén current	kA	6958	6958
I_{net}	kA	30.7	18.5
f_m		0.978	0.933
Energy loss ϵ	kJ	17.1	2.1
Efficiency	%	96.9	98.1

needed to power the inner cathode tips. In both cases, the crossover conductors are 3 or 4 bars with a great deal of space in between them. Not shown are power feeds for the copper magnets and magnet coils for controlling the anode plasma.

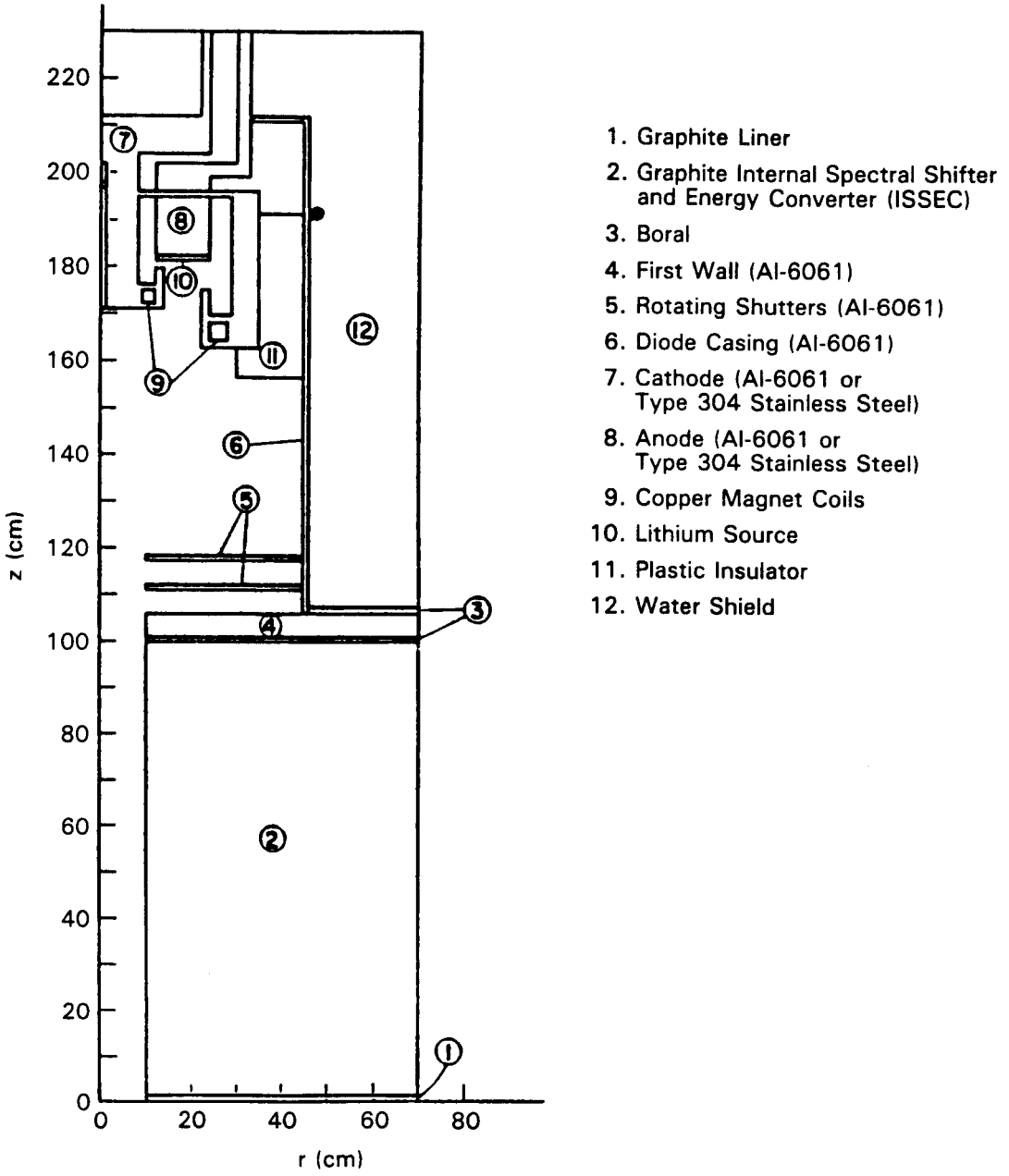

Figure 3.4.1. The r-z geometrical model of the TDF ion diode used in the two-dimensional neutronics and activation calculations.

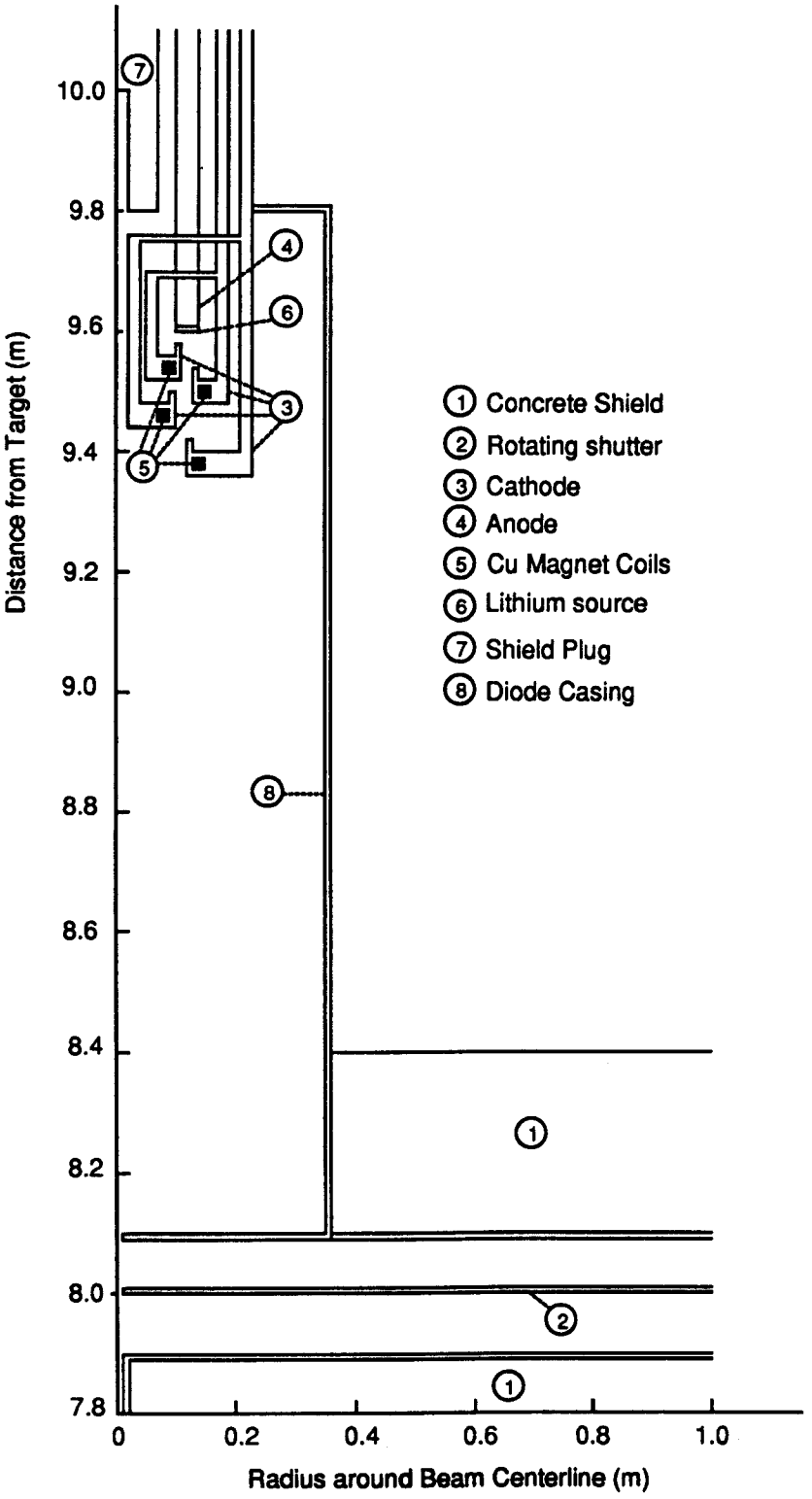

Figure 3.4.2. The r-z two-dimensional neutronics model of the LIBRA-SP ion diode.

References for Section 3

1. M. G. Mazarakis, et al., "Light Ion Pulsed Power Induction Accelerator for the Laboratory Microfusion Facility," Proceedings of the 15th Biennial Particle Accelerator Conference (1993) IEEE Publ. Serv.
2. S. Miyamoto, et al., "Intense Light Ion Beam Divergence in Single-Stage and 2-Stage Diodes," *IEEE Transactions on Plasma Science*, **21**, 567 (1993).
3. S. A. Slutz and M. P. Desjarlais, "Theory of Multistage Intense Ion-Beam Acceleration," *J. Appl. Phys.*, **67**, 6705 (1990).
4. D.L. Henderson, M.E. Sawan, and G.A. Moses, "Radiological Dose Calculations for the Diode Region of the Light Ion Fusion Target Devolpment Facility," *Fusion Technology* **13**, 594 (1986).

4. Target Calculations

4.1. Introduction

High-gain targets to be used in inertial confinement fusion (ICF) power reactors are expected to release $\sim 10^2 - 10^3$ MJ of energy in the form of x-rays, energetic ions, and neutrons [1-3]. This energy originates in the central, highly compressed core of an ICF target due to fusion of deuterium (D) and tritium (T). The primary fusion products of D-T reactions are α-particles (^{4}He) and 14 MeV neutrons, while secondary products from D-D and D-^{3}He reactions include lower energy neutrons, gamma photons, and charged particles (^{3}He, T, and protons). Because charged particles have relatively short mean free paths, the bulk of this energy is deposited within the target. Energy is transferred from the hot central fuel region to the outer layers of the target by radiation, conduction, and mass motion (kinetic energy) leading to release of x-rays and ion debris. On the other hand, a significant fraction of the neutrons escape the target. It is important to understand the partitioning of energy during the target explosion phase because it provides information critical to the design of ICF target chambers.

Below, we describe calculations of the fusion burn and explosion energetics of the ICF target for the LIBRA-SP light ion fusion reactor design [4]. In this design, the spherical target is irradiated with 24 Li ion beams (12 prepulse and 12 full power) containing a total energy of 7.2 MJ. The peak beam power on target is 330 TW and the pulse width of the full power beams is 20 ns. Internal pulse shaping of the x-ray flux onto the capsule [5] is expected to lead to a gain of about 80, thus producing a total target yield of approximately 550-600 MJ.

The purpose of this investigation is to begin to address quantitatively the *explosion* dynamics of the LIBRA target. It is anticipated that the physics of the *implosion* phase will be addressed in a future study. To study the explosion dynamics, we start with an already-imploded configuration which represents a reasonable representation of the target plasma conditions at the instant of ignition. The evolution of the target breakup is then simulated using the PHD-IV radiation-hydrodynamics code [6]. This code computes the

Table 4.1.1. LIBRA-SP Target and Ion Beam Parameters

	LIBRA-SP
Total absorbed beam energy	7.2 MJ
Peak beam power (main + prepulse)	330 TW
Hohlraum radius	0.7 cm
Yield	589 MJ
Peak beam intensity	54 TW/cm^2
Target gain	82

time-dependent fusion burn and energy transport within the target. The calculations also utilize new equation of state (EOS) and opacity models developed at Wisconsin [7]. The primary goal of the calculations is to make quantitative predictions for the time-dependent target x-ray flux and ion debris energy. These quantities can then be used to determine the response of the target chamber first wall to the target microexplosion.

The original LIBRA [1] and LIBRA-LiTE [8] designs utilized scaled versions of targets originally designed for heavy ion beam reactors [2] because of classification issues in the U.S. However, recent declassification of light ion targets now allows the use of more realistic target configurations [9]. The LIBRA-SP target design, shown in Fig. 4.1.1, is based on the target design for the Laboratory Microfusion Facility (LMF) [9]. Several of the LIBRA-SP target parameters are listed in Table 4.1.1. The two targets are designed with the same strategy. The beam ions penetrate the Hohlraum case and deposit in a low density carbon or plastic foam that is doped with high Z impurity to control the deposition profile. The foam heats to 200-300 eV, creating the drive radiation which is confined by the Hohlraum case. The radiation burns through the pulse-shaping layer around the capsule, shortening the pulse of radiation in the process. The capsule is then driven to implosion by the reshaped radiation pulse. This design has been studied in detail for the LMF target [9]. The predicted gain for the LIBRA-SP design is compared with that of other ICF reactor conceptual design studies in Fig. 4.1.2.

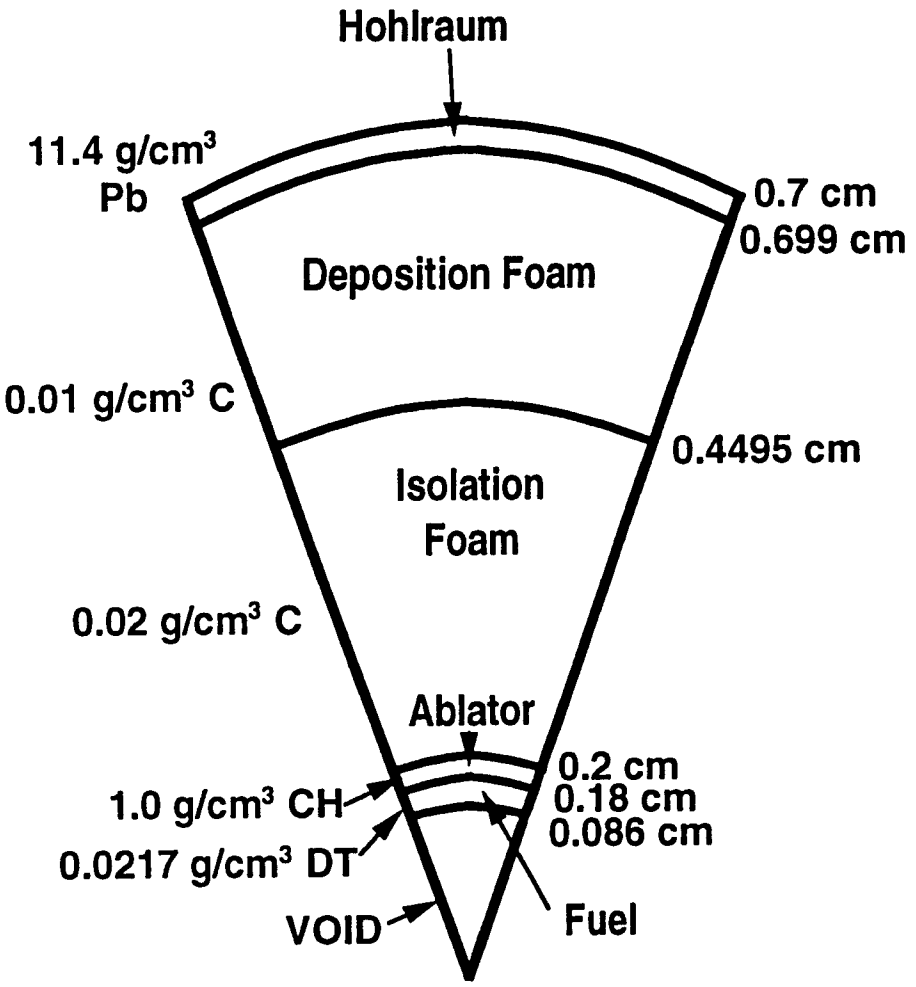

Figure 4.1.1. Schematic of initial target configuration for LIBRA-SP.

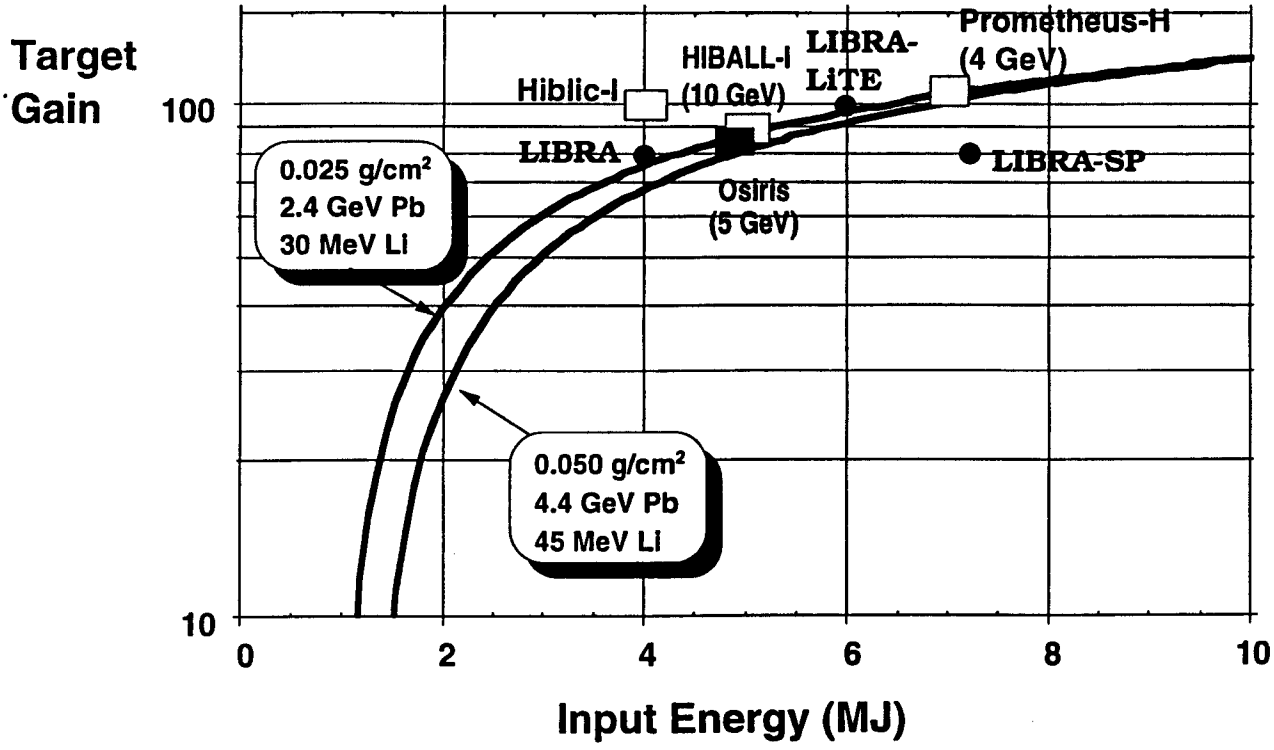

Figure 4.1.2. Comparison of target gains from several ICF reactor conceptual design studies. The performance of targets that rely on internal pulse shaping is slightly degraded from other ICF target designs.

4.2. Physics Models

4.2.1. PHD-IV Target Simulation Code

PHD-IV [6] is a plasma radiation-hydrodynamics code with models for ion beam energy deposition and fusion burn designed to model ICF target physics processes. It is a 1-D Lagrangian code which solves the single-fluid equation of motion with pressure contributions from electrons, ions, radiation, and fast charged particle reaction products. Energy transfer in the plasma is treated with a 2-temperature model — i.e., separate ion and electron temperatures. Thermal conduction through each species is treated using Spitzer's form of the thermal conductivity. The electron conductivity is flux-limited. Radiation emission and absorption terms couple the electron temperature equation to the radiation transport equations. In addition, the electron and ion temperature equations contain source terms that couple them to the ion beam energy deposition calculation and the energy deposited from the fusion reactions.

The simulations for the LIBRA-SP target utilize a hybrid equation of state model which couples high-density thermodynamic properties calculated using a muffin-tin model to lower density properties which are computed using a detailed configuration accounting model. Multigroup opacities are computed using the EOSOPA code (see below). Radiation is transported using a multigroup flux-limited diffusion model [10]. A total of 200 frequency groups was used in the simulation described below. The time-dependent radiation energy density equations are solved using implicit finite difference techniques.

Fusion reaction equations for DT, DD, and D-^{3}He are solved and the reaction products are transported and slowed using a time-dependent particle tracking algorithm. In addition, PHD-IV includes an ion beam energy deposition package to model the time which includes contributions to the stopping power from both bound and free electrons. However, this latter package was not required for the microexplosion simulation described below.

4.2.2. EOS and Opacity Models

The equation of state covers a wide domain of densities and temperatures. It consists primarily of three contributions: (1) the zero-temperature isotherm, (2) a thermal electronic component, and (3) a thermal ionic part. We have used a hybrid model in the equation of state calculations: a detailed configuration accounting (DCA) model is used for the low-density, high-temperature regime, while a "muffin-tin" model [11] is used for the high-density regime.

In the detailed configuration accounting model, each isolated ion in the plasma is in equilibrium with free electrons. Plasma effects on each atomic system are considered as perturbations. Ion abundances and level occupation numbers are obtained from detailed ionization balance calculations. In our LIBRA-SP calculations, the EOS's are obtained for plasmas with local thermodynamic equilibrium (LTE) populations. Continuum lowering effects are accounted for in the opacity calculations using an occupation probability formalism [12]. The following contributions are included in the equations of state: (1) the translational energy of ions and atoms, (2) the energy of partially degenerate electrons, (3) configuration effects from Coulomb interactions (Debye-Hückel corrections), and (4) atomic internal contributions (excitations and ionizations).

The muffin-tin model is used to accurately compute the equation of state for high-density plasmas. It is applicable to electrons on the zero-temperature isotherm as well as for any finite temperature. It has much of the simplicity of an isolated atom model but captures much of the physics of the band-structure model. In particular, it provides an accurate description of cohesion and the behavior of solids under compression. This model also describes an isolated atom or an ion in equilibrium with an electron gas in low density cases. Hence the muffin-tin model smoothly connects high-density electron degenerate regime and low-density plasma regime. This smooth connection provides thermodynamic consistency of calculated equations of state over a wide domain of temperatures and densities.

Our hybrid model is designed to provide reliable equations of state over a wide range of temperatures and densities. Figure 4.2.1 shows our results for energy and pressure isotherms of aluminum. In the low-density regime, the nonlinear behavior due to ionization/excitation is clearly seen. The cohesive, degenerate, and pressure ionization effects are observed for the high-density regime. Figure 4.2.2 shows a comparison of calculated shock Hugoniots with experimental data for Al and Au. It can be seen that the agreement is good.

In order to be able to treat properly the transfer of radiation in LIBRA targets, it is necessary to have values of the opacity for both low-Z and high-Z elements in a wide range of conditions. Radiation is absorbed by atoms and ions via the following types of processes: (1) bound-bound transitions (line absorption); (2) bound-free transitions (photoionization); (3) free-free transitions (Bremsstrahlung); (4) scattering of photons by electrons. In principle, the calculations of opacity for low-Z and high-Z systems are the same. In practice, however, they must be treated differently. We use a detailed term accounting (DTA) method for low-Z systems, and use an unresolved transition array (UTA) model for high-Z systems.

For high-Z atomic systems, especially for the ions in electronic configurations with open d or f shells, each configuration contains a very large number of levels. As a consequence, the number of lines corresponding to the bound-bound transitions between these levels are so numerous that it is impractical to do detailed line accounting calculations. On the other hand, these lines are so closely packed that intrinsic broadening effects suffice to merge them together. Because of this characteristic of high-Z line spectra, an unresolved transition array (UTA) model [13] can be used to compute high-Z opacities. The UTA model uses an average transition between configuration-averaged atomic levels to represent the numerous possible transitions (the transition array) between configurations. The splitting effect of these lines is accounted for by using a line shape for each transition array which is determined from Slater integrals. It is very important to include line broadening due to this UTA effect. Figure 4.2.3 shows a comparison of gold opacities calculated with and without this broadening effect. The curve on the left was calculated with normal line shapes which include Doppler, natural, and electron impact broadening, while the curve on the right also includes UTA broadening. It

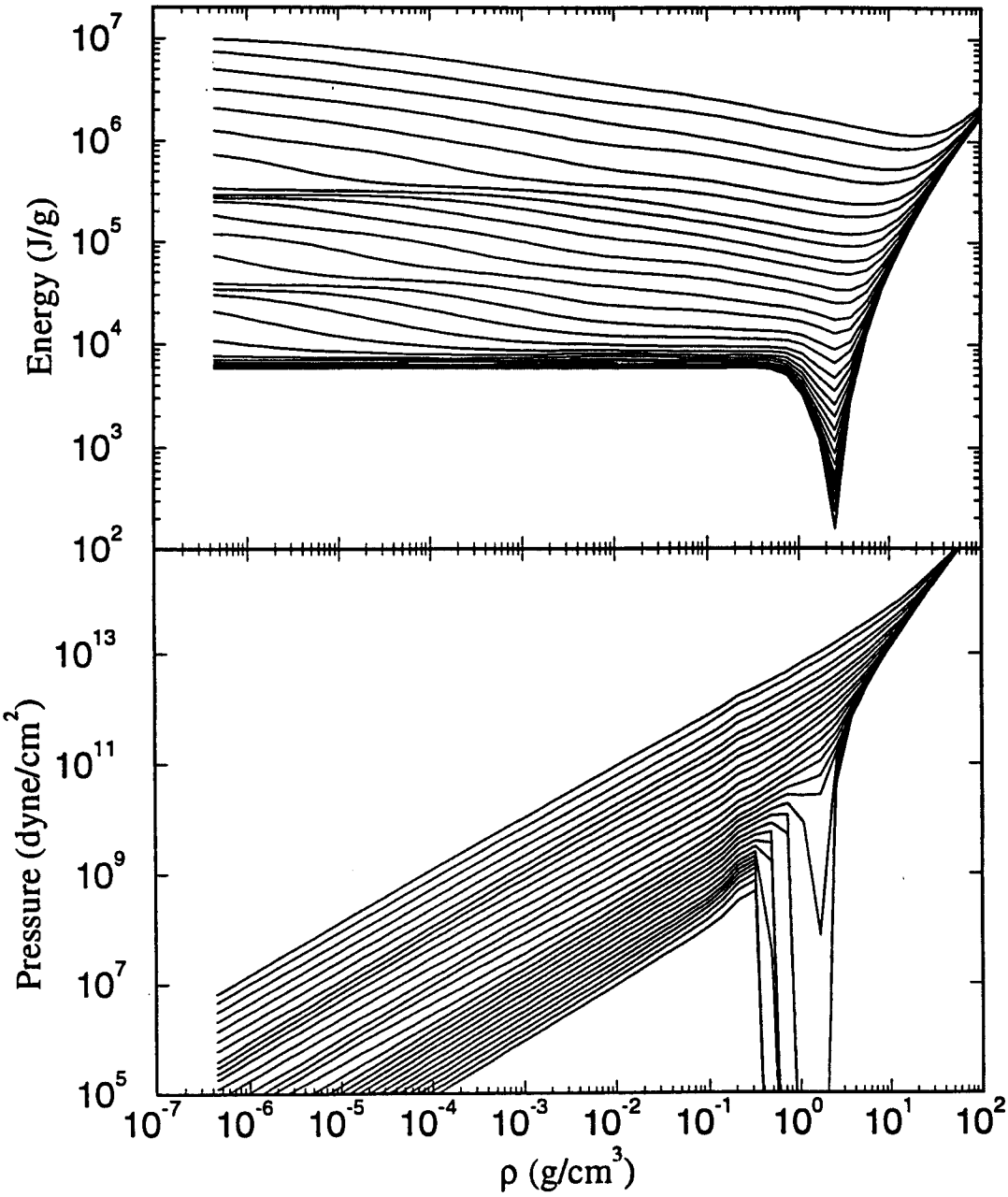

Figure 4.2.1. Energy and pressure isotherms calculated for Al using hybrid equation of state model.

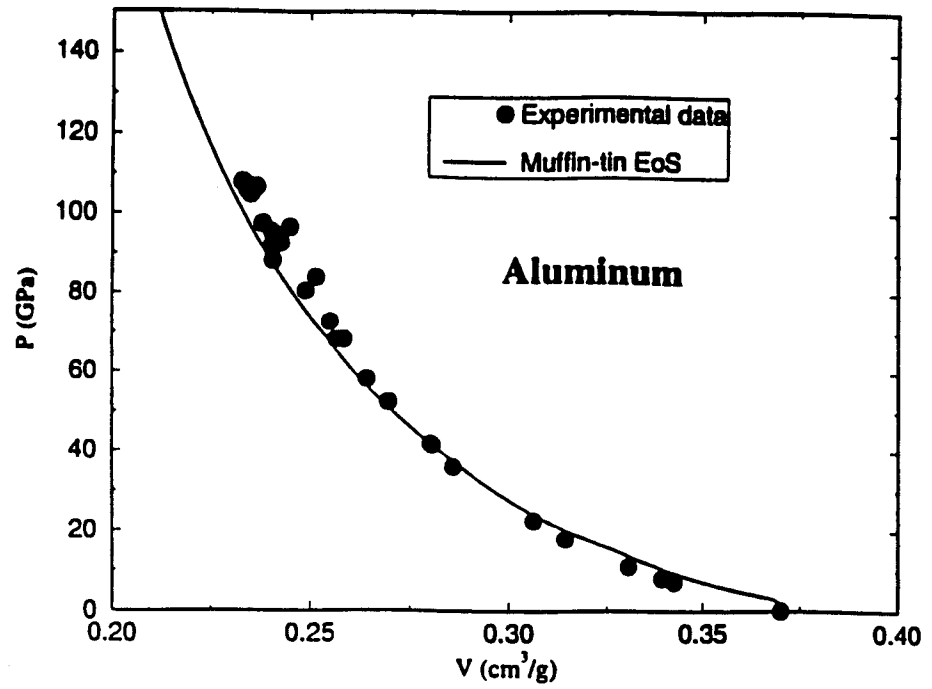

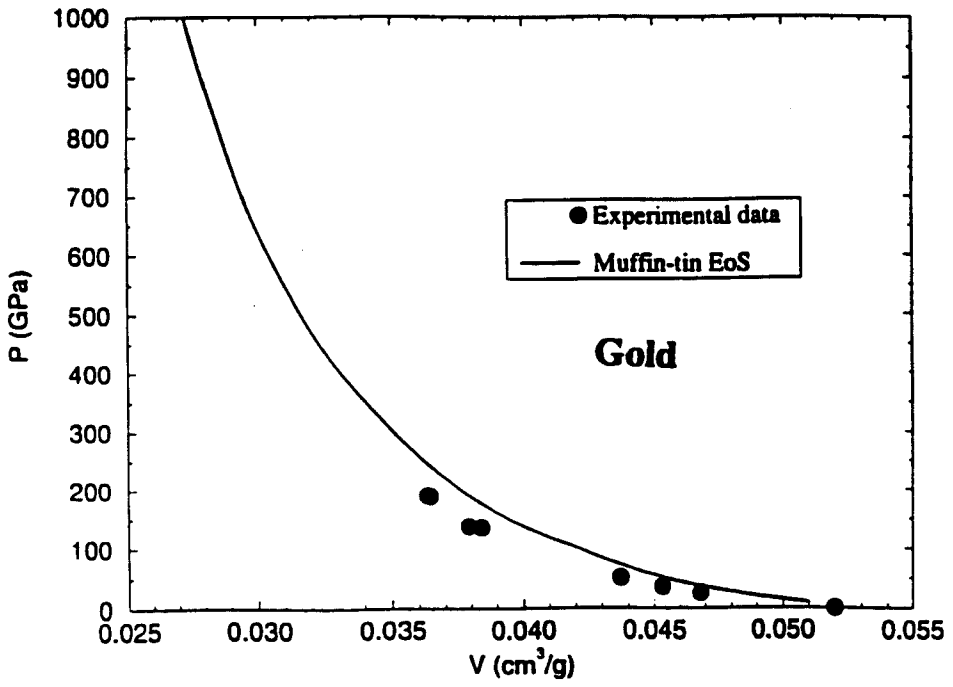

Figure 4.2.2. Comparison of calculated shock Hugoniots with experimental data for Al and Au.

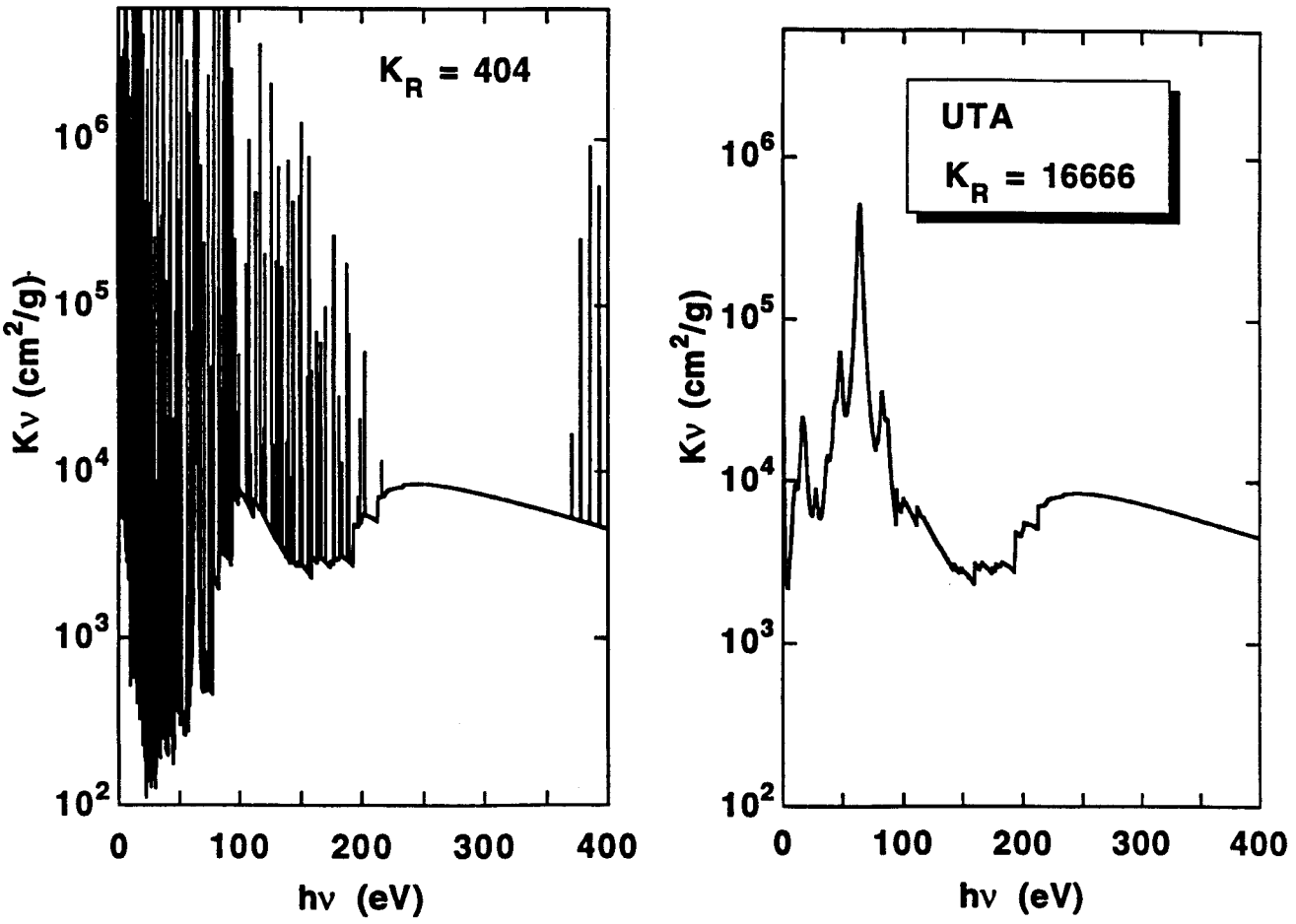

Figure 4.2.3. Frequency-dependence of Au opacity from calculations neglecting (left) and including (right) broadening due to UTA's.

is seen that the non-UTA result leads to a mean Rosseland opacity that is a factor of 40 lower than the UTA result. The UTA model is more accurate and is used in our Pb opacity calculations for the LIBRA target.

To assess the reliability of our opacity calculations, we have compared our results with other theoretical results [14]. In general, we find good agreement with some of the more reputable opacity codes (e.g., OPAL [15] and STA [16]).

4.3. Results

Conditions at the start of ignition assumed for the microexplosion simulation are shown in Fig. 4.3.1. At present, we simply assume these conditions can be roughly achieved using the beam parameters discussed above in conjunction with an x-ray internal pulse shaping scheme [9]. Clearly, however, a numerical simulation of the implosion is required to provide a more accurate target configuration at ignition.

The LIBRA-SP target is composed of 4 materials: the central DT fuel, a CH ablator, C deposition and isolation foams, and an outer Pb case (Hohlraum). At the start of the PHD-IV simulation, each of the material regions is assumed to have a uniform temperature and density, with the values indicated in Fig. 4.3.1. The exception to this is the DT fuel, which consists of a central hot spot surrounded by two other DT regions of successively higher density and lower temperature. The outer Pb region is assumed to have expanded by almost three orders of magnitude by the start of ignition. A total of 100 spatial zones was used in the simulation. At the start of the simulation, the areal density of the central hot spot is 0.3 g/cm^2, while that of the entire DT fuel is 3.3 g/cm^2. The fusion burn begins in the hot DT core which is initially at 8 keV. The burn region then propagates outward engulfing the entire DT region. By the end of the simulation a burn fraction of approximately 35% is achieved.

Results from the simulation are shown in Figs. 4.3.2 through 4.3.6. Figure 4.3.2 shows the time-dependent position of the Lagrangian zones, which indicate the material motion in the target. Figures 4.3.3 and 4.3.4 describe the energy partitioning and radiation flux histories. Figure 4.3.5 shows time-integrated spectra for the radiation flux escaping the

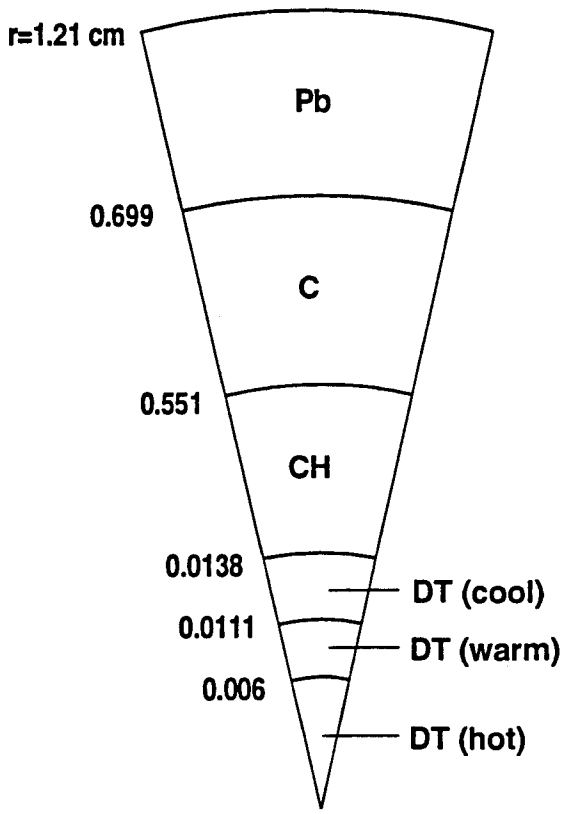

	Mass (mg)	Material	T (keV)	ρ (g/cm^3)
	120	Pb	0.1	0.020
	17.4	C	0.25	0.024
	9.1	CH	0.25	0.013
	4.2	DT (cool)	0.1	800
	0.8	DT (warm)	0.5	166
	0.0045	DT (hot)	8	50

Figure 4.3.1. Conditions at the start of ignition assumed for the PHD-IV LIBRA-SP simulation.

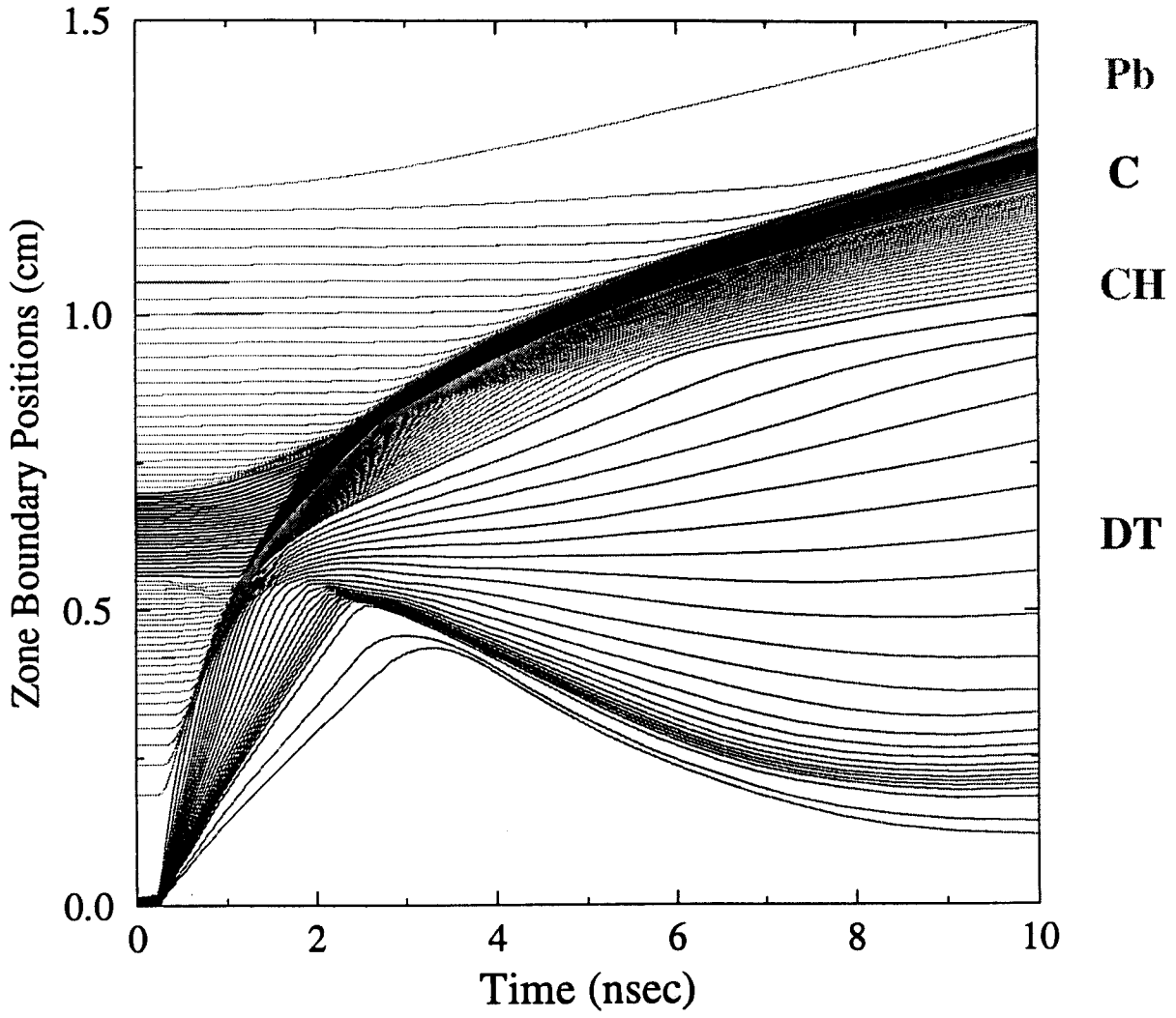

Figure 4.3.2. Time-dependence of Lagrangian zone boundaries.

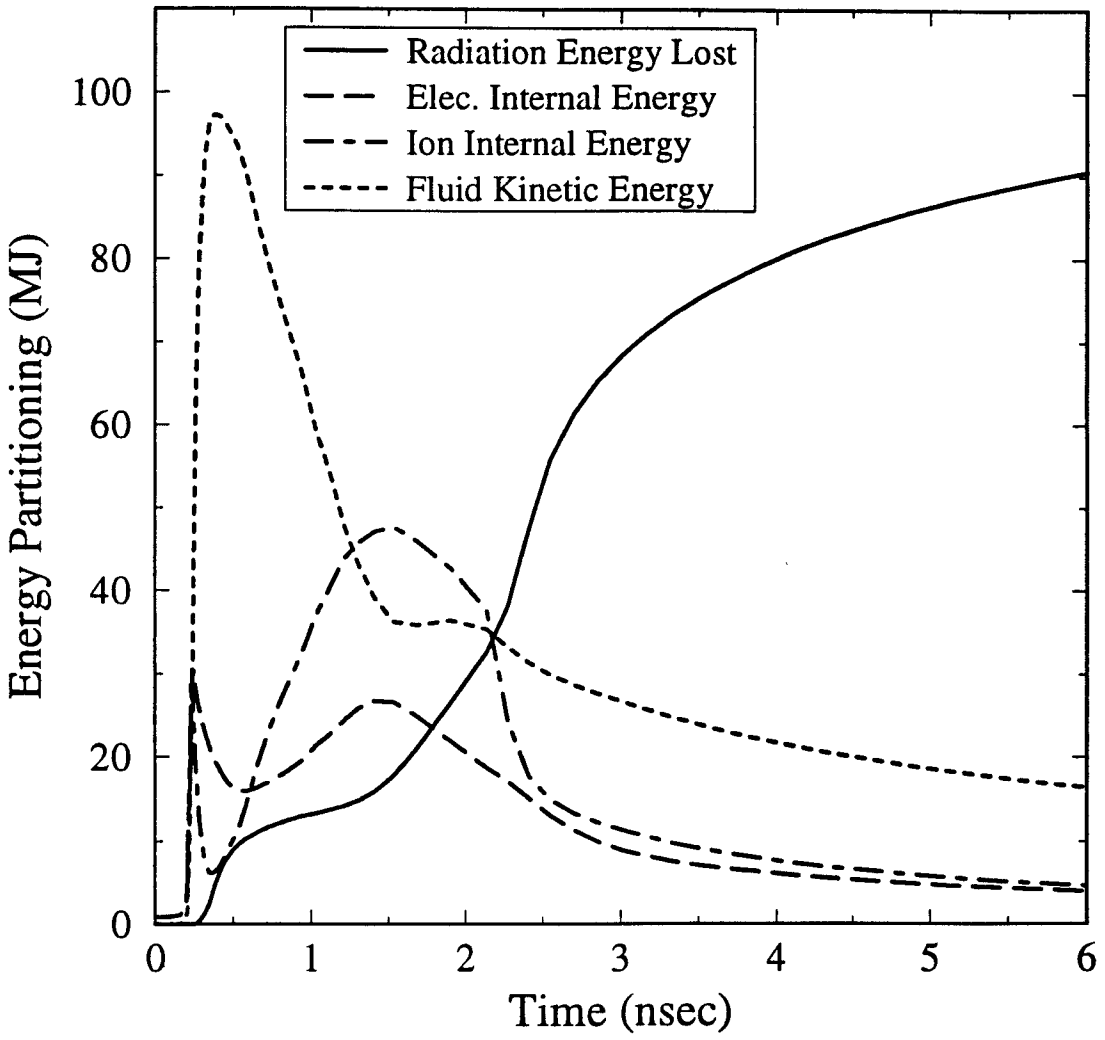

Figure 4.3.3. Time-dependence of energy partitioning in LIBRA-SP target.

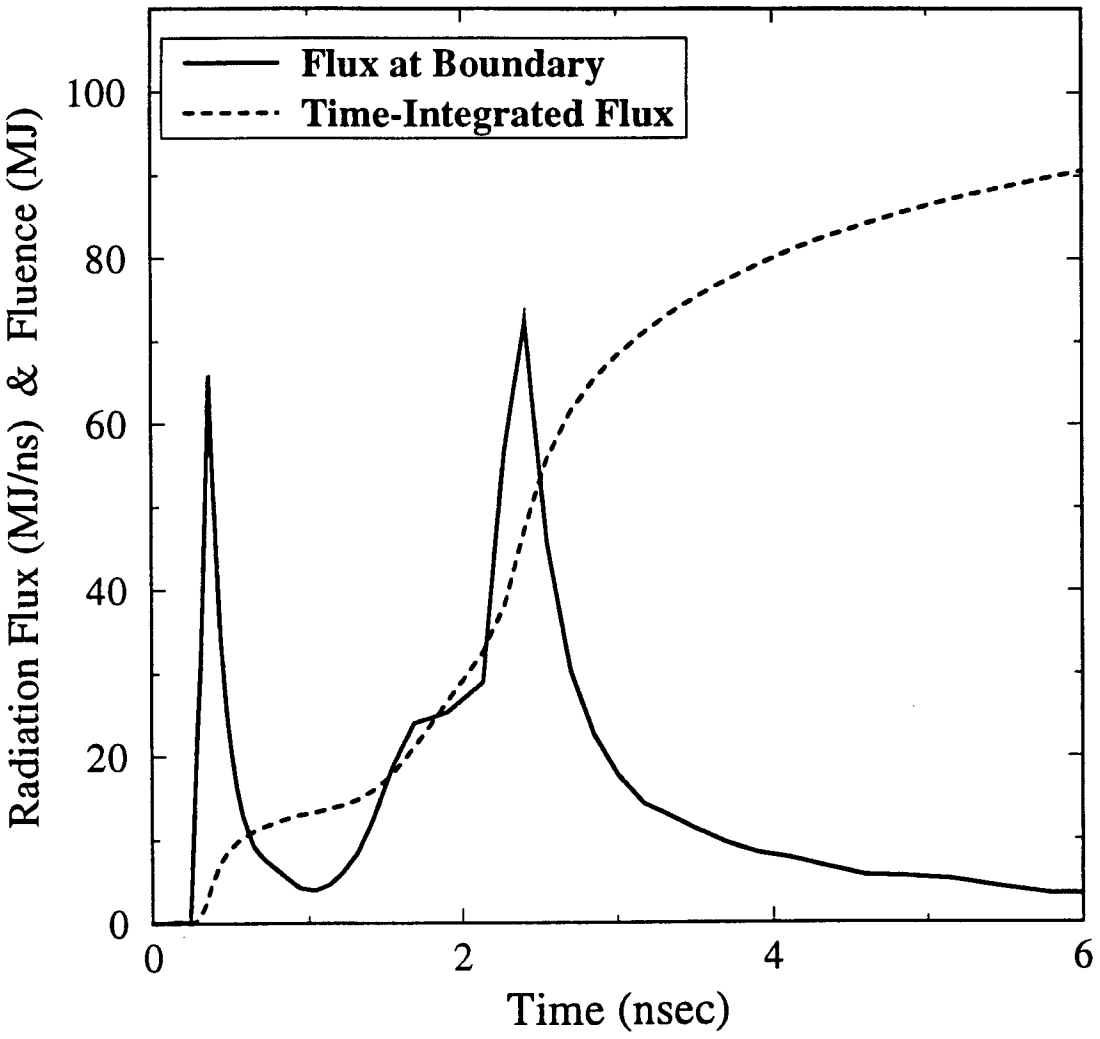

Figure 4.3.4. Time-dependent and time-integrated radiation power emitted from the boundary of the LIBRA-SP target.

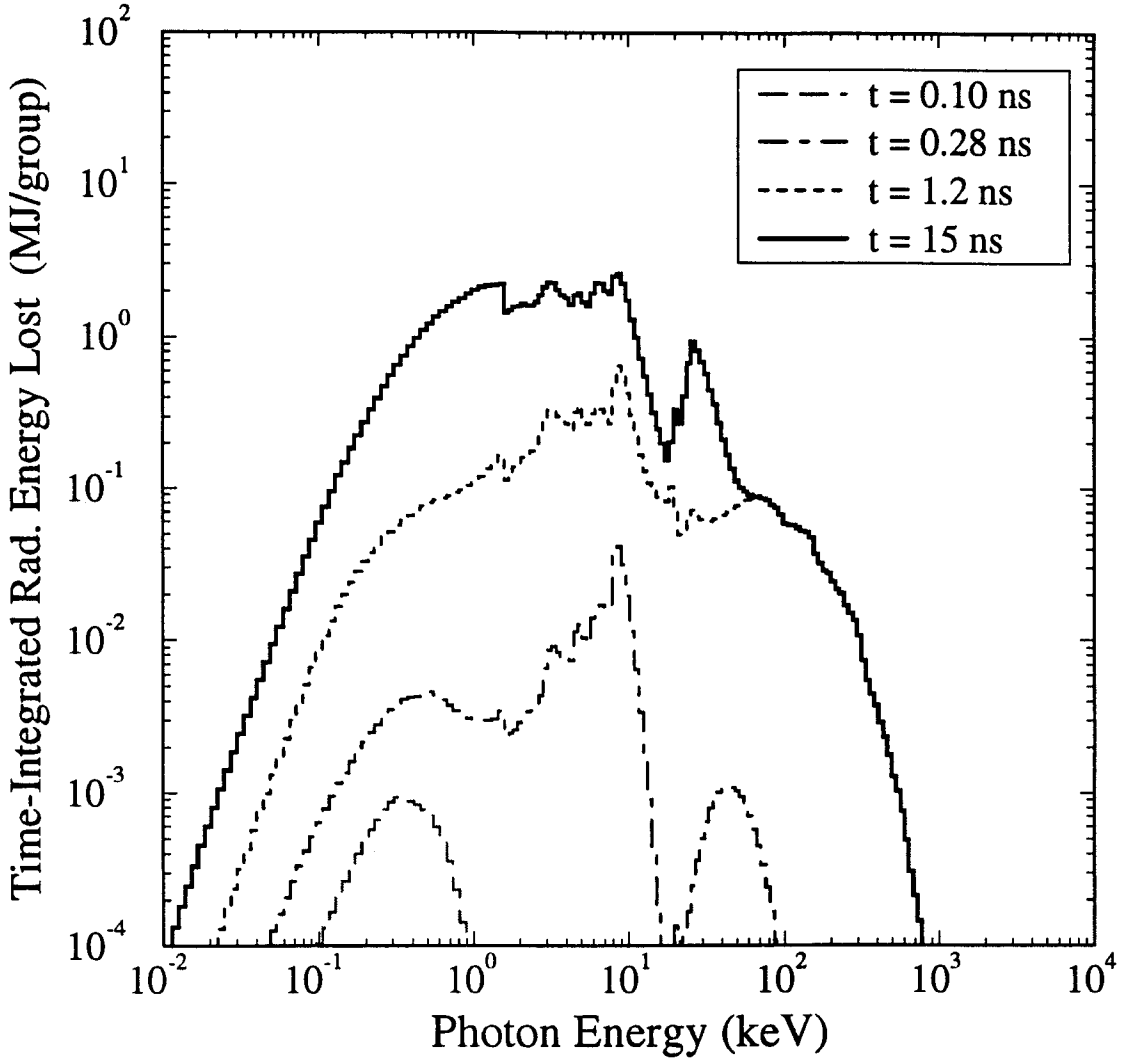

Figure 4.3.5. Time-integrated spectra of radiation emitted from the target boundary at several simulation times.

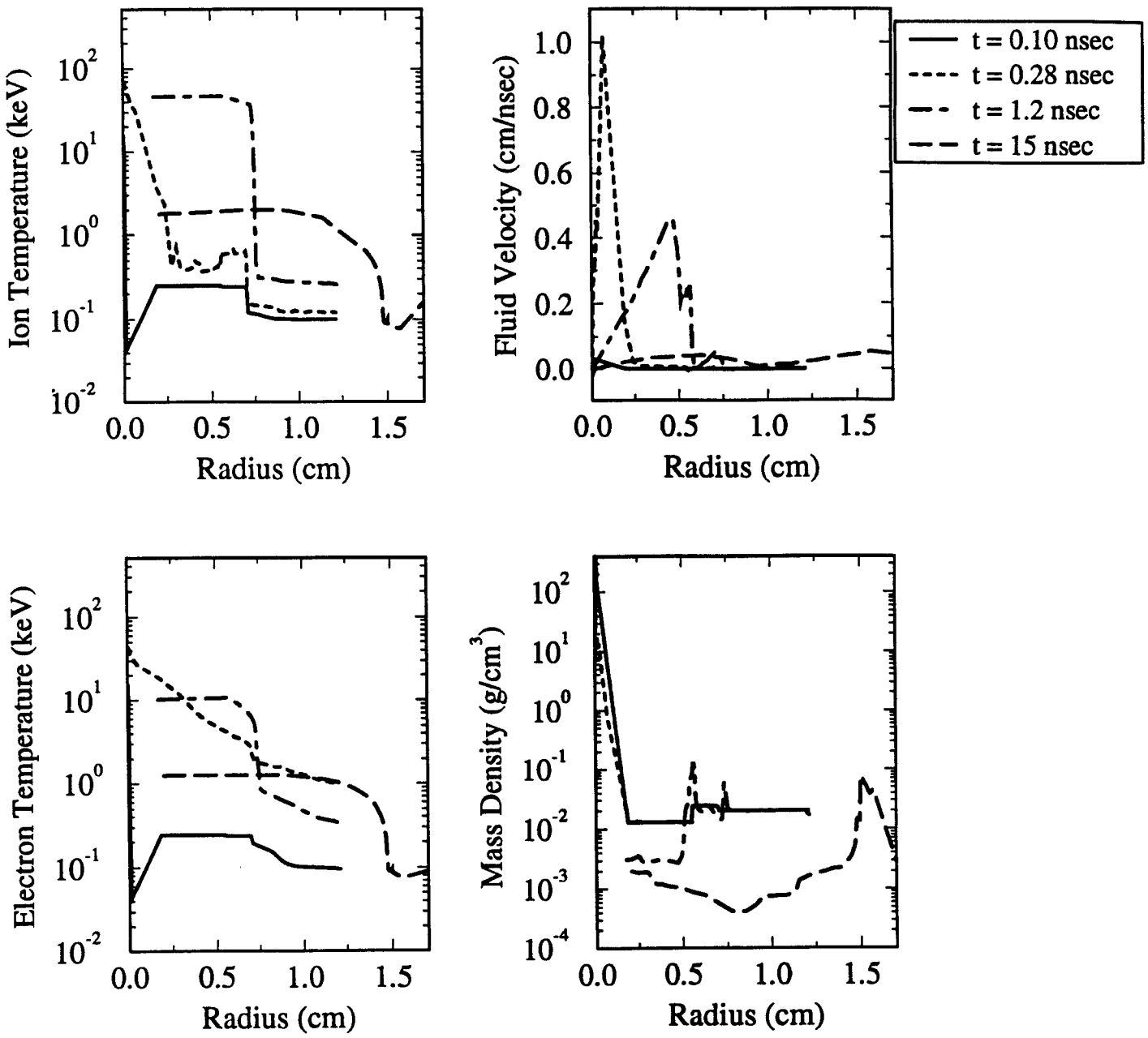

Figure 4.3.6. Radial profiles of ion temperature, electron temperature, fluid velocity, and mass density at several simulation times.

target at several simulation times. Figure 4.3.6 shows radial profiles for the ion and electron temperatures, fluid velocity, and mass density at several simulation times.

The fusion burn phase lasts approximately 200 ps and produces a peak ion temperature in the DT fuel of about 300 keV. The DT expands rapidly outward, converting its internal energy into kinetic energy. Note that at 0.4 ns, 98 MJ (or roughly 80% of the total α-particle energy released by the DT fuel) is in the form of kinetic energy (almost all of it in the DT). Figure 4.3.1 shows a strong shock propagating radially outward through the outer CH, C, and Pb regions. Shortly after the shock enters the Pb region, somewhat more than half of the DT kinetic energy has been converted back into internal energy throughout the target.

The radiation flux from the target is characterized by two main peaks (Fig. 4.3.3). The first occurs from about 0.2 to 0.5 ns, and is due to hard x-rays emitted directly from the high-temperature DT. By this time, the DT has a significantly larger radius than near the start of ignition, and therefore has a larger radiating surface area. By 1 ns, about 11% of the total α-particle energy generated during the burn phase (i.e., about 13 MJ) escapes the target in the form of hard x-rays. Fig. 4.3.4 shows that virtually all hard x-rays with $h\nu \gtrsim 50$ keV are emitted by this time.

A burst of softer x-rays is emitted from the target from about 1.5 to 5 ns. These x-rays in large part originate in the Pb region, where electron temperatures reach as high as several keV during this time (see Fig. 4.3.5). By 5 ns, a total of 85 MJ has been radiated from the target, and by the end of the simulation (t = 20 ns) a total of 97 MJ of radiative energy has escaped the target. The frequency dependence of the escaping radiation (Fig. 4.3.4) shows the bulk of the radiation comes out between 10^{-1} and 10^{2} keV, with the spectrum being clearly non-Planckian. The structure seen in the spectra is due to the fact that the temperature in the Pb region decreases as the radius increases. These features are thus due to absorption (as opposed to emission), which result from cooler regions absorbing radiation emitted from the higher temperature Pb at smaller radii. In particular, the Pb M-shell and L-shell photoabsorption edges can be seen near 1.6 and 10 keV, respectively.

Table 4.3.1. Debris Ion Kinetic Energies

Species	Energy (MJ)	Energy per Ion (keV)
H	0.30	0.46
D	0.44	0.69
T	0.101	1.05
He^3	0.047	1.40
C	2.25	10.9
Pb	17.3	309

Table 4.3.2. Results for LIBRA-SP Target Burn Simulation

	PHD-IV Results	Corrected for Neutron Reabsorption
Total yield	589 MJ	589 MJ
Neutron yield	472 MJ	383 MJ
X-ray yield	97 MJ	1687 MJ
Debris ion yield	20 MJ	35 MJ
Energy lost in endoergic reactions	–	4 MJ

By the end of the simulation a total of 20 MJ remains in the form of kinetic (debris ion) energy. The partioning of the energy between the various target ion species in the PHD-IV simulation is shown in Table 4.3.1. The debris ion energy, along with the time- and frequency-dependent x-ray spectra, are then used in the LIBRA-SP target chamber simulations to determine the response of the PERIT units and LiPb liquid jet shield to the target explosion. Note that the results listed in Table 4.3.1 do not include the effects of neutron energy deposition within the target.

The overall partitioning of energy at the end of the PHD-IV simulation is shown in Table 4.3.2. Also shown in the right column are the values corrected for the redeposition of neutron energy within the target. Details of the neutron transport calculation are discussed in the next section. Overall, approximately 65% of the total energy released by the high-gain target escapes the target in the form of neutrons, while the x-ray and debris ion energy account for 28% and 6% of the energy release, respectively.

Table 4.4.1. Target Data at Ignition

Region	Material	Density (g/cm^3)	Radius Range (cm)
1	DT	230	0-0.0173
2	CH	0.013	0.0173-0.55
3	C	0.024	0.55-0.6983
4	Pb	11.4	0.6983-0.7

4.4. Target Neutronics

The initial split of energy from a DT fusion reaction is one 14.1 MeV neutron and one 3.5 MeV alpha particle. In an inertial confinement fusion reactor, the DT fuel is heated and compressed to extremely high densities before it ignites. Therefore, neutron fuel interactions cannot be neglected. This results in significant softening of the neutron spectrum as a result of elastic and inelastic collisions with the target constituent materials. In addition, neutron multiplication occurs as a result of (n,2n) and (n,3n) reactions and gamma photons are produced. The energy deposited by the neutrons and gamma photons heats the target and ultimately takes the form of radiated x-rays from the hot plasma and expanding ionic debris.

Neutronics calculations have been performed for the LIBRA-SP target using the one-dimensional discrete ordinates code ONEDANT [17]. The LIBRA-SP target utilizes 5 mg of DT fuel. Although the DT fuel areal density (ρR) value changes during ignition, a value of 4 g/cm^2 is used in the target neutronics calculations. This is representative of the temporal average during ignition and burn. The target data at ignition used in the calculations are given in Table 4.4.1. The calculations were performed using spherical geometry and 30 neutron - 12 gamma group cross section data based on the ENDF/B-VI nuclear data evaluation [18]. A uniform 14.1 MeV neutron source was used in the compressed DT fuel zone.

Due to (n,2n) and (n,3n) reactions occurring in the target, 1.073 neutrons are emitted from the target for each DT fusion reaction. These neutrons carry an energy of 11.43 MeV implying that the average energy of neutrons emitted from the target is 10.65 MeV. It is

Table 4.4.2. Nuclear Energy Deposition in Target

Region 1	2.53896 MeV/DT fusion
Region 2	0.00345 MeV/DT fusion
Region 3	0.00039 MeV/DT fusion
Region 4	0.00002 MeV/DT fusion
Total	2.54282 MeV/DT fusion

interesting to note that only 61.2% of the neutrons emitted from the target are uncollided 14.1 MeV neutrons. For each DT fusion reaction, 0.0005 gamma photons are emitted from the target with an average energy of 2.4 MeV. The energy spectra of neutrons and gamma photons emitted from the LIBRA-SP target are shown in Figs. 4.4.1 and 4.4.2, respectively.

The total energy deposited by neutrons and gamma photons in the target was calculated to be 2.543 MeV per DT fusion. Almost all of the energy is deposited in the DT fuel zone as demonstrated by the results in Table 4.4.2. This is a direct result of the relatively large ρR value for the DT fuel region. When the 3.5 MeV energy carried by the alpha particle emerging from the fusion reaction is added, a total energy of 6.043 MeV per DT fusion is found to be carried by x-rays and target debris following the microexplosion. Performing an energy balance for the target indicates that 0.127 MeV of energy is lost in endoergic reactions per DT fusion. The detailed partitioning of the energy produced from the target is listed in Table 4.4.3. For the LIBRA-SP DT fuel yield of 589 MJ, the target yield is calculated to be 584.8 MJ. The neutron and gamma yields are 382.5 and 0.04 MJ, respectively, while the combined x-ray and debris yield is 202.3 MJ.

4.5. Discussion and Future Work

We have performed preliminary calculations for the fusion burn and microexplosion of the LIBRA-SP target. Our results predict a total of 589 MJ of fusion energy is released, providing a gain of 82. The energy released in the form of neutrons is 383 MJ (65%). The bulk of this energy, because of the relatively long mean free paths of neutrons, is deposited

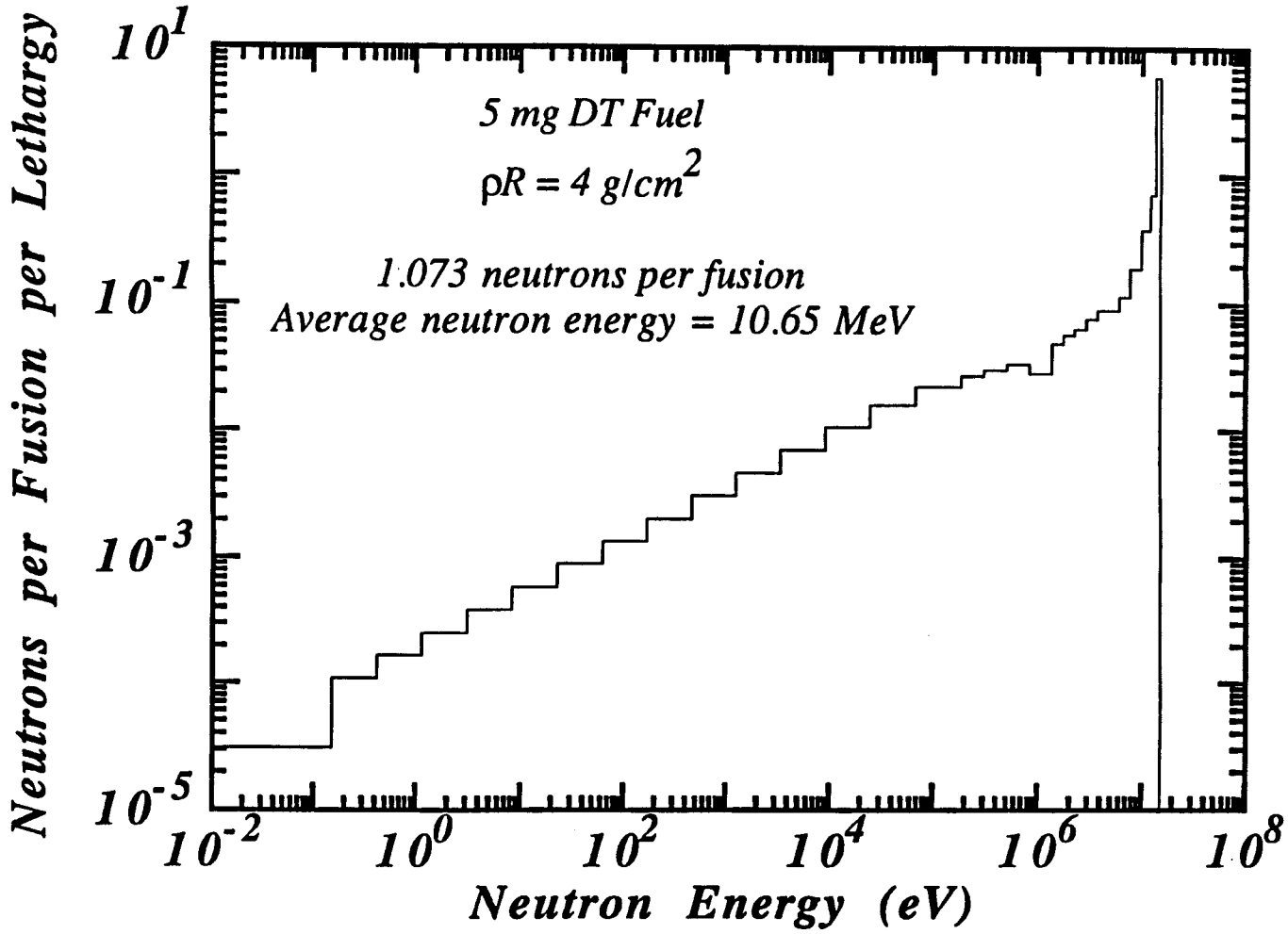

Figure 4.4.1. Energy spectrum of neutrons emitted from the LIBRA-SP target.

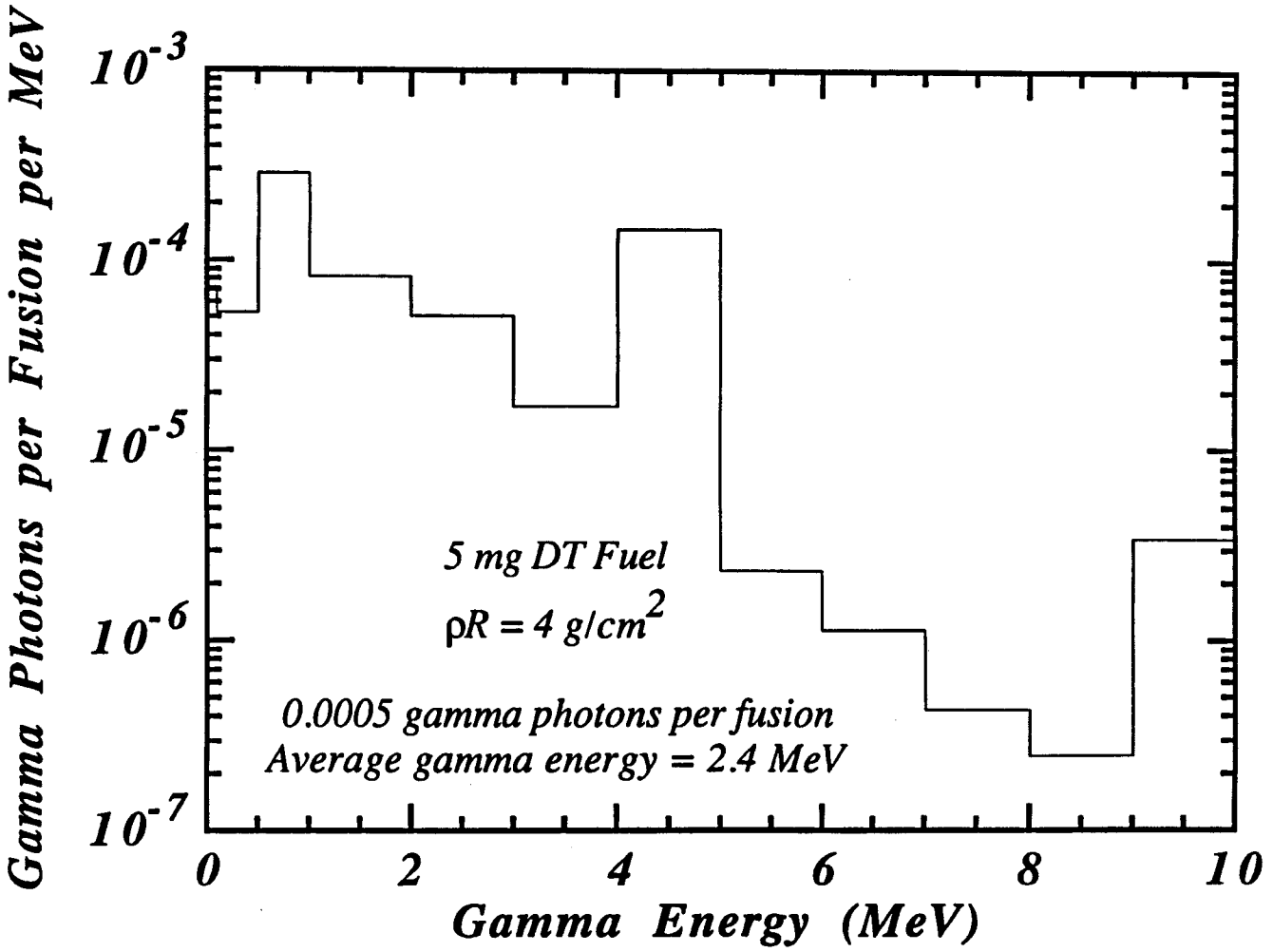

Figure 4.4.2. Energy spectrum of gamma photons emitted from LIBRA-SP target.

Table 4.4.3. Energy Partitioning from LIBRA-SP Target

Fusion energy	17.6 MeV/DT fusion
Energy carried by neutrons	11.429 MeV/DT fusion (64.94%)
Energy carried by gamma photons	0.001 MeV/DT fusion (0.006%)
Energy carried by x-rays and debris	6.043 MeV/DT fusion (34.34%)
Energy lost in endoergic reactions	0.127 MeV/DT fusion (0.72%)

in the LiPb blanket (PERIT units). Approximately 28% (167 MJ) of the target energy is emitted in the form of x-ray radiation, while 6% (35 MJ) is released in the form of debris ion kinetic energy. The x-ray and debris energy is stopped within the first few microns of the LiPb liquid jets located in front of the PERIT units. The response of the jets to the target x-ray and debris will be addressed elsewhere.

The purpose of these calculations has been to make quantitative predictions for the release of energy from high-gain ICF targets. However, much work remains to be done. Implosion calculations must be done to determine an accurate picture of the target conditions at the start of ignition. In addition, a more accurate, self-consistent simulation of the fusion target microexplosion requires the modeling of the reabsorption of neutron absorption within the target. It is anticipated that these items will be addressed in future work.

4.6. Target Injection

The LIBRA-SP target is injected into the target chamber with the proper positioning and timing to be irradiated with the driver beams with proper symmetry to ignite the target. The injection is made from a point near the equator of the target chamber, as shown in Fig. 4.6.1. The injection system includes a pneumatic gun, sabot and sabot catcher, a tracking system and a target. The heating of the target is much less severe than in previously published works because the previously classified target design insulates the cryogenic capsule

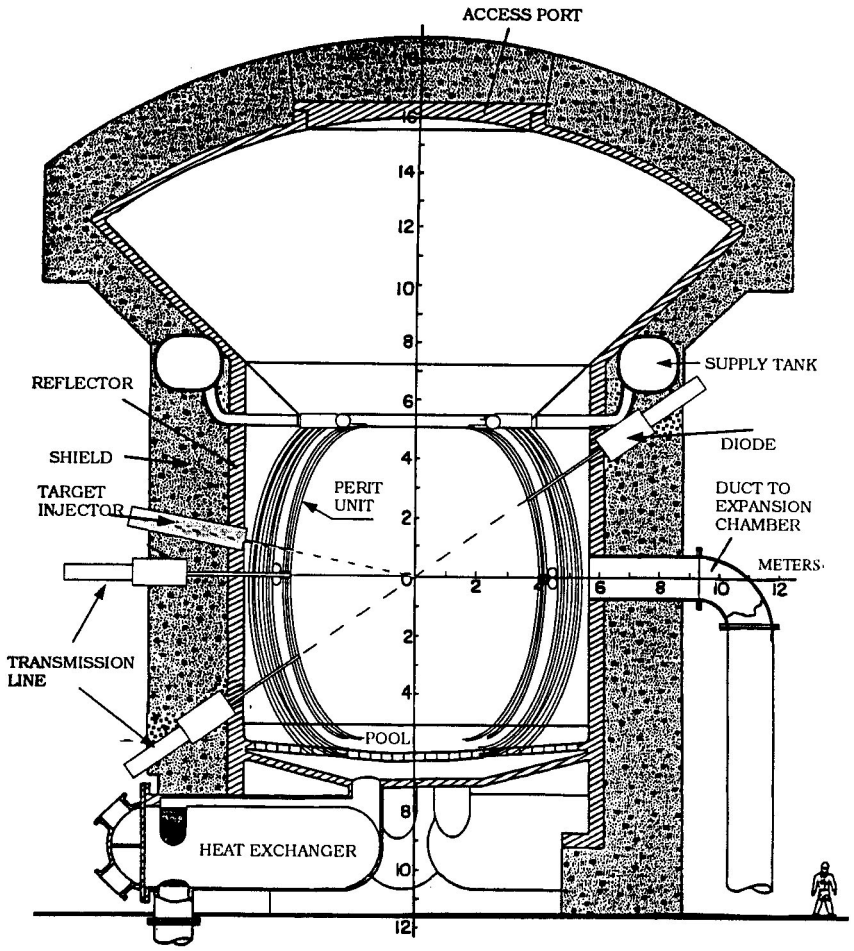

Figure 4.6.1. Cross-sectional picture of target chamber of LIBRA-SP, showing position of target injector gun and flight path of target.

very well from the chamber environment. This frees the design of the injector system. Parameters for this system have been adjusted for the LIBRA-SP conditions.

The pneumatic gun has been investigated for the HIBALL reactor [19] and we have decided to use the same system, with the parameters adjusted to the LIBRA-SP conditions. The gun parameters are given in Table 4.6.1, where the parameters for LIBRA-SP are compared with those for HIBALL. Since the distance to be traveled is less and the target heating constraint is less restrictive, we can reduce the gun muzzle velocity for LIBRA-SP. This leads to a reduced acceleration applied to the target. The ability of the target to survive acceleration is an outstanding critical issue, so a reduction in the acceleration makes

Table 4.6.1. Target Injection Parameters

	HIBALL	LIBRA-SP
Longitudinal positioning tolerance	0.5 mm	0.25 mm
Lateral positioning tolerance	0.7 mm	0.19 mm
Distance from muzzle to target	12 m	9 m
Target speed	200 m/s	100 m/s
Projectile mass (target + sabot)	2 g	2 g
Gas pressure	0.5 MPa	0.25 MPa
Gas species	D_2	D_2
Gas entering target chamber per shot	1.6 mg	0.8 mg
Acceleration distance	2 m	2 m
Acceleration	10^4 m/s^2	5×10^3 m/s^2
Acceleration time	20 ms	28 ms
Total target travel time	80 ms	118 ms

the system more credible. Another constraint is the positioning tolerance of the target. In the end, if it is found that the target can survive higher acceleration, the gun barrel can be shortened. Lower injection velocities lead to tighter tolerances on the longitudinal target positions because beam tracking is used to synchronize the driver firing with the target, whose position is sensed by a tracking system. Lower accelerations lead to lower gun gas pressures and less material puffed into the chamber by the gun.

The target tracking system, whose parameters are given in Table 4.6.2, is taken to be the same as in HIBALL [20]. Recent work in the Airborne Laser Program [21] has shown that very high resolution tracking is possible. The tracking tolerances required for LIBRA-SP are possible using methods devised for the ALP. The methods have been adapted to ICF [22], where the tracking is done before the target enters the target chamber using a laser Doppler method for the target velocity and sets of crossed lasers to measure time and position of the target. Because the tracking is outside of the target chamber in LIBRA-SP, the distance traveled after the last tracking measurement is much longer than in HIBALL, where the tracking occurred in the chamber. This method avoids subjecting the lasers to the harsh target chamber environment.

Table 4.6.2. Target Tracking Parameters

	HIBALL	LIBRA-SP
Lateral tracking	none	none
Distance traveled after tracking	3 m	10 m
Precision of arrival time	± 1 μs	± 2 μs

The heating of the target during injection is not severe for LIBRA-SP because of the target design shown in Fig. 4.6.2. The very low thermal diffusivity of the low density carbon foam insulates the cryogenic capsule from thermal conduction. Heat transfer calculations show that little heat is conducted through the foam. The insulation is so good that heat from the β decay of tritium in the capsule is a potentially greater concern to the target survival. In future considerations we plan to study the β decay heating and devise a method of increasing the conductivity of the foam. With the modified target design, we will perform heat transfer calculations including the β decay heating and the external heat sources.

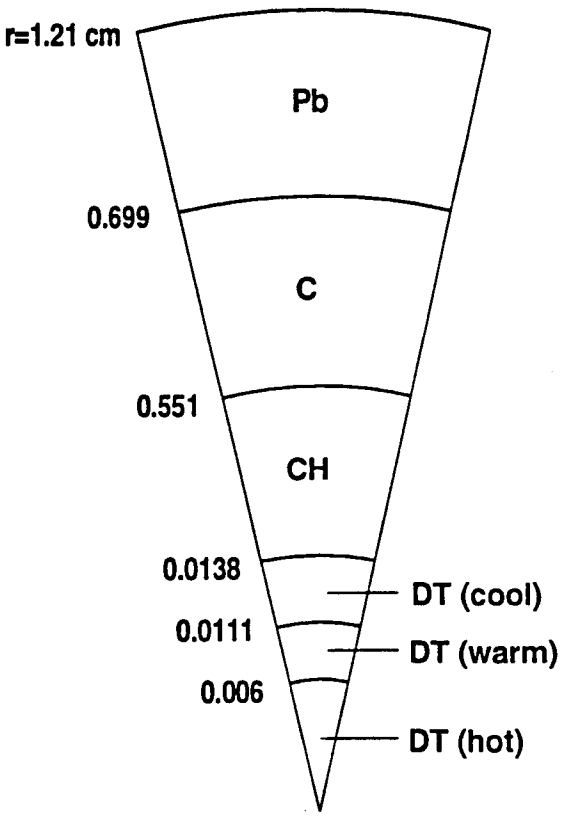

Mass (mg)	Material	T (keV)	ρ (g/cm^3)
120	Pb	0.1	0.020
17.4	C	0.25	0.024
9.1	CH	0.25	0.013
4.2	DT (cool)	0.1	800
0.8	DT (warm)	0.5	166
0.0045	DT (hot)	8	50

Figure 4.6.2. The LIBRA-SP target.

References for Section 4

1. B. Badger et al., "LIBRA – A Light Ion Beam Fusion Conceptual Reactor Design," University of Wisconsin Fusion Technology Institute Report, UWFDM-800 (revised Feb. 1990).
2. B. Badger et al., "HIBALL – A Conceptual Heavy Ion Beam Driven Fusion Reactor Study, Preliminary Report," University of Wisconsin Fusion Technology Institute Report UWFDM-450 and KfK-3202.
3. I. N. Sviatoslavsky, et al., "A Near Symmetrically Illuminated Direct Drive Laser Fusion Power Reactor-SIRIUS-P," Eleventh Topical Meeting on the Technology of Fusion Energy, New Orleans, LA, June 1994.
4. G. L. Kulcinski, et al., "Evolution of Light Ion Driven Fusion Power Plants Leading to the LIBRA-SP Design," Eleventh Topical Meeting on the Technology of Fusion Energy, New Orleans, LA, June 1994.
5. R. Olson, private communication, 1994.
6. G. A. Moses, G. Magelssen, R. Israel, T. Spindler, and B. Goel, "PHD-IV – A Plasma Hydrodynamics, Thermonuclear Burn, Radiative Transfer Computer Code," University of Wisconsin Fusion Technology Institute Report UWFDM-194, Aug. 1985.
7. P. Wang, "EOSOPA – A Code for Computing the Equations of State and Opacities of High-Temperature Plasmas with Detailed Atomic Models," Fusion Power Associates Report FPA-93-8, Dec. 1993.
8. B. Badger et al., "LIBRA-LiTE – A Commercial Light Ion Fusion Power Plant," FPA-91-4 and University of Wisconsin Fusion Technology Institute Report UWFDM-880, Dec. 1991.
9. R. Olson, private communication, 1994.
10. G. A. Moses, R. R. Peterson, and T. J. McCarville, "MF-FIRE – A Multifrequency Radiative Transfer Hydrodynamics Code," *Comput. Phys. Commun.*, **36**, 249 (1985). R. R. Peterson, J. J. MacFarlane, and G. A. Moses, "CONRAD – A Combined

Hydrodynamics-Condensation/Vaporization Computer Code," University of Wisconsin Fusion Technology Institute Report UWFDM-670 (revised July 1988).

11. D. A. Liberman, *Phys. Rev.*, **B20**, 4981 (1979).
12. D. G. Hummer and D. Mihalas, *Ap. J.*, **331**, 794 (1988).
13. C. Bauche-Arnoule, J. Bauche, and M. Klapisch, *Adv. At. Mol. Phys.*, **23**, 131 (1988).
14. P. Wang and J. J. MacFarlane, Third International Opacity Workshop and Code Comparison Study, MPI Quantenoptik, Garching, March 7-11, 1994.
15. C. A. Iglesias, F. J. Rogers, and B. G. Wilson, *Ap. J. Lett.*, **322**, L45 (1987).
16. A. Bar-Shalom, J. Oreg, W. H. Goldstein, D. Sharis, and A. Zigler, *Phys. Rev.*, **A40**, 3183 (1989).
17. R. O'Dell et al., "User's Manual for ONEDANT: A Code Package for One-Dimensional, Diffusion-Accelerated, Neutral Particle Transport," Los Alamos National Laboratory, LA-9184-M, 1989.
18. P. F. Rose, "ENDF/B-VI, The U.S. Evaluated Nuclear Data Library for Neutron Reaction Data," Summary Documentation Report ENDF 201, U.S. National Nuclear Data Center, 1992.
19. R. Kreutz, "Pellet Delivery for the Conceptual Inertial Fusion Reactor HIBALL," *Fusion Tech.* **8**, 2708 (1985).
20. M.J. Monsler, "Laser Fusion: An Assessment of Pellet Injection, Tracking and Beam Pointing," Technology of Controlled Nuclear Fusion (Proc. 3rd Mtg. Santa Fe, 1978) American Nuclear Soc. (1978) 1186.
21. Airborne Laser Laboratory, Rep. AFWL-TC-8C, Kirtland Air Force Base, Albuquerque, NM (1988).
22. M.J. Monsler in "Energy from Inertial Fusion," IAEA, Vienna, Austria (1995), p. 175.

5. Design of PERIT Units

5.1. Overall Design

LIBRA-SP is a conceptual design study of an inertially confined 1000 MWe fusion power reactor utilizing self-pinched light ion beams. There are 24 ion beams altogether. Figure 5.1.1 is a cross sectional view of the reaction chamber which is an upright cylinder with an inverted conical roof resembling a mushroom, and a pool floor. The vertical sides of the cylinder are occupied with a blanket zone consisting of many perforated rigid ferritic steel tubes with a packing fraction of about 50% through which the breeding/cooling material, liquid lead-lithium, flows. This blanket zone, besides breeding T_2 and converting neutronic energy to thermal energy, also provides protection to the reflector/vacuum chamber so as to make it a lifetime component. The distance from chamber center to the first row of tubes is 4.0 m, the thickness of the blanket zone is 1.25 m and the length of the tubes is 10.4 m in two segments of 5.2 m each between supports. The perforated rigid tubes are called PERIT (Perforated Rigid Tubes) units and are made of solid HT-9 ferritic steel. The idea behind this concept is to make the tubes rigid and not flexible, as in LIBRA-LiTE's INPORT units, so they can withstand shock, and to make them perforated so they can maintain a wetted surface through the jet fan spray. There are two rows of 7 and 8 cm diameter PERIT units arranged at 14 cm between centerlines at midplane in the circumferential direction as well as between rows. These front tubes are configured to totally shadow the rear zone, and the spaces between the rows are determined from dynamic motion considerations. The rear tubes are 15 cm in diameter and there are 7 rows of them. Their sole function is to transport the PbLi which moderates neutrons and breeds T_2. Behind the blanket is a 50 cm thick HT-9 ferritic steel reflector which is also the vacuum boundary. Finally, the whole chamber is surrounded by a steel reinforced concrete shield which varies in thickness from place to place but is nominally 2.7 m.

Figure 5.1.1 also shows vacuum tubes located behind the shield/blanket zone at the chamber midplane. There are six such tubes leading to an expansion tank situated below the reaction chamber. The function of this tank is to provide volume for the vapor to expand

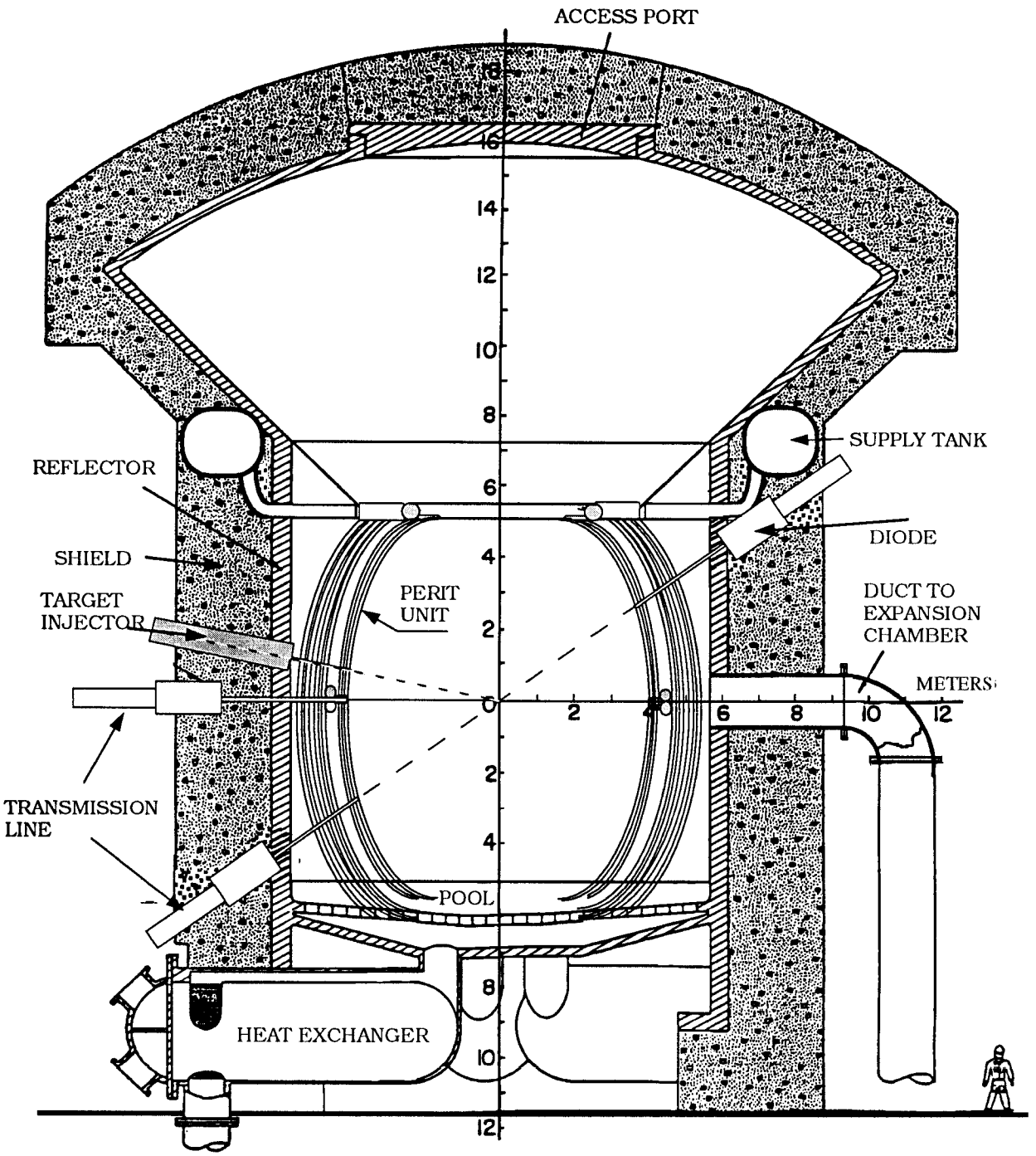

Figure 5.1.1. Cross-sectional view of the reactor chamber.

into, following a shot. As the vapor flows into the expansion tank it exchanges heat with the PERIT units, and cools itself by virtue of an isentropic expansion. Vacuum pumps which are attached to the expansion tank then evacuate the noncondensable species in preparation for the next shot.

The chamber roof is not protected with PERIT units and for this reason is removed to a distance of 16 m from the target, also making it a lifetime component. The roof with its integral shield is designed to be removed to provide access during internal reactor chamber component maintenance. Since the roof will be cooled, it also will condense vapor and have a wetted surface which will be vaporized after each shot. Another function of the mushroom shape is to protect the side walls which are shadowed by the PERIT units and to provide additional volume in the chamber for the vapor to expand into.

Figure 5.1.2 shows the distribution of PERIT units and the shield/blanket zone at midplane. Figure 5.1.3 shows a view of one of the PERITs feed/return arrangement. PERITs are made of ferritic steel HT-9 consisting of two tubes stacked on top of each other; each is 5.30 m long and has an inner bore of 7 cm and an outer diameter of 7.6 cm. Each segment of the cooling tubes has a separate manifold at its top end. The coolant feed pumps only supply the liquid metal to the open liquid tank at the top of each segment group. The liquid metal flows under the effect of gravity down the coolant tubes and through the perforations. A very thin sheet of liquid metal that jets from the tube's perforations (fan sheet spray) is provided at a short distance from the tube to be the first defense against target x-rays and microexplosion debris. Figure 5.1.4 is a view of three of the PERIT units showing these fan sheet sprays. The rest of the shield/blanket zone is made of ferritic steel HT-9. The PbLi coolant enters the reactor at 370°C and exits at an average temperature of 500°C. After flowing through the PERIT and shield/blanket zone the PbLi collects in the bottom pool. The collected PbLi drains through a perforated plate into a sump leading to the intermediate heat exchangers (IHX) located in the base of the chamber. In the IHX the PbLi exchanges heat with liquid PbLi, which in turn is pumped to a steam generator. A fraction of the PbLi

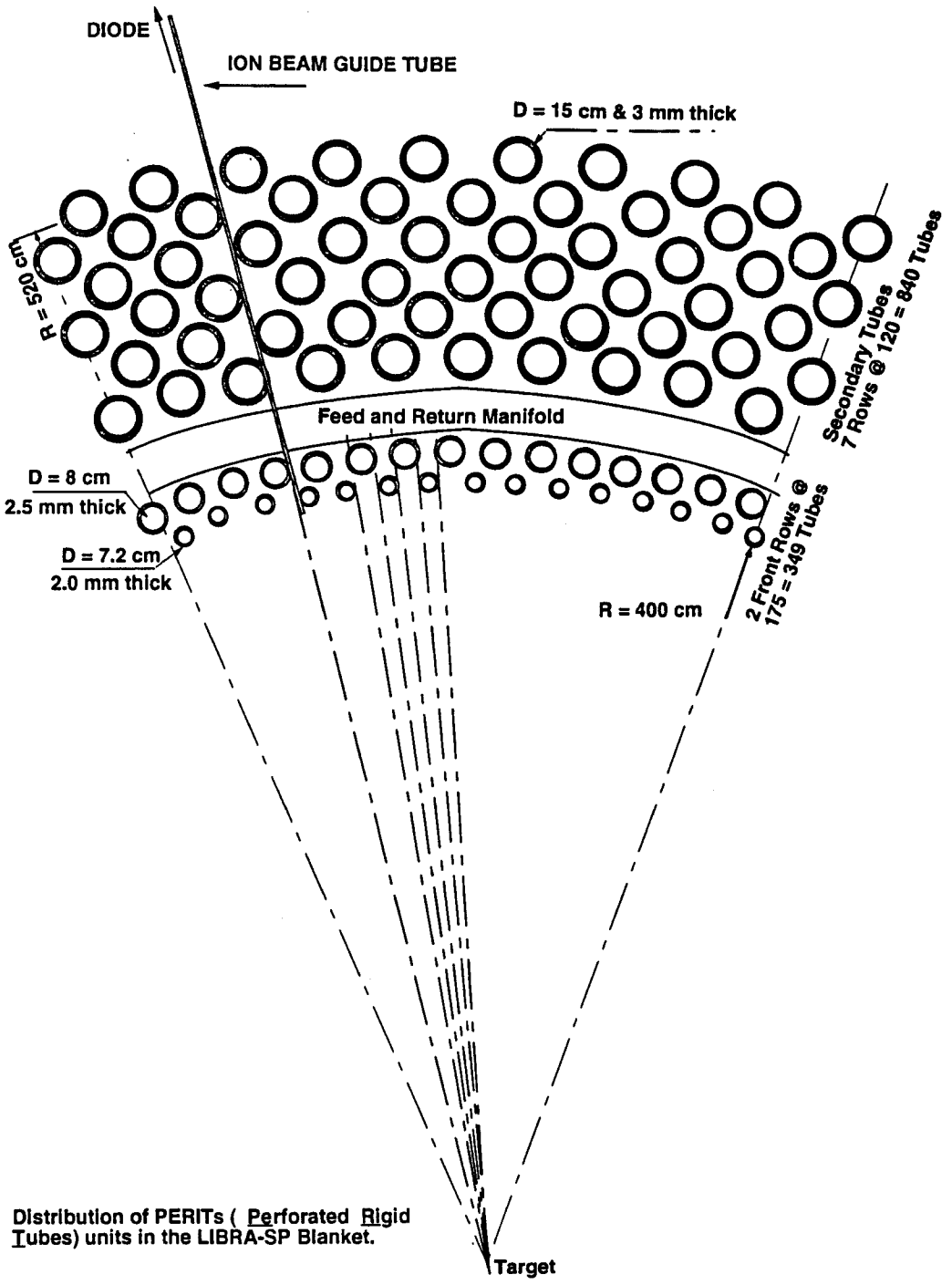

Figure 5.1.2. The distribution of PERIT units and the shield/blanket zone.

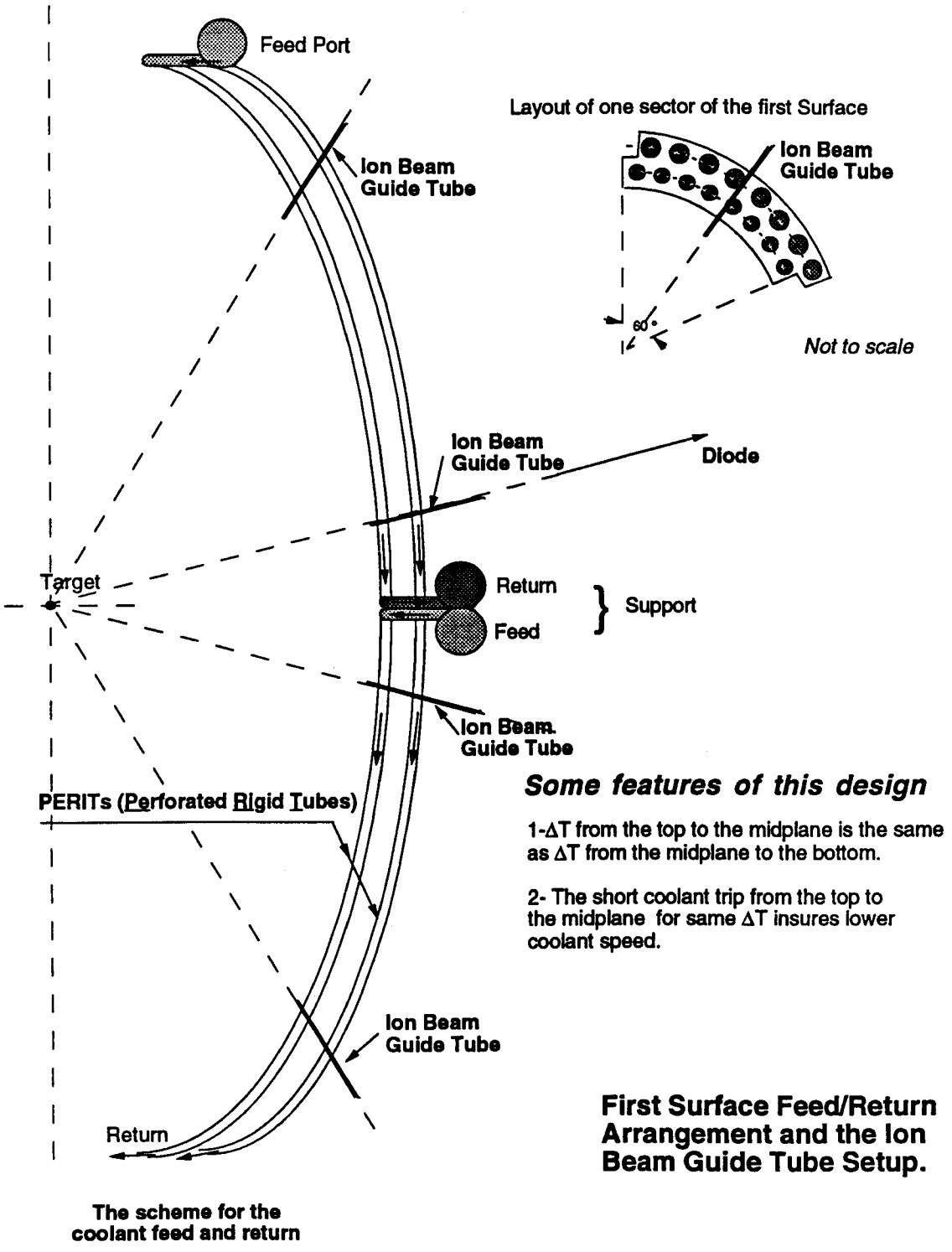

Figure 5.1.3. First surface feed/return arrangement.

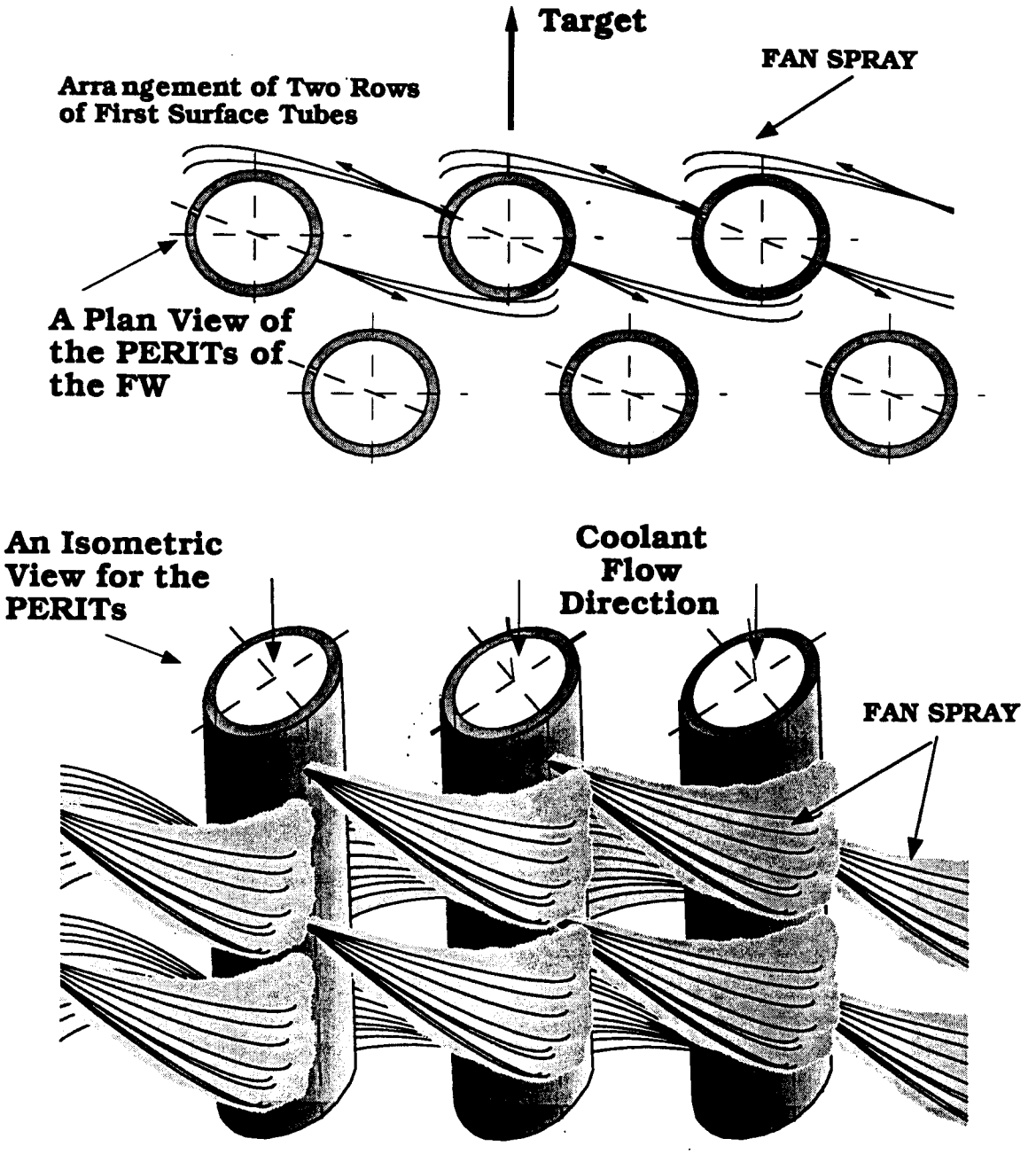

Figure 5.1.4. First surface protection by fan sheet spray.

flow is diverted to a T_2 removal system. Steam is used in a double reheat cycle to generate electricity at 43% efficiency.

5.2. First Surface Support

The first surface is the first two rows of the PERIT units. The support takes the shape of a cage that conforms with the shape of the coolant tubes. Figure 5.2.1 shows a general sketch of the cage. Note that it is shaped like a barrel with two supporting rings at the midplane. The top ring holds the end of the top segment of the first two rows of the PERIT units. Similarly, the lower ring holds the beginning of the bottom segment of the PERIT units. The cage is made of HT-9 tubes that are actively cooled with LiPb. The poloidal parts are always in the shadow of the first row of coolant tubes. The supporting rings will be protected with the liquid metal sheet jet. The coolant tubes are connected to the supporting rings through a connection of the pin type that only allows rotational movement around the pin axis. Figure 5.2.2 shows some details of this pinned connection. The coolant tubes thus have fixed-fixed end boundary conditions in the circumferential direction (toroidal direction), and hinged-hinged end boundary conditions in the radial direction (poloidal direction). The supply tanks are located in the concrete shield at 12 different locations at higher level (50 cm) than the intake manifold of the coolant tubes. The coolant flows by gravity through the coolant tubes. Note that the weight of the liquid metal coolant causes enough pressure to run the system. The pumping power is needed to run the coolant through the external loops (heat exchanger, T_2 extraction,$\cdots$) and to raise the coolant to the supply tanks. The connection between the supply tank manifolds and the coolant tube inlets and exits are flexible to tolerate the movement of the tubes due to the target explosion. The cage is supported on the concrete shield. A preliminary estimate for the total amount of LiPb inside the cavity is about 250 m^3, and the volume of the HT-9 tubes is about 16 m^3.

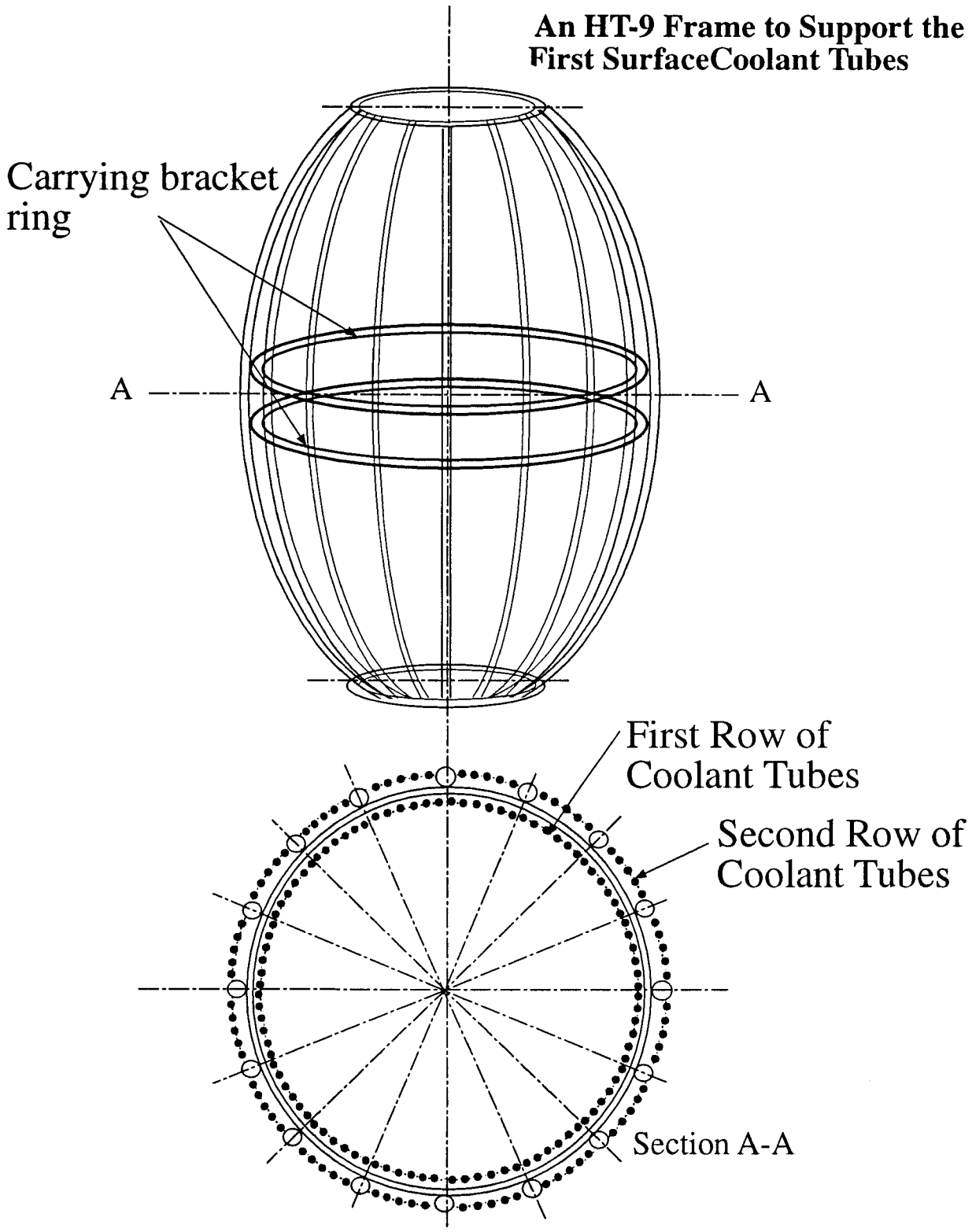

Figure 5.2.1. First surface support arrangement.

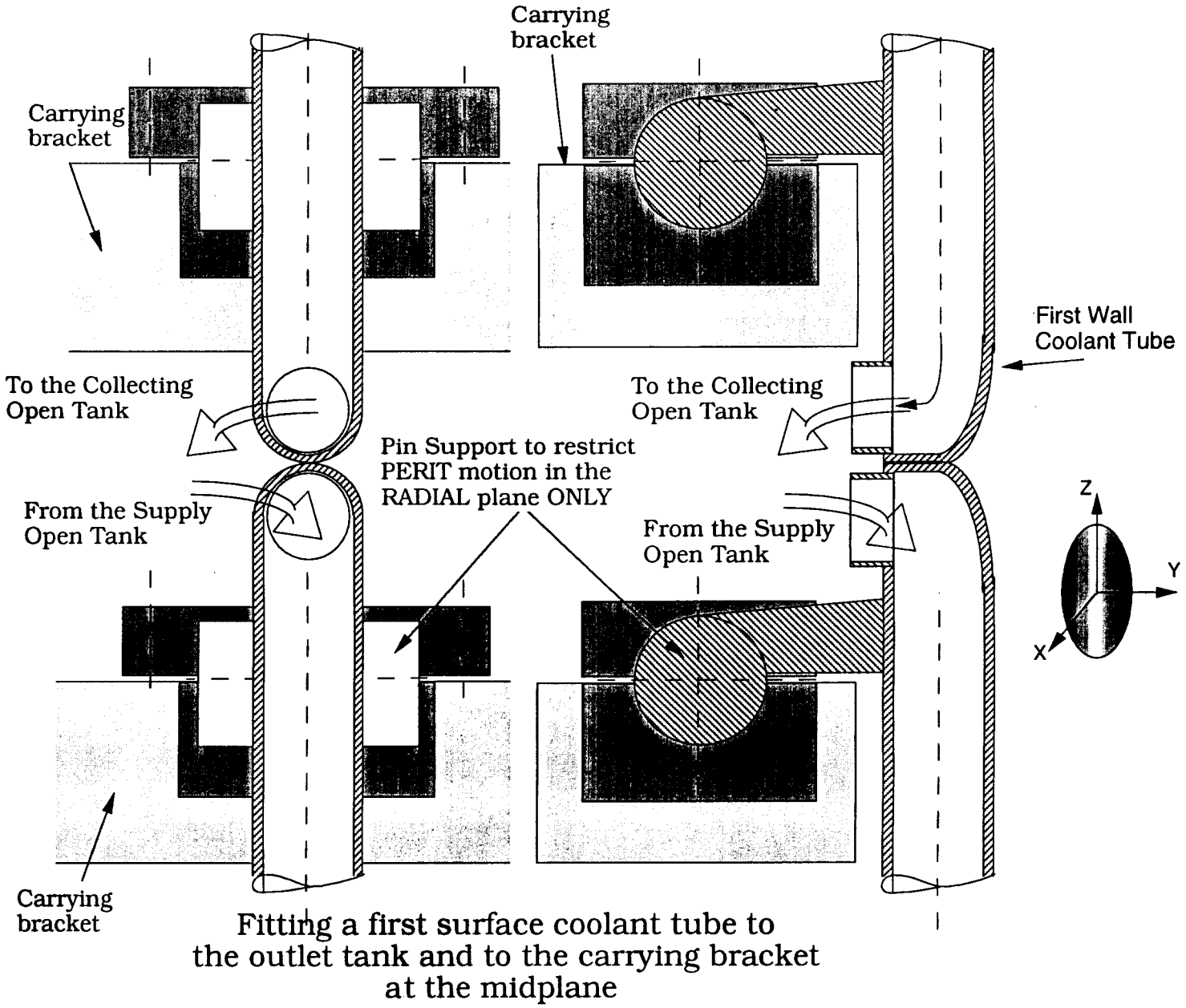

Figure 5.2.2. Pin-type connection of supporting rings to coolant tubes.

5.3. First Surface Protection

5.3.1. Motivation and Introduction

One of the major changes in the LIBRA design is the method used for the first surface protection. In the previous designs of LIBRA and LIBRA-LiTE, we flexible woven steel tubes, INPORT (INhibited flow PORous Tubes) units, are used [1,2,3]. In this way the coolant is allowed to seep through the porous wall of the flexible woven steel tube to keep the coolant tube outer surface wet all the time. The target microexplosion releases x-rays, neutrons and ion debris that deposit in the target chamber vapor and structure. The x-rays are deposited in the liquid metal film on the INPORTs and rapidly vaporizes some of the liquid. This vapor expands into the target chamber exerting a relatively high impulsive load on the INPORTs. To limit the resulting three dimensional motion of the tubes, axial tension must be applied on the INPORTs.

A major motivation for switching from the flexible woven INPORT units to the solid PERIT units is due to the uncertainty with respect to the applied tension needed for the INPORT units. This applied tension is a major input parameter in determining the natural frequency of the INPORT units and, therefore, has control on the mode and the deflection of the oscillations. Not only is it important that the tension is correct from the start of pulsing, but it is imperative that it does not change with time. A small change in the tension could drive the tubes toward the fundamental or a harmonic frequency with dire consequences to the operation of the reactor. It would be impossible to vary the tension of each individual INPORT unit during operation and even more impossible to ascertain that the tension will stay constant over time. Such uncertainty is due to the possibility that the tensioning mechanism will itself loosen, or the material properties of the tubes changing from radiation and other effects. Other second order effects, such as changes in the porosity of the woven material and deviation from a circular tube shape, have also been taken into account in making the switch from woven to solid tubes.

5.3.2. Recent Work and Discussion

LIBRA-SP uses solid coolant tubes for the first surface, blanket and shield to improve the performance of the target chamber. Shortening the coolant tube span will improve both mechanical and thermal hydraulics characteristics of the first surface tubes.

Formation of Liquid Sheets. Conventional thinking about the formation of liquid sheets may be visualized by considering a fluid that is issuing from an orifice with an elongated exit, or even from a slit, to produce the required liquid sheet which is flattened in the direction of the long axis of the orifice. But, due to surface tension and the eccentricity in the jet cross section the fluid velocity in the direction of the longest axis of the jet cross section is much greater than it is in the perpendicular direction. Energy is conserved and each particle then travels at a constant speed. Due to differences in pressure between the jet center and the jet free surface, the jet eventually will transform itself to a diverging jet with its longest axis becoming normal to the original one [4]. Practically this method is not useful.

Liquid sheets are either flat or conical. In this work, our attention will be concentrated on flat liquid sheets.

When two equal cylindrical coplanar jets collide they form an expanding sheet in the plane at right angles to the line containing their axes. If the two jets are coaxial the sheet is symmetrical so that its thickness at any point depends only on distance from the axis. This condition is sketched in Fig. 5.3.1 (a). If the jets are coplanar but not coaxial and meet at an angle 2θ the sheet formed is not symmetrical but it is flat and it bisects the angle between them. The sheet expands radially from the region of the collision and extends furthermost in the direction of the component of velocity of the jets in the plane of the sheet. This condition is indicated in Fig. 5.3.1 (b). As the angle θ decreases the extension of the sheet in the opposite direction decreases and eventually disappears leaving the sheet in the condition shown in Fig. 5.3.1 (c) [4].

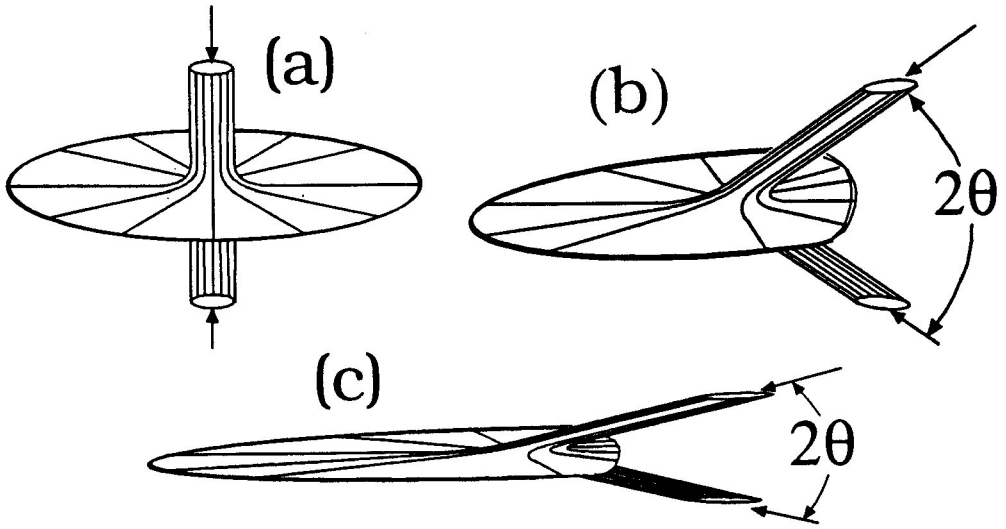

Figure 5.3.1. Sketch of sheets formed by impact of two cylindrical jets [4].

In practice, in the fan sheet nozzle, two streams of liquid are made to impinge behind an orifice by specially designed approach passages and a sheet is formed in a plane perpendicular to the plane of the streams. The principle is illustrated in Fig. 5.3.2 (a) which shows liquid flowing through a rectangular orifice formed at the end of the rectangular tube. Under these conditions the flow through the orifice is constricted in only one plane and the streamlines converge to form an origin of pressure behind the orifice. A flat sheet is produced as the liquid freely spreads through the orifice limited only by the side walls. The spreading angle of the sheet can further be increased by extending the opening to the sides of the orifice, as in Fig. 5.3.2 (b). A commercial nozzle is shown in Fig. 5.3.2 (c). It is designed on this principle, made of ceramic material and contains a rectangular orifice which is produced by the interpenetration of two rectangular slots.

In the absence of surface tension, the edges of the sheet would travel in straight lines from the orifice so that a sector of a circle would be formed. However, as a result of surface tension, the edges contract and a curved boundary is produced as the sheet develops beyond the orifice. Liquid at the edge moves along the curved boundary, and later becomes disturbed and disintegrates. When this occurs, the resulting drops sustain the direction of flow of the edge at the point at which the drops are formed and remain attached to the

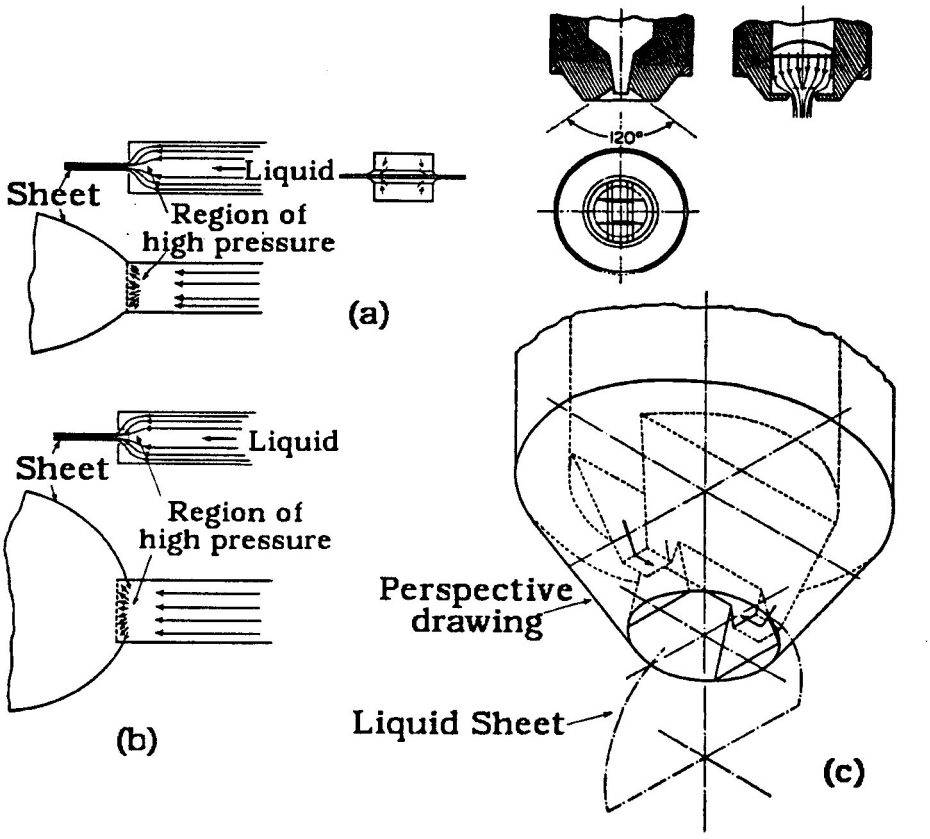

Figure 5.3.2. Sketch of mechanism of flow through fan sheet nozzles [5].

receding surface by thin threads which rapidly disintegrate into streams of drops (Fig. 5.3.3) [4]. The breakdown of the edges is restrained by viscosity. At higher injection velocities the contraction is less pronounced, and the placid sheet eventually becomes ruffled, and experiences violent oscillations due to a flag-like instability caused by the reaction of the surrounding gas with the sheet. The sheet then disintegrates before the two edges coalesce.

5.3.3. Analysis of Flow in Sheets

In order to examine the nature of the fluid stream lines in a fan sheet, investigators [4,5] have used photographs of jets containing aluminum particles. Figure 5.3.3 demonstrates the direction of flow of liquid within the sheet and as it passes through the sheet edges into the ambient atmosphere. Two points of interest can be observed:

1. The sheet streaklines are straight and unaffected by the curved boundaries.

2. The drops leave the edges tangentially at an angle different from that of the streak.

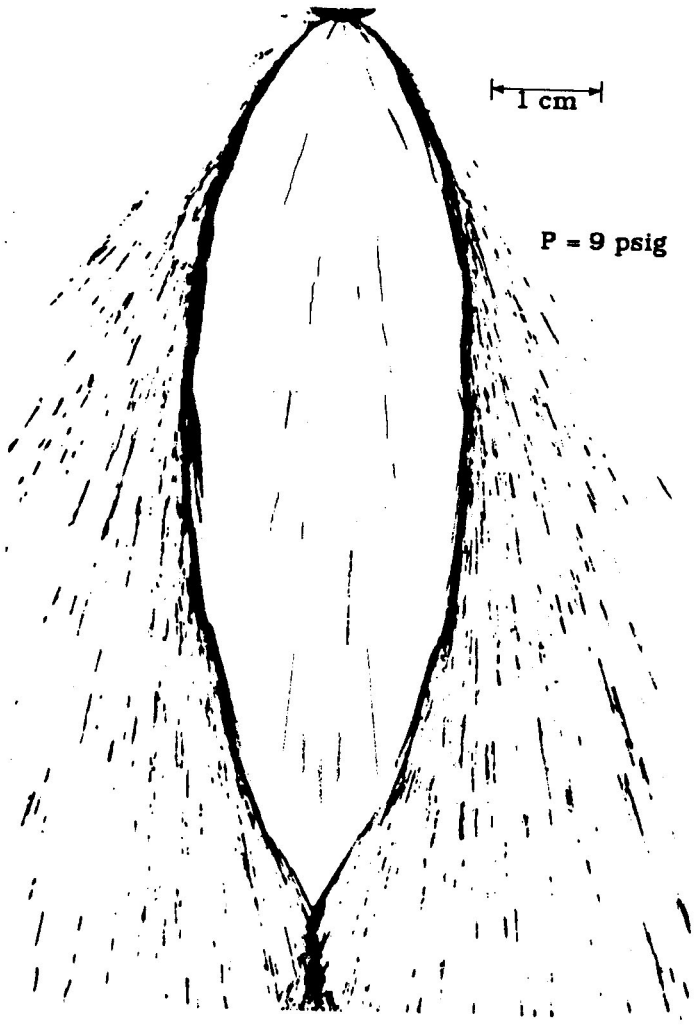

Figure 5.3.3. Streaklines in a sheet spray.

Measurements from successive photographs with different conditions indicate that the stream velocity is constant along the sheet and its absolute value depends only on the differential injection pressure.

It will be assumed for the following analysis that,

1. The liquid flows from the nozzle as if there were a line of high pressure perpendicular to the sheet.
2. The contraction of the edges by surface tension does not affect the flow pattern of the sheet, i.e. the liquid corresponding to the "vanished" part of the sheet is concentrated at the curved boundary.

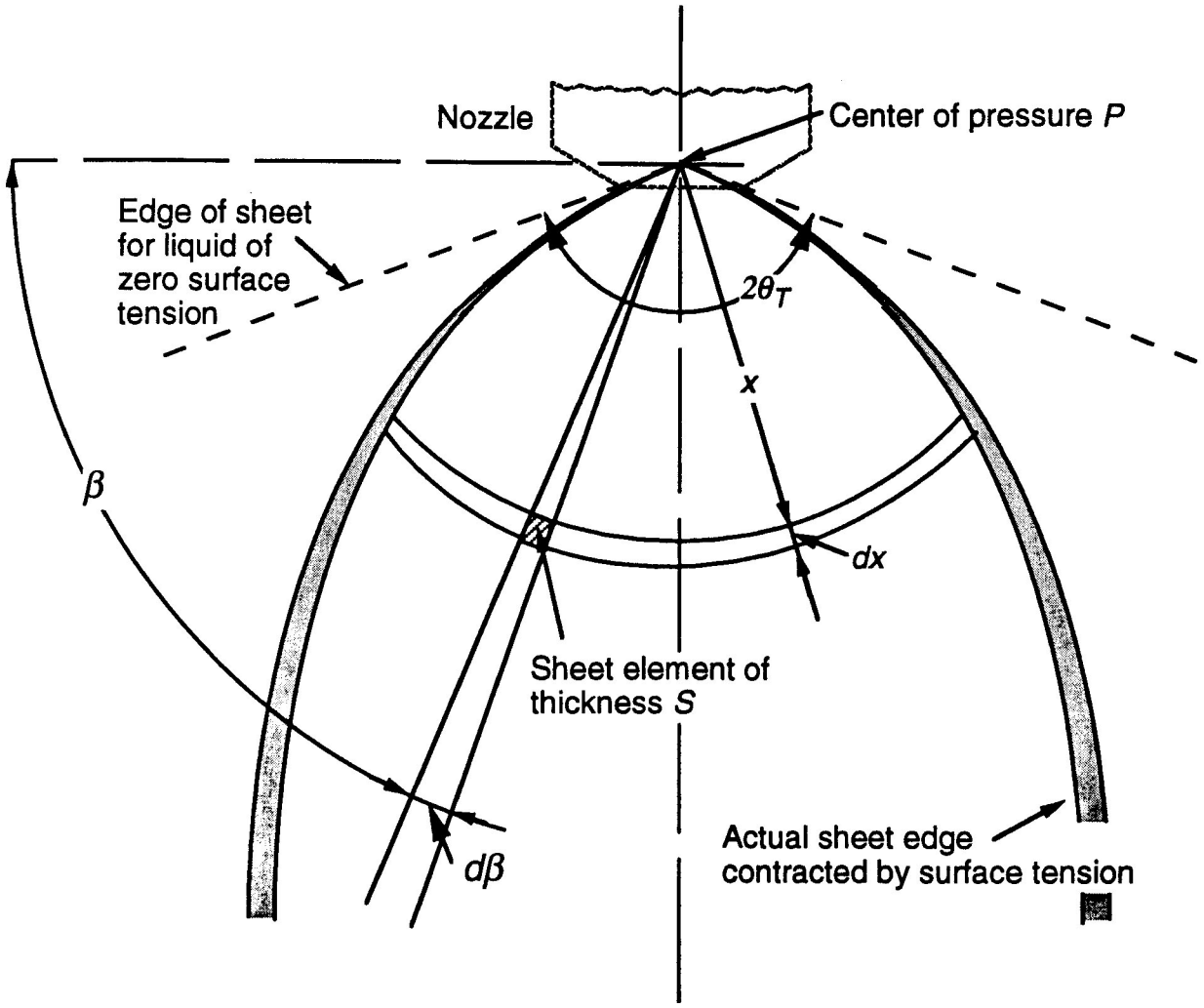

Figure 5.3.4. Flow parameters in sheet analysis.

Figure 5.3.4 shows a diagram of this simplified flow pattern. θ_T is the angle at which the sheet edges first issue from the orifice, and x is the radial distance of a point on the edge from the pressure center.

G. I. Taylor [4] and N. Dombrowski, et al. [5] analyzed this problem and the latter reached an approximate expression for the trajectory

$$x = g \cdot P \cdot K \cdot C_Q^2[1 - \sin(\beta + \theta)]/(2\gamma)$$

with a boundary condition of $\beta = \pi/2 - \theta$ as $x \to 0$, where:

g gravitational acceleration

P the differential injection pressure

K constant $= S \cdot x$

S sheet thickness

C_Q orifice discharge coefficient

b the angle defined in Fig. 5.3.4

g the free surface energy per unit area (surface tension coefficient).

From this simple analysis of the flow it can be seen that θ_T, the sheet angle at the orifice, and the trajectory of the sheet edge may be predicted from a knowledge of the sheet thickness as expressed in terms of K. Then after substitution of the value K, we obtain an expression for the sheet thickness, S:

$$S = (2\gamma)/g \cdot P \cdot C_Q^2 \left[1 - \sin\left(\beta + \theta\right)\right].$$

Using the parameters from Table 5.5.1 the calculations are performed to design the required nozzle needed to produce a satisfactory liquid metal sheet for LIBRA-SP. Figure 5.3.5 shows the trajectory of the sheet edge of the liquid PbLi for a 5 mm $\times$ 1.5 mm fan spray nozzle. Figure 5.3.5 also shows the sheet thickness distribution along the jet with an average value of 37 μm. To get full coverage for the PERIT every consecutive sheet must overlap. The required overlap gives the distance between each consecutive nozzle to be 8 cm.

From the structural dynamics (fatigue) point of view, it is better to have the perforations as close as possible to the bending plane (less stress concentration). Then, the direction of the jet is chosen to make the sheet 1.0 mm away from the surface of the next PERIT. This makes the angle ϕ approximately equals to 13° (Figure 5.3.5). Exactly on the opposite side of the PERIT there is another system of perforations but staggered 4.0 cm in the vertical direction to complete the coverage of the cavity first surface. The mechanical advantage of having both perforations on the opposite sides is that the lateral jet reaction is canceled.

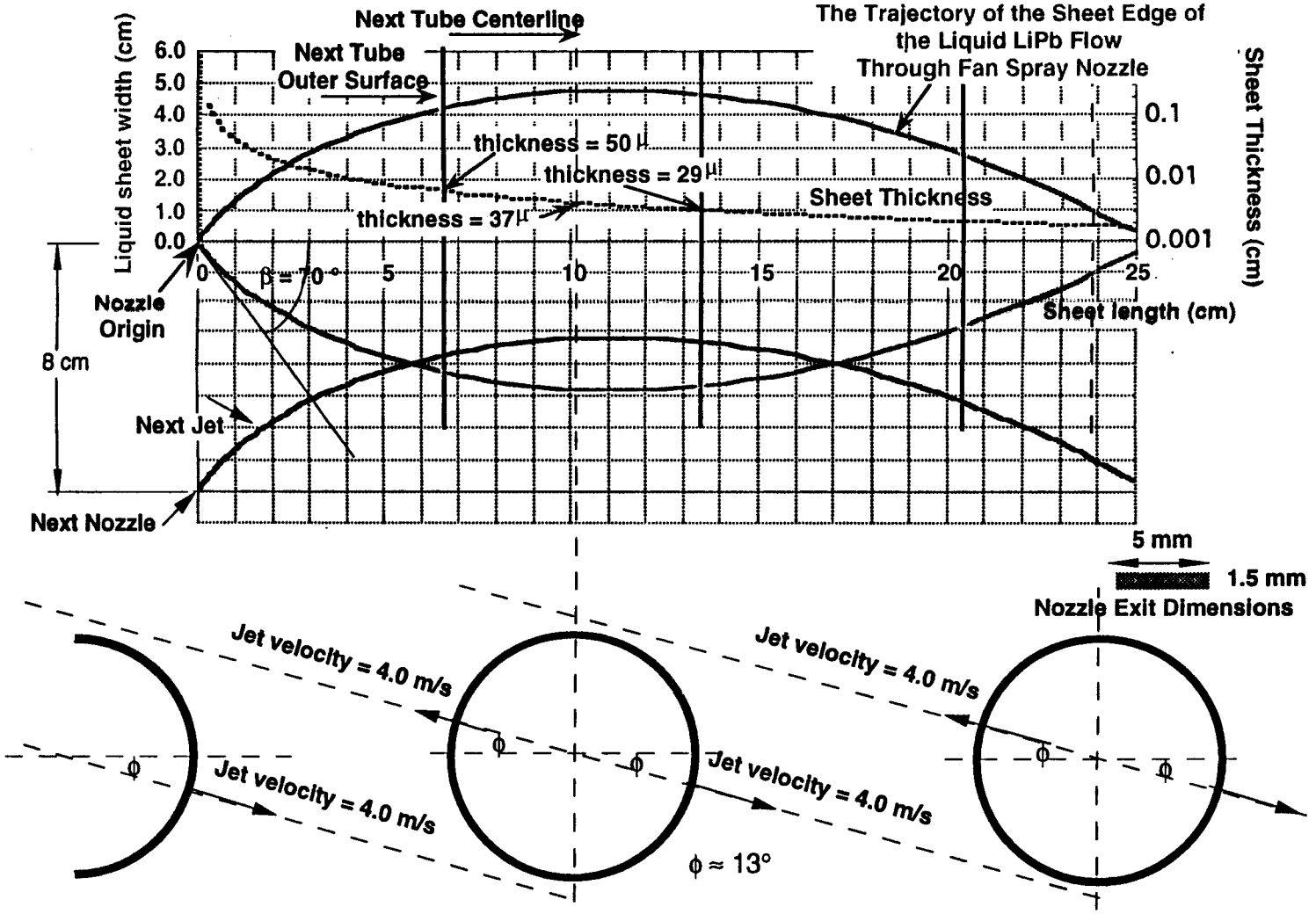

Figure 5.3.5. The fan spray jet trajectory and the first row of the first surface coolant tubes.

5.4. Mechanical Response

5.4.1. Interaction of Target Emanations with Spray

In LIBRA-SP, a thin spray of liquid $Pb_{83}Li_{17}$ protects the PERITs from direct damage by the target x rays and debris ions. This scheme is shown in Fig. 5.4.1. The deposition of target x rays and debris ions in the spray causes an explosive expansion of the region of the spray facing the target. This blows a small amount of vapor into the middle of the chamber, drives a shock through the spray, and accelerates the bulk of the spray toward the PERITs. The BUCKY computer code has been used to study these phenomena in the LIBRA-SP target chamber.

The BUCKY computer code use a one-dimensional Lagrangian mesh to model the hydrodynamic motion and energy tranport in a fluid. In the calculation discussed here, the Lagrangian mesh is in slab geometry. BUCKY was first developed in 1994 by combining the CONRAD [6], PHD-IV [7] and NLTERT [8] codes. Target x rays and debris ions are applied as time-dependent sources from one side of the mesh. The x-ray deposition in the spray is calculated with x-ray stopping powers from fits to experimental data [9], that are modified to include the effects of depletion of the inner-shell electrons. The deposition of ion debris in the spray is calculated with a modified Mehlhorn model [10]. This model includes range-shortening effects that occur as increased temperature of the stopping medium (the spray in this case) leads to more free electrons for stopping. The equation-of-state and opacity of $Pb_{83}Li_{17}$ is determined by interpolation from data tables.

The equation-of-state and opacity of $Pb_{83}Li_{17}$ data tables are provided by calculations with the EOSOPA code [11]. The equation-of-state and opacities are calculated with the same models described in the section on target burn calculations (Section 4.2.2). The equation-of-state for $Pb_{83}Li_{17}$ is calculated with a hybrid model using Detailed Configuation Accounting (DCA) for low density and a "Muffin Tin" model for high density. This approach insures that the important ionization effects are seen at low density and that cohesion and the effects of degenerate electrons appear at high density. The equation-of-state of $Pb_{83}Li_{17}$ is

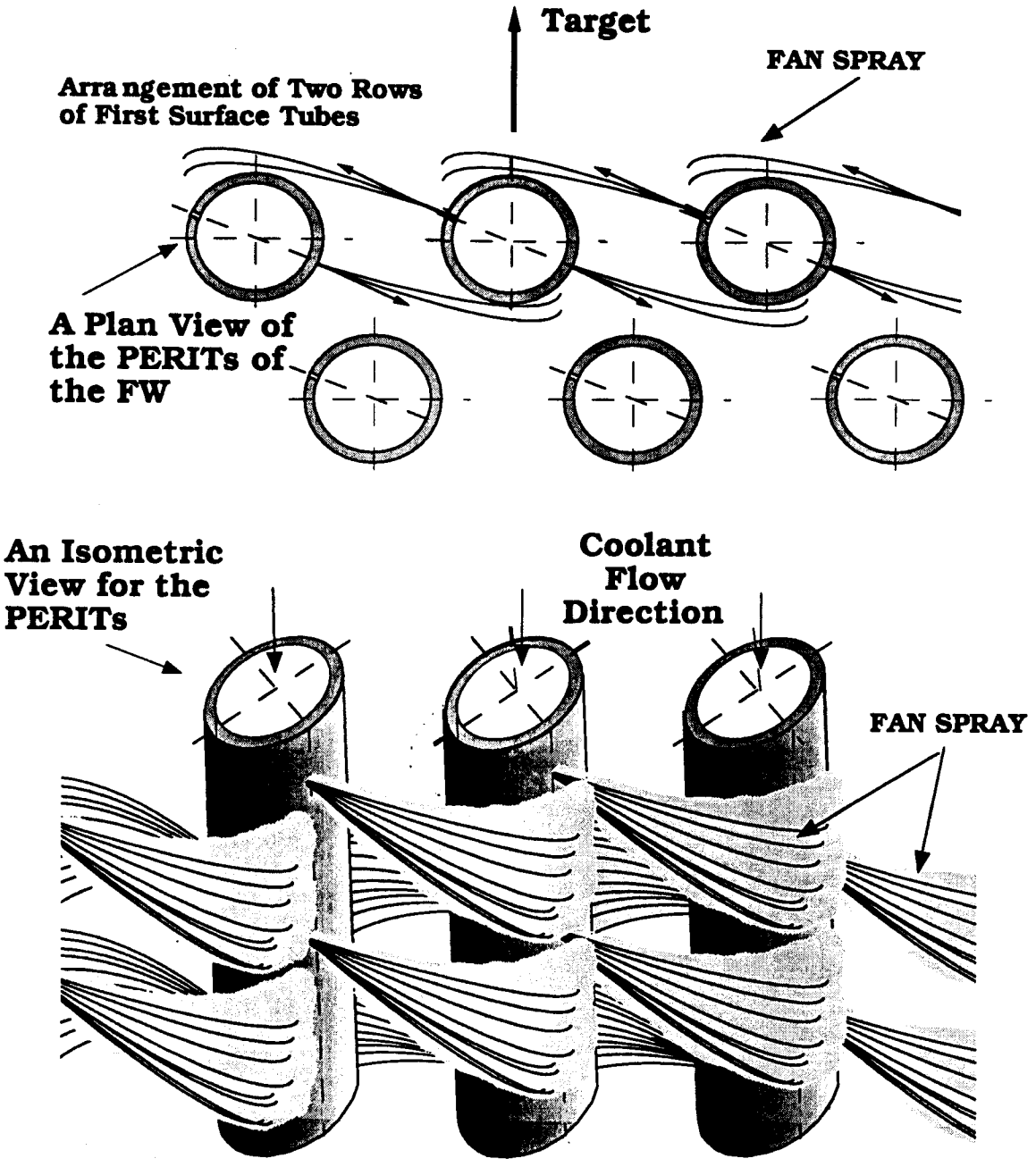

Figure 5.4.1. $Pb_{83}Li_{17}$ spray protection scheme for PERITs in LIBRA-SP.

Table 5.4.1. Debris Ion Kinetic Energies

Species	Energy (MJ)	Energy per Ion (keV)
H	0.30	0.46
D	0.44	0.69
T	0.101	1.05
He^3	0.047	1.40
C	2.25	10.9
Pb	17.3	309

Table 5.4.2. Energy Partitioning for LIBRA-SP Targets

	PHD-IV (MJ)	Corrected for Neutron Deposition (MJ)
Total yield	589	589
Neutrons	472	383
X rays	97	168
Debris ions	20	35

shown in Fig. 5.4.2 and Fig. 5.4.3 . The opacity for $Pb_{83}Li_{17}$ is calculated with an Unresolved Transition Array (UTA) method for the Pb component and a DCA for the low atomic number Li component. The opacity of $Pb_{83}Li_{17}$ at densities of $0.1\rho_o$ and $10^{-3}\rho_o$ (where ρ_o is the normal density) and an ion temperature of 10 eV is shown in Fig. 5.4.4. One sees in this figure that the high density, Stark broadening smooths many of the features in the opacity.

The target emanation results presented in Section 4.3 are used as source terms for these calculations. Those were the results of a calculation with the PHD-IV code before the BUCKY code was created. The x-ray spectrum, integrated up to various times, is shown in Fig. 5.4.5. The radiant power history is shown in Fig. 5.4.6 The energy in variuos debris ion species is given in Table 5.4.1. The PHD-IV calculations did not include any neutron deposition within the target, so neutron deposition calculations within the target were performed with the ONEDANT [12] code to arrive at the energy partitions shown in Table 5.4.2. The calculation presented here is in a slab geometry, so the results of the target simulations must be normalized to provide the proper fluence and flux per unit area at the

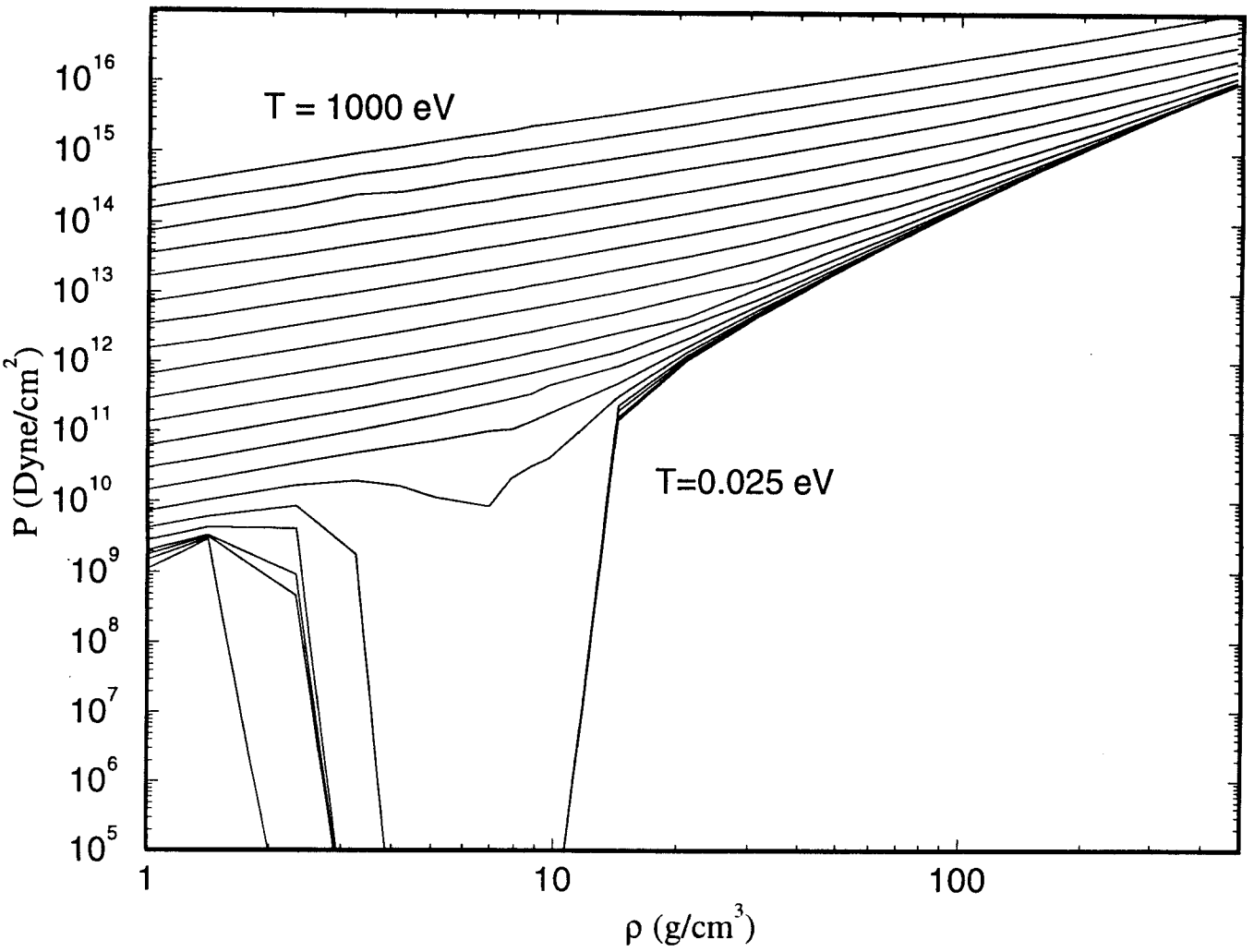

Figure 5.4.2. Pressure of $Pb_{83}Li_{17}$ versus mass density at particular temperatures.

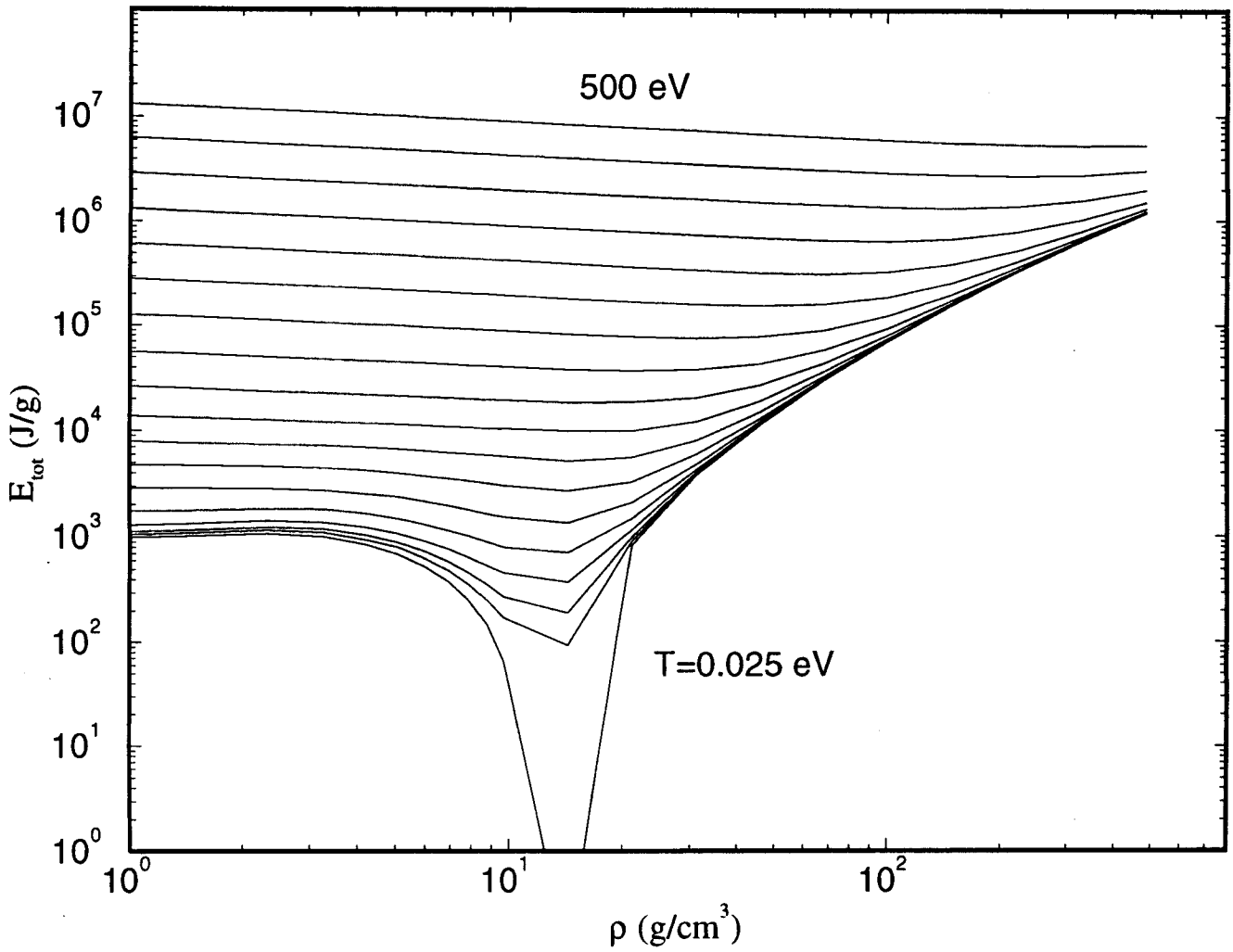

Figure 5.4.3. Energy density of $Pb_{83}Li_{17}$ versus mass density at particular temperatures.

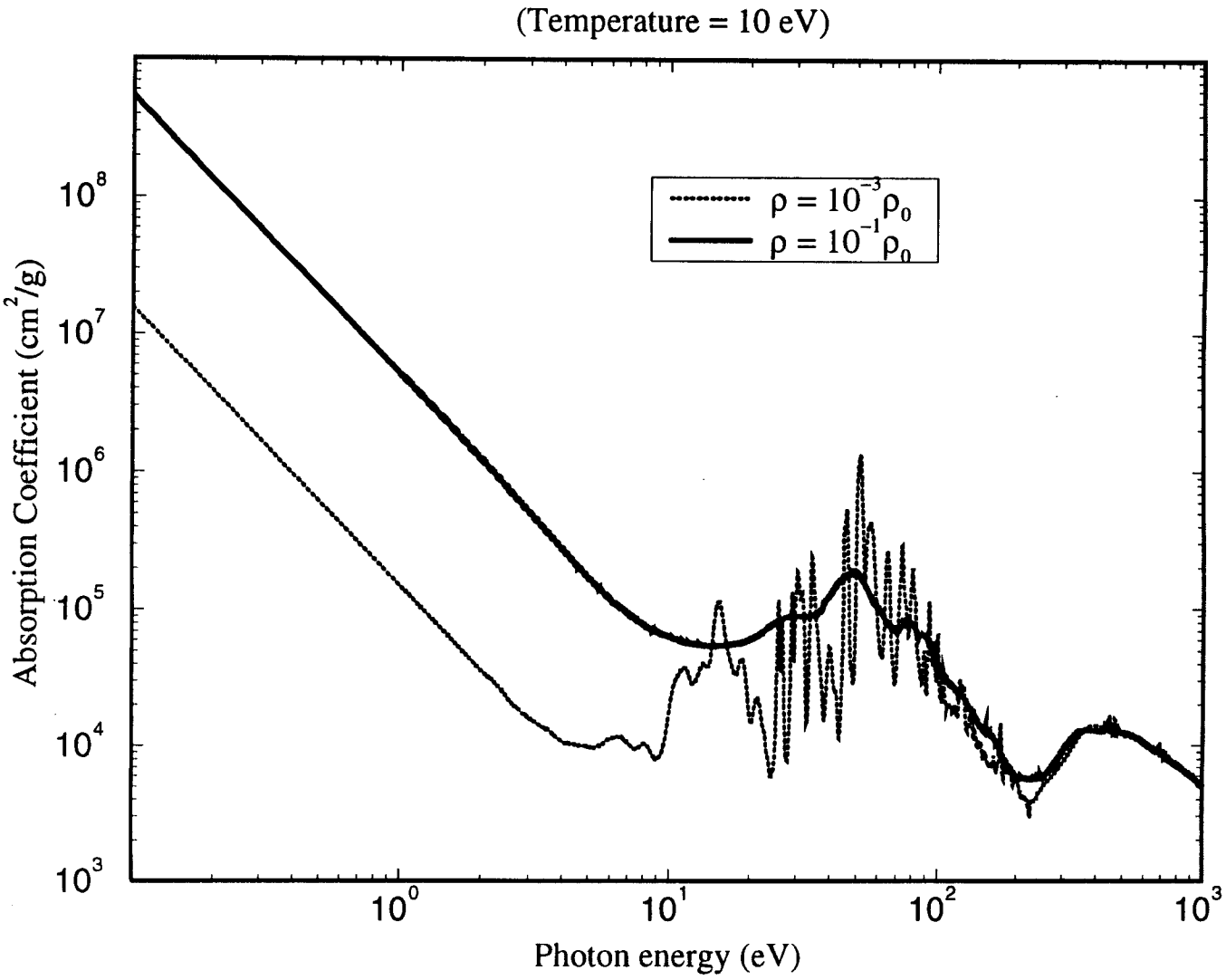

Figure 5.4.4. Opacity of $Pb_{83}Li_{17}$ versus photon energy at several simulation times.

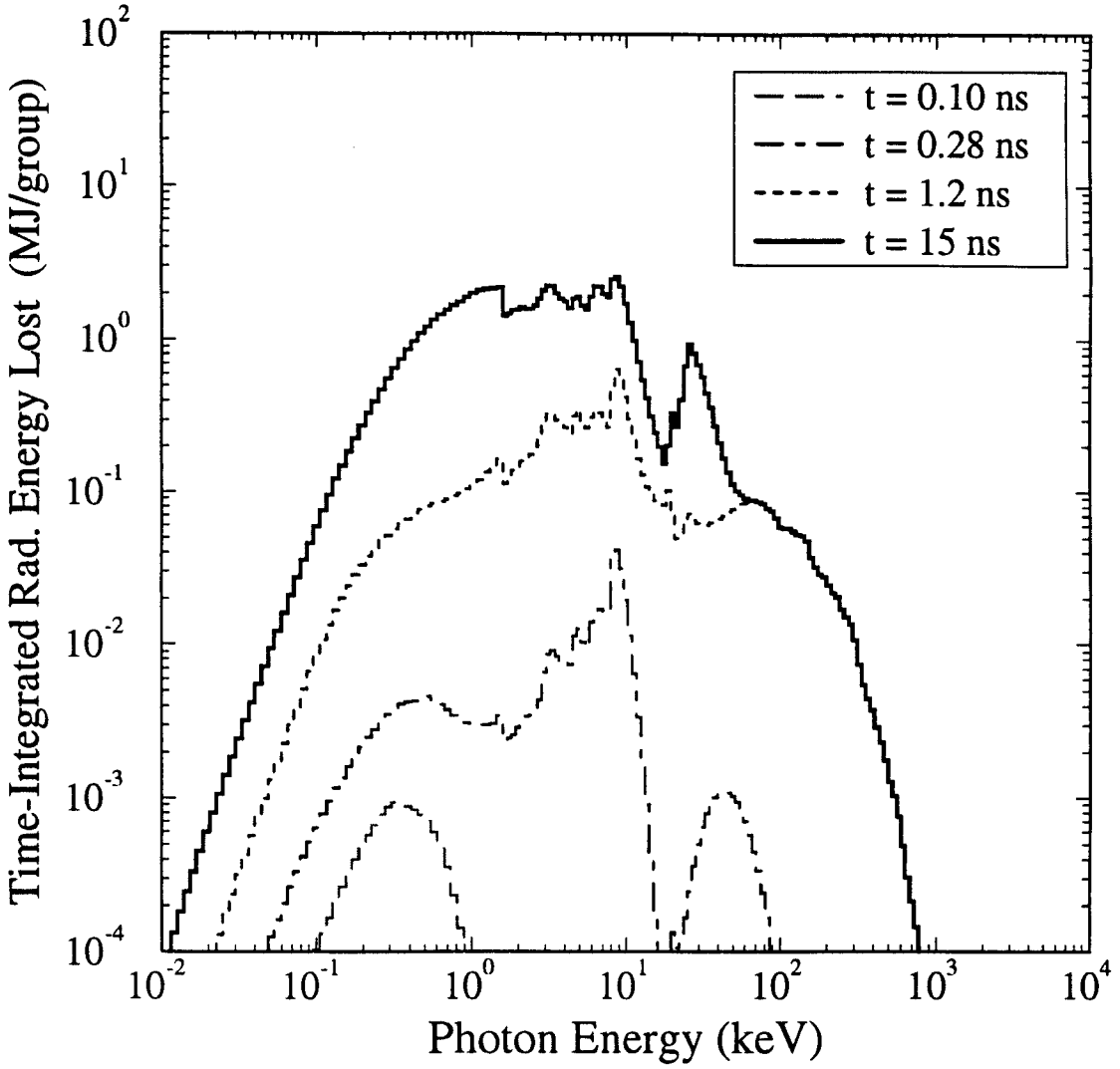

Figure 5.4.5. Time-integrated spectra of radiation emitted from the target boundary at several simulation times.

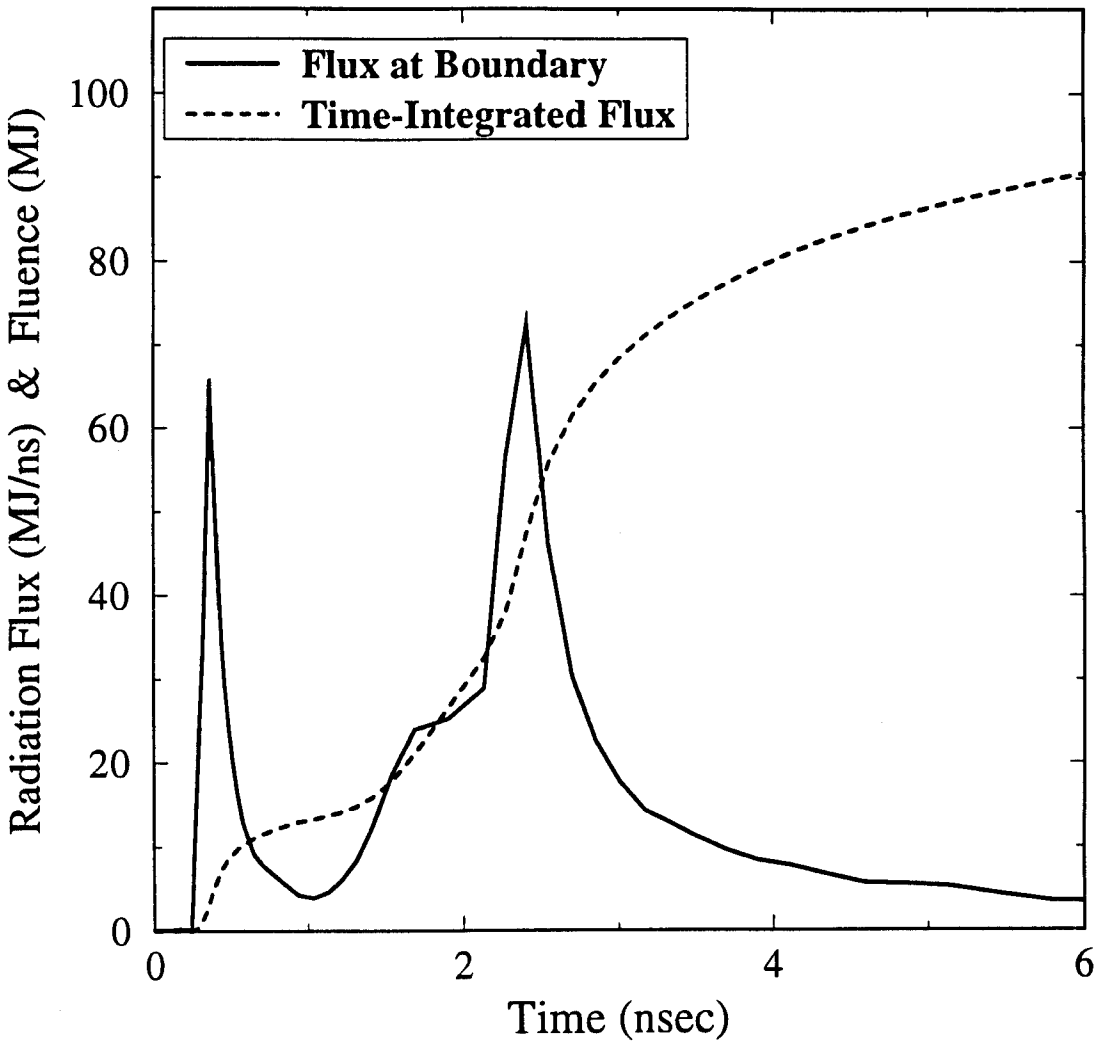

Figure 5.4.6. Time-dependent and time-integrated radiation power emitted from the boundary of the LIBRA-SP target.

Table 5.4.3. Energy Partitioning of LIBRA-SP Spray

	Fluence (J/cm^2)
Total yield	239
Neutrons	190
X rays	83.6
Debris ions	17.4

Table 5.4.4. Summary of BUCKY Simulation of Spray Behavior

Initial Spray Thickness	40 μm
Spray Velocity	1.8×10^4 cm/s
Shock Velocity	5.7×10^4 cm/s
Peak Pressure on PERITs	11 GPa
Impusive Pressure on PERITs	71 Pa-s
Mass Blown into Chamber	1.15 mg/cm^2

surface of the PERITs. The PERITs are positioned 4 m from the target. Since the target emanations expand as a one-dimensional sphere, the x-ray and debris yield in Table 5.4.2 must be divided by 2.01×10^6 cm^2, to obtain the fluences in Table 5.4.3. These fluences are then applied to the side of the spray facing the target and the simulation with BUCKY is performed.

The results of a BUCKY simulation of the reaction of the spray to the target is summarized in Table 5.4.4. The $Pb_{83}Li_{17}$ spray is initially 40 μm thick and at a temperature of 600°C. The hydrodynamic motion of the fluid is shown Fig. 5.4.7, where the positions of the Lagrangian zone boundaries are plotted against time. In this simulation, the PERITs are artificially placed 140 μm in back of the spray, to reduce computer time. In reality, the spray will be at least several mm in front of the PERITs. One can see that the spray mostly remains intact. The spray actually compresses somewhat because the initial density was slightly higher than the density of minimum energy, shown in Fig. 5.4.3. Because the spray mostly remains intact, placing the PERITs very close to the spray loses very little information since the spray will coast at a constant speed until it strikes the PERITs. In the simulation the spray collides with the PERITs at 0.8 μs, so the spray is moving at

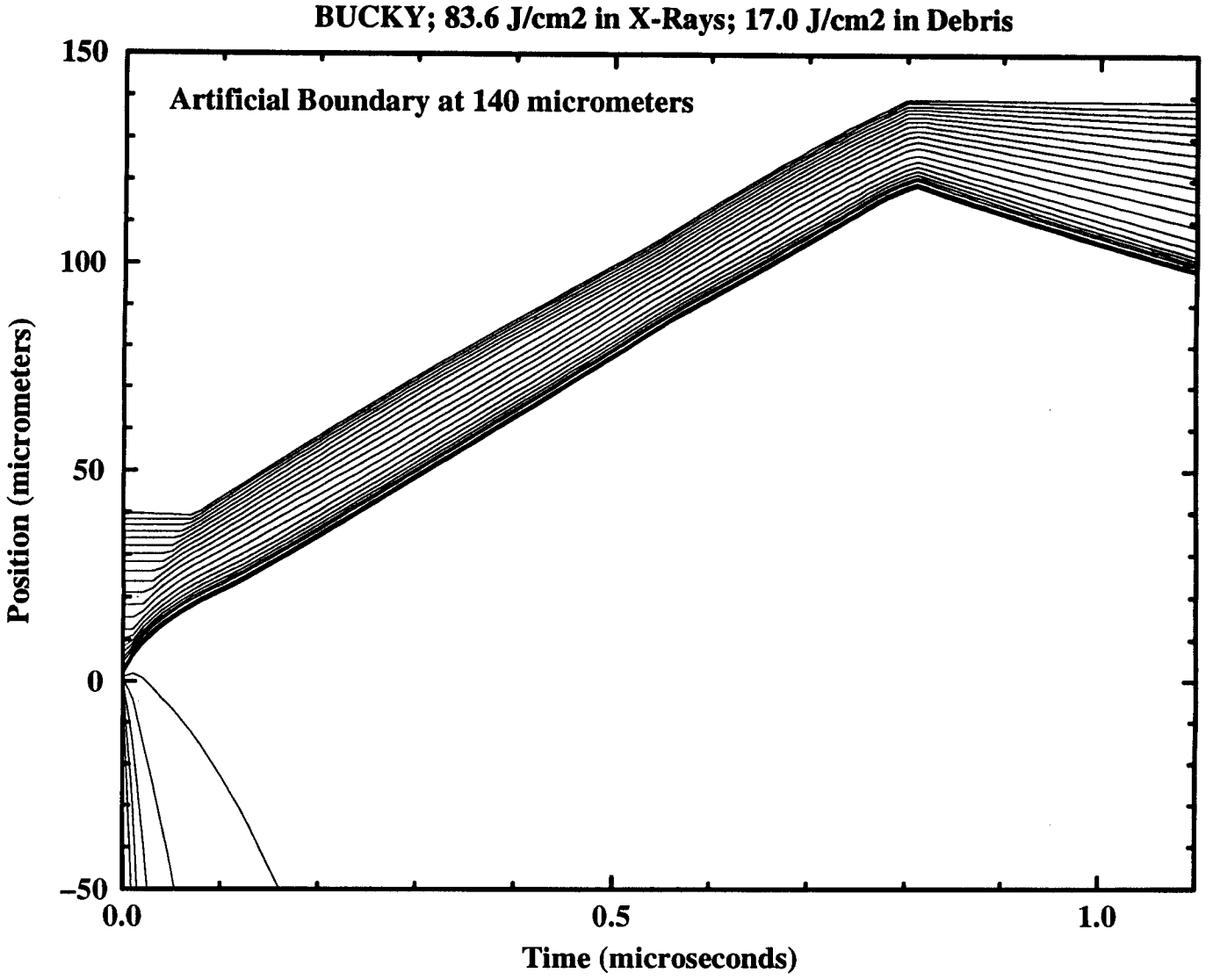

Figure 5.4.7. Hydromotion of $Pb_{83}Li_{17}$ irradiated by target x rays and debris ions in the LIBRA-SP target chamber. Lagrangian zone boundaries are plotted against time from a calculation with the BUCKY code.

about 1.8×10^4 cm/s. At the time of collision, the pressure on the PERITs quickly rises to about 11 GPa, as is shown in Fig. 5.4.8. The spray begins to disperse after the collision. A total impulsive pressure of 71 Pa-s is applied of the whole pulse. A shock is initially driven through the spray by the rapid deposition of target energy, which is shown in Fig. 5.4.9. The shock reaches the back of the spray at about 0.07 μs, so the average shock speed is about 5.7×10^4 cm/s. About 1.15 mg/cm^2 of the spray are blown in to the middle of the target chamber.

There are several issues that this calculation raises. The peak pressure on the PERITs is sufficient to launch shocks into the PERITs. These shocks could damage the material over time. The effects of neutron heating of the spray are not included, and they may lead to the spray disassembling before it reaches the PERITs. This would lower the peak pressure on the PERITs and reduce the effect of the shocks. It is unknown what effect the material blown into the chamber middle will have on the chamber clearing. These issues will be addressed in the next phase of the LIBRA-SP study.

5.4.2. Mechanical Response of the PERIT Units

It is expected that the first two rows of PERIT units will be subjected to the radial impulse load from the blast wave. The primary response of the tube will be a radial displacement (or planar displacement), however, it has been shown that the tubes could begin to "whirl" under certain operating conditions. If three-dimensional motion were to take place, it is assumed that the maximum displacement would not be greater than the maximum planar displacement. It is assumed that the pressure load is uniformly distributed over the length of the tube and is applied at the rep rate of the reactor. Since the flow velocity of the fluid is low, the fluid is considered stationary and the effects of moving liquid are neglected. Stationary fluid in a tube adds mass to the system without changing the flexural rigidity of the tube. Characterizing the planar motion and the resulting stresses in the PERIT units was the focus of this study.

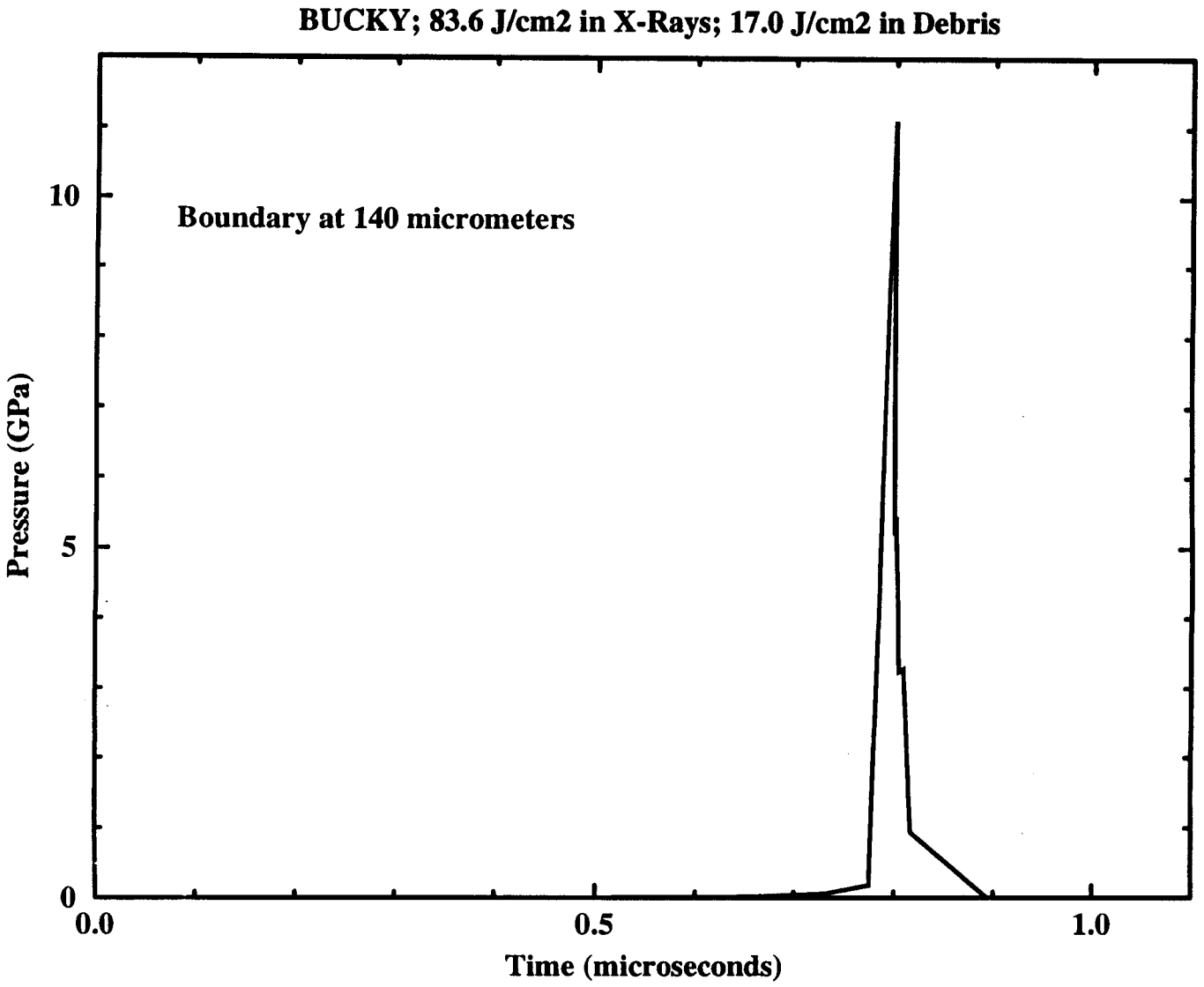

Figure 5.4.8. Pressure on the surface of PERITs due to the collision of $Pb_{83}Li_{17}$ spray.

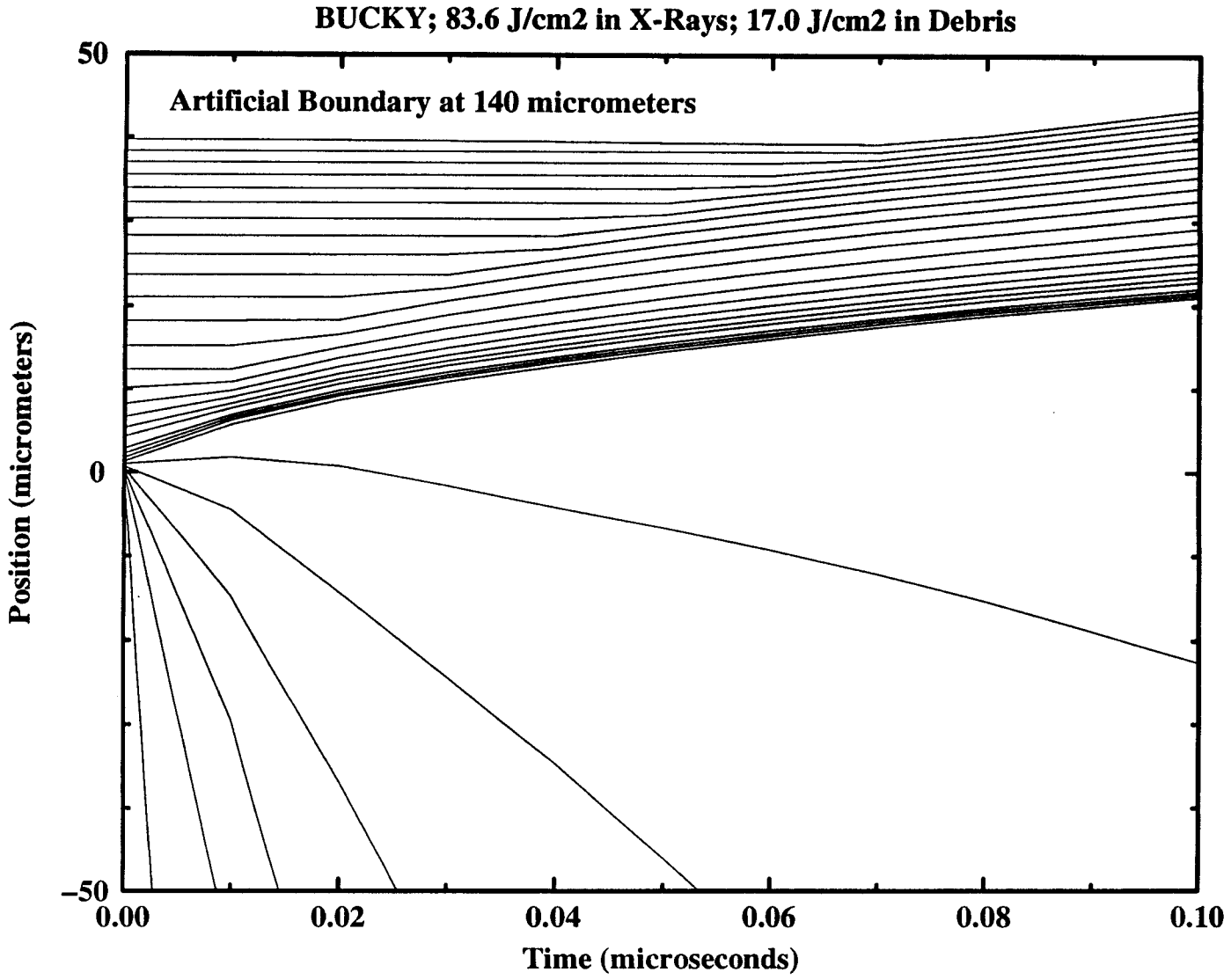

Figure 5.4.9. Hydromotion of $Pb_{83}Li_{17}$ irradiated by target x rays and debris ions in the LIBRA-SP target chamber. Lagrangian zone boundaries are plotted against time from a calculation with the BUCKY code.

The general equation of motion describing the mechanical response of the PERIT units under sequential impulse loading can be expressed as

$$EI\,\frac{\partial^4 y}{\partial x^4} + \gamma\frac{\partial^2 y}{\partial t^2} + \kappa\frac{\partial y}{\partial t} = 2RI_p \sum_{n=0}^{n\tau_{imp}\le t} \delta(t - n\tau_{imp})$$

$$\begin{aligned}
y &= \text{radial displacement coordinate}\\
x &= \text{spatial coordinate}\\
t &= \text{time}\\
E &= \text{modulus of elasticity of the tube}\\
I &= \text{area moment of inertia of the tube}\\
\gamma &= \text{mass per unit length of the tube including fluid}\\
\kappa &= \text{coefficient of viscous damping per unit length}\\
\delta &= \text{Dirac delta function}\\
R &= \text{outer radius of the tube}\\
I_p &= \text{impulse pressure}\\
\tau_{imp} &= \text{impulse period.}
\end{aligned}$$

The homogeneous solution using separation of variables is given by:

$$\begin{aligned}
y_h(x,t) &= \sum_{i=1}^{\infty} Q_i(t)\,\phi_i(x)\\
\phi_i(x) &= \text{orthogonal mode shape that satisfies the boundary conditions}\\
Q_i(t) &= e^{-\zeta_i\omega_i t}\left[A_i\,\sin((\omega_d)_i\,t) + B_i\,\cos((\omega_d)_i\,t)\right]\\
(\omega_d)_i &= \omega_i\sqrt{1-\zeta_i^2}\\
\omega_i &= \left(\frac{\lambda_i}{L}\right)^2\sqrt{\frac{EI}{\gamma}}
\end{aligned}$$

where ζ_i represents the equivalent modal damping factor, L is the length of the tube, λ_i is the separation constant prescribed by the boundary conditions and A_i and B_i are constants determined by initial conditions. For this problem, the homogeneous solution represents the motion of the tube before the sequential impulses. If the tube is initially at rest, then the homogeneous solution is equal to zero, i.e., $A_i = B_i = 0$.

Variation of parameters can be used to find the particular solution. Consequently, a solution of the following form is assumed:

$$y_p(x,t) = \sum_{i=1}^{\infty} T_i(t)\phi_i(x)$$

where $Q_i(t)$ has been replaced by an unknown function $T_i(t)$. Inserting the assumed solution in the governing equation and using the orthogonality property of the shape functions and the integration property of the delta function, it can be shown that

$$T_i(t) = \frac{2RD_i}{\gamma C(\omega_d)_i} q_i(t)$$

$$q_i(t) = \sum_{n=0}^{n\tau_{imp} \le t} e^{-\zeta_i \omega_i (t - n\tau_{imp})} \sin\left[(\omega_d)_i t - (\omega_d)_i n\tau_{imp}\right]$$

where

$$C = \int_0^L \phi_i^2(x) dx$$
$$D_i = \int_0^L I_p(x)\phi_i(x) dx \,.$$

For this case, $I_p(x)$ represents the distribution of the blast wave along the span of the tube. In this study, the pressure load is distributed uniformly over the length of the tube, therefore $I_p(x) = I_p$, a constant.

Combining the above results, the general solution for the displacement of the beam starting from rest is given by

$$y(x,t) = \frac{2R}{\gamma C} \sum_{i=1}^{\infty} \frac{D_i}{(\omega_d)_i} \phi_i(x) q_i(t) \,.$$

By examining the time function $q_i(t)$, one observes that each impulse starts a free vibration solution and the total response is the superposition of all the free vibrations. As time progresses, a free vibration solution is diminished by the damping factor, so only the most recent impulses or corresponding free vibration solutions contribute to the tube's displacement.

In a beam, the bending stress, σ, is equal to

$$\sigma(x,t) = Ec \frac{\partial^2 y}{\partial x^2}$$

where c is the perpendicular distance from the tube's neutral axes to the point of interest. Then the general expression for the bending stress in the beam driven by sequential impulses

is given by

$$\sigma(x,t) = \frac{2REc}{\gamma C} \sum_{i=1}^{\infty} \frac{D_i}{(\omega_d)_i} \frac{d^2\phi_i(x)}{dx^2} q_i(t) \,.$$

The above solutions give the displacement and stress of a PERIT unit starting from rest and driven by periodic impulses of constant magnitude. Other situations can be easily studied by making small changes in the general solution. By varying the impulse period, τ_{imp}, the effect of non-periodic impulses can be studied; this will occur during the startup of the reactor. By skipping a term in the time summation, $q_i(x)$, the effect of a missed target can be analyzed. Also the consequences of different pressure loads can be examined by changing the value of I_p.

The above solutions were derived for arbitrary boundary conditions. To date, two different end conditions have been examined, i.e., pinned-pinned and clamped-clamped. Because of the generality of the derivation, other more complicated boundary conditions can be studied by using their associated shape functions. The following orthogonal shape functions for a pinned-pinned and clamped-clamped beam are found in reference [13] (for convenience the integration constants have been included):

Pinned-Pinned Beam:

$$\begin{aligned} \phi_i(x) &= \sin \frac{\lambda_i x}{L} \\ \lambda_i &= i\pi \end{aligned}$$

$$\begin{aligned} C &= \int_0^L \phi_i^2(x)dx = \frac{L}{2} \\ D_i &= \int_0^L I_p(x)\phi_i(x)dx = \begin{cases} 0 & \text{for even } i \\ \frac{2I_pL}{\lambda_i} & \text{for odd } i \end{cases} \end{aligned}$$

Clamped-Clamped Beam:

$$\phi_i(x) = \cosh \frac{\lambda_i x}{L} - \cos \frac{\lambda_i x}{L} - \alpha_i(\sinh \frac{\lambda_i x}{L} - \sin \frac{\lambda_i x}{L})$$

$$\alpha_i = \frac{\cosh \lambda_i - \cos \lambda_i}{\sinh \lambda_i - \sin \lambda_i}$$

$$\cos \lambda_i \cosh \lambda_i = 1$$

$$C = L$$

$$D_i = \begin{cases} 0 & \text{for even } i \\ \frac{4\alpha_i I_p L}{\lambda_i} & \text{for odd } i \end{cases}$$

Notice that because D_i is zero for even i, the even modes will not contribute to the total displacement or the stress. The reason for this is that the even or anti-symmetric modes are not excited by the uniform or symmetric pressure load. For a system with non-symmetric boundary conditions or non-symmetric pressure loading, all modes will contribute to the modal solution.

For the proposed LIBRA-SP cavity, a number of the PERIT design parameters have been set by power requirements and heat transfer requirements, e.g., using HT-9 as the tube material and LiPb as the liquid metal. Table 5.4.5 lists the system parameters that have been used to calculate the mechanical response. A constant equivalent viscous damping of 2% was used to show the effect that damping has on the dynamic displacements and stresses. The magnitude of the impulse load was calculated at 71 Pa-s, so calculations were performed using impulse loads of 50 Pa-s, 71 Pa-s and 100 Pa-s. The results scale linearly so the displacements and stresses can be easily determined for any impulse magnitude.

The length of the tubes remained as a design parameter to be optimized. Parametric studies were performed to determine the necessary length to preclude resonant conditions and minimize the radial displacements and normal stresses. Figure 5.4.10 shows the midspan displacement amplitude as a function of the impulse frequency (or rep rate) for a clamped-clamped tube of length 5.3 m with a damping level of 2.0%. A maximum allowable displacement of 3.5 cm has also been noted on the figure. For a rep rate of 3.88 Hz, the absolute displacement of the tube is well below the allowable. The corresponding stresses are given in Fig. 5.4.11 with the yield strength of the material [14] marked as shown. Both figures illustrate the frequencies or rep rates associated with resonant conditions, i.e., the

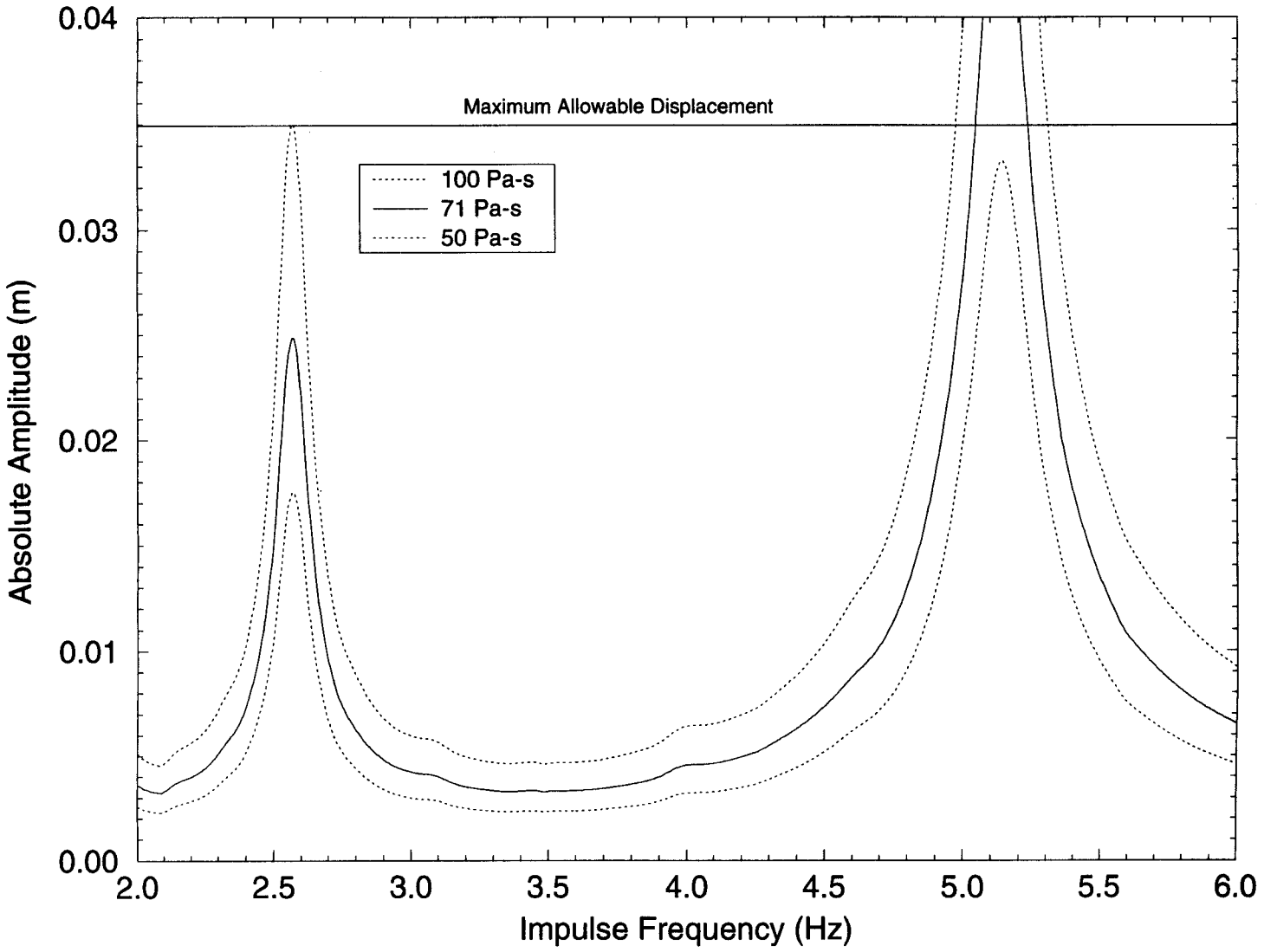

Figure 5.4.10. Maximum radial displacement of clamped-clamped PERIT units as a function of impulse frequency. Damping has been set to 2%.

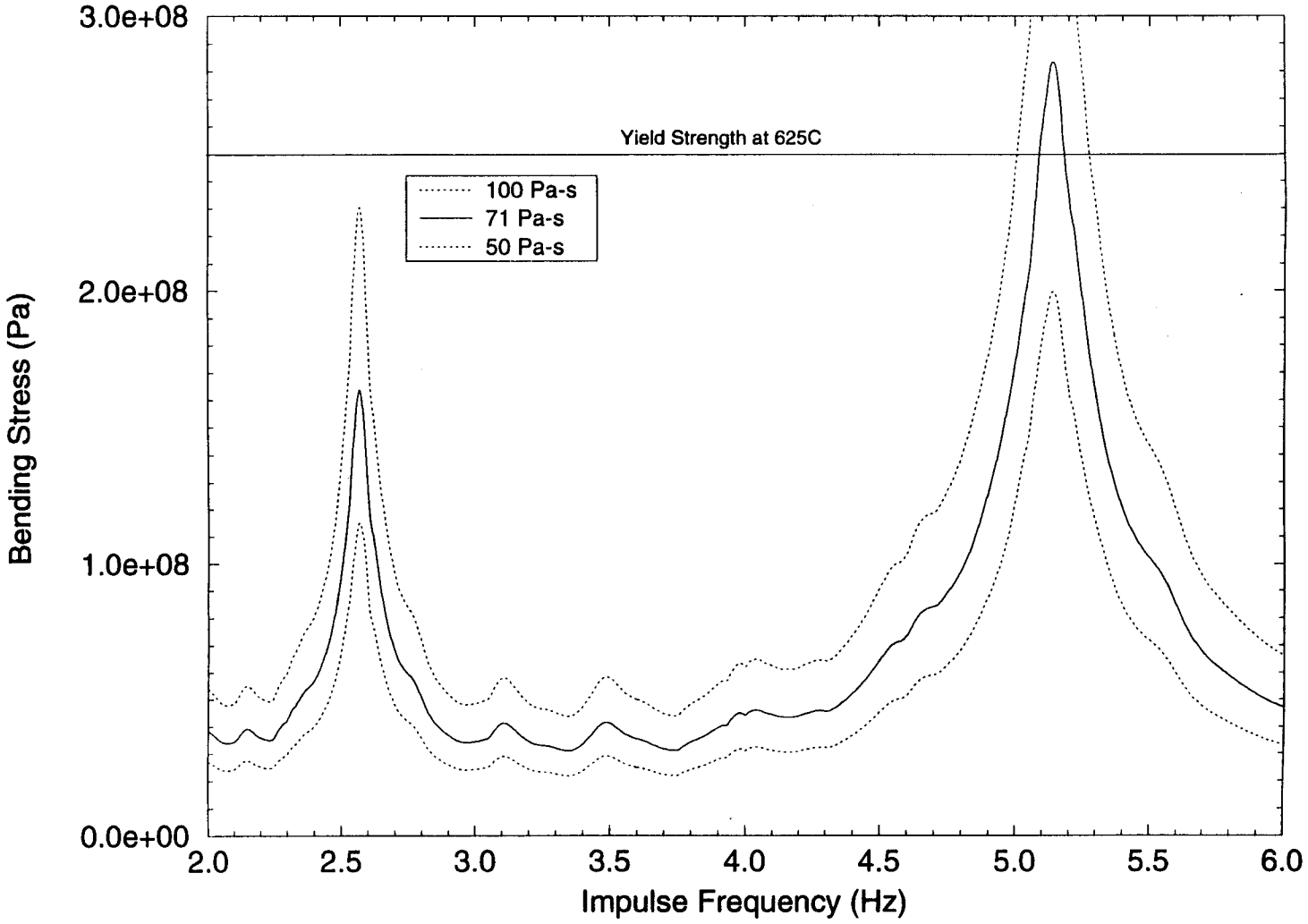

Figure 5.4.11. Maximum normal stress of clamped-clamped PERIT units as a function of impulse frequency. Damping has been set to 2%.

Table 5.4.5. PERIT System Parameters

Tube outer diameter	3.5 cm
Tube thickness	3 mm
Tube length	5.3 m
Impulse	71 Pa-s
Rep rate	3.88 Hz
Equivalent viscous damping	$\zeta_i = 2.0\%$
Density of LiPb	$\rho_{\mathrm{LiPb}} = 9440$ kg/m^3
Flow velocity	1.0 – 4.0 m/s
Density of HT-9 at 500°C	$\rho_{\mathrm{HT-9}} = 7625$ kg/m^3
Elastic modulus of HT-9 at 500°C	$E = 163.0$ GPa
Maximum temperature	619°C
Yield strength at 625°C	250 MPa

peaks in the response curves. These peaks would effectively shift as the length of the tube changes. Therefore, it is necessary to establish the free span of the tube at approximately 5.3 m. Figure 5.4.12 shows, for a pinned-pinned tube of length 5.3 m, the midspan displacement as a function of the impulse frequency. The corresponding stresses are given in Fig. 5.4.13.

5.5. Neutronics Analysis

5.5.1. Calculational Method

Neutronics analysis has been performed for the LIBRA-SP chamber using one-dimensional spherical geometry calculations for the different regions surrounding the target. The discrete ordinates code ONEDANT [15] was utilized along with 30 neutron – 12 gamma group cross section data based on the most recent ENDF/B-VI nuclear data evaluation [16]. A point source is used at the center of the chamber emitting neutrons and gamma photons with the LIBRA-SP target spectrum. The target spectrum takes into account neutron multiplication, spectrum softening and gamma generation resulting from the interaction of the fusion neutrons with the dense target material as discussed in Section 3. The results presented here are normalized to a 589 MJ DT fuel yield and a repetition rate of 3.88 Hz which correspond to a fusion power of 2285 MW.

5.5.2. PERIT Tube Region

The primary goal of the neutronics analysis performed for LIBRA-SP is to determine the blanket design that satisfies tritium self-sufficiency, large energy multiplication (M), and wall protection requirements. The blanket is made of banks of PERIT tubes with 0.5 packing fraction. The $Li_{17}Pb_{83}$ eutectic with 90% ^6Li enrichment is used as breeder and coolant. It flows in tubes which are made of the ferritic steel alloy HT-9. The tubes consist of 8 vol.% HT-9 and 92 vol.% $Li_{17}Pb_{83}$. A 0.5 m thick reflector consisting of 90 vol.% HT-9 and 10 vol.% $Li_{17}Pb_{83}$ is used behind the blanket. A minimum local (1-D) tritium breeding ratio (TBR) of 1.3 is required in the PERIT tubes and reflector. This relatively high TBR is required to achieve overall tritium self-sufficiency with a simple roof design that does not have a breeding blanket. In addition, the PERIT tubes are required to provide adequate protection for the front of the reflector (chamber wall) to make it last for the whole reactor life. In this study, we adopted a conservative end-of-life dpa limit of 150 dpa for the ferritic steel HT-9. Hence, for 30 full power years (FPY) of operation, the peak dpa rate in the HT-9 chamber wall should not exceed 5 dpa/FPY.

Several calculations have been performed to determine the blanket thickness required for adequate chamber wall protection. This scoping analysis implied that the PERIT tube zone (blanket) should be 1.2 m thick. In the reference LIBRA-SP chamber design, the inner chamber wall radius is 5.2 m. The front surface of the PERIT units is at a radius of 4 m and is exposed to a neutron wall loading of 7.4 MW/m^2.

The peak dpa rate in the PERIT units is 94.2 dpa/FPY implying a lifetime of 1.6 FPY. A gradual reduction in the damage rate and consequently the replacement frequency for the PERIT tubes is obtained as one moves toward the back of the blanket. The peak helium production rate is 436 He appm/FPY. The peak dpa rate in the chamber wall is 4.2 dpa/FPY implying an end-of-life damage of 126 dpa. The chamber will last for the whole reactor life. The peak helium production rate is only 0.9 He appm/FPY. Since spherical geometry has been used in the calculations, the damage rates given above represent the worst case

conditions at the midplane of the cylindrical chamber. The radial variation of damage rate in HT-9 at the reactor midplane is shown in Fig. 5.5.1.

The local TBR is 1.481 and the local blanket and reflector nuclear energy multiplication M_n, defined as the ratio of nuclear heating to the energy of incident neutrons and gamma photons, is 1.285. The spatial variation of nuclear heating has been calculated for use in the thermal hydraulics analysis. The results at the midplane are given in Fig. 5.5.2. The power density peaks at 18.3 W/cm^3 in the front PERIT tubes and drops to 2.4 W/cm^3 in the back tubes. The peak power density in the chamber wall is 0.52 W/cm^3. This large drop is due to the large neutronic and gamma attenuation in the enriched $Li_{17}Pb_{83}$ used in the PERIT tube region.

5.5.3. Reactor Roof

The roof of the chamber is a large dome that is required to be a lifetime component. The roof is 50 cm thick and consists of 90 vol.% HT-9 and 10 vol.% $Li_{17}Pb_{83}$. Figure 5.5.3 shows the peak dpa rate in the roof as a function of distance from the target. Based on these results, the roof of the LIBRA-SP chamber is located at 17 m from the target to ensure that it lasts for the whole reactor lifetime. The roof is exposed to a neutron wall loading of 0.41 MW/m^2. The peak dpa and helium production rates in the HT-9 roof are 4.88 dpa/FPY and 23.6 He appm/FPY, respectively. These results imply that the roof is a lifetime component. The end-of-life peak damage in the roof is 146 dpa for a 30 FPY reactor lifetime. The local TBR and M_n values are 0.499 and 1.349, respectively.

5.5.4. Bottom Pool

The bottom of the chamber consists of a lithium lead pool which is formed by the coolant flowing through the PERIT tubes. It drains through a 25 cm thick perforated plate made of HT-9, which acts as a reflector as well as a shock damper. This perforated splash plate consists of 80 vol.% HT-9 and 20 vol.% $Li_{17}Pb_{83}$. The LiPb drains into a sump leading to an intermediate heat exchanger. The LiPb thickness in the sump behind the perforated plate is taken to be 0.3 m. The depth of the LiPb pool at the bottom of the reactor was

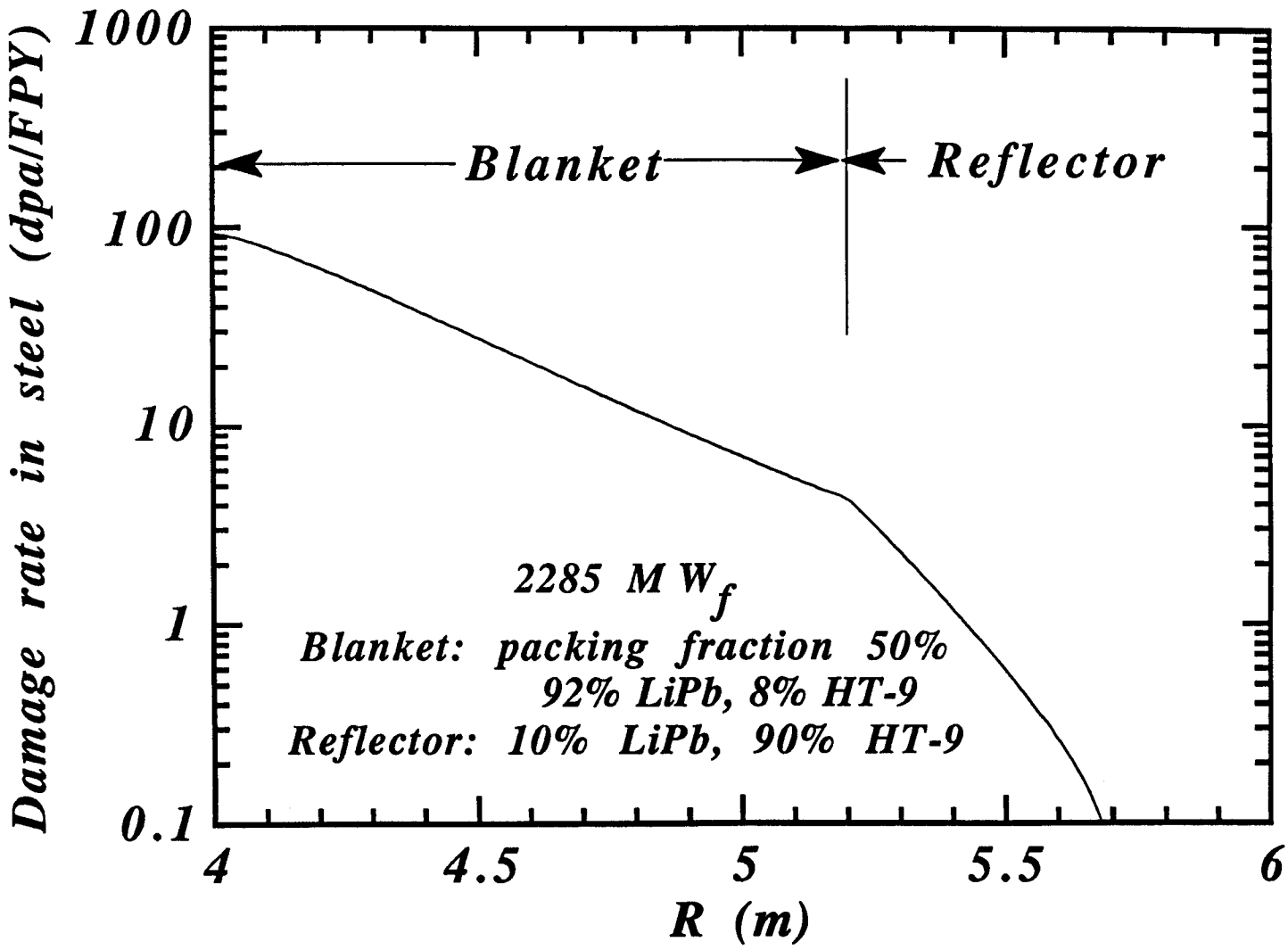

Figure 5.5.1. Radial variation of damage at reactor midplane.

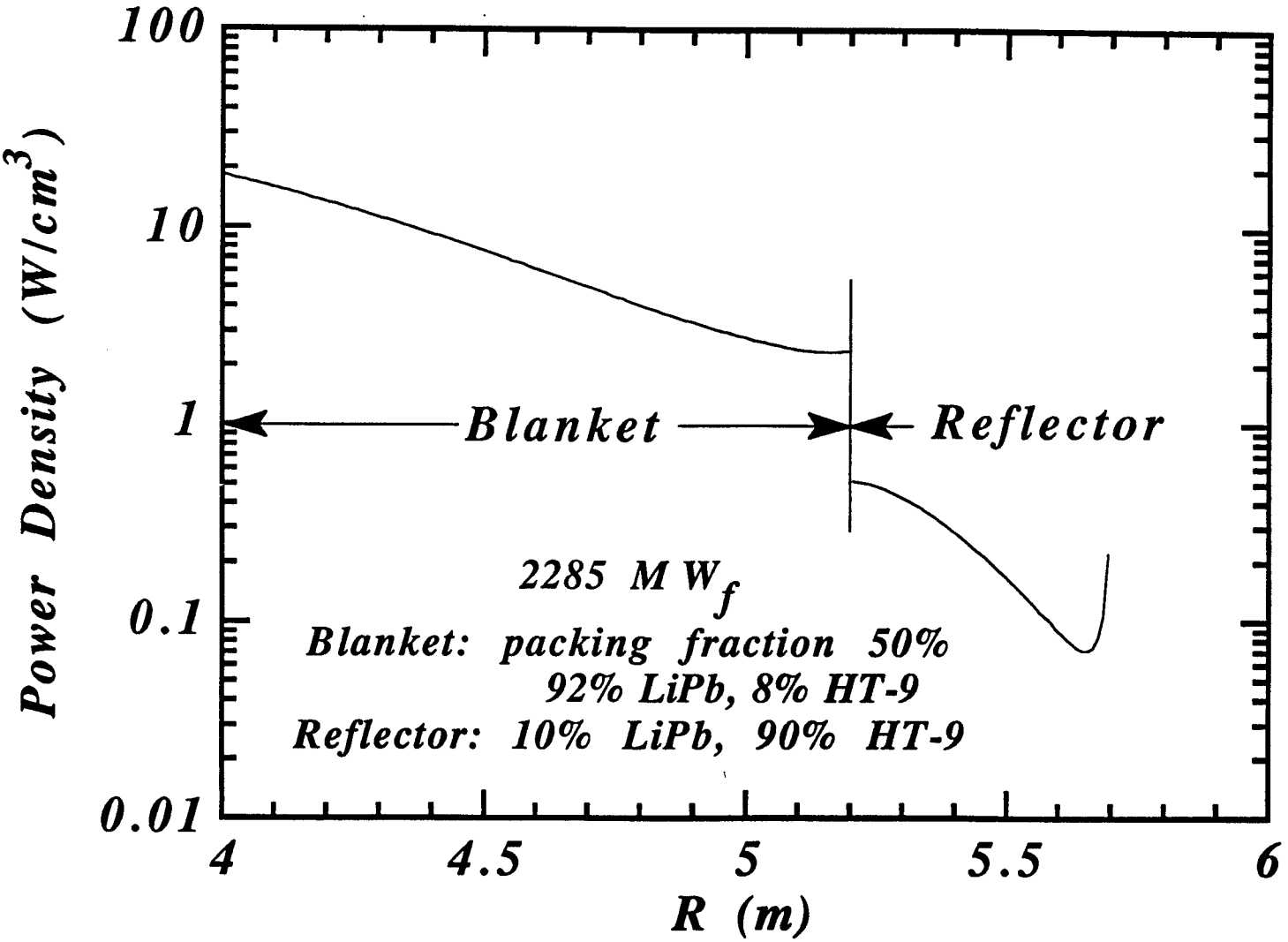

Figure 5.5.2. Radial variation of power density at reactor midplane.

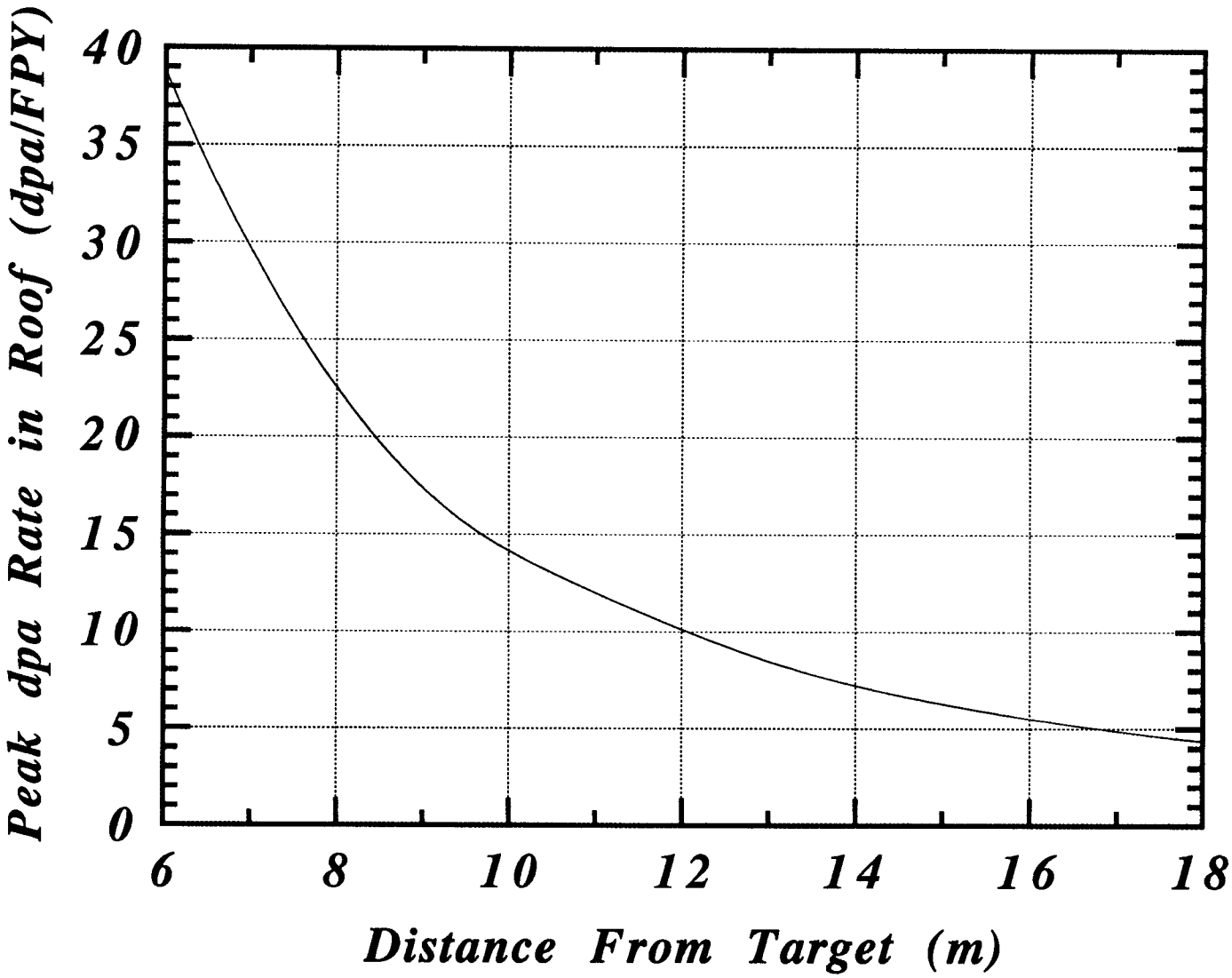

Figure 5.5.3. Peak damage rate in roof as a function of distance from target.

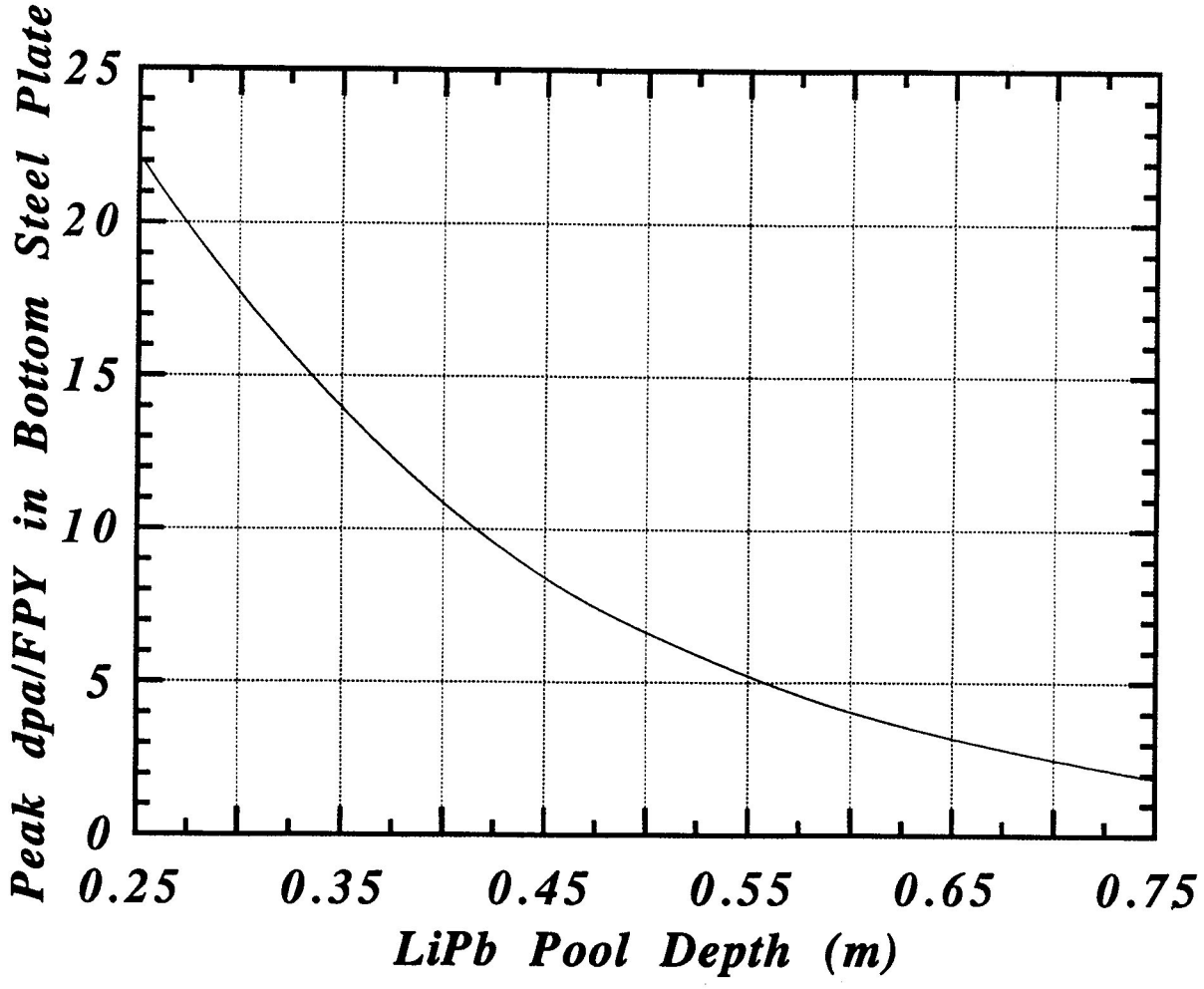

Figure 5.5.4. Peak damage rate in the bottom plate as a function of pool depth.

determined to allow the bottom perforated plate to be a lifetime component. The upper surface of the pool is at 5 m from the target and is exposed to a neutron wall loading of 4.74 MW/m^2. Figure 5.5.4 shows the peak damage rate in the bottom plate as a function of pool depth. The results indicate that the pool depth should be at least 0.6 m implying that the bottom plate should be located at 5.6 m from the target. The peak dpa and helium production rates in the HT-9 bottom perforated plate are 4 dpa/FPY and 1.04 He appm/FPY, respectively. The end-of-life peak damage in the bottom plate is only 120 dpa implying that it will be a lifetime component. The local TBR and M_n values are 1.592 and 1.273, respectively.

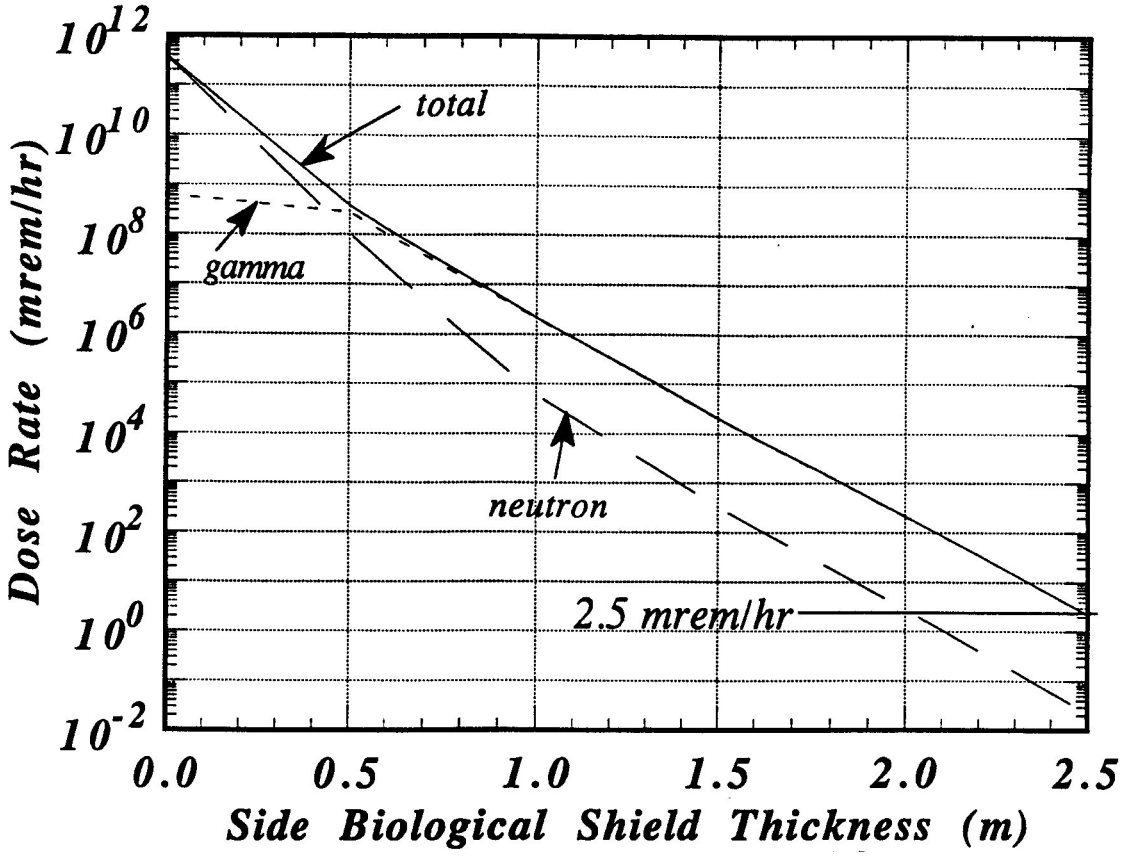

Figure 5.5.5. Effect of side biological shield thickness on dose rate during reactor operation.

5.5.5. Biological Shield Design

The reactor shield is designed such that the occupational biological dose rate outside the shield does not exceed 2.5 mrem/hr during reactor operation. The biological shield consists of 70 vol.% concrete, 20 vol.% carbon steel C1020 and 10 vol.% He coolant. The required biological shield thickness was determined for both the reactor side and reactor roof. Figure 5.5.5 gives the dose rate at the back of the shield at the reactor midplane as a function of shield thickness. A 2.5 m thick shield is required to yield an acceptable operational dose rate of 2.23 mrem/hr. Figure 5.5.6 shows the effect of roof biological shield thickness on dose rate during reactor operation. The results indicate that the biological shield thickness above the roof should be 2.6 m thick. This yields an acceptable operational dose rate of 1.8 mrem/hr.

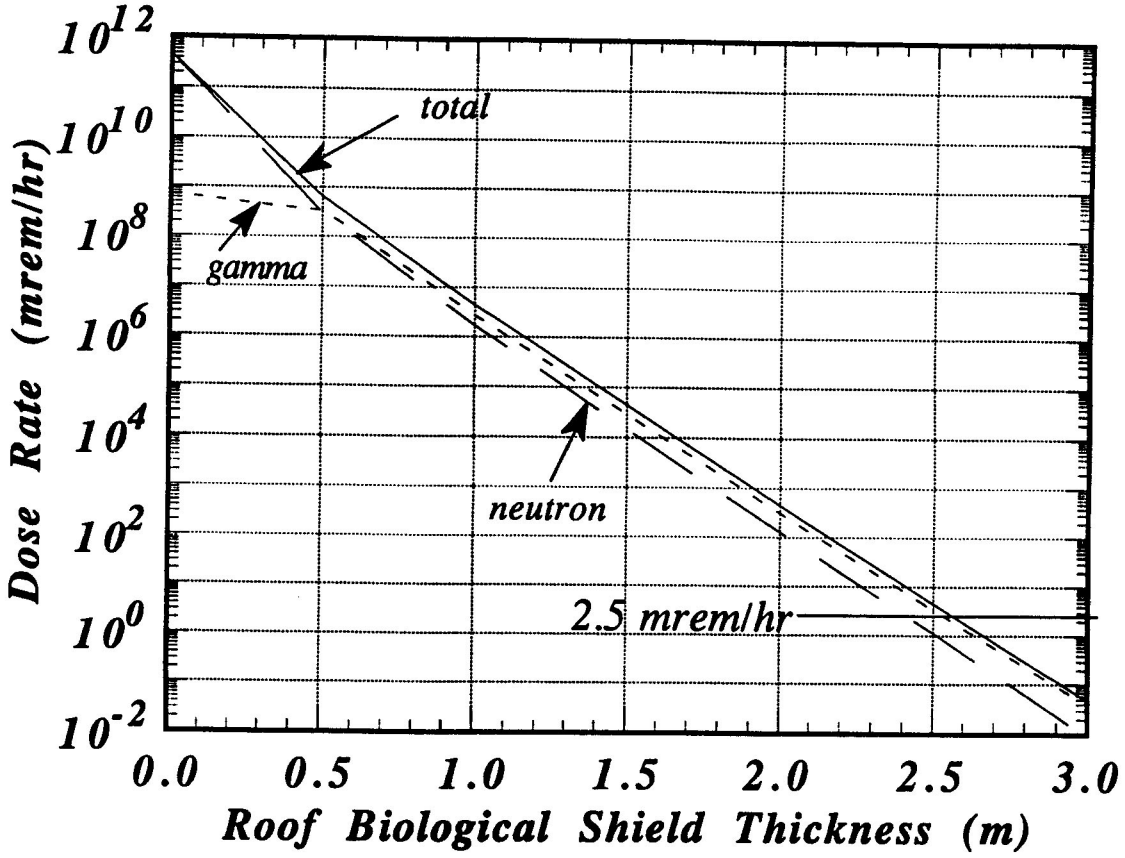

Figure 5.5.6. Effect of roof biological shield thickness on dose rate during reactor operation.

5.5.6. Overall Reactor Neutronics Parameters

Table 5.5.1 lists the main neutronics parameters for the different regions of the reactor chamber. Using the coverage fractions and local nuclear parameters calculated for the different reactor regions surrounding the target, the overall reactor TBR and M_n can be determined. There are 24 beam ports with a diameter of 2 cm each. Only 0.004% of the source neutrons stream directly into these ports. Source sections in a cone with conical angle of 26.56° will impinge directly on the roof. Similarly, source neutrons directed towards the pool in a cone with the same conical angle will impinge directly on the pool. The rest of the source neutrons will go directly to the PERIT tubes in the reactor side. The results given in Table 5.5.2 indicate that the overall TBR and M_n values in LIBRA-SP are 1.435 and 1.288, respectively.

Table 5.5.1. Neutronics Parameters for the Different Regions of LIBRA-SP

Coolant/breeder	$Li_{17}Pb_{83}$ Eutectic
Lithium enrichment	90% ^6Li
Blanket	
Chamber wall radius	5.2 m
Inner radius of blanket	4 m
Neutron wall loading	7.4 MW/m^2
TBR	1.481
M_n	1.285
Peak PERIT dpa rate	94.2 dpa/FPY
Peak PERIT He production rate	436 He appm/FPY
Power density in the front INPORT tube	18.3 W/cm^3
Minimum PERIT lifetime	1.6 FPY
Peak chamber wall dpa rate	4.2 dpa/FPY
Peak chamber wall He production rate	0.92 He appm/FPY
Peak power density in chamber wall	0.52 W/cm^3
Chamber wall lifetime	30 FPY
Roof	
Distance from target	17 m
Thickness	0.5 m
Neutron wall loading	0.41 MW/m^2
TBR	0.499
M_n	1.349
Peak dpa rate	4.88 dpa/FPY
Peak He production rate	23.6 He appm/FPY
Lifetime	30 FPY
Bottom	
Distance of pool surface from target	5 m
$Li_{17}Pb_{83}$ pool depth	0.6 m
TBR	1.592
M_n	1.273
Peak dpa rate in steel plate	4 dpa/FPY
Peak He production rate in steel plate	1.04 He appm/FPY
Lifetime	30 FPY
Biological Shield	
Thickness at midplane	2.5 m
Operational dose rate at back of side shield	2.23 mrem/hr
Thickness above roof	2.6 m
Operational dose rate at back of roof shield	1.8 mrem/hr

Table 5.5.2. Overall Reactor Tritium Breeding Ratio and Energy Multiplication

Region	Coverage Fraction	TBR	M_n
PERIT	89.438%	1.481	1.285
Beam ports	0.004%	0	0
Roof	5.279%	0.499	1.349
Pool	5.279%	1.592	1.273
Total reactor	100%	1.435	1.288

To take into account the surface energy deposited by x-rays and ion debris and the energy lost in target endoergic reactions, an overall energy multiplication factor (M_o) is defined as the ratio of total power deposited to the DT fusion power. For the target design used here, M_o is related to M_n via

$$M_o = 0.9928\ [0.6541\ M_n + 0.3459]\ .$$

The overall energy multiplication for the reference LIBRA-SP design is 1.18 implying a total power of 2695 MW deposited in the chamber with 784 MW deposited at the front surfaces by x-rays and debris and 1911 MW deposited volumetrically by neutrons and gamma photons.

5.6. Thermal Hydraulic Analysis

5.6.1. Introduction

The thermal hydraulics performance of the PERIT tubes and the rest of the blanket/shield zone is discussed in the next section.

5.6.2. Geometry

The PERIT units in the LIBRA-SP blanket have the configuration of a barrel shape surrounding the target at the center of the reactor chamber. The general shape of the reactor chamber is a mushroom-like configuration, the stem being the cooling units, and the head is the roof (Fig. 5.1.1). The cooling units consist of two groups. The first one is at the front (PERIT units) and the second are solid curved circular tubes in the back. Both are made of

vertically curved ferritic stainless steel, low activation HT-9 tubing. A detailed description of these two groups follows:

- First group: The front group consists of one row of solid perforated metallic tubing. The perforated walls of this system of tubing allow the internal coolant/breeder fluid to jet through the perforated walls and form flat thin vertical sheets of liquid metal as previously described in Section 5.3. Also, it wets the outer surface of the tube. The lead-lithium sheet jet and the wetted wall is designed to protect the metallic material from x-rays, charged particles and target/reaction debris.
- Second group: The secondary tubes consist of 8 concentric rows of solid HT-9 tubing. The first group after the PERITs is staggered to close the gap between the PERIT tubes. The rest are positioned in the back behind the feed and return manifold (Fig. 5.1.2). It is expected that the lead-lithium vapor will recondense on all of the tube surfaces. The general parameters for the PERIT unit geometry are as follows:

The front (PERIT) group	
Number of rows	1
Number of tubes/row	175
Diameter of each tube (cm)	7.0
Diameter of the first row (cm)	800.0

The second group	
Number of rows	8
Number of tubes/row	175/first - 120/rest
Total number of tubes	1015
Diameter of each tube (cm)	8.0/first - 15/rest

5.6.3. Thermal Hydraulics Calculations

In Section 5.5 the neutronics analysis is given, which utilizes a one-dimensional model to calculate the distribution of the volumetric nuclear heating in the blanket and PERIT unit.

Also, in Section 1, results of a one-dimensional hydrodynamics calculation are given which determines the cavity performance and accounts for the effects of vaporization/condensation processes on the surface heat flux. The steady state nuclear heating distribution at the midplane is shown in Fig. 5.5.2. For thermal hydraulics calculations consider the following thermal load assumptions of the first surface (FS) of the LIBRA-SP reactor:

- The first surface is the first two rows of the coolant tubes (the first 20 cm of the blanket).
- According to the spatial distribution of the neutron heating, nearly 37% of the total neutron heating is generated in the first 20 cm of the blanket.
- All X-ray and debris power is consumed in evaporating PbLi (6.62 kg per shot).
- All PbLi vapor eventually will recondense on the first surface only and cools down to 620°C.

Table 5.6.1 presents the results, using these assumptions.

Figure 5.6.1 shows the temperature variation and variation of coolant speed in the first row of PERIT units. Figure 5.6.2 shows the maximum temperature in the HT-9 of the first row of PERIT units using a 1-D thermal model. The maximum surface temperature of the HT-9 is chosen not to exceed 625°C to avoid the rapid decline in the HT-9 mechanical properties. Figure 5.6.3 shows a graph of the heat transfer coefficient used for liquid metal (PbLi) at a temperature of 400°C and tube diameter of 7.0 cm. Figures 5.6.4, 5.6.5 and 5.6.6 show the material data base used for liquid metal (PbLi) here and in Section 5.3. Figure 5.6.7 shows a graph of the material data base used for structural material (HT-9).

5.6.4. Tube Surface Temperature

A 2-D finite element model is prepared to analyze thermally the status of the PERITs at the midplane where the coolant exits from the upper section at 430°C. The same situation happens at the bottom where the coolant exits from the lower section at 430°C to the pool. For this analysis the following input values are used:

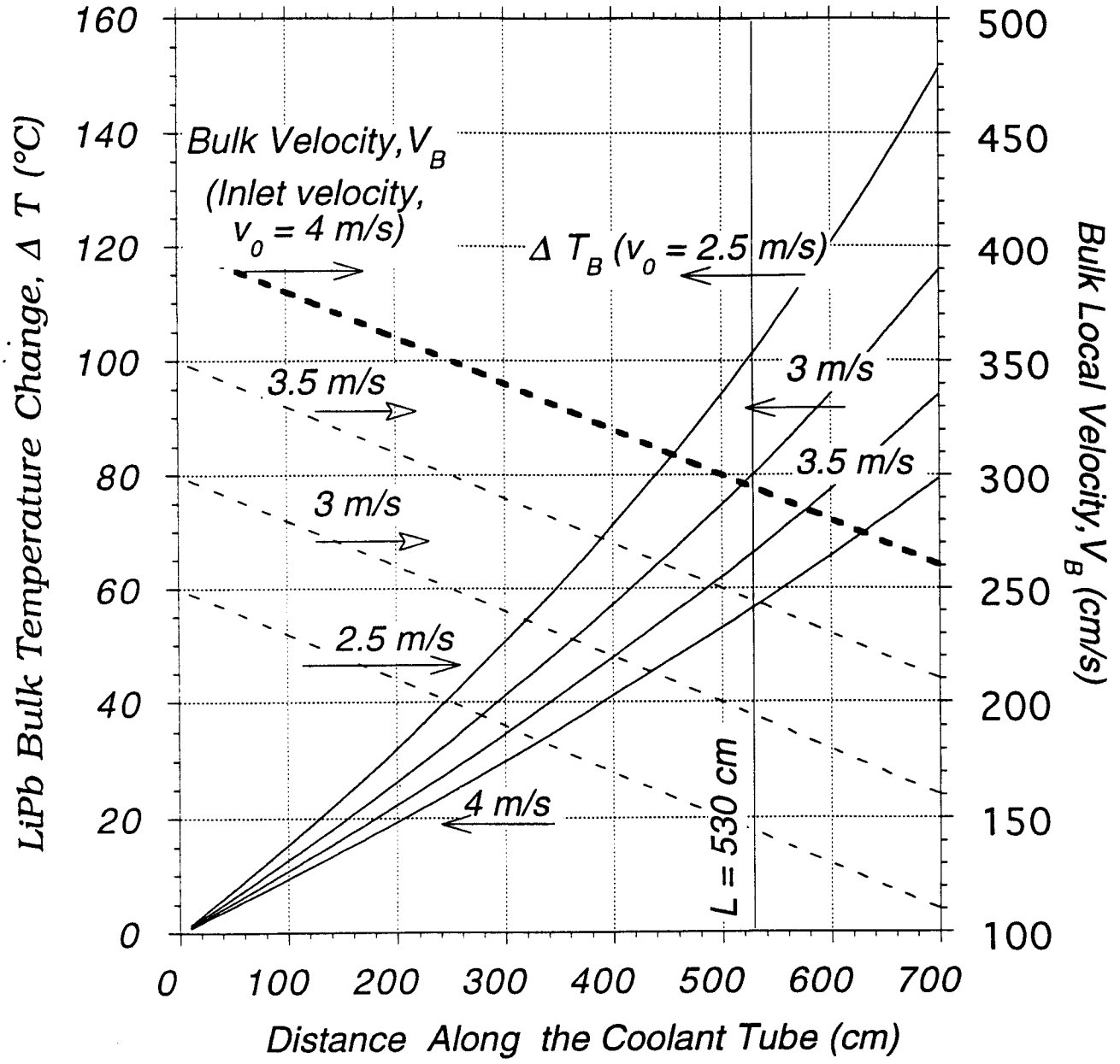

Figure 5.6.1. The temperature variation and variation of coolant speed in the first row PERITs.

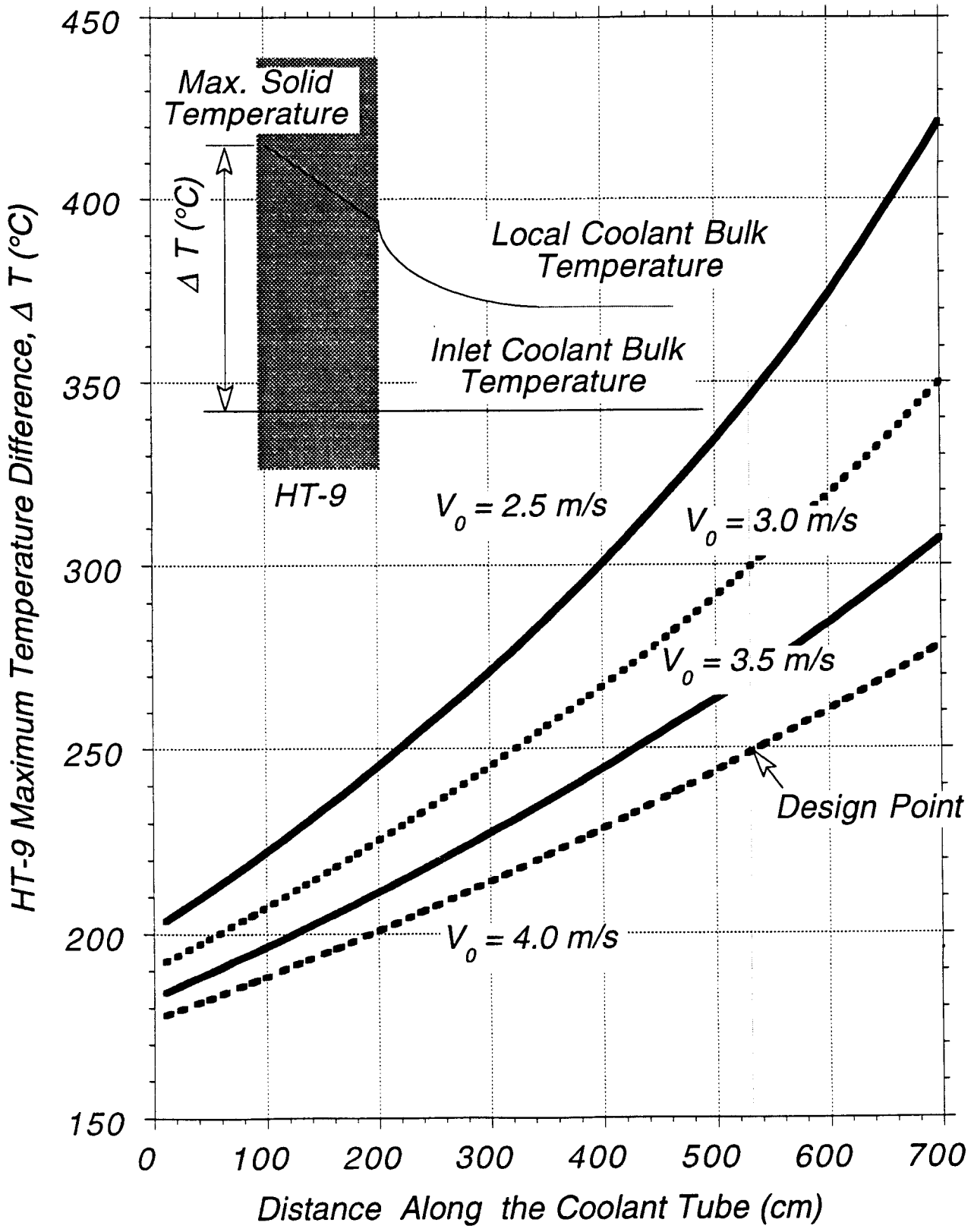

Figure 5.6.2. Maximum temperature in the HT-9 of the first row PERIT.

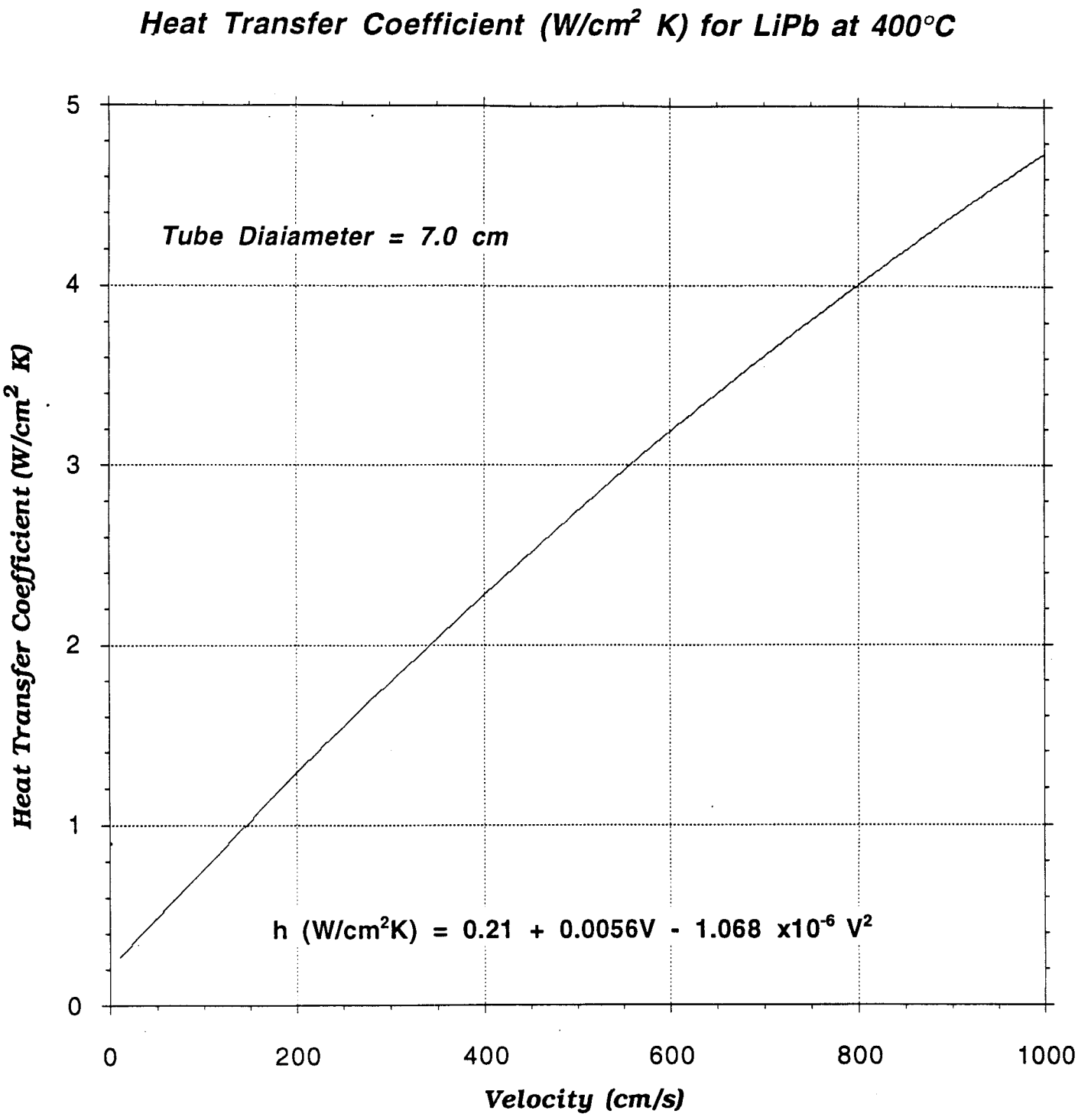

Figure 5.6.3. A graph of the heat transfer coefficient used for liquid metal (PbLi).

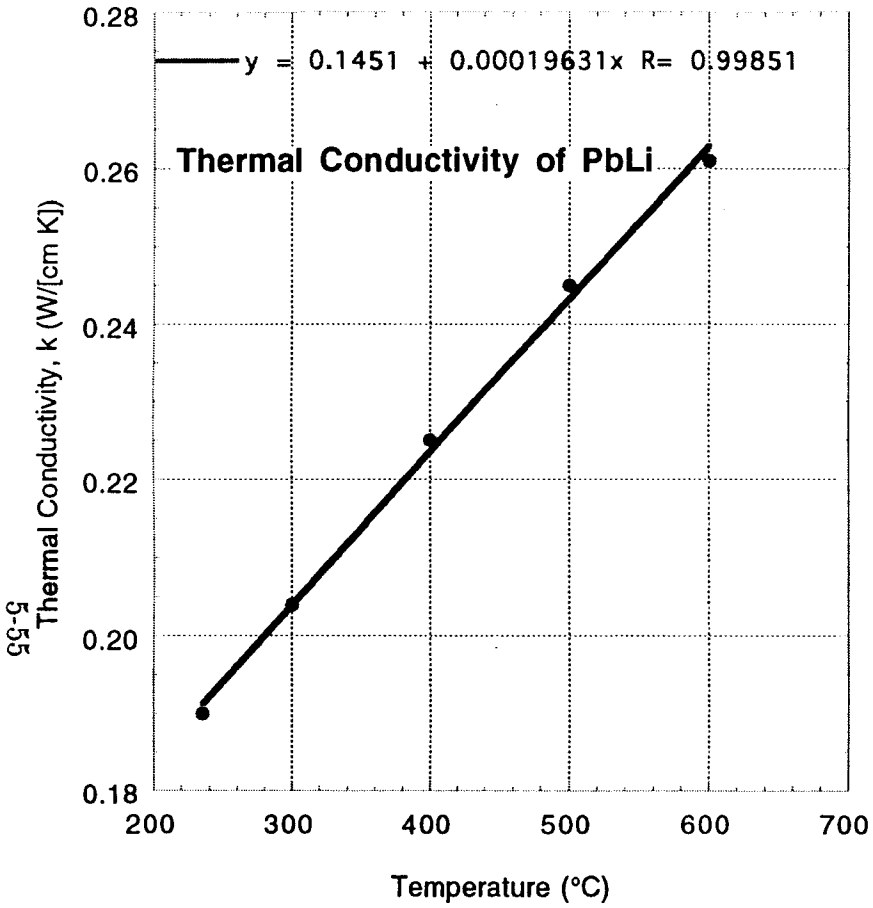

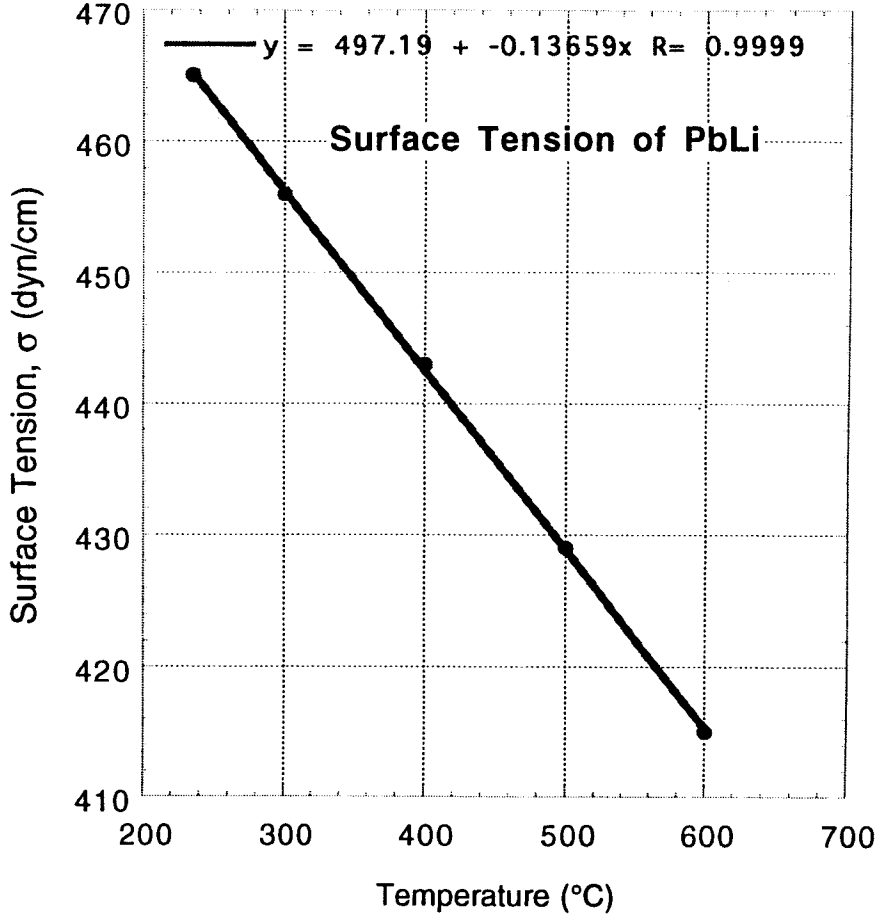

Figure 5.6.4. A graph of the material data base used for liquid metal (PbLi), thermal conductivity and surface tension.

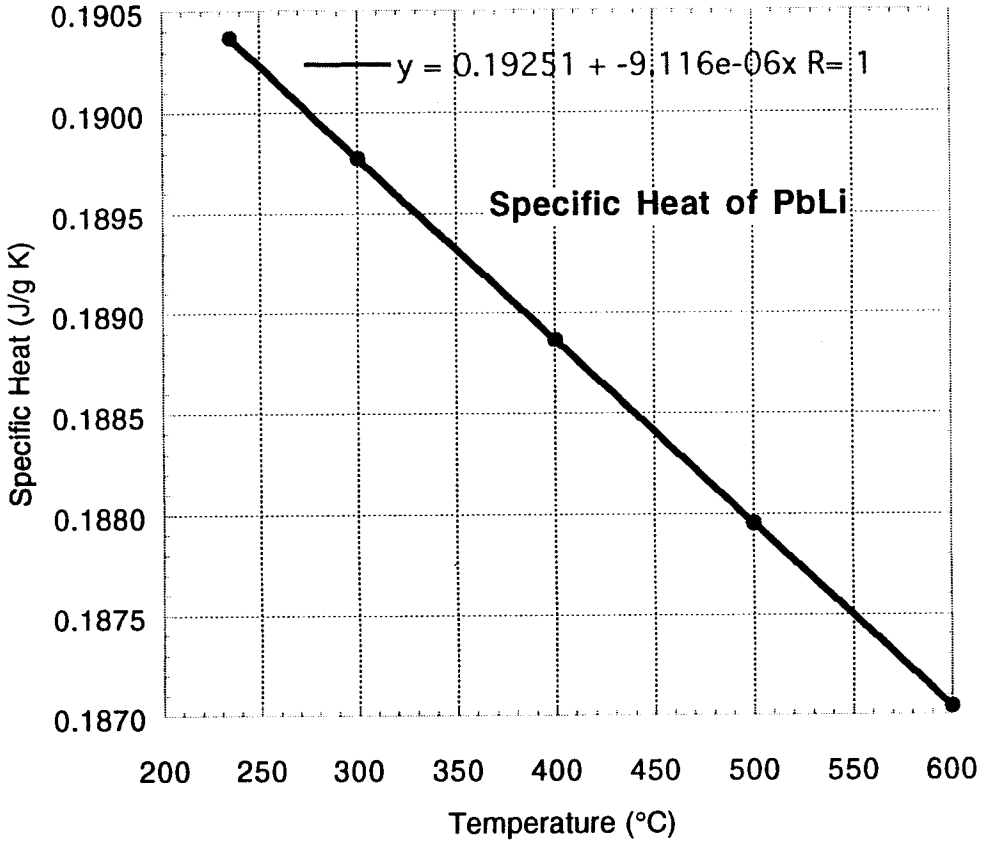

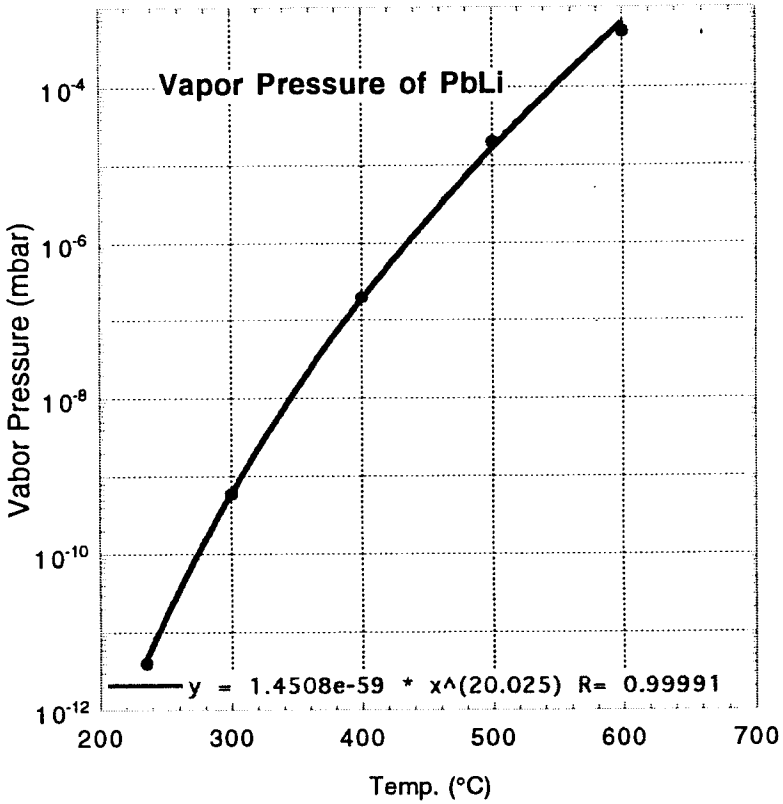

Figure 5.6.5. A graph of the material data base used for liquid metal (PbLi), specific heat and vapor pressure.

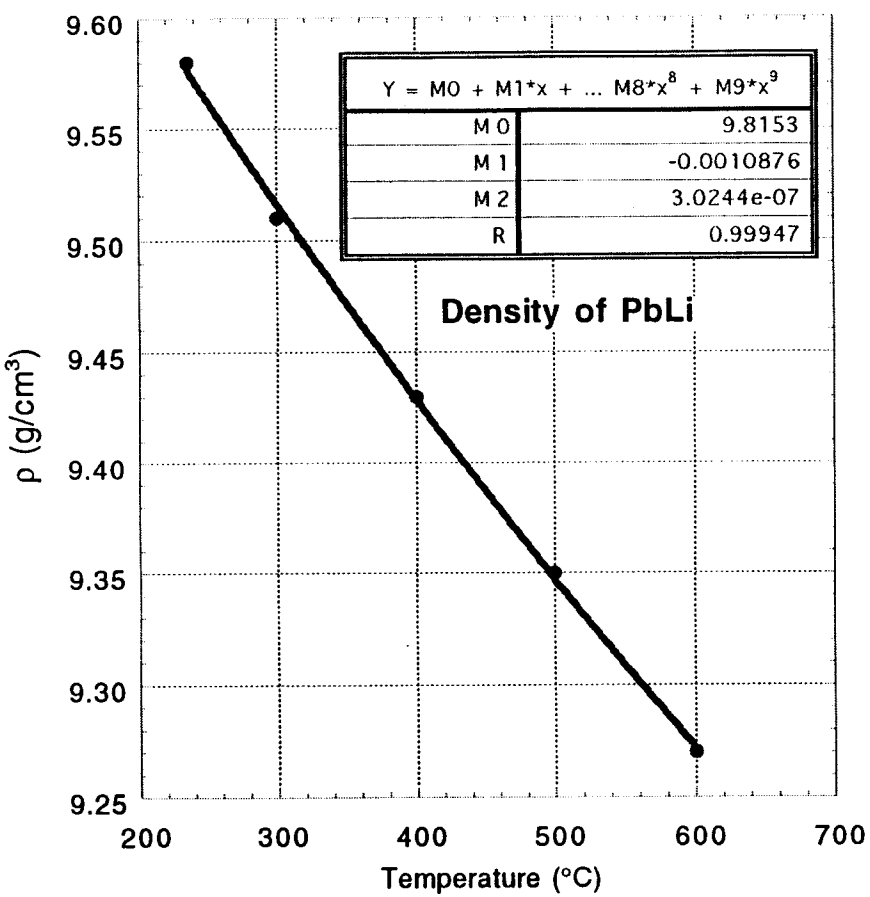

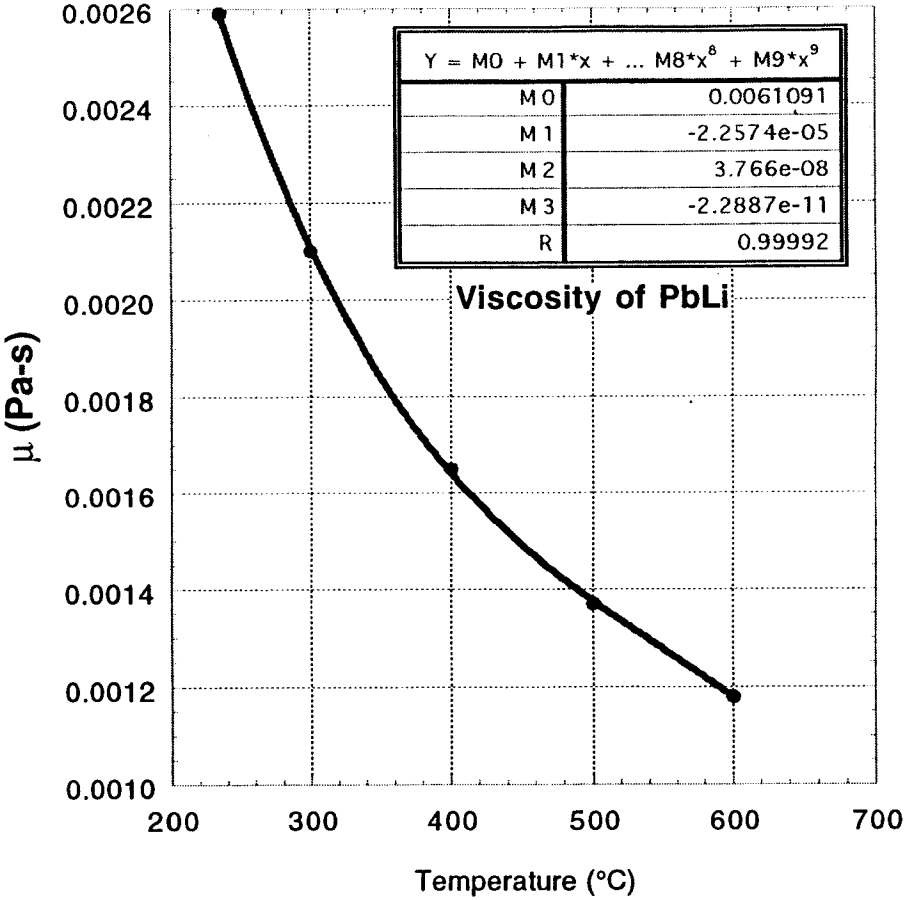

Figure 5.6.6. A graph of the material data base used for liquid metal (PbLi), density and viscosity.

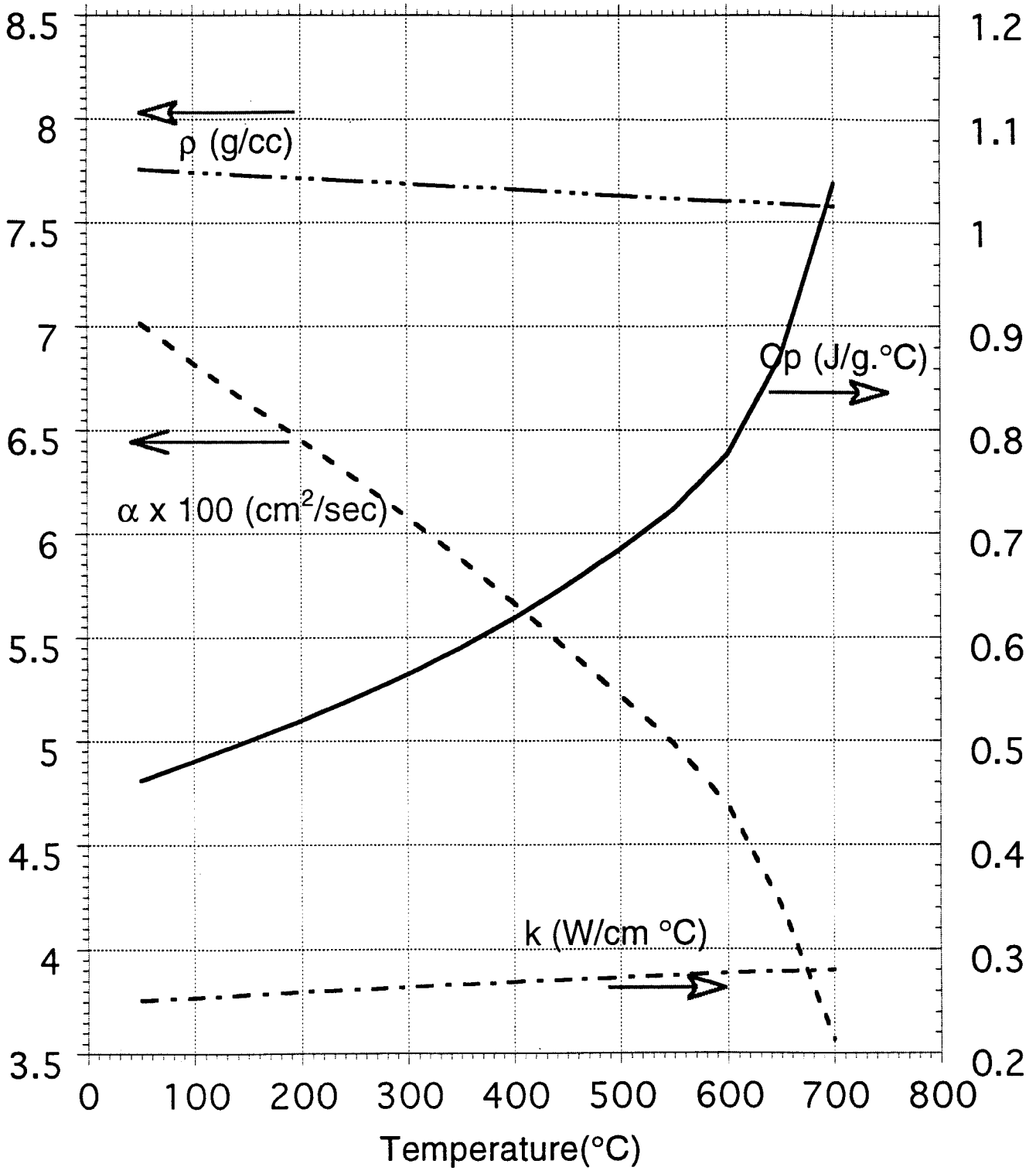

Figure 5.6.7. A graph of the material data base used for structural material (HT-9), specific heat, density, thermal conductivity an thermal diffusivity.

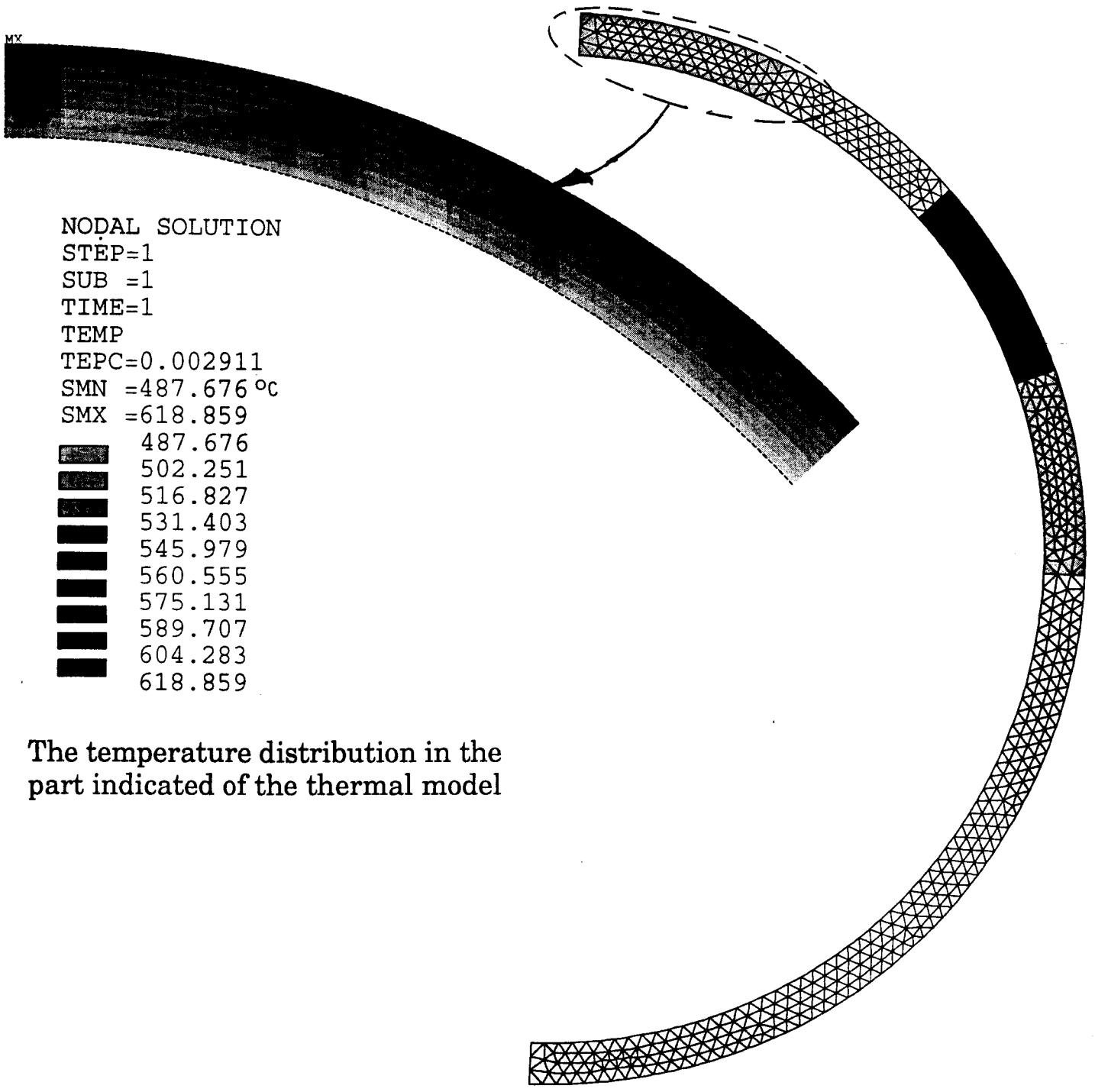

The temperature distribution in the part indicated of the thermal model

Figure 5.6.8. The finite element model for half of a PERIT.

Table 5.6.1. Thermal Hydraulics Parameters

Number of the coolant tubes in the FS	350
Total surface area (m^2)	1910.6
Weight of evaporated PbLi/shot (kg)	6.62
Thickness of PbLi recondensed per second (mm)	1.35
Heat flux due to recondensation at FS (W/cm^2)	107
Maximum value of volumetric heating at FS (W/cm^3)	36.6
Average nuclear volumetric heating in front tube (W/cm^3)	35.03
Temperature rise in the coolant tube wall (HT-9 wall thickness = 3 mm) due to:	
1. Surface heat flux only (condensation) (°C)	117.5
2. Volumetric heating only (°C)	7.5
Total temperature rise in the FS coolant tube wall (°C)	125
Maximum FS coolant velocity (at inlet) (m/s)	4.0
Minimum FS coolant velocity (at exit) (m/s)	2.9
Inlet FS coolant bulk temperature (°C)	370
Exit FS coolant bulk temperature (°C)	430 (32.32×10^4 kg/s)
Average coolant bulk temperature of outside coolant (°C)	650 (12.26×10^4 kg/s)
Exit blanket coolant bulk temperature (°C) (V = 17.4 cm/s)	600 (5.23×10^4 kg/s)
Total mass flow rate (kg/s)	49.78×10^4
HX inlet coolant bulk temperature (°C)	502
Pumping power (inside cavity) (MW)	47.61

Coolant temperature (°C)	430
Heat transfer coefficient (W/cm^2K)	2.20
HT-9 thermal conductivity (W/cm^2K)	0.24893+5.228e-5T-1.0818e-8T^2
Surface heat flux (W/cm^2K)	107
Tube thickness (mm)	3

The results of this analysis show that the temperature distribution in the circumferential direction (θ-direction) is nearly homogeneous at a maximum of 619°C at the outer surface and at a minimum of 487.5°C at the inner surface. The maximum temperature using 1-D thermal analysis is 625°C. We expect a slightly lower value of the maximum temperature when using 3-D thermal analysis because of the conduction in the third dimension. Figure

5.6.8 shows the finite element model and the temperature distribution in the first 45° sector of the PERIT.

References for Section 5

1. G. L. Kulcinski, et al., "The INPORT Concept – An Improved Method to Protect ICF Reactor First Wall," J. Nucl. Matls., 102 & 104, 103-108 (1981).
2. B. Badger et al., "LIBRA – A Light Ion Beam Fusion Conceptual Reactor Design," University of Wisconsin Fusion Technology Institute Report, UWFDM-800, Feb. 1990.
3. B. Badger et al., "LIBRA-LiTE – A Commercial Light Ion Fusion Power Plant," FPA-91-4 and University of Wisconsin Fusion Technology Institute Report, UWFDM-880, Dec. 1991.
4. G. I. Taylor, "Formation of Thin Flat Sheets of Water," The Scientific Papers of Sir Geoffrey Ingram Taylor, Edited by G. K. Batchelor, Trinity College, Cambridge, UK, Vol. IV, Paper #33, pp. 378-396, 1971.
5. N. Dombrowski, D. Hasson and D. E. Ward, "Some Aspects of Liquid Flow Through Fan Spray Nozzles," Chemical Engineering Science, Pergamon Press Ltd., London, Vol. 12, pp. 35-50, 1960.
6. R. R. Peterson, J. J. MacFarlane, and G. A. Moses. "CONRAD – A Combined Hydrodynamics–Condensation/Vaporization Computer Code," University of Wisconsin Fusion Technology Institute Report UWFDM–670 (July 1988).

7. G. A. Moses, G. Magelssen, R. Isreal, T. Spindler, and B. Goel, "PHD-IV – A Plasma Hydrodynamics, Thermonuclear Burn, Radiative Transfer Computer Code," University of Wisconsin Fusion Technology Institute Report UWFDM –194 (August 1985).

8. J. J. MacFarlane, "Collisional-Radiative Equilibrium Model for the CONRAD Radiation–Hydrodynamics Code," University of Wisconsin Fusion Technology Institute Report UWFDM – 937 (December 1993).

9. F. Biggs and R. Lighthill, "Analytical Approximations for X-Ray Cross Sections III," Sandia National Laboratories Report SAND-0070 (August 1988).

10. T. A. Mehlhorn, "A Finite Material Temperature Model for Ion-Driven ICF Targets," *J. Appl. Phys.* **52**, 6522 (1981)

11. P. Wang, "EOSOPA – A Code for Computing the Equations of State and Opacities of High–Temperature Plasmas with Detailed Atomic Models," Fusion Power Associates Report FPA–93–8 (December 1993).

12. R. O'Dell, et al., "User's Manual for ONEDANT: A Code Package for One–Dimensional, Diffusion–Accelerated, Neutral Particle Transport," Los Alamos National Laboratory Report LA–9184–M (1989).

13. R. D. Blevins, *Formulas for Natural Frequency and Mode Shape*, Robert E. Krieger Publishing Co., Malabar, FL, 1987, p. 108.

14. Nuclear Systems Handbook, Vol. 1, Design Data (March 1984)

15. R. O'Dell et al., "User's Manual for ONEDANT: A Code Package for One-Dimensional, Diffusion-Accelerated, Neutral Particle Transport," Los Alamos National Laboratory, LA-9184-M, 1989.

16. P. F. Rose, "ENDF/B-VI, The U.S. Evaluated Nuclear Data Library for Neutron Reaction Data," Summary Documentation Report ENDF 201, U.S. National Nuclear Data Center, 1992.

6. Beam Ports and Diode Damage Assessment

6.1. Diode Enclosure Environment

The diodes' atmosphere must be physically separated from that of the reactor chamber, since they require a much higher vacuum to operate properly. The pressure in the chamber just prior to a shot is 0.2 torr at 300 K or 0.52 torr at the maximum LiPb temperature of 773 K. However, the pressure in the diodes' enclosure must not exceed 10^{-4} torr, more than three orders of magnitude lower. The beam port aperture for the self-pinched propagation must be ~ 2 cm in diameter. Such a large hole connecting the huge volume of the reactor chamber to the very small volume of the diodes makes it impossible to maintain a pressure of 10^{-4} torr by using steady state differential pumping. It has always been assumed that some sort of shutter system will be used to isolate the diodes from the reaction chamber. Several schemes have been envisioned, such as counter rotating double discs as well as single discs. In these schemes, holes in the rotating discs overlap with the beam aperture in the chamber at the moment the beam is fired, thus ingesting the chamber atmosphere only when the aperture is open. There are some steady state leaks taking place through the clearances around the discs, but they are small and can be pumped out by the vacuum system in each of the diode enclosures.

6.1.1. Double Rotating Discs

In this scheme, two discs with holes at the same radius are mounted on concentric uniaxial shafts and rotate at different speeds either in the same direction or in opposing directions. The slow disc rotates at the rep-rate of the reactor, while the fast disc rotates at a much higher rotational speed. The holes in the two discs overlap at many points depending on the rotation of the high speed disc and one of these points overlaps with the beam aperture. Thus the beam aperture is open onto the chamber only for the duration it takes for the high speed disc to sweep across it. All the other times when the high speed disc overlaps with the beam aperture, it is obscured by the slow disc. Although this scheme is very effective for limiting the time the diode enclosure is in communication with the chamber,

it is complicated and would be prone to failure in the severe environment of a fusion reactor. Further, we have found that a single disc rotating at a slow rate can perform the function of isolating the two environments and be much more reliable.

6.1.2. Single Rotating Discs

The scheme adopted for LIBRA-SP has a single rotating disc with a radius of 25 cm and a 2 cm diameter hole located at a radius of 20 cm. The disc rotates at a frequency equal to the rep-rate of the reactor and the time the beam aperture is open is determined by rotation frequency and the radius at which the hole is located from the shaft. Using the disc parameters and a rep-rate of 3.9 Hz, the time it takes for the hole in the disc to sweep across the beam aperture is 8.2 ms and the beam aperture is fully open at 4.1 ms.

The beam, after passing through the beam aperture, travels down a tube 150 cm long, which puts it beyond the limit of the blanket composed of PERIT tubes, and then travels through open space to the target at the reactor center. This tube plays a major role in the dynamics of the chamber gas. Its conductance limits the access of gas from the chamber thus minimizing the total amount ingested during the time the beam port is open.

6.1.3. Modeling the Problem

Figure 6.1.1 is a schematic of the system, showing the diode enclosure connected to the beam tube through the beam aperture. The rotating disk is shown with the hole 180° from the beam aperture. It is entirely enclosed in the space between the diode and the beam tube which is sealed to the diode enclosure. This means that gases which fill the disc enclosure can only come through the beam tube.

Figure 6.1.2 is a plot of the overlapped aperture area and the cumulative area time product as a function of time. This cumulative area-time product curve will be used in computing the effective conductance of the beam aperture. The conductance of the system is the sum of the inverse of each individual conductance if they are located in series. This will be done for the first 4.1 ms of the beam aperture opening when the pressure in the reaction chamber is low, and for the second 4.1 ms, after the pulse, when the chamber pressure is high.

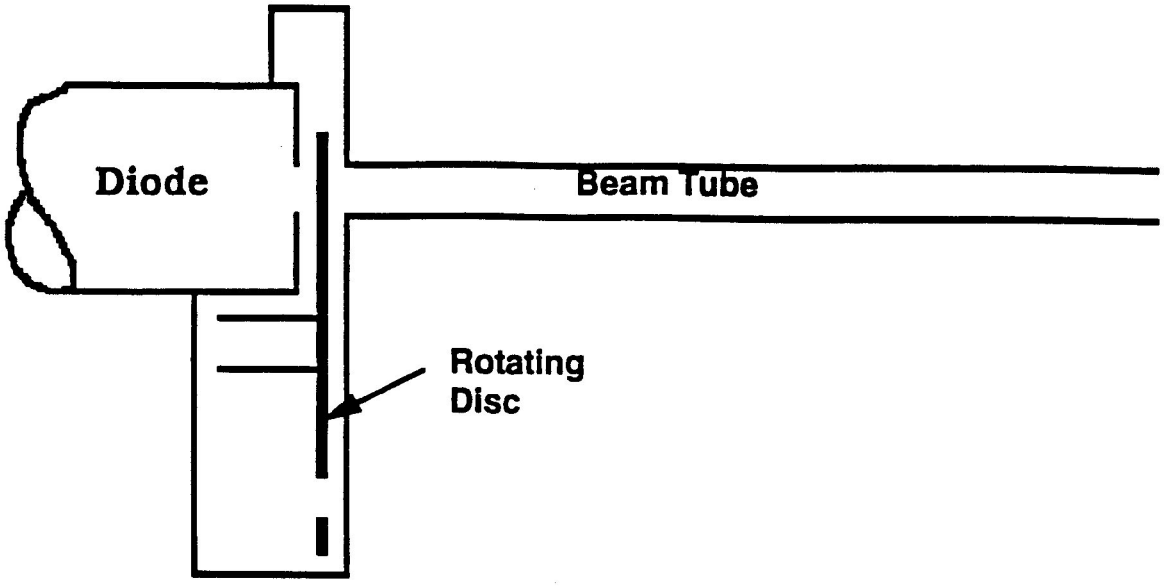

Figure 6.1.1. Schematic of diode/chamber interface.

The total throughput is the sum of the gas leakage over the 8.2 ms. This throughput raises the pressure in the diode enclosure and must be evacuated back to 10^{-4} torr in $\sim$ 250 ms before the next pulse arrives.

6.1.4. System Conductances

The conductance of a cylindrical tube in the viscous flow regime is expressed as [1]:

$$C = \frac{r^4(\overline{p})}{1.91\eta L} \qquad \ell/\mathrm{s}$$

where r is the tube radius in cm, $\overline{p}$ is the average pressure in torr, η is the gas viscosity in poises (g/cm·s) and L is the tube length in cm.

The pressure in the reaction chamber prior to the pulse is 0.52 torr (consistent with an atom density of $7 \times 10^{15}/\mathrm{cm}^3$ at $T = 770$ K), the pressure in the diode enclosure is 10^{-4} torr, which gives the average pressure $\overline{p}$ of 0.26 torr. Viscosity of He gas at 770 K is 3.94×10^{-4} poise and is independent of pressure, and the tube length L is 150 cm. The beam tube conductance is:

$$C_{bt} = \frac{(1)^4(0.26)}{(1.91)(3.9 \times 10^{-4})(150)} = 2.3\,\ell/\mathrm{s}\,.$$

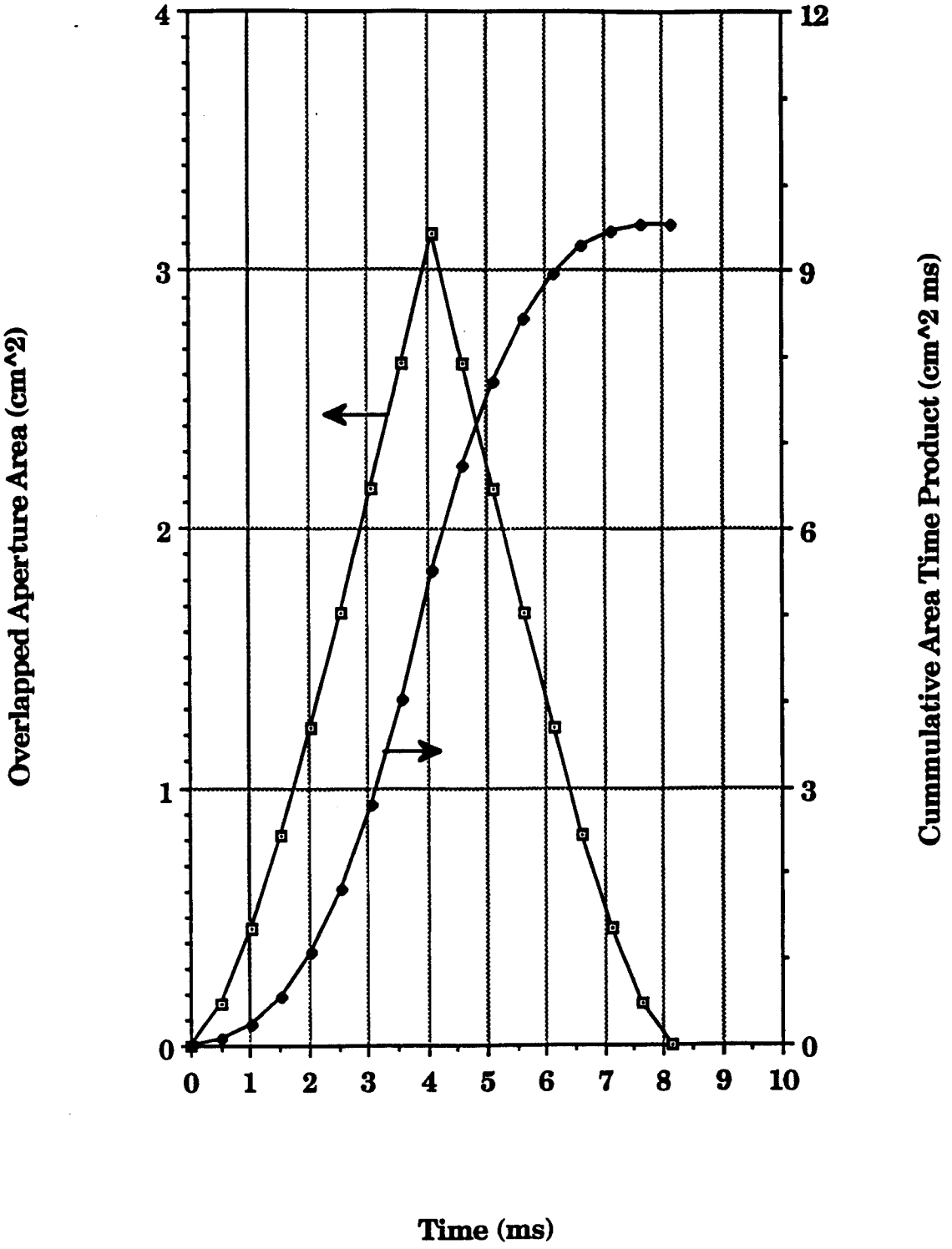

Figure 6.1.2. Overlapped aperture area and cumulative area-time product as functions of time.

The beam aperture changes with time as the hole in the disc overlaps with it. To calculate an equivalent constant aperture we make use of the area-time product curve in Fig. 6.1.2. At 4.1 ms the cumulative area-time product is 5.5 cm^2ms which is an equivalent area of 1.34 cm^2 or an aperture radius of 0.65 cm. The conductance of an aperture in the viscous flow regime is [1]:

$$C = \frac{1.142 \times 10^{-2} r^2}{\eta(1 - p_1/p_0)} \qquad \ell/\mathrm{s}$$

where p_0 is the source pressure and p_1 the sink pressure in torr. The conductance of the aperture is then:

$$C_a = \frac{1.142 \times 10^{-2}(0.65)^2}{3.9 \times 10^{-4}(1 - 10^{-4}/0.52)} = 12.25\ \ell/\mathrm{s}\,.$$

The conductance of the system consisting of the tube and aperture, which are in series is:

$$\frac{1}{C_s} = \frac{1}{C_{bt}} + \frac{1}{C_a}$$

and

$$C_s = \frac{C_{bt} C_a}{C_{bt} + C_a} = \frac{(2.3)(12.25)}{2.3 + 12.25} = 1.94\ \ell/\mathrm{s}\,.$$

The same procedure is followed for determining the conductances after the pulse, the remaining 4.1 ms when the pressure and temperature in the chamber rise, and the He gas viscosity also rises as a result of the higher temperature.

The target yield is 589 MJ, of which 34%, or 200 MJ, is in x-ray and ion debris, which when deposited in the gas raises the pressure in the chamber to 260 torr. Although this pressure does not last the full 4.1 ms, we will use it to make the calculation conservative. Under these conditions the equivalent conductance of the system is 6.93 ℓ/s.

6.1.5. Required Pumping Speed

Using the conductances determined above we can now calculate the throughput which is ingested into the diode enclosure during the 8.2 ms. In the first 4.1 ms, the throughput is:

$$(1.94\ \ell/\mathrm{s})(0.52\ \mathrm{torr}) = 1.0\ \mathrm{torr}\ \ell/\mathrm{s}$$

and the total quantity is

$$\frac{1.0 \text{ torr } \ell}{\text{s}} \left(\frac{4.1}{1000}\right) \text{ s} = 4.1 \times 10^{-3} \text{ torr } \ell \,.$$

In the second 4.1 ms the throughput is:

$$(6.93 \ \ell/\text{s})(260 \text{ torr}) = 1802 \text{ torr } \ell/\text{s}$$

and the total quantity is 7.39 torr ℓ. It is estimated that the volume of the diode enclosure is $1.7{\times}10^5$ cm^3 or 170 liters. The pressure rise in the diode enclosure is $\frac{7.39 \text{ torr } \ell}{170 \ \ell}$ or $4.3{\times}10^{-2}$ torr.

The vacuum pump capacity must reduce the pressure from 4.3×10^{-2} torr to $1{\times}10^{-4}$ torr in <256 ms. The capacity will be based on 230 ms. The equation for determining pumping speed is:

$$S = \frac{V}{t} \ln p_1/p_2$$

where S is pump speed in ℓ/s, V the enclosure volume in liters, t is time in seconds, p_1 is initial pressure and p_2 is final pressure. The pump speed is:

$$S = \frac{170}{0.23} \ln \frac{4.3 \times 10^{-2}}{1 \times 10^{-4}} = 4482 \, \ell/\text{s} \,.$$

Each diode will need a pump of such capacity close coupled to it, to maximize the conductance in the coupling joint. Pumps of such capacity are readily available, utilizing turbomolecular units backed up by roots blowers. Table 6.1.1 gives the parameters of the diode evacuation system.

6.2. Neutronics Analysis

6.2.1. Calculational Method

Radiation damage to the sensitive components of the diodes is affected by the detailed geometrical configuration and neutron streaming through the ports. A multi-dimensional neutronics calculation is required to properly model the complicated geometrical configuration. Two-dimensional neutronics calculations have been performed to estimate the expected damage levels in the diode components. The calculated neutron flux distribution is also utilized in the diode activation calculations. The discrete ordinates code TWODANT [2]

Table 6.1.1. Diode Vacuum System Parameters

Initial He atom density in chamber (#/cm^3)	7×10^{15}
Initial chamber pressure in chamber (torr)	0.52
Pressure in chamber after a pulse (torr)	260
Volume of reaction chamber (m^3)	2325
Pressure required in diode enclosure (torr)	10^{-4}
Volume of diode enclosure (m^3)	0.17
Diode beam aperture diameter (cm)	2.0
Diameter of beam tube (cm)	2.0
Length of beam tube (cm)	150
Rotating disc diameter (m)	0.5
Hole in the disc is at a radius of (m)	0.2
Rep-rate of reactor (Hz)	3.9
Rep-rate of disc (Hz)	3.9
Pressure rise in diode enclosure (torr)	4.3×10^{-2}
Pump capacity for each diode (ℓ/s)	4500

was utilized along with cross section data based on the most recent ENDF/B-VI evaluation. The P_3-S_8 approximation was used in the calculations. The results presented here are normalized to the DT fusion power of 2285 MW.

The region around a beam penetration was modeled in r-z geometry with the target represented by an isotropic point source on the z-axis. This included, in addition to the diode itself, the PERIT region, the reflector, the biological shield and the rotating discs. The two-dimensional model used in the calculations is shown in Fig. 6.2.1 for the diode region. A right-reflecting boundary is used at a radius of 1.5 m which is roughly half the distance between the centerlines of adjacent diodes. A vacuum boundary is used at the top. The calculation utilizes a total of 9196 mesh points (44 radial $\times$ 209 axial).

In order to model the detailed three-dimensional geometry for the deterministic two-dimensional discrete ordinates calculation, several adaptations were made to yield the idealized geometrical model shown in Fig. 6.2.1. The actual planes of symmetry cannot be included in the two-dimensional geometrical model, necessitating the use of a cylindrical reflecting boundary to account for the contribution from the surrounding regions. Even

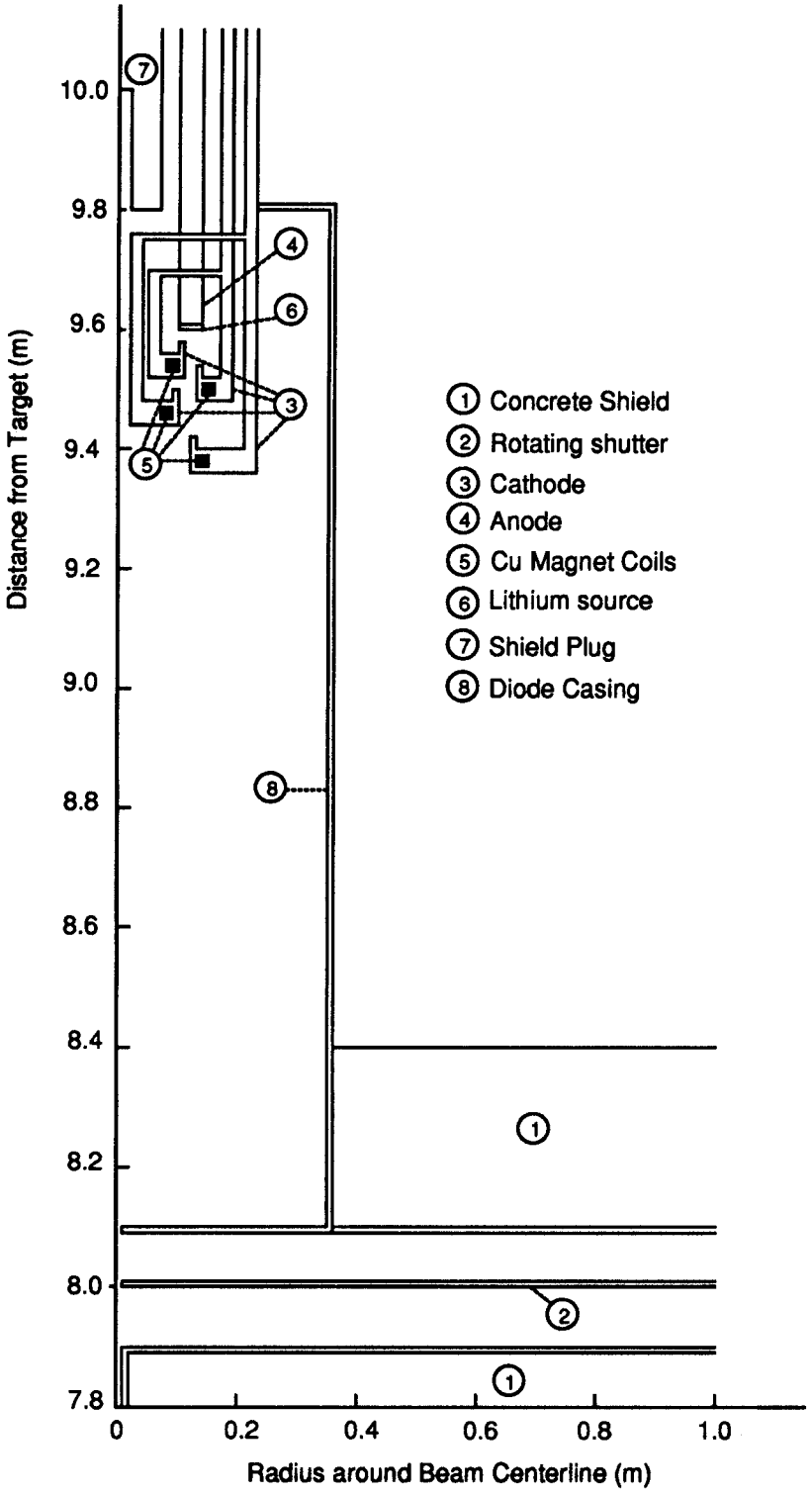

Figure 6.2.1. The r-z two-dimensional neutronics model.

though the cylindrical reflecting boundary is located at half the distance between the centerlines of the two adjacent diodes, its use is equivalent to surrounding the modeled diode by diode penetrations at all azimuthal locations. This tends to overestimate the flux and give conservative damage values in the diode area.

An inherent problem associated with multidimensional discrete ordinates calculations with localized sources is referred to as the "ray effect." It is related to the fact that the angular flux is given only in certain discrete directions. It is, therefore, not possible to exactly represent the component in the normal direction ($\mu = 1$) along the beam penetration which can lead to underestimating neutron streaming. The ray effect has been fully mitigated by use of the first collision method [3]. In this method, the uncollided flux is determined analytically and the volumetrically distributed first collision source is used in the calculations.

6.2.2. Radiation Damage Considerations

The diode components most sensitive to radiation damage are the diode casing, cathodes, anodes, and the magnets. The diode casing as well as the cathodes and anodes are assumed to be made of type 304 stainless steel. In this study, we adopted a conservative end-of-life dpa limit of 150 dpa for 304 SS. In the magnet coils, we are concerned with both electrical and mechanical degradation from neutron-induced transmutations. An additional irradiation problem is radiolytic decomposition of the water coolant, leading to corrosion and erosion product formation.

Among the most important mechanisms mentioned above, only one was found during the MARS [4] study as lifetime limiting for the normal magnet, namely the neutron-induced swelling in the ceramic insulator. Among the common ceramic insulators that are used in the normal magnets, spinel ($MgO{\cdot}Al_2O_3$) is of particular interest in the high-neutron-irradiation environment because of the superior absence of swelling in this insulator. Assuming that a 3 vol.% neutron induced swelling in polycrystalline spinel can be accommodated in the normal magnet structure without causing stress problems, the neutron-fluence limit for the

use of solid-polycrystalline spinel is 4×10^{22} n/cm^2 (E > 0.1 MeV) in the temperature range 100 to 300°C.

If an organic insulator such as epoxy or polyimide is used in the magnet, the dose limit will be more restrictive. Based on existing experimental data, the total absorbed dose in the insulator should not exceed $\sim 5 \times 10^9$ Rads [5] to avoid significant degradation in mechanical strength. This corresponds to a fast neutron fluence of $\sim 5 \times 10^{18}$ n/cm^2 (E > 0.1 MeV). This fluence limit is about four orders of magnitude lower than the limit for ceramic insulators. The impact of using organic insulators on the lifetime of the diode magnets will be assessed.

6.2.3. Proposed Design Modifications

Since the beam port diameter is only 2 cm, no source neutrons will impinge directly on the anode, cathodes, magnets and diode casing. These components will be subjected only to lower energy secondary neutrons. To reduce the flux and consequently the damage in the diode components, a neutron trap is utilized in the shield plug. Such a trap was found to reduce the neutron flux in the diode components by about an order of magnitude. Moving the neutron trap farther from the diode will result in additional reduction in the neutron flux and diode damage. Additional reduction can also be achieved by tapering the inner surface of the beam tube along the direct line-of-sight of source neutrons. This ensures that no source neutrons will impinge directly on the beam tubes producing secondary neutrons that will stream into the diode. Using this simple geometrical modification will result in the diode components being exposed only to secondary neutrons produced in the neutron trap. As explained above, these secondary neutrons can be reduced more by locating the neutron trap farther away from the target. The model used here assumes that the neutron trap is located at 10 m from the target. In addition, the beam tube is not tapered because of the limitations on modeling the geometry for two-dimensional calculations. Hence, the results presented here are expected to be conservative and lower flux and damage levels will result from three-dimensional calculations with the geometrical modifications, discussed above, properly modeled.

6.2.4. Radiation Damage in Diode Components

Figure 6.2.2 shows the variation of the dpa and helium production rates along the diode casing. The damage peaks at locations adjacent to the cathodes. This is due to the contribution from secondary neutrons produced in the diode components. The helium to dpa ratio is higher at these locations because of the relatively harder neutron spectrum due to proximity to the neutron trap compared to parts of the casing close to the chamber where the neutrons are slowed down considerably in the chamber and shield material. The peak dpa and helium production rates in the diode casing are 1.9×10^{-4} dpa/FPY and 6.8×10^{-4} He appm/FPY, respectively. Assuming a 30 FPY reactor operation, the end-of-life peak dpa and helium production in the coil casing are 0.006 dpa and 0.02 He appm, respectively. These very low damage levels imply that the diode casing is a lifetime component by a very large margin.

Figure 6.2.3 gives the damage rate variation along the inner and outer cathode feeds. Damage in the diode casing is also included for comparison. It is clear that the damage in the cathode feeds is higher than that in the casing at distances greater than ~ 9.7 m from the target. This is a direct result of their proximity to the neutron trap and the fact that they provide additional attenuation for secondary neutrons going from the neutron trap to the diode casing. Damage in the casing is larger than that in the cathode feeds at locations closer to the chamber due to the contribution of secondary neutrons streaming from the chamber. For the cathode feeds this component is attenuated by the cathodes and magnets. Damage in the cathode feeds peaks at 10 m from the target where the neutron trap is located. The peak dpa rates are 1.38×10^{-3} and 8×10^{-4} dpa/FPY for the inner and outer cathode feeds, respectively. This leads to peak end-of-life damage levels of only 0.041 and 0.024 dpa in the inner and outer cathode feeds. This implies that the cathode feeds will be lifetime components. As shown in Fig. 6.2.4, damage in the anode feed, which is closer to the neutron trap, is higher than that in the cathode feeds and the casing. The peak damage

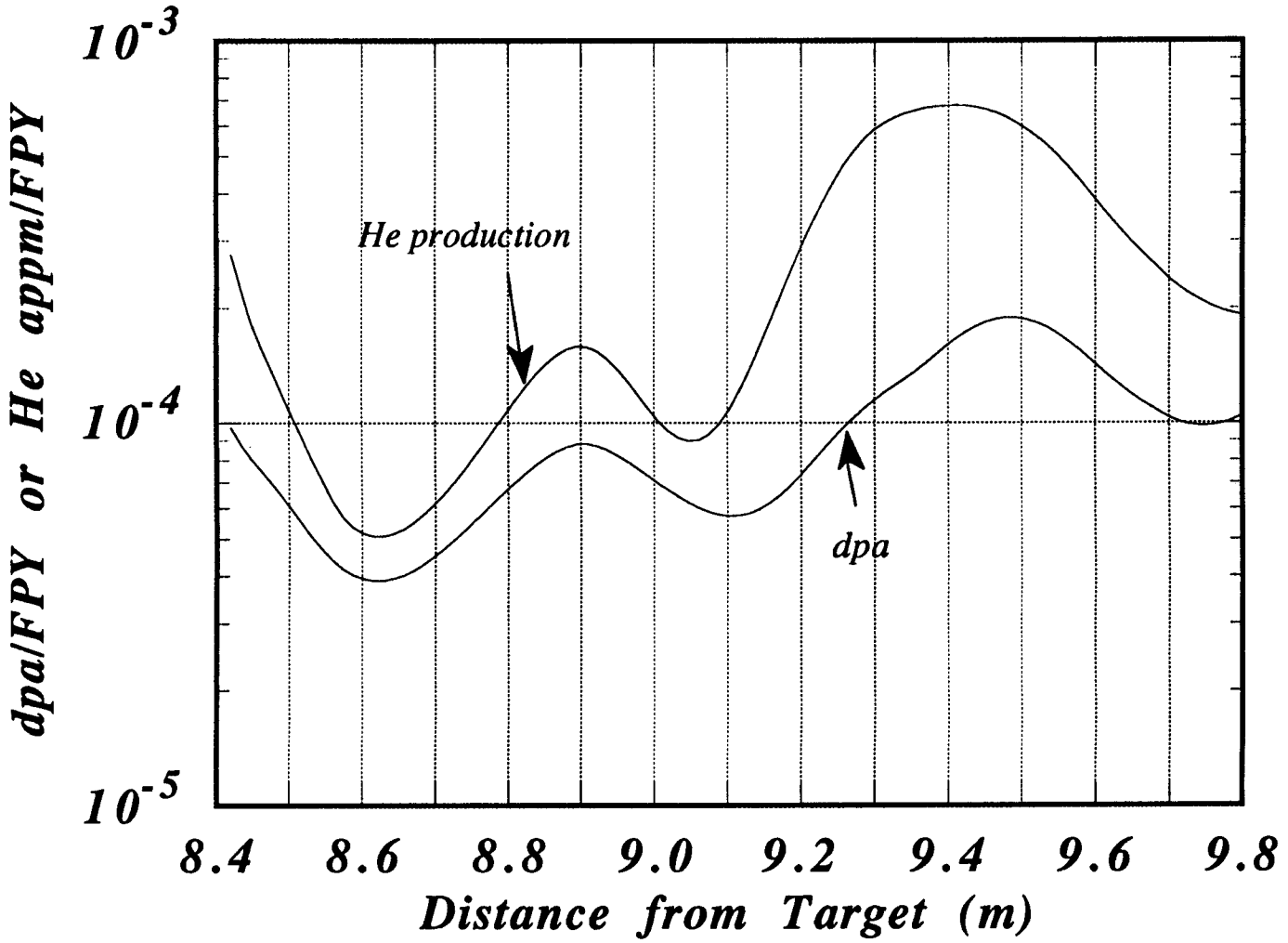

Figure 6.2.2. Variation of dpa and helium production along the diode casing.

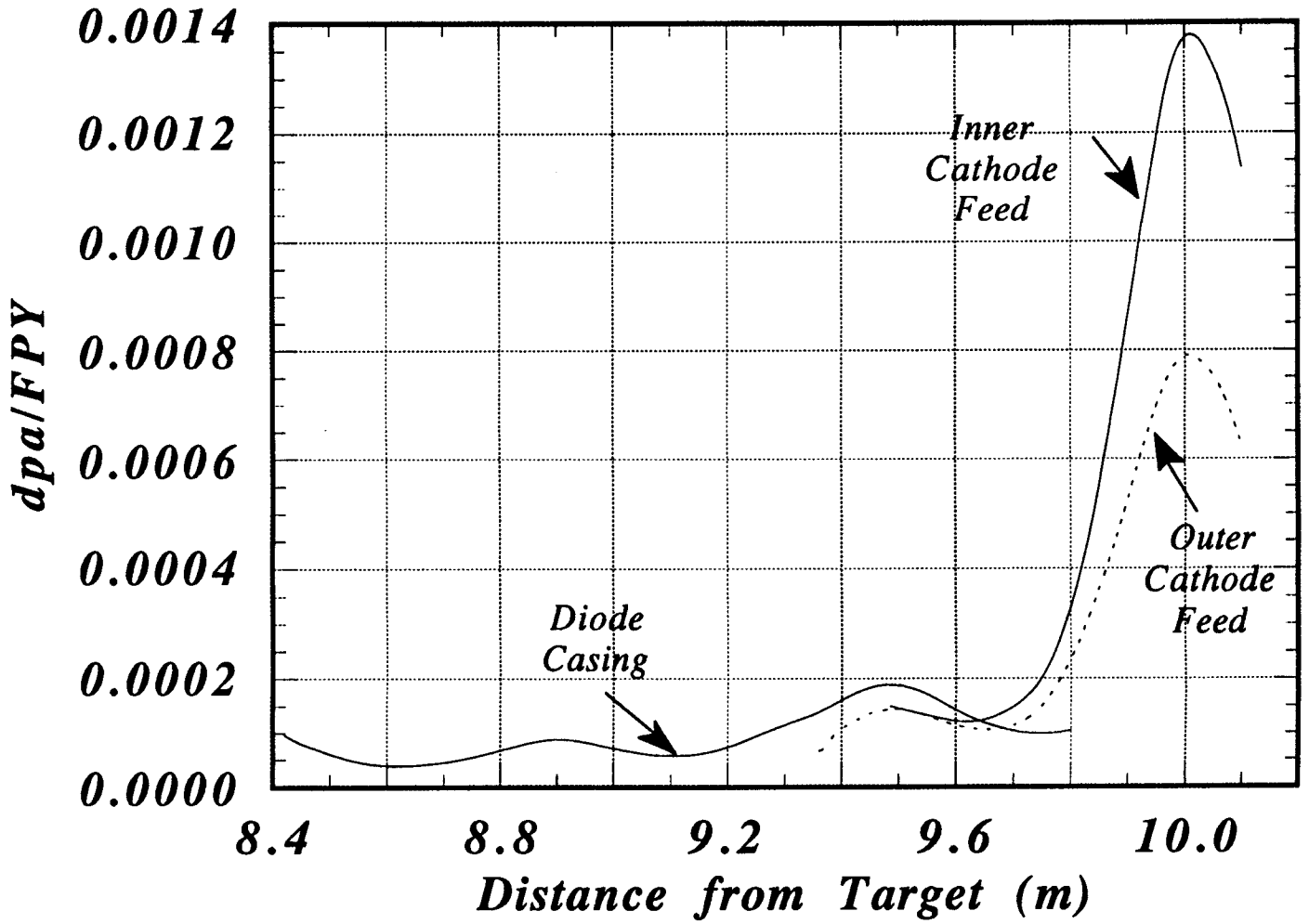

Figure 6.2.3. Damage rate in the cathode feeds and diode casing.

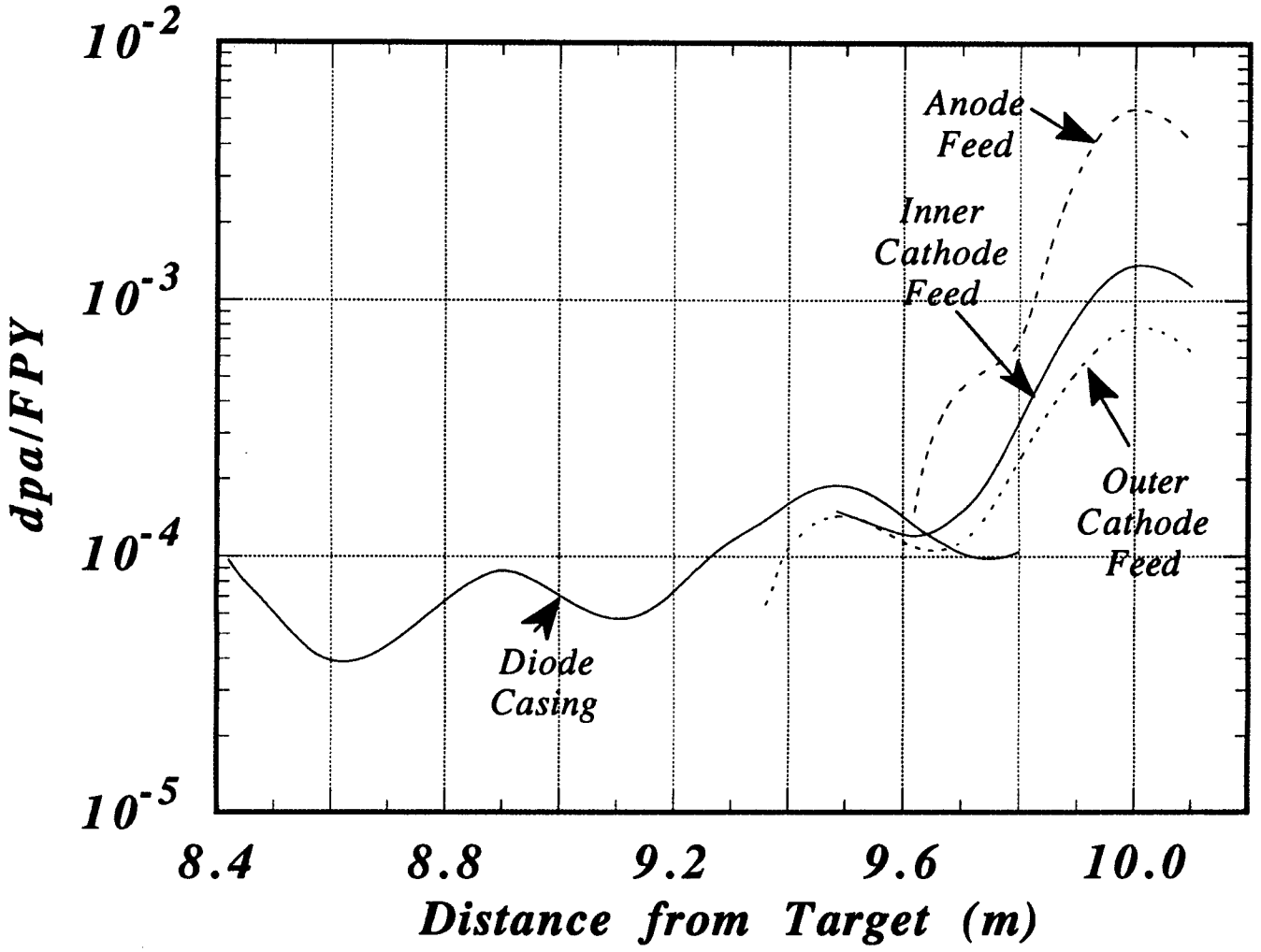

Figure 6.2.4. Damage rate in the anode feed, cathode feeds, and diode casing.

rate is 5.5×10^{-3} dpa/FPY and the end-of-life damage is 0.165 dpa. This is still about three orders of magnitude lower than the damage limit.

Table 6.2.1 gives the peak end-of-life dpa and helium production at the tips of the four cathode components. These are identified as cathode 1, 2, 3, and 4 in the order of distance from the target with cathode 1 being the farthest from the target and cathode 4 being the closest to the target. These damage levels are lower than those in the cathode tip feeds. The end-of-life damage levels at the cathode tips are very small with the largest being only 0.006 dpa for the cathode tip closest to the neutron trap (cathode 1). The damage at the tips of cathode 2 and cathode 3 are lower because they are located farther from the neutron trap. The damage at the tip of cathode 4 is still lower than that for cathode 1 but is slightly higher than those in cathodes 2 and 3. This is due to the fact that even though it is protected from neutrons scattered back from the neutron trap, it is directly exposed to secondary neutrons streaming from the chamber.

The end-of-life fast neutron fluence (E > 0.1 MeV) is given in Table 6.2.2 for the four magnet coils located in the cathode components. The neutron fluence values are comparable for the four coils with the largest fluence being 8.67×10^{18} n/cm^2 for cathode 4. These values are much lower than the 4×10^{22} n/cm^2 fluence limit for ceramic insulators. Hence, if ceramic insulators are used in the coils, they will be lifetime components. On the other hand, the results indicate that coils utilizing organic insulators might need to be replaced once during the reactor life. However, it should be noted that coil replacement might not be needed even with organic insulation if the geometrical modifications such as tapering the beam tubes and moving the neutron trap farther from the target are implemented. This needs to be confirmed by three-dimensional calculations. The peak end-of-life dpa and helium production in the neutron trap located at 10 m from the target are 153 dpa and 1914 He appm and the peak nuclear heating is estimated to be ~ 5 W/cm^3. Although the damage level is slightly higher than the design limit, it should be noted that the neutron trap is not subject to significant stresses. In addition, moving the trap farther from the target will reduce the damage level.

Table 6.2.1. Damage in the Cathode Tips After 30 FPY Operation

	dpa	He appm
Cathode 1	6.12×10^{-3}	1.03×10^{-2}
Cathode 2	4.00×10^{-3}	3.48×10^{-3}
Cathode 3	3.51×10^{-3}	3.42×10^{-3}
Cathode 4	4.29×10^{-3}	6.78×10^{-3}

Table 6.2.2. End-of-Life Fast Neutron Fluence in the Magnet Coils

	Fast Neutron Fluence (E > 0.1 MeV)
Cathode 1	7.65×10^{18}
Cathode 2	6.39×10^{18}
Cathode 3	6.12×10^{18}
Cathode 4	8.67×10^{18}

References for Section 6

1. H. A. Steinberg, "Handbook of High Vacuum Engineering," Reinhold Publishing Corp., 1963.

2. R. Alcouffe et al., "User's Guide for TWODANT: A Code Package for Two-Dimensional, Diffusion-Accelerated, Neutral-Particle Transport," LA-10049-M, Los Alamos National Laboratory (March 1984).

3. R. Alcouffe, R. O'Dell, and F. Brinkley, Jr., "A First-Collision Source Method that Satisfies Discrete S_n Transport Balance," *Nucl. Engr. and Design* **105**, 198 (1990).

4. B. G. Logan et al., "MARS Mirror Advanced Reactor Study Commercial Fusion Electric Plant," Lawrence Livermore National Laboratory, UCRL-53480 (1984).

5. W. Daenner, L. El-Guebaly, M. Sawan, et al., "Neutron Shielding and Its Impact on the ITER Machine Design," *Nucl. Engr. and Design* **16**, 183 (1991).

7. Tritium and Safety Analysis

7.1. Tritium Issues

The principal tritium systems considered in this study are related to the fueling and breeding functions. These systems consist of many components, each designed for a specific processing function. The functions of these sub-components are briefly described and their tritium inventories are estimated. Such information is required in order to evaluate the potential radiological hazard to plant personnel and the local environment due to routine and off-normal release of tritium.

7.1.1. Target Fuel Preparation

The targets will be filled with liquid DT, as described in the LIBRA [1] study, and stored in a target fabrication facility adjacent to the reactor building. Each capsule contains 5.81 mg (DT) and 335,000 targets per day are required; however, only one-hour batches will be prepared at a time so that only $\sim$ 49 g(T) is being processed. In addition, two batches of filled targets are stored in a cryogenic freezer at $\sim$ 19 K so that a uniformly thick coating of solid DT can form on the inside of the capsule. The total vulnerable tritium which could be released in a severe accident is $\sim$ 147 g(T), as noted in Table 7.1.1.

The daily amount of tritium processed in this facility is $\sim$ 1200 g. Experience at TSTA [2] has indicated that with proper design of gloveboxes surrounding all processing equipment, the tritium release to the stack would be only $\sim$ 12 Ci/day. A one-day supply of prepared targets will be stored in a cryogenically cooled vault. This vault will be attached to an evacuated tank of sufficient size so that it can accommodate all of the tritium gas without external release. A one-day's supply of purified, but not processed, T_2 may be stored on getter alloys in another vault. With no source of heat within this vault which would initiate the evoluation of T_2 gas, no release of tritium would occur.

Table 7.1.1. Tritium Inventory and Potential Release

Location/System	Inventory g	Tritium Routine Release Ci/d	Tritium Accidental Release g(T)
Target Factory			
In process	147	12	147
Storage	1200	0	0
Reactor Building			
Target injector	49	12	49
Breeder alloy	2	0	2
Fuel Reprocessing Building			
Gas handling equipment	106	13	106
Cryo-still	193	13	0
Storage Vault	1200	0	0
Steam Generator			
Water release	0	65	0
Total	2897	Air 50 Ci/d Water 65 Ci/d	304

7.1.2. Reactor Building Tritium Inventory

A one-hour supply of targets (49 g(T)) is kept in the target injector facility above the reactor. All of this tritium could be released in a major reactor accident; however, the routine release from the frozen fuel would be low, ~ 12 Ci/d.

The LiPb coolant-breeder contains tritium which must be separated and recycled, as described later. The steady-state tritium inventory in this molten alloy is ~ 2 g. Because all of this hot liquid is multiply contained, the routine tritium release to the environment is negligible. A major rupture in this piping would cause some of the hot liquid to come in contact with air or water. This alloy was selected, however, because it does not react vigorously with the atmosphere or water and a solidified surface coating would prevent reactions which would release all of the dissolved tritium.

The fuel reprocessing equipment receives DT gas separated from the liquid breeder in the vacuum disengager and the helium gas (a product of the fusion reaction) evacuated from the reactor cavity. These gases are chemically purified through a series of absorbers and filters. Such equipment contains $\sim$ 2 hr of inventory, $\sim$ 106 g(T). Finally, the fuel gases are liquified and introduced into a cryogenic distillation column where pure DT is recovered from the He and excess D_2 (added as a carrier in the breeder separation chamber). Special techniques [3] have been developed so that the liquid in the cryo-still would contain only $\sim$ 193 g(T). The routine release from the enclosures surrounding the reprocessing equipment should be only 26 Ci/d. In the event of a severe accident rupturing the fuel reprocessing system all the tritium could be released, 106 g(T). The cryo-still, however, is installed in a sealed refrigerated box which contains an evacuated chamber sufficiently large so that all the DT gas, if released, can be captured.

7.1.3. Tritium Breeding and Recovery from the Liquid $Li_{17}Pb_{83}$ Alloy

The use of the eutectic alloy, 17 at.% Li – 83 at.% Pb, has been proposed as the tritium breeder in the LIBRA series of fusion power reactor studies. The two principal radiological concerns in the use of this alloy are: (1) the generation of ^{210}Po from the neutron irradiation of traces of ^{209}Bi in the Pb, and (2) the efficient extraction and containment of the tritium produced from neutron irradiation of the Li. Recently, Hubberstey, et al. [4] have proposed that the Bi can be continuously removed from the liquid alloy to a level of $\sim$ 3 wppm, which would significantly reduce the generation of ^{210}Po. The proposed extraction and containment of the tritium is discussed in this report.

Introduction. The efficient extraction of tritium from the breeder blanket of proposed fusion power reactors is essential to the continuous operation of the facility. When a liquid breeding material is utilized, which is also the heat transfer fluid (usually designated as the self-cooled breeder), the design of the tritium system becomes even more challenging because the tritium must be extracted at the rate of its formation and the tritium concentration (pressure) in the heat transfer fluid must be sufficiently low so that

the permeation of tritium through the steam generator to the discharge coolant water meets acceptable environmental standards. In order to meet such requirements, designers have utilized several options, namely (1) remove the tritium to a sufficiently low concentration that the heat transfer fluid can go directly to the SG; (2) insert an intermediate heat transfer circuit between the primary loop and the SG so that additional T can be removed; or (3) utilize double-walled SG pressure tubes with a high pressure gas flowing through the annulus which will rapidly dilute and remove the T_2. The ultimate selection of one of these options will depend upon the research and development progress of each concept.

Additionally, a variety of procedures have been proposed for the extraction of tritium from the heat transfer fluids (HTF). For a fluid with a high solubility for the H isotopes, such as metallic Li, two techniques have been proposed, namely (1) extraction of tritium on an insoluble getter, such as yttrium, or (2) extraction of the tritium into a fused salt with subsequent recovery of the H-isotopes by electrolysis of the fused salt, as proposed by Calaway, et al. [5]. The fused salt technique requires further study because of the concern that the fused salt may become entrained into the liquid breeder and carried into the reactor blanket where it may form undesirable radioactive products or initiate corrosion of the piping.

For the self-cooled breeder concepts with lower H-isotopic solubility constants, such as the fused salt, FLIBE, or the metallic alloy, $Li_{17}Pb_{83}$, very low concentrations of T must be attained in order to maintain low T_2 pressures. No getters have been identified which are insoluble in the LiPb alloy [6]. As a result, techniques based upon gas-sparing have been suggested in which the tritium is transferred directly from the liquid phase to a gas phase [7]. Preliminary calculations indicated that the gas-sparing technique in which bubbles are formed within the liquid would not be successful because the gas-liquid surface area was not sufficiently large [8]. Consequently, the concept was developed in which the heat transfer fluid is dispersed into small droplets ($< 500\,\mu$m dia.) which fall through an evacuated chamber. Although experimental verification of this technique has not been demonstrated for tritium removal, rigorous studies of the parameters involved have been accomplished by Dolan, et al. [9] for use with the FLIBE breeder proposed for the HYLIFE study.

The utilization of a large evacuated chamber, which may be 5 m dia. × 5 m high, for tritium extraction adds to the complexity of the heat transfer fluid circuit design. For instance, the designers in the HYLIFE study utilized two degassing units in series ahead of the SG in order to reduce the T_2 pressure at the SG. In this study, the hot HTF is sent directly from the reactor to the nearby SG, thus reducing the length of the hottest piping; subsequently, the fluid is directed to the Vacuum Degassing Chamber (VDC). Additionally, only a portion of the HTF flow may be directed to the degassing unit as described in this study. In either case, the tritium removal rate in the degassing unit must be the same as its generation rate within the reactor; consequently, the average T-concentration in the HTF, for the case in which only a partial flow is directed to the degassing unit, is higher than for the case in which all of the HTF is directed to T_2 degassing.

The utilization of the vacuum extraction for T_2 from the LiPb breeder has been utilized since 1984 in the Mirror Advanced Reactor Study [10] and continued in the LIBRA (Light Ion Beam ICF) reactor studies [11]. This concept has been reevaluated for the LIBRA-SP study because of the recent experimental measurements of (1) the rate of the diffusion of T in the liquid LiPb [12], (2) the mass transfer rate of T_2 from the liquid alloy [13,14] and (3) the recent studies of the vacuum disengager for tritium removal from FLIBE [9]. The items considered in the design of the LIBRA-SP tritium extraction system are delineated in the following sections.

Design of the Vacuum Disengager for Tritium Removal. The removal of T atoms from the liquid droplets to the gas phases requires several molecular processes; namely: (a) diffusion or convection of the T atoms from the bulk to the surface of the droplet (in small droplets, convection is not important); (b) mass transport of the T atoms through a stagnant fluid boundary layer existing between the fluid and the gas phase; (c) heterogeneous reactions at the liquid surfaces in which two T atoms combine to form a T_2 molecule, and (d) escape of the T_2 molecule from the surface and its diffusion through the gas phase.

The diffusion coefficients of T atoms in the liquid have been measured over a series of temperatures with reasonably good agreement between the experimental results, Fig. 7.1.1.

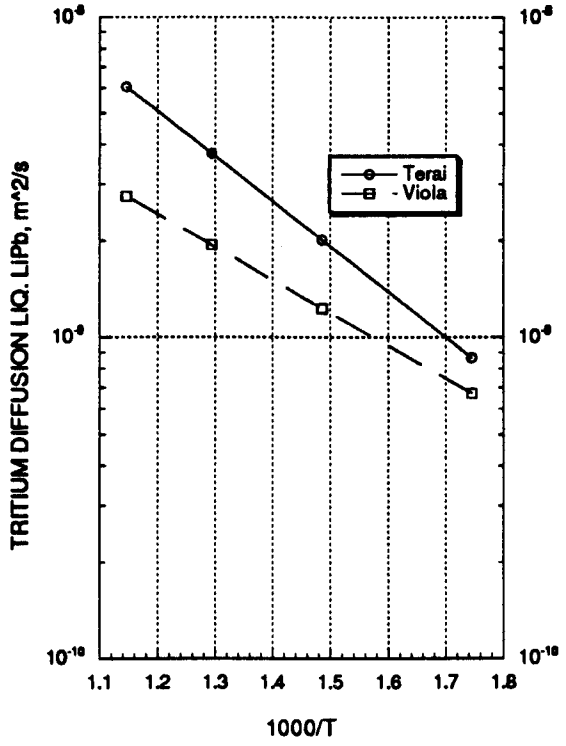

Figure 7.1.1. Tritium diffusion coefficient in the liquid alloy $Li_{17}Pb_{83}$ as a function of temperature as determined by Terai [12] and quoted by Viola [14].

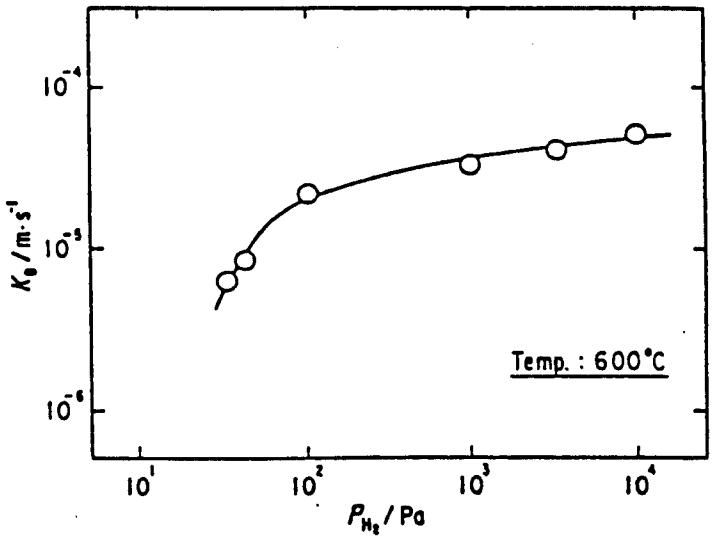

Figure 7.1.2. Mass transfer coefficient of tritium from the liquid alloy, $Li_{17}Pb_{83}$, as a function of the H_2 pressure in He sweep gas at 600°C (from Terai [13]).

The measurement of the mass transfer of T atoms through the surface layer can be limited, however, by the heterogeneous surface reaction in which two T atoms combine to form a T_2 molecule. As shown in Fig. 7.1.2 from Terai [12], the mass transfer coefficient is rather constant when an external H_2 atmosphere is maintained in the pressure range of 10^4 to 10^2 Pa; however, the measured values decrease rapidly at H_2 pressure $< 10^2$ Pa. Similarly, Viola, et al. [14] obtained reasonable measurements when the external D_2 pressure was maintained between 5×10^2 to 5×10^3 Pa. Comparison of the mass transfer coefficient measurement as a function of temperature, Fig. 7.1.3, indicates that the values obtained by Viola, et al., are higher and were used in this study. It is suggested that the lower values by Terai may be due to a contaminated surface oxide layer because the liquid was held in an alumina crucible.

The study of the evolution of gases from a liquid droplet by Dolan, et al. [9] indicates that the non-dimensional time, F_0, required for the fractional evolution of the gas from the droplets is related to the size of the droplets and the properties of the gas atoms in the liquid, as defined by the dimensionless quantity, Bi (Biot number) and illustrated by the plot (Fig. 7.1.4) in which the quantities are defined as:

F_0 (Fourier number) = $D_F t/a^2$

Bi (Biot number) = ah_m/D_F

when D_F = diffusion coefficient for tritium in the liquid droplet, t = residence time of the drop in the vacuum chamber, a = radius of the drop (m), and h_m = mass transfer coefficient at the droplet surface. Based upon the exit temperature from the steam generator (673 K) and experimental values for the LiPb at this temperature, $D_F = 1.62 \times 10^{-9}$ m^2/s and, $h_m = 5.74 \times 10^{-5}$ m/s; hence, for a drop of $a = 50\,\mu$m, Bi = 1.77.

Next, it is necessary to specify the fractional removal of tritium expected in the Degassing Unit. As previously noted, the mass transfer of tritium from LiPb is very slow at H-isotopic gas pressures below 10^2 Pa. If the T_2 concentration in the LiPb were permitted to increase to yield T_2 pressures of 10^3 Pa (T_2), the inventory of tritium and its permeation through the SG would be exceedingly large; hence, D_2 or H_2 are added to give the additional H-isotopic pressures. For this study, we propose that D_2 at a pressure

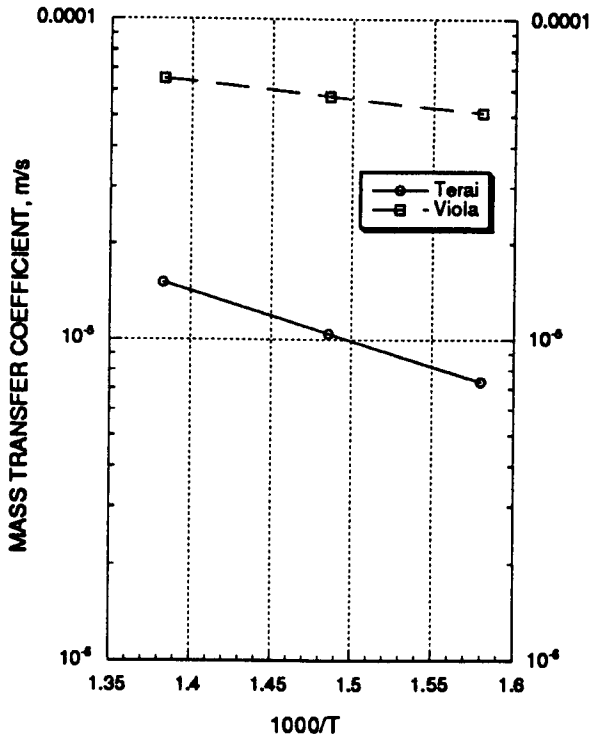

Figure 7.1.3. Mass transfer coefficient of tritium from the liquid alloy $Li_{17}Pb_{83}$ as a function of temperature at H_2 pressures $> 10^3$ Pa from Terai [13] and Viola [14].

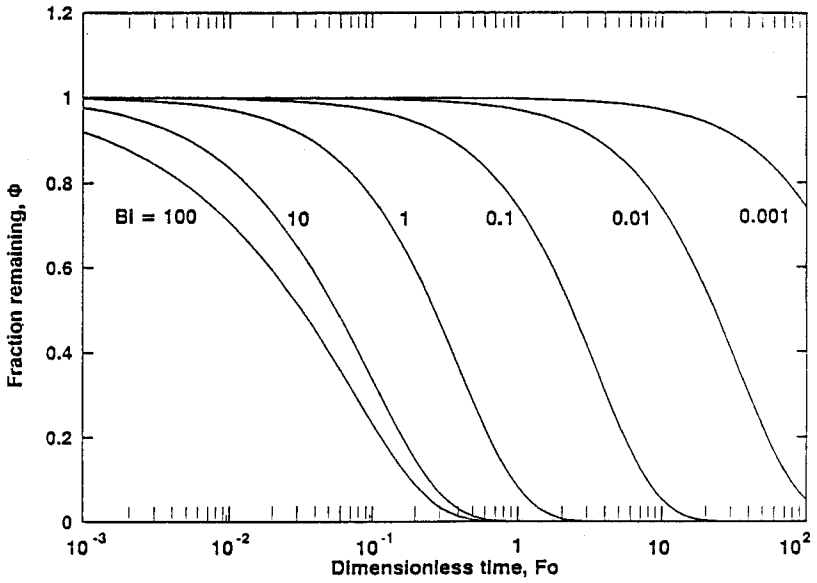

Figure 7.1.4. Relationship of the Biot numbers to the Fourier numbers for the degassing of a soluble gas in a liquid droplet from Dolan et al. [9].

of 10^3 Pa be injected into the LiPb immediately ahead of the Degassing Unit and that the vacuum system be maintained at a D_2 pressure of 10^2 Pa, a pressure decrease of $\sim$ 90%. However, as noted by Dolan, et al. the spray of droplets in the Degassing Unit impedes the free-path of the molecules in the gas phase so that an "effective" gas pressure in the unit would be $\sim 2.5 \times 10^2$ Pa. The D+T are soluble in the LiPb coolant with a solubility constant $k_s = 1.0 \times 10^{-7}$ at.frac. (H-isotope)/$Pa^{1/2}$ [15] at 400°C, the exit coolant temperature from the steam generator. (For the purpose of this study it will be assumed that all the H-isotopes have the same solubility constant.) The concentration of the H-isotopes (mostly D_2) in the liquid LiPb will be 3.1×10^{-6} at.frac. D at the entrance to the degassing unit and 1.0×10^{-6} at.frac. D at the exit from the unit, giving 33% as the fraction remaining. Because of isotopic dilution, the same fractional removal of tritium is assumed.

The use of the excess D_2 pressure to increase in the effective D+T concentrations brings into question the solubility limits for the H-isotopes in liquid LiPb alloy, which has not been measured directly. Veleckis [16] has reported for solid LiPb alloys that the initial addition of H_2 to this solid formed a homogeneous alloy; however, when the H-solubility concentration was exceeded a new phase, presumbably LiH, was formed and the H_2 pressure remained constant until all the Li, in the alloy, was consumed. Using this information, Veleckis [17] suggested that the H solubility in the liquid $Li_{17}Pb_{83}$ could be determined from the intersection of the line determined by the Sievert's constant for the homogeneous solubility of H_2 in the liquid alloy and the plateau pressure of H_2 in the 2 phase region as determined by Pierini [18]. Such a plot, Fig. 7.1.5, suggests that the H-solubility limits for this alloy are 12×10^{-6} at.frac. H at 400° and 15×10^{-6} at.frac. H at 500°C. The maximum solubility of the D+T isotopes in this study is only 3×10^{-6} at.frac. (D+T) approx. 1/4 of saturation limit; hence, the potential for the formation of the compound LiD is unlikely but needs to be experimentally verified.

Because the use of the D_2 overpressure to aid in the evolution of tritium appears reasonable, the Degassing Unit design can be proposed. Reference to Fig. 7.1.4 indicates that for Bi = 1.77 and 33% H-isotopes remaining in the drops, $F_0 = 0.32$; hence, the time

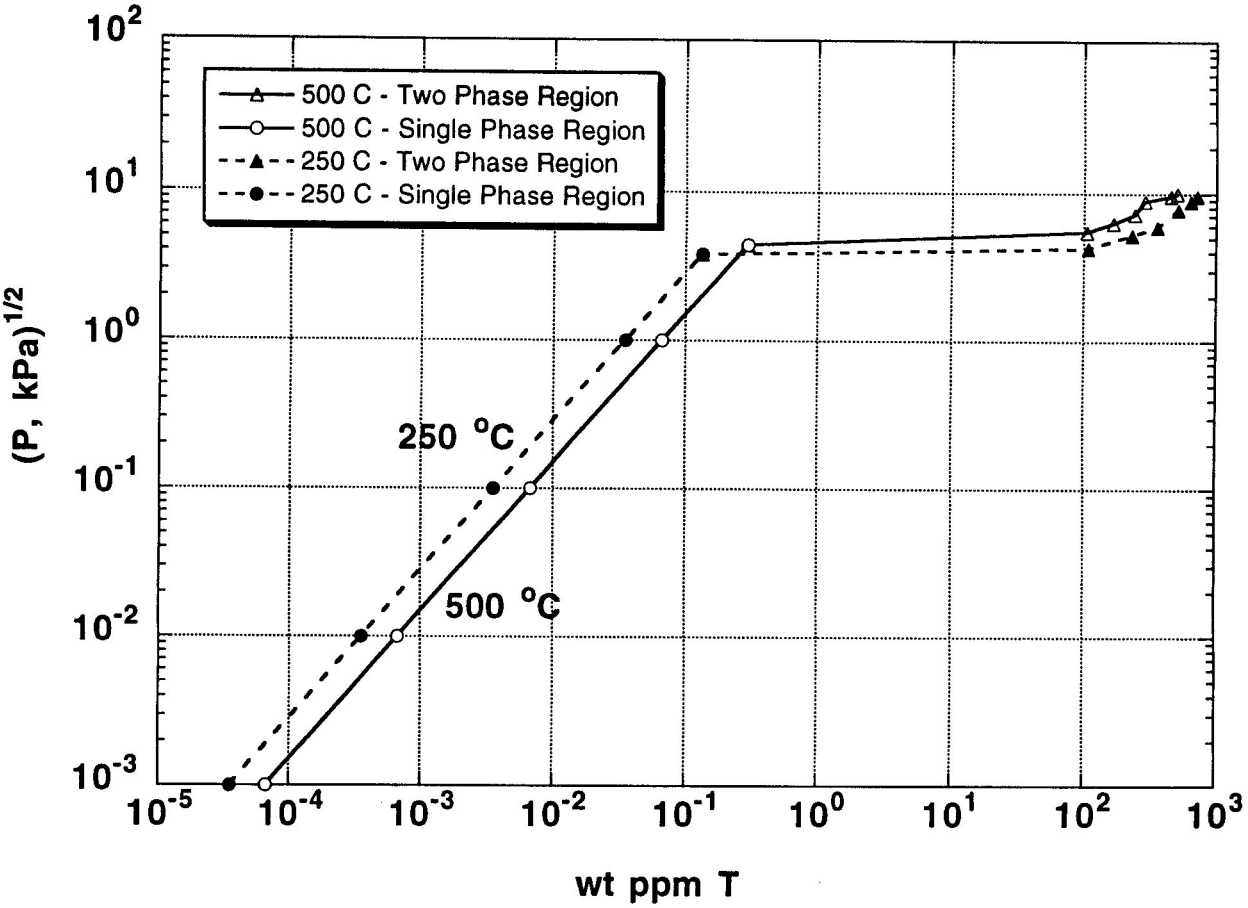

Figure 7.1.5. Proposed phase diagram for the dissolution of tritium in the liquid alloy $Li_{17}Pb_{83}$ from data by Chan and Veleckis [15] and Pierini, et al. [18]

of fall for the droplets is 0.50 s. The time of fall, t_f, is related to the height of the degassing unit by the relationships,

$$t_f = (\beta - 1)\, v_0/g \qquad \text{and} \qquad \beta = (1 + 2gz/v_0)^{1/2}$$

where v_0 = the initial fluid velocity at the entrance to the degassing unit, g = the acceleration of gravity and z = height of the chamber. If $v_0 = 5$ m/s, the flow rate in the remainder of the system, then, is $z = 3.7$ m.

The total flow from the reactor is 5×10^5 kg (LiPb)/s at a density of 9600 kg/m^3 for a volume flow rate of 52 m^3/s at $v_0 = 5$ m/s. Only 30% of this flow is directed to the degassing unit. At the top of the degassing unit, a plate with 50 μm holes is used to form the 100 μm OD droplets. The holes compose 10% of the surface area of the plate; hence the plate needs to be 3.2 m in radius. The size of the degassing unit would be, therefore, $\sim$ 6.4 m OD $\times$ 4.0 m high.

Design of the Liquid Breeder Flow Circuit. Based upon the design of the vacuum degassing unit, the liquid breeder flow circuit has been proposed, Fig. 7.1.6. The fuel targets delivered to the reaction chamber contain equal atomic amounts of D+T at the rate of 4.24×10^{-3} g.at. (each)/s. Approximately 30% of the fuel undergoes fusion (1.27×10^{-3} g.at/s for D and T), leaving 2.97×10^{-3} g.at/s (each) of D+T unburned in the reactor's chamber. In addition, the neutrons emitted from the fusion process, are captured in the surrounding LiPb alloy in the PERIT tubes with a tritium breeding ratio of ~ 1.30; consequently, an additional 1.73×10^{-3} g.at/s T is generated giving a total input of 4.70×10^{-3} g.at. T/s. This D+T together with the target debris and the coolant flowing at the rate of 5×10^5 kg/s (3×10^6 moles/s) are swept into the coolant pool at the bottom of the chamber and directed to the steam generator followed by the vacuum degassing and fuel cleanup units. During each pass of the coolant the T concentration increases, therefore, by 1.6×10^{-9} at.frac. T.

The flow from one pass of the coolant through the reactor could be sent directly to the degasser for tritium removal; however, the degasser would need to be extremely larger. For this reason, the T-concentration is permitted to increase so that only a fraction of the coolant flow, approximately 30%, is diverted to the degasser. The maximum T-concentration permitted in this circulating breeder is determined by the T-permeation rate at the SG as described in the next section. In order to determine the T-concentration in the circulating LiPb, the rate of T extracted in the degasser must equal the T-input to the breeder in the reactor cavity, and is determined by the relationship,

$$30\%\, \dot{m} \times (1 - F_T) C_1 = \dot{T} = 4.70 \times 10^{-3} \text{ at.frac. T/s}$$

where $\dot{m}$ = breeder flow rate, 3×10^6 moles LiPb/s; C_1 = concentration of T at entrance to degasser; F_T = fraction of T remaining in the breeder at the exit from the degasser (33%); hence $C_1 = 7.8 \times 10^{-9}$ at.frac. T.

Based upon this value of C_1 the LiPb flow diagram (Fig. 7.1.6) indicates the D and T concentrations in the various branches of the circuit. Note that the T (14.9 mg T/s)

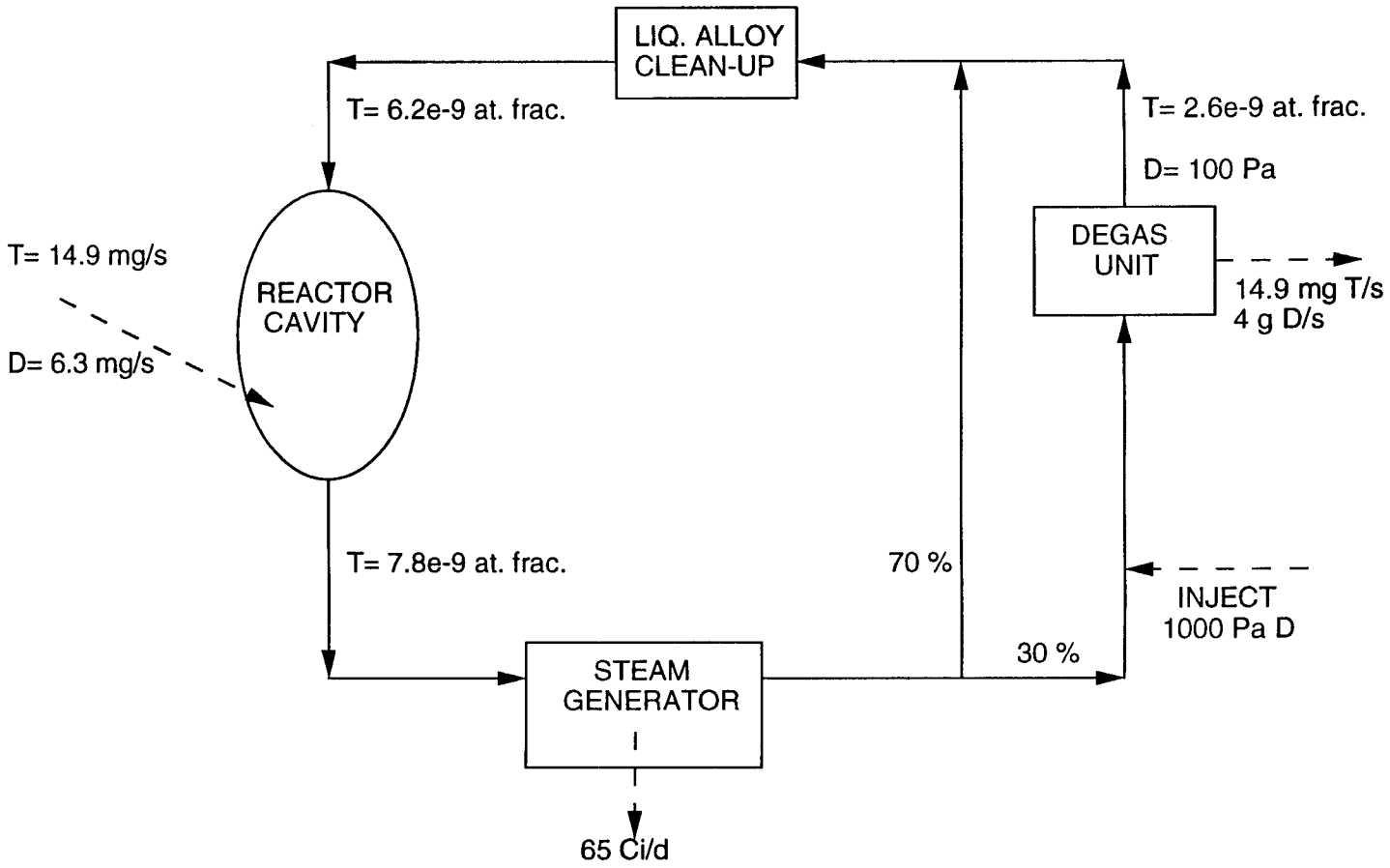

Figure 7.1.6. Flow diagram for the injection and removal of tritium from the liquid $Li_{17}Pb_{83}$ heat transfer fluid in LIBRA-SP.

accumulated during the transit of the reactor is removed in the degassing unit, while the 4.0 g D/s added to the flow circuit ahead of the degassing unit is removed, also during the degassing.

Evaluation of Tritium Release at the Steam Generator (SG). Continuous release of tritium by permeation through the SG from the LiPb breeder to the steam system must be controlled in order to meet environmental regulations. Such control is principally achieved by adjustments to the T_2 pressure of the LiPb within the SG. The permeation of T_2 through the ferritic steel of the SG is given by the relationship.

$$\varphi_{T_2} = \frac{2 \times 10^5 \,\mathrm{Ci/d \cdot mm}}{\mathrm{m^2 \cdot Pa}_{T_2}^{1/2}} \exp - \frac{46.4 \,\mathrm{kJ/mol}}{\mathrm{RT}} .$$

In the LIBRA-SP study, the SG has the following approximate parameters: surface area = 3000 m^2; tube thickness = 2 mm; average temperature = 438°C (711 K) giving,

$$\varphi_{T_2} = \frac{1.2 \times 10^5 \,\mathrm{Ci/d}}{\mathrm{P}_{T_2}^{1/2}} .$$

Neglecting an oxide barrier on the steam-side of the tubes which could reduce the permeation by a factor of 10-100, one could permit a T-release of $\sim$ 200 Ci/d; hence, the T_2-pressure could be up to 2.8×10^{-6} Pa. In this study, this allowable T_2 pressure is greatly exceeded, however, by the 250 Pa of D_2 which remains in the LiPb in order to achieve efficient mass transfer of T_2 from the droplets; hence, most of the T-atoms will exist as molecular DT. In such situations, Bell, et al. [19] specify that the partial pressure of T_2, causing permeation, can be calculated by use of the equilibrium reaction: $T_2 + D_2 = 2\,DT$, giving the equilibrium constant, k_e,

$$k_e = \frac{(\mathrm{P}_{DT})^2}{(\mathrm{P}_{T_2})(\mathrm{P}_{D_2})} .$$

At elevated temperatures, $k_e = \sim 4$.

In order to determine the partial pressure of T_2 in the SG in this study the above relationship is rearranged to give;

$$\mathrm{P}_{T_2} = \frac{(\mathrm{P}_{DT})^2}{k_e(\mathrm{P}_{D_2})} .$$

In order to solve this equation, one utilizes the information (Fig. 7.1.6) that the T-concentration entering the SG, $S_T = 7.8 \times 10^{-9}$ at.frac. T; hence $S_{DT} = 15.6 \times 10^{-9}$ at.frac. (D+T), due to the DT molecules dissolved in the liquid LiPb. Because

$$S_{DT} = k_s(P_{DT})^{1/2} \text{ and } k_s = \frac{1.2 \times 10^{-7}\,\text{at.frac.(D + T)}}{\text{Pa}_{\text{DT}}{}^{1/2}} \qquad \text{at } 500^{\circ}\text{C}\,,$$

the calculated $\text{P}_{\text{DT}} = 1.7 \times 10^{-2}$ Pa, additionally previously defined values as $\text{P}_{\text{D}_2} = 250$ Pa and $k_e = 4$; therefore $\text{P}_{\text{T}_2} = 2.89 \times 10^{-7}$ Pa. When this value for P_{T_2} is substituted in the tritium permeation relationship above, the value of φ_{T_2} is only 65 Ci/d, a very acceptable release rate.

On the other hand, the P_{D_2} is 250 Pa giving a value of $\varphi_{D_2} = 126$ g/d. At a cost of $\sim$ \$10/g of D_2 this could represent an operational expense of \$1260/d. Perhaps H_2 could be utilized instead of D_2; however, the molecules HT and HD complicate the cryogenic purification of T_2 and the additional expense to the cryogenic distillation system from the use of H_2 would have to be determined.

Vacuum Power Requirements. The use of a vacuum degassing system for the extraction of T from the breeder-coolant requires an evaluation of the operational pressure and the subsequent power requirements of the vacuum system, which are obtained from the operational design of the degassing system. The quantity of gas to be extracted is dominated by the excess D_2 added ahead of the degassing unit, i.e., 1.95 g.at. (D)/s (0.98 moles D_2/s). At 673 K this gas load is equivalent to 5.5×10^3 Pa·m^3/s. For a base pressure of 10^2 Pa, the pump speed must be 55 m^3/s. This pressure range and speed can be accomplished with a Roots Vacuum Pump; however, experience with tritium handling would recommend several oil-free pumping systems which have been developed. For illustrative purposes, however, a Balzers Roots Vacuum Pump has been selected, rated at 25,000 m^3/h which requires 55 kW of electrical power; consequently, this pumping system requires 0.4 MWe which for the 1000 MWe power plant is a minor 0.04% of power generated by the power plant.

In summary, the vacuum degassing system appears to be a viable option for the removal of tritium from the LiPb breeder. Experimental verification of the process is necessary, however.

7.2. Environmental and Safety Assessment

7.2.1. Introduction

A strong emphasis has been given to the environment and safety issues in the LIBRA-SP reactor design. Low activation ferritic steel (modified HT-9) has been used in the blanket and reflector to avoid a high level of induced radioactivity in both regions. Similarly, the use of LiPb as a coolant and breeder eliminates the hazard posed by the energy producing chemical reactions usually associated with the use of lithium and hence reduces the risk of mobilizing the radioactive inventory present in the reactor. The methodology used in this analysis does not depend on the probability of accident initiating scenarios. We have rather adopted the principle of considering the worst possible accident scenario. To evaluate the possible radiological hazard to the public, we used a two step approach in calculating the possible off-site dose. The first step in our approach is the identification of the sources and locations of the radioactive inventories inside the reactor building. However, since the existence of radioactivity does not in itself represent a safety hazard, the second step in our approach was to consider a set of pessimistic but rather credible accident scenarios for mobilizing and releasing the radioactive inventory.

In this section a detailed activation analysis has been performed in order to calculate all possible radioactive inventories for the current LIBRA-SP design. Results of the radioactivity calculations are used to evaluate the following:

a. The biological dose rate at different locations inside the reactor containment following shutdown to assess the feasibility of hands-on maintenance.

b. The radwaste classification for each region of the reactor.

c. The maximum public dose from routine operational effluents.

d. The off-site doses from accidental release of the radioactive inventories present in the containment building, target factory and fuel reprocessing facility.

7.2.2. Safety Design Goals

The main safety goals pursued for the LIBRA-SP reactor design are:

1. Limiting the need for remote maintenance and allowing for hands-on maintenance by reducing the biological dose rate following shutdown below 25 μSv/hr by increasing the biological shield where it is possible.
2. Disposing the reactor structure and coolant as either Class A or Class C low level wastes as regulated by the Nuclear Regulatory Commission's (NRC) 10CFR61 guidelines.
3. Limiting the public dose to the maximally exposed individual (MEI) from routine operational effluents to less than 5 mrem/yr.
4. Producing the lowest possible whole-body (WB) early dose during a conservative accident scenario. The low off-site dose will allow for the avoidance of early fatalities in case of an accidental release of radioactivity.
5. Eliminating the need for the use of N-Stamp nuclear grade components.

7.2.3. Off-Site Definitions

Off-site dose is used to predict the degree of radiological hazard to the public posed by any routine or accidental release of radioactivity from the reactor. However, the health effects to the various human organs are dependent on both the length and method of exposure. While dose from external exposure (cloudshine and groundshine) is only limited to the length of the exposure, decay of the radionuclides inside the irradiated body (from inhalation and ingestion) leads to a continuous internal exposure. In this chapter we used the following dose definitions:

Prompt Dose at 1 km: The dose delivered to a particular organ at 1 km from the release, from cloudshine during plume passage, 7 days of groundshine and the dose commitment over an organ-dependent critical acute time period from inhalation during plume passage.

WB: Whole body, t_{acute} = 2 days.

BM: Bone marrow, t_{acute} = 7 days.

Lung: Lung, t_{acute} = 1 year.

LLI: Lower large intestine, t_{acute} = 7 days.

WB Early Dose: The whole body early dose, where early dose is the dose from initial exposure; i.e., cloudshine during plume passage, 7 days of groundshine, plus the 50-year dose commitment from radioactivity inhaled during plume passage.

WB Chronic Dose at 1 and 10 km: The whole body dose at 1 and 10 km from the release due to both initial and chronic (50-year) exposures.

Inh + grd: Chronic exposure considers the 50-year groundshine exposure plus the 50-year dose commitment from inhaled resuspended radioactivity.

Ing: Chronic exposure considers the ingestion pathway only.

Total: Chronic exposure considers all three pathways: groundshine, resuspension and ingestion.

Cancers: Total number of cancers in a 50-mile radius from initial and chronic exposure.

Sum Organs: The number of cancers where the body is treated as a sum of individual organs and calculations are based on organ-specific dose factors and dose responses.

WB: The number of cancers where the body is treated as a single organ and the whole body dose conversion factors and dose response are used.

Population Dose WB (Man-Rem): Total whole body man-rem due to both initial exposure plus an 80-year chronic exposure to the whole body.

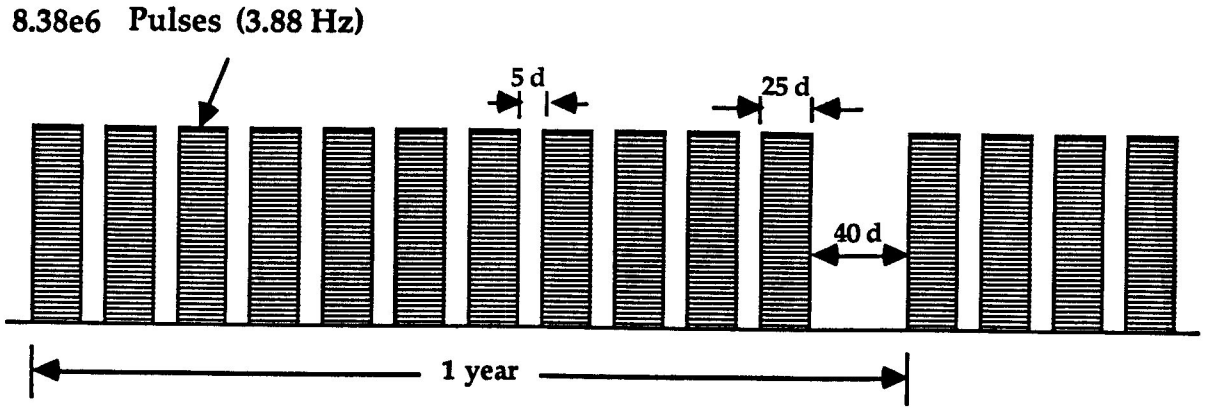

Figure 7.2.1. Pulse sequence used in activation analysis.

7.2.4. Calculational Procedure

Neutron transport calculations have been performed using the discrete ordinates neutron transport code TWODANT [20]. The analysis uses a P_3 approximation for the scattering cross sections and S_8 angular quadrature set. The reactor has been modeled in spherical geometry with a point source at the center of the chamber. The source emits neutrons and gamma photons with energy spectra determined from target neutronics calculations for a specific light ion fusion target. The neutron flux obtained from the neutron transport calculations has been used in the activation calculations. The calculations have been performed using the computer code DKR-ICF [21]. The DKR-ICF code allows for accurate modeling of the pulsing schedule. The pulse sequence used in the activation calculations is shown in Fig. 7.2.1. In order to achieve 75% availability, the reactor has been assumed to shut down for a period of 5 days following every 25 days of operation for routine maintenance and for the last 40 days of each calendar year for an annual extended maintenance. The radioactivity generated in the reactor chamber and shield has been calculated for the 40 year reactor lifetime. Radioactivity induced in the diode has also been calculated for the same reactor lifetime.

The decay gamma source produced by the DKR-ICF code is used with the adjoint neutron flux to calculate the biological dose rate after shutdown using the DOSE [21] code.

The dose rate calculations have been performed at different locations inside the reactor containment as well as in the vicinity of the diode. The activation results have been also utilized in the radwaste classification and the off-site dose calculations performed by the FUSCRAC3 [22] code. The off-site doses are produced by the accidental release of the radioactive inventory from the reactor containment building assuming the worst case weather conditions. Finally, the EPA code AIRDOS-PC [23] has been used to estimate the off-site dose due to the routine release of tritium.

7.2.5. Reactor Activation

The reactor has been modeled in spherical geometry with a point source at the center of the chamber. The source emits neutrons and gamma photons with energy spectra determined from target neutronics calculations for a generic single shell target [24]. The radioactivity generated in the blanket, reflector, shield and LiPb breeder of LIBRA-SP has been calculated for the 40 year reactor lifetime with 75% availability. The reactor blanket and reflector are made of a low activation ferritic steel (modified HT-9). The chamber is surrounded by a biological shield to allow for hands-on maintenance at selected locations behind it. The steel-reinforced concrete shield is made of 70% concrete, 20% mild steel and 10% helium coolant. In the mean time a separate calculation has been performed for the LiPb coolant. The residence time of the LiPb coolant in the chamber is 5 seconds. The total inventory of LiPb takes 15 seconds to go through the reactor chamber. Therefore, the coolant activity has been calculated to allow for the fact that LiPb spends only 33% of the time exposed to neutrons in the reactor chamber. The total activity generated in the different regions of LIBRA-SP as a function of time following shutdown is shown in Fig. 7.2.2.

The total activity in the blanket at shutdown is 721 MCi and drops to 498 MCi in one day and 307 MCi in one year. The activity induced in the reflector at shutdown is 924 MCi and drops to 407 MCi in one day and 63 MCi after one year. Most of the steel-reinforced concrete shield activity is due to its steel component. At shutdown, the total activity amounts to 41.2 MCi and drops to 6.9 MCi within a day and 3.69 MCi within a

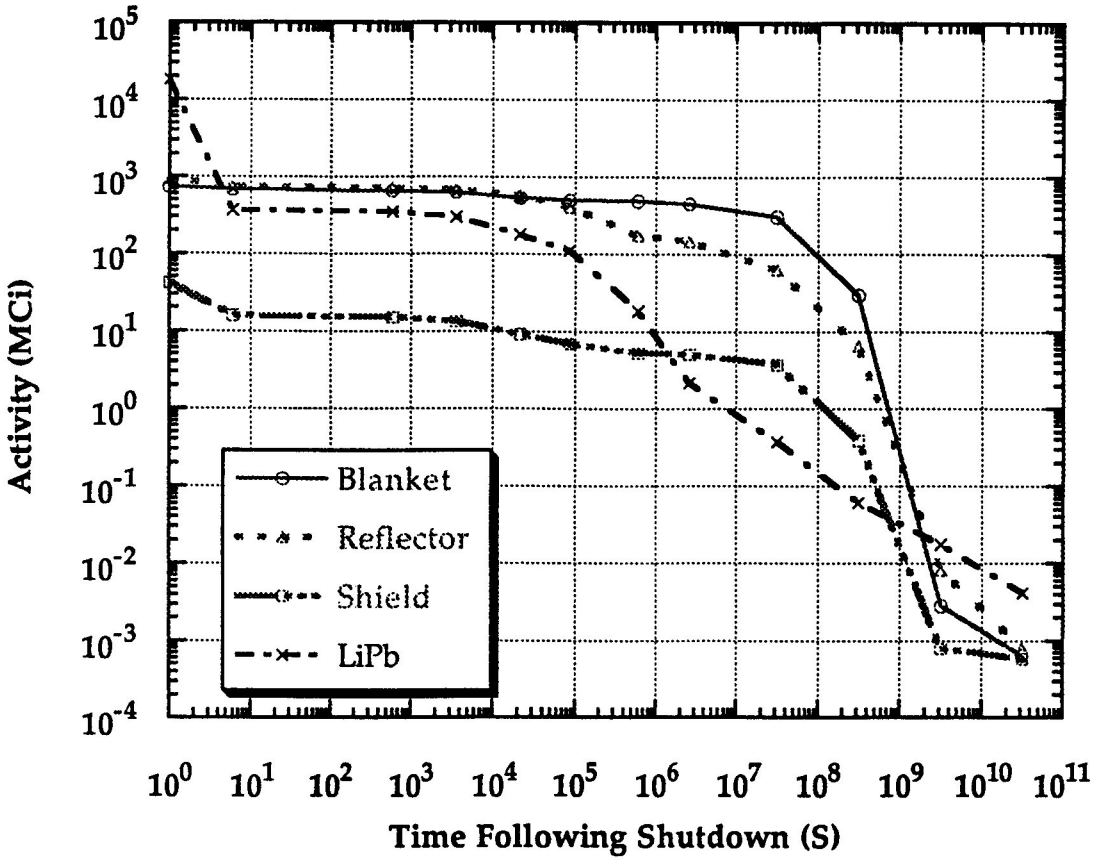

Figure 7.2.2. Activity following shutdown in different regions of LIBRA-SP.

year. On the other hand, due to the rapid decay of ^{207m}Pb ($T_{1/2}$ = 0.8 s), the activity of LiPb drops from 1790 MCi to 370 MCi within a minute from shutdown. The LiPb activity drops to 110 and 0.37 MCi during the first day and first year following shutdown, respectively. Table 7.2.1 shows the dominant contributors to the activity generated during different time periods following shutdown. Table 7.2.2 compares the activity, decay heat and biological hazard potential (BHP) in the blanket and reflector regions. The biological hazard potential has been calculated using the maximum permissible concentration limits in air for the different isotopes according to the Nuclear Regulatory Commission (NRC) regulations specified in 10CFR20 [25].

The temporal variation of the decay heat and BHP after shutdown is similar to that of the activity. In general, the decay heat and biological hazard potential are dominated for the

Table 7.2.1. Dominant Contributors to Radioactivity

Time After Shutdown	Shield	LiPb
< 1 day	^{56}Mn, ^{54}Mn, ^{55}Fe	^{207m}Pb, ^{209}Pb, ^{203}Hg
1day – 1 yr	^{55}Fe, ^{54}Mn, ^{187}W	^{204}Tl, ^{110m}Ag, ^{108m}Ag
1 yr – 10 yr	^{55}Fe, H^3, ^{54}Mn	^{204}Tl, ^{108m}Ag, ^{205}Pb
> 10 yr	^{14}C, ^{63}Ni, ^{53}Mn	^{205}Pb, ^{108m}Ag, ^{208}Bi

Table 7.2.2. Radioactivity After Shutdown

Time After	Activity (MCi)		Decay Heat (MW)		BHP (km^3 air)	
Shutdown	Blanket	Reflector	Blanket	Reflector	Blanket	Reflector
0	721	924	2.99	3.34	3.7e+8	1.63e+9
1 hour	620	684	2.18	2.88	8.9e+7	8.02e+7
1 day	498	407	0.46	1.09	8.2e+7	5.54e+7
1 week	480	175	0.42	0.18	8.01e+7	3.2e+7
1 month	449	147	0.39	0.14	7.5e+7	2.7e+7
1 year	307	63	0.22	5.63e-2	3.7e+7	9.24e+6
10 years	29	6.5	1.23e-2	1.05e-2	1.05e+6	2.0e+6
100 years	2.78e-3	8.2e-3	1.39e-6	2.72e-6	1.02e+4	4.1e+4

most part by the same nuclides shown in Table 7.2.1. One value which is useful for predicting the thermal response of the structure to a loss of coolant accident is the integrated decay heat. Fig. 7.2.3 shows the integrated decay heat generated following shutdown in the different regions of LIBRA-SP. The integrated decay heat generated during the first day following shutdown in the blanket and reflector are 78 and 150 GJ, respectively. The integrated decay heat generated in the reactor shield following shutdown is very low. Only 13 GJ of decay heat is generated in the shield during the first month following shutdown.

Biological dose rate calculations have been performed at selected locations to assess the possibility of hands-on maintenance. Fig. 7.2.4 shows the calculated dose rates as a function of time following shutdown. At all locations, ^{56}Mn ($T_{1/2}$ = 2.6 hr) and ^{54}Mn ($T_{1/2}$ = 313 day) dominate the biological dose rates during the first day. The dose is dominated by ^{54}Mn and ^{55}Fe ($T_{1/2}$ = 2.7 yr) within the first few years.

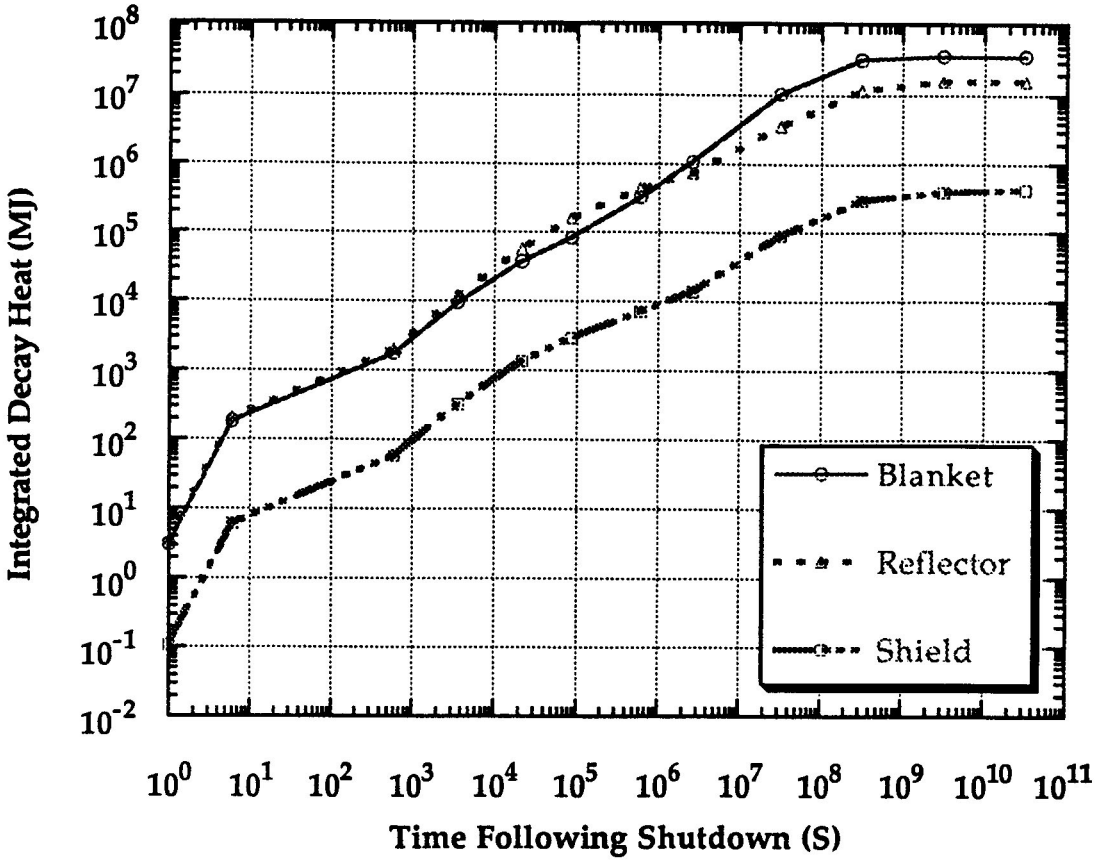

Figure 7.2.3. Integrated decay heat following shutdown in different regions of LIBRA-SP.

As shown in the figure, hands-on maintenance is impossible anywhere inside the reactor chamber. The size of the concrete biological shield required for acceptable occupational dose rate during operation has not been determined. In this calculation an 80 cm thick shield was used. As a result only remote maintenance is possible behind the biological shield. Increasing the shield thickness should allow for the possibility of hands-on maintenance. The dose rate behind the biological shield drops to 13.6 μSv/hr after one year following shutdown. A limit of 25 μSv/hr for hands-on maintenance is used in this analysis assuming that the maintenance personnel work for 40 hours a week and 50 weeks a year. Hence, hands-on maintenance will only be allowed behind the current 80 cm concrete shield after 1 year following shutdown.

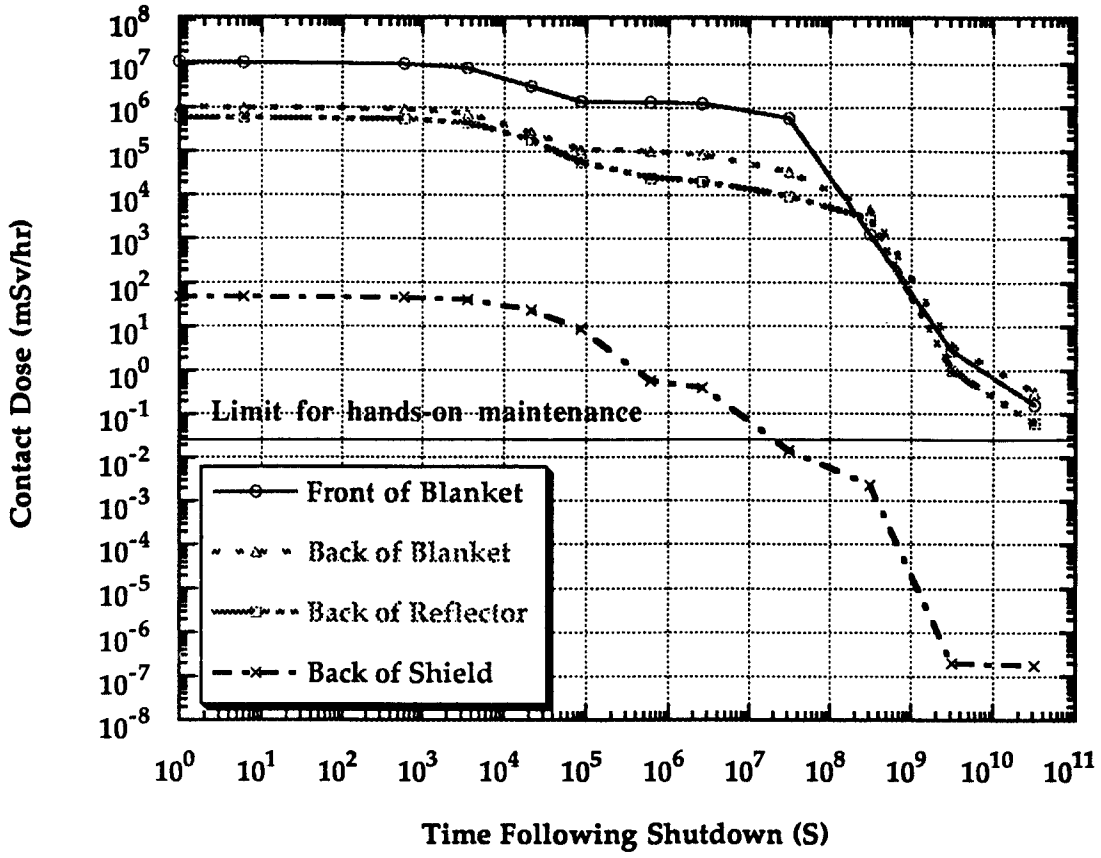

Figure 7.2.4. Contact dose rates following shutdown.

7.2.6. Diode Activation

Two-dimensional coupled neutron-gamma transport calculations are performed using the two-dimensional discrete ordinates neutron transport code TWODANT. An inherent problem associated with multi-dimensional discrete ordinates calculations with localized sources is referred to as the "ray effect". It is related to the fact that the angular flux is given only in certain discrete directions. It is, therefore, not possible to exactly represent the component in the normal direction ($\mu = 1$) along the beam penetration which can lead to underestimating neutron streaming. We have fully mitigated the ray effect by using the first collision method [26]. In this method, the uncollided flux is determined analytically and the volumetrically distributed first collision source is used in the calculations. The problem has been modeled in spherical geometry with a point source at the center of the chamber.

Table 7.2.3. Dose Rates Near the Diode (mSv/h)

Time Following Shutdown	Near Diode Casing ($z = 950$ cm)	Near Transmission Lines ($z = 980$ cm)
At shutdown	3.4×10^3	5.96×10^3
1 min	3.34×10^3	5.87×10^3
10 min	3.13×10^3	5.51×10^3
1 h	2.67×10^3	4.71×10^3
6 h	1.37×10^3	2.48×10^3
1 day	8.6×10^2	1.62×10^3
1 week	7.56×10^2	1.45×10^3
1 month	6.48×10^2	1.26×10^3
1 year	1.85×10^2	4.35×10^2
10 year	1.83×10^1	6.7×10^1
100 year	3.77×10^{-2}	5.57×10^{-2}
1000 year	2.28×10^{-2}	3.35×10^{-2}

An R-Z geometry is utilized with the target represented by an isotropic point source on the Z-axis. Fig. 6.2.1 shows the two-dimensional model used in the calculations. The diode casing, cathodes and anodes are assumed to be made of type 304 stainless steel. The magnet is made of copper and uses epoxy as an organic insulator.

The contact dose values due to streaming neutrons at the outer casing of the diode ($z = 950$ cm) and near the transmission lines ($z = 980$ cm) are shown in Table 7.2.3. The dose rates during the first few minutes following shutdown are dominated by ^{28}Al and ^{52}V ($T_{1/2} = 3.76$ min) produced from ^{51}V (n, γ), ^{52}Cr (n, p), and ^{55}Mn (n, α) reactions. The high content of manganese in the steel chamber results in ^{56}Mn ($T_{1/2} = 2.578$ hr) being the major contributor to the dose rate up to one day. Even though most of the ^{56}Mn is produced as a result of the ^{55}Mn (n, γ) reaction, a significant amount is also produced by the ^{56}Fe (n, p) reaction. In the period between 1 day and 10 years, as in the case of the aluminum chamber, ^{54}Mn and ^{60}Co dominate the dose rate produced in the steel chamber. Beyond ten years after shutdown, the dose rate is primarily dominated by radionuclides induced from the steel impurities. The two major contributors are ^{94}Nb ($T_{1/2} = 2 \times 10^4$ yr) produced from

^{93}Nb (n,γ) and ^{94}Mo (n,p), and ^{93}Mo ($T_{1/2}$ = 3,500 yr) produced from ^{92}Mo (n,γ) and ^{94}Mo $(n,2n)$ reactions. The dose rates near the diode are too high at all times following shutdown. Hence, access to the area near the diode should be only limited to remote maintenance.

7.2.7. Radwaste Classification

The waste disposal ratings for LIBRA-SP have been evaluated according to both the NRC 10CFR61 [27] and Fetter [28] waste disposal concentration limits (WDL). The 10CFR61 regulations assume that the waste disposal site will be under administrative control for 100 years. The dose at the site to an inadvertent intruder after the 100 years is limited to less than 500 mrem/year. The waste disposal rating (WDR) is defined as the sum of the ratio of the concentration of a particular isotope to the maximum allowed concentration of that isotope taken over all isotopes and for a particular class. If the calculated WDR ≤ 1 when Class A limits are used, the radwaste should qualify for Class A segregated waste. The major hazard of this class of waste is to individuals who are responsible for handling it. Such waste is not considered to be a hazard following the loss of institutional control of the disposal site. If the WDR is > 1 when Class A WDL are used but ≤ 1 when Class C limits are used, the waste is termed Class C intruder waste. It must be packaged and buried such that it will not pose a hazard to an inadvertent intruder after the 100 year institutional period is over. Class C waste is assumed to be stable for 500 years. Using Class C limits, a WDR > 1 implies that the radwaste does not qualify for shallow land burial. Fetter developed a modified version of the NRC's intruder model to calculate waste disposal limits for a wider range of long-lived radionuclides which are of interest for fusion researchers than the few that currently exist in the current 10CFR61 regulations. Fetter's model included more accurate transfer coefficients and dose conversion factors. However, while the NRC model limits the whole body dose to 500 mrem or the dose to any single organ (one of seven body organs) to 1.5 rem, the Fetter limits are based on the maximum dose to the whole body only.

Table 7.2.4. Waste Disposal Ratings (WDR) of the Different Regions of LIBRA-SP

WDR	Blanket	Reflector	LiPb	Shield
Class A (10CFR61 limits)	40.5 (1.62) (^{94}Nb, ^{3}H)	8.5 (7.66) (^{94}Nb, ^{60}Co)	0.2 (0.064) (^{63}Ni, ^{60}Co)	(0.125) (^{14}C, ^{94}Nb
Class C (10CFR61 limits)	2.57 (0.103) (^{94}Nb, ^{14}C)	0.68 (0.61) (^{94}Nb, ^{14}C)	9.6e-4 (3.2e-4) (^{63}Ni)	(8.64e-3) (^{14}C, ^{94}Nb
Class C (Fetter limits)	41.5 (1.66) (^{192m}Ir, ^{158}Tb)	28.4 (2.56) (^{192m}Ir, ^{108m}Ag)	40 (13.1) (^{108m}Ag, ^{208}Bi)	(2.78e-3) (^{94}Nb, ^{14}C)

• All WDR values are given after a one year cooling period.

The specific activities calculated for the different radionuclides have been used to evaluate the radwaste classification of the blanket, reflector, shield and LiPb breeder. Table 7.2.4 shows the waste disposal ratings (WDR) for each of the reactor regions in the compacted and non-compacted (between brackets) forms. Compacted values correspond to crushing the solid waste before disposal. On the other hand, non-compacted values are based on averaging over the total volume of a particular region implying that internal voids will be filled with concrete before disposal. As shown in the table, the blanket may only qualify for disposal as Class C low level waste if it were disposed in its non-compacted form and only according to the 10CFR61 limits. The reflector could qualify for Class C waste in both forms according to 10CFR61 limits. Due to the low induced activity in the biological shield, it could qualify as Class A waste. About 70% of the Class A waste disposal rating of the shield is contributed by tritium due to the high boron content of the concrete. ^{63}Ni ($T_{1/2}$ = 100 yr) produced from ^{63}Cu and ^{94}Nb ($T_{1/2}$ = 20,000 yr) produced from ^{93}Nb and ^{94}Mo are the other major contributors. Both ^{63}Ni and ^{94}Nb are generated in the steel component of the shield.

According to the 10CFR61 limits, LiPb could qualify for shallow land burial as Class A waste after extracting all the tritium. On the other hand, if Fetter limits are used, LiPb will not qualify for disposal as Class C waste. It is important to keep in mind that the

waste disposal concentration limits used to calculate the waste disposal rating of the LiPb breeder are those assigned for the disposal of solid waste. Hence, LiPb has to be in solid form before such disposal can take place and the feasibility/practicality of such a process has to be determined.

7.2.8. Routine Atmospheric Effluents

The radiological dose to the population in the vicinity of the reactor site due to the routine release of tritium has been estimated by using the EPA AIRDOS-PC code. The code calculates the effective dose equivalent (EDE) as mandated by 40 CFR 61.93 and 61.94 to the maximally exposed individual (MEI) and at several distances from the point of release. Dose values are computed from ingestion, inhalation, air immersion and ground surface pathways. As discussed in Section 7.1, we considered the routine release of tritium from the reactor building, steam generator, fuel reprocessing facility and the target factory.

Assuming the release parameters listed in Table 7.2.5 and using meteorological conditions at different cities, we calculated the dose expected at typical locations near Boston, Chicago, Albuquerque and Los Angeles. A summary of the results is shown in Table 7.2.6. The worst dose was in the Los Angeles area but was only 2.39 mrem/yr. More than 85% of the doses at all sites are incurred via the ingestion pathway. The estimated doses at all sites are far below the current EPA effluent limit of 10 mrem/yr and less than the 5 mrem/yr limit adopted by ITER. It is important to keep in mind that the estimated dose values strongly depend on the stack height. For example, using a 35 meter stack height results in an EDE of 13 mrem/yr at the site boundary (1 km) if the Los Angeles meteorological conditions were used. The rule of thumb for determining the necessary stack height is to use 2.5 times the height of the nearest tall building in order to avoid downwash of the plume into the wake of the building [29]. A shorter stack must be justified with appropriate analysis.

7.2.9. Containment Accident Analysis

Another source of potential off-site doses which are of concern in LIBRA-SP are the doses produced by an accidental release of the radioactive inventory in the containment

building. In this section we calculated the potential off-site doses using the worst release characteristics as defined by the ESECOM [30] methodology (Table 7.2.7). The doses are due to the release of some of the radioactive inventory of the blanket, reflector, shield and LiPb. In addition, we calculated the doses produced by the release of all the tritium contained in the reactor building during an accident. To account for the worst possible accident, a containment failure is postulated in order to produce significant off-site dose even though the probability of such a failure is very low.

Table 7.2.5. Routine Atmospheric Release Parameters

• Site Information	
Locations	Albuquerque Boston Chicago Los Angeles
Temperature	15°C
Rainfall	75 cm/yr
• Emission Information	
Year-Round Averaging	
Stack Height	75 m
Stack Diameter	30 cm
Momentum	1 m/s
• Tritium Pathways	
Reactor Building	12 Ci/day
Steam Generator	40 Ci/day
Fuel Reprocessing	26 Ci/day
Target Factory	12 Ci/day
Total (adjusted for 75% availability)	24,640 Ci/yr

Table 7.2.6. Dose to the Maximally Exposed Indvidual (MEI)

Site	Dose (mrem/yr)	Distance (m)
Albuquerque	1.78	1000
Boston	0.75	3000
Chicago	1.09	1000
Los Angeles	2.39	3000

Table 7.2.7. Activation Product Release Characteristics

Pasquill Stability Class	F
Wind Speed	1 m/s
Inversion Layer Height	250 m
Deposition Velocity	0.01 m/s
Duration of Release	0.05 hr
Population Density	50 person/km^2
Ground Level Release	
Site Boundary	1 km and 10 km
Initial Plume Dimensions	
Sigma-Y	100 m
Sigma-Z	50 m
Percentage of Land	
Crop Farming	15%
Milk/Meat Products	15%
Groundshine Shielding	
Prompt Dose	0.7
Chronic Dose	0.33

During a loss of coolant accident (LOCA) or loss of flow accident (LOFA), a large increase in the steel structure temperature could lead to the mobilization and partial release of the radioactive inventory. Under adiabatic conditions, the decay heat generated within the first ten hours following a LOCA would increase the blanket temperature by $\sim$ 400°C. Under the same conditions, the decay heat generated in the reflector would increase its temperature by $\sim$ 100°C. Since the blanket and reflector peak operating temperatures are $\sim$ 625 and 400°C, respectively, the full mobilization of the structure radioactive products is impossible. The highest temperature a structure would reach determines the release fraction of its radioactive products. Off-site dose calculations have been performed using steel experimental volatility rates [31]. HT-9 volatility rates at 600 and 1000°C in dry air were used in this analysis for the reflector and blanket, respectively. To estimate conservative release fractions, we assumed a 10 hour LOCA in which the 1 hour release rates have been used for the full 10 hours to account for any possible loss of iron oxide protection. At 600°C, the reflector produces a whole body early dose at the site boundary of 253 mrem. Most

of the dose is produced by the manganese isotopes, ^{54}Mn and ^{56}Mn. On the other hand, at 1000°C, the blanket would produce a WB early dose of 8.91 rem. In addition to the manganese isotopes, ^{32}P is the third major contributor to the off-site dose from the blanket.

The decay heat generated in the steel-reinforced concrete shield is very low. The decay heat generated within the first 2 months following a LOCA would only increase the shield temperature by < 3°C. Most of the radioactive inventory is contributed by the mild steel portion of the shield. Since the shield average operating temperature is 500°C, off-site dose calculations have been performed using adjusted PCA volatility rates at 600°C in dry air. At 600°C, the whole body early dose at the site boundary is 37.1 mrem. Most of the dose is produced by the manganese isotopes, ^{54}Mn and ^{56}Mn. Even at 1000°C, the shield would only produce a WB early dose of 88.2 mrem.

LiPb is used as a coolant and breeder in LIBRA-SP. The steady state tritium inventory in LiPb is kept very low (3 g) by its continuous removal during the reactor operation. We calculated the potential off-site dose produced by the mobilization of LiPb during an accident where a breach of the containment is postulated. Following every fusion explosion, x-rays vaporize about 6.62 kg of LiPb. A simultaneous breach in the containment and chamber would allow cold air to flow into the chamber. The air starts cooling the LiPb vapor and hence reduces its vapor pressure. As LiPb vapor pressure falls, it starts condensing rapidly. The LiPb alloy was selected because it does not react vigorously with air or water. Nevertheless, we performed the off-site dose calculation assuming that all of the 6.62 kg of the vapor LiPb is mobilized and released to the environment. The resulting whole body early dose at the site boundary is 142 mrem. More than 65% of the dose is produced by tritium present in the LiPb at the onset of an accident. The rest of the dose is caused by ^{203}Pb, ^{110m}Ag and ^{210}Po.

The final source of potential off-site doses considered in this analysis is produced by the accidental release of the tritium from the reactor containment. The two sources of tritium inside the reactor containment are the target injector and breeder loops. While the target injector contains as much as 49 grams of tritium (one hour supply), the LiPb breeder

Table 7.2.8. Potential Off-Site Doses

	Blanket (1000°C)	Reflector (600°C)	Shield (600°C)	LiPb (6.62 kg)	Tritium (60 g)	Total
Prompt Dose at 1 km (Rem)						
WB	7.7	1.02e-1	3.17e-2	5.55e-2	5.98e-2	7.95
BM	9.87	3.61e-1	4.57e-2	1.06e-1	2.18e-1	10.59
Lung	14.5	5.52e-1	8.85e-2	2.13e-1	4.78e-1	15.84
LLI	6.33	2.29e-1	4.10e-2	4.77e-2	7.43e-2	6.73
WB Early Dose (Rem)						
At 1 km	8.91	2.53e-1	3.71e-2	1.42e-1	4.58e-1	9.8
At 10 km	5.86e-1	1.65e-2	2.29e-3	2.54e-2	4.58e-2	6.76e-1
WB Chronic Dose at 1 km (Rem)						
Inh + Grd	135	5.61e-1	5.46e-2	2.60e-1	6.31e-1	136.51
Ingestion	374	48.6	1.73	7.40	23.69	455.42
Total	509	49.1	1.79	7.66	24.34	591.94
WB Chronic Dose at 10 km (Rem)						
Inh + Grd	9.36	3.75e-2	3.38e-3	3.95e-2	1.46e-1	9.59
Ingestion	25.9	3.36	1.20e-1	1.32	5.5	36.2
Total	35.2	3.4	1.23e-1	1.36	5.62	45.8
Cancers						
Sum Organs	90.44	17.67	6.25e-1	1.696	6.99	117.42
WB	52.47	9.146	3.25e-1	3.763	14.21	79.92
Population Dose (Man-Rem)						
WB	3.32e+5	5.79e+4	2.06e+3	2.38e+4	9.01e+4	5.06e+5

present in the reactor system has a steady state inventory of only 2 g. As shown in Sec. 7.2.2, the maximum amount of tritium that may be released from the in reactor degassing unit and piping during an accident is 2 g. Assuming a 100% release, the whole body early dose produced by the release of all of the 51 g of tritium is 459 mrem.

Table 7.2.8 shows the potential off-site doses produced by simultaneous occurrence of the four previous scenarios. The total whole body dose at the site boundary mounts to 9.8 rem which is far below the 200 rem value recommended by the ESECOM study as a threshold for avoidance of early fatalities.

7.2.10. Doses from the Target Factory and Fuel Reprocessing Facilities

As shown in Section 7.1, the target factory will produce a total of 337,000 targets/day. The daily amount of tritium processed in the factory is about 1200 g. However, the total vulnerable inventory present in the factory at any moment and which could be released in a severe accident is only 147 grams of tritium. Similarly, the fuel reprocessing facility contains a 2-hr amount of vulnerable inventory, or about 106 grams of tritium, which might be released in a severe accident. As shown in Table 7.2.9, assuming 100% release of tritium from both facilities during an accident would result in whole body early doses of 1.3 and 0.95 rem for the target factory and fuel reprocessing facility, respectively.

7.2.11. Nuclear Grade Components

N-Stamp nuclear grade components are only required if the estimated off-site dose released is above the 25 rem limit. As shown in the previous analysis, none of the reactor components would produce an off-site whole body early dose in excess of 25 rem during a conservative accident scenario. However, a total release of the steel structure radioactive inventory would produce an off-site dose which exceeds the 25 rem limits. In such a case some N-Stamp components would be required. Since such a total release is quite impossible due to the lack of sources of energy which are sufficient to mobilize the steel structure, we reached the conclusion that none of the reactor components would require nuclear grade materials. Similarly, due to the low tritium inventory present in the target factory and fuel reprocessing facility at any moment, we can also avoid the use of nuclear grade components in the proposed facilities.

Table 7.2.9. Off-Site Doses Due to Tritium Release from the Target Factory and Fuel Reprocessing Facilities

	Target Factory	Fuel Reprocessing
Prompt Dose at 1 km (Rem)		
WB	1.7e-1	1.24e-1
BM	6.18e-1	4.52e-1
Lung	1.36	9.91e-1
LLI	2.11e-1	1.55e-1
WB Early Dose (Rem)		
At 1 km	1.3	9.51e-1
At 10 km	3.03e-1	2.22e-1
WB Chronic Dose at 1 km (Rem)		
Inh + Grd	1.79	1.31
Ingestion	67.37	49.25
Total	69.2	50.55
WB Chronic Dose at 10 km (Rem)		
Inh + Grd	4.15e-1	3.03e-1
Ingestion	15.64	11.43
Total	16.06	11.74
Cancers		
Sum Organs	19.86	14.52
WB	40.42	29.55
Population Dose (Man-Rem)		
WB	2.56e+5	1.87e+5

References for Section 7

1. B. Badger, G. A. Moses, et al., "LIBRA - A Light Ion Beam Fusion Conceptual Reactor Design, University of Wisconsin, UWFDM-800, KfK-4710, Chapter 9, 1989.
2. J. L. Anderson, "Experience of TSTA Milestone Run with 100-Gram-Level of Tritium," *Fusion Tech.*, **14**, 438 (1988).
3. K. B. Woodall, S. K. Sood and A. Busigin, "Conceptual Design of a Laboratory Scale Impurity Detritiation and Hydrogen Isotope Separation System," Abstract: Fourth Topical Mtg. of Tritium Technology, Albuquerque, Sept. 29-Oct. 4, 1991.
4. P. Hubberstey, T. Sample, M. J. Capaldi, and M. G. Barker, "Pb-17Li-Bismuth Interactions: An Electrical Resistance Study," *J. Nucl. Materials*, **217**, 93-103 (1994).
5. W. F. Calaway, "Electrochemical Extraction of Hydrogen from Molten LiF-LiCl-LiBr and Its Application to Liquid Lithium Fusion Reactor Blankets," *Nucl. Tech.*, **39**, 63 (1978).
6. N. P. Bhat and H. U. Borgstedt, "Oxygen in the Liquid-Metal Fusion Reactor Blanket and Its Possible Influence on the Compatibility with Materials," *Fusion Tech.*, **21**, 52 (1992).
7. G. Pierini, A. M. Polcaro, P. F. Ricci and A. Viola, "Tritium Recovery from Liquid $Li_{17}Pb_{83}$ Alloy Blanket Material," *Nucl. Eng. Design/Fusion*, **1**, 159 (1984).
8. K. A. Plute, E. M. Larsen and L. J. Wittenberg, "Tritium Recovery from Liquid Lithium-Lead by Vacuum Degassing," *Nucl. Tech./Fusion*, **4**, 407 (1983).
9. T. J. Dolan, G. R. Longhurst and E. Garcia-Otero, "A Vacuum Disengager for Tritium Removal from HYLIFE-II Reactor FLIBE," *Fusion Tech.*, **21**, 1949 (1992).
10. B. G. Logan, et al., "MARS – Mirror Reactor Study," Lawrence Livermore National Laboratory, UCRL-53480, July 1984.
11. B. Badger, et al. "LIBRA – A Light Ion Beam Fusion Conceptual Reactor Design," University of Wisconsin Fusion Technology Institute Report UWFDM–800 (February 1990).

12. T. Terai, S. Nagai, T. Yoneoka and Y. Takahashi, "Diffusion Coefficient of Tritium in Molten Lithium-Lead Alloy ($Li_{17}Pb_{83}$) Under Neutron Irradiation at High Temperature," *J. Nucl. Materials*, **187**, 247 (1992).

13. T. Terai, S. Nagai, T. Yoneoka and Y. Takahashi, "Mass Transfer Coefficient of Tritium in Molten Li-Pb Alloy ($Li_{17}Pb_{83}$) to Environmental Gas Under Neutron Irradiation," *Fusion Eng. Design*, **17**, 237 (1991).

14. A. Viola, G. Pierini, P. L. Lolli-Ceroni and K. Douglas, "Kinetics of Deuterium Desorption from Pb-17Li Eutectic," *Fusion Eng. Design*, **14**, 249 (1991).

15. Y. C. Chan and E. Veleckis, "A Thermodynamic Investigation of Dilute Solutions of Hydrogen in LiPb Alloys," *J. Nucl. Materials*, **122 & 123**, 935 (1984).

16. E. Veleckis, "Thermodynamic Investigation of the Li-Al and Li-Pb Systems by the Hydrogen Titration Method," *J. Less-Common Materials*, **73**, 49 (1980).

17. E. Veleckis, personal communication, November 27, 1985.

18. G. Pierini, A. M. Polcaro, P. F. Ricci and A. Viola, "Solubility of Hydrogen in Molten $Li_{17}Pb_{83}$ Alloy," *J. Chem. Eng. Data*, **29**, 250 (1984).

19. J. T. Bell, J. D. Redman and H. F. Bittner, "Tritium Permeability of Structural Materials and Surface Effects on Permeation Rates," Proc. Tritium Technology in Fission, Fusion and Isotopic Applications, Amer. Nuc. Soc., April 28-May 1, 1980, Dayton, Ohio, pp. 49–53.

20. R. Alcouffe et al., "User's Guide for TWODANT: A Code Package for Two-Dimensional, Diffusion–Accelerated, Neutral Particle Transport," LA-10049-M, Los Alamos National Laboratory (March 1982).

21. D. L. Henderson and O. Yasar, "DKR-ICF: A Radioactivity and Dose Rate Calculation Code Package," UWFDM-714, Vol. 1, University of Wisconsin (April 1987).

22. L. J. Porter, "Upgrade of a Fusion Accident Analysis Code and Its Application to a Comparative Study of Seven Fusion Reactor Designs," PFC/RR-89-10, Massachusetts Institute of Technology (June 1989).

23. User's Guide for AIRDOS-PC, Version 3.0, EPA 520/6-89-035, U. S. Environmental Protection Agency, Office of Radiation Programs, Las Vegas, NV (December 1989).

24. D. L. Henderson, M. E. Sawan, and G. A. Moses, "Radiological Dose Calculations for the Diode Region of the Light Ion Fusion Target Development Facility," *Fusion Technology*, **13**, 594 (1988).

25. Nuclear Regulatory Commission, 10CFR part 20, "Standards for Protection Against Radiation," (1975).

26. R. Alcouffe, R. O'Dell, and F. Brinkley, Jr., "A First-Collision Source Method that Satisfies Discrete S_n Transport Balance," *Nuclear Eng. & Design*, **105**, 198 (1980).

27. Nuclear Regulatory Commission, 10CFR part 61, "Licensing Requirements for Land Disposal of Radioactive Waste," Federal Register, FR 47, 57446 (1982).

28. S. Fetter, E. Cheng and F. Mann, "Long Term Radioactive Waste from Fusion Reactors," *Fusion Engineering and Design*, **13**, 239-246 (1990).

29. USNRC Regulatory Guide 1.145/Rev. 1 (February 1983).

30. J. P. Holdren et al., "Report of the Senior Committee on Environmental, Safety, and Economic Aspects of Magnetic Fusion Energy," UCRL-53766, Lawrence Livermore National Laboratory (1989).

31. S. J. Piet et al., "Initial Experimental Investigation of the Elemental Volatility from Steel Alloys for Fusion Safety Applications," EGG-FSP-8459, Idaho National Engineering Laboratory (April 1989).

8. Preliminary Economic Analysis

A preliminary cost analysis has been made for the LIBRA-SP reactor based on the current estimates of power and mass. As previously, the analysis is made with the FUSCOST [1] code which has specific capabilities for light ion beams. The cost algorithms in FUSCOST are in 1986 dollars. The actual consumer price index for power and electrical machinery is used to escalate the costs to 1995 dollars. Figure 8.1.1 shows this consumer price index between 1986 and 1994 [2].

The main difference in the LIBRA-SP and LIBRA-LiTE [3] costing is in the indirect costs. These differences are shown below:

	LIBRA-LiTE	LIBRA-SP
Construction factor (%)	10	12
Home office factor (%)	10	5.2
Field office factor (%)	10	6
Owners cost factor (%)	5	15
Project contingency factor (%)	5	17.3

The new indirect costs are more in line with current power plant construction costs and have been adopted from the latest Inertial Fusion Energy Comparison study [4]. These new indirect costs add 14.4% to the cost of the reactor and to the cost of electricity. For this reason, when we compare the relative COE for the two reactors, it will be done with the new indirect costs.

Table 8.1.1 lists the parameters used in the economic model.

8.1. Driver Cost

As in the case of LIBRA-LiTE, the cost of the driver dominates the direct costs. The algorithm which gives the cost in 1986$ is:

$$\text{Driver (1986 M\$)} = (271.2 + 3.414\ \text{CRR})\ (\text{DET/EFF} \cdot 17.7)^{0.8}$$

where CRR is the chamber rep-rate, DET is the driver energy on target and EFF is overall driver efficiency. For LIBRA-SP with a 7.2 MJ driver at 3.9 Hz, the cost is 359.16 M$ in 1986 and is 440 M$ in 1995 when escalated according to the consumer price index.

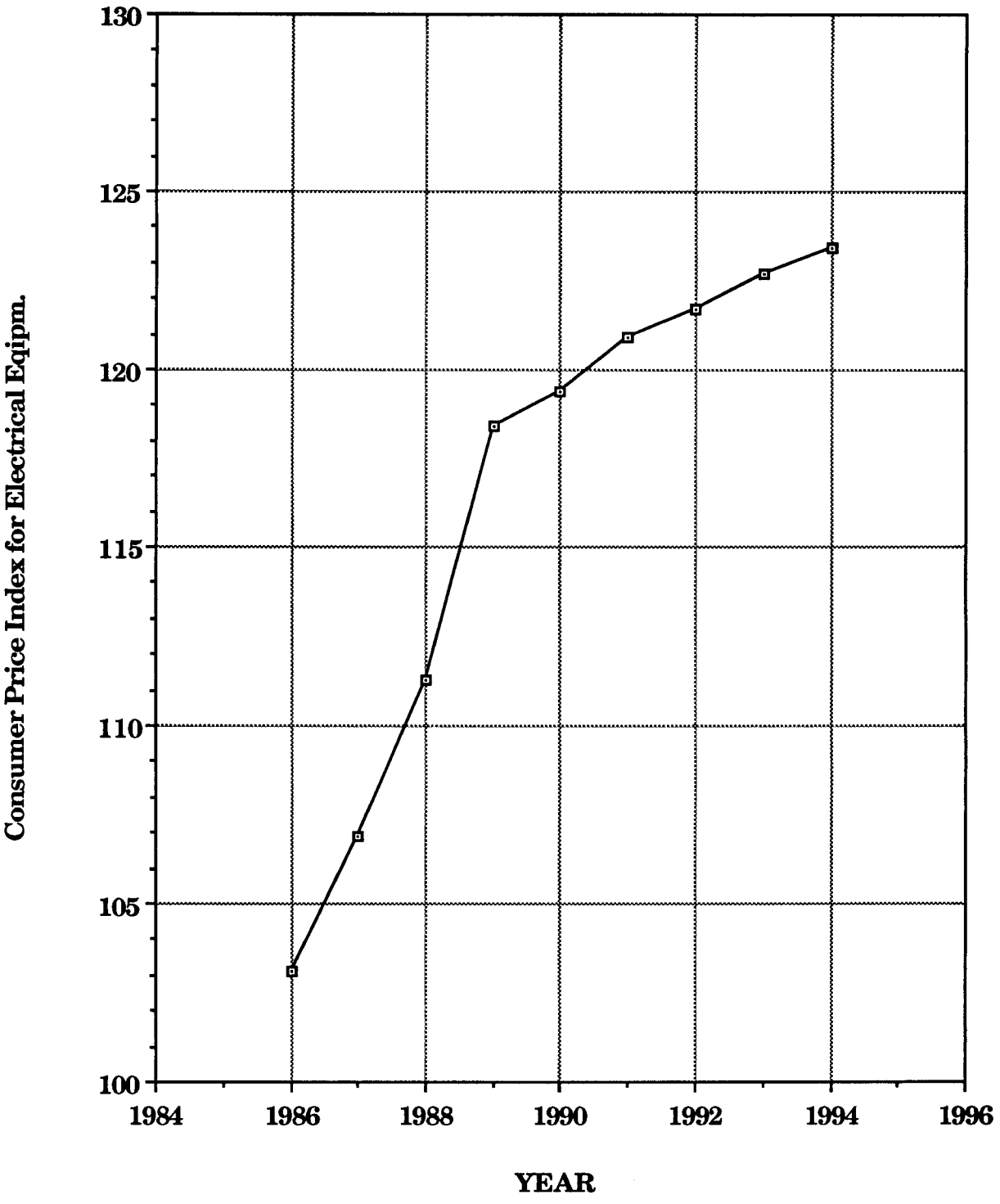

Figure 8.1.1. Consumer price index for electrical equipment from 1986 to 1994.

Table 8.1.1. LIBRA-SP Economic Model Parameters

Plant availability (%)	75
Construction time (yr)	6
Plant life (yr)	30
Consumer price index from 1986–1994	1.196
Construction factor (%)	12
Home office factor (%)	5.2
Field office factor (%)	6.0
Owners cost factor (%)	15.0
Project contingency (%)	17.3
Interest rate on capital (%)	8
Fraction of capital borrowed (%)	100
Years of accelerated tax depreciation	10
Investment tax credit rate (%)	8
Property tax rate (%)	2
Levelized interior replacement cost fraction (%)	1

8.2. Reaction Chamber Costs

The second highest cost item is the chamber at 267 M$. The cost of the enriched LiPb accounts for 43.3% (115.6 M$), the cost of structural steel for 30.6% (81.7 M$), the cost of concrete for 22% (58.7) and the cost of the perforated tubes for 4.1% (10.9 M$). Figure 8.2.1 shows the breakdown of the chamber costs.

Table 8.2.1 compares the use of natural Li in LIBRA-LiTE with enriched LiPb in LIBRA-SP. The penalty in using LiPb is in the density, ~ 20 times higher than Li. Thus, although the unit cost of natural Li is higher than the enriched LiPb, the total cost of the coolant is higher in LIBRA-SP by a factor of 6.3.

8.3. Remaining Direct Costs

Figure 8.3.1 gives a breakdown of the direct costs which add up to 1772 M$ (1995). Besides the driver and reactor chamber, the dominant costs are buildings (245 M$), turbine plant (244 M$), heat transfer equipment (236 M$), and electric plant (130 M$). It is interesting to note that heat transfer equipment for LiPb is more expensive than for Li

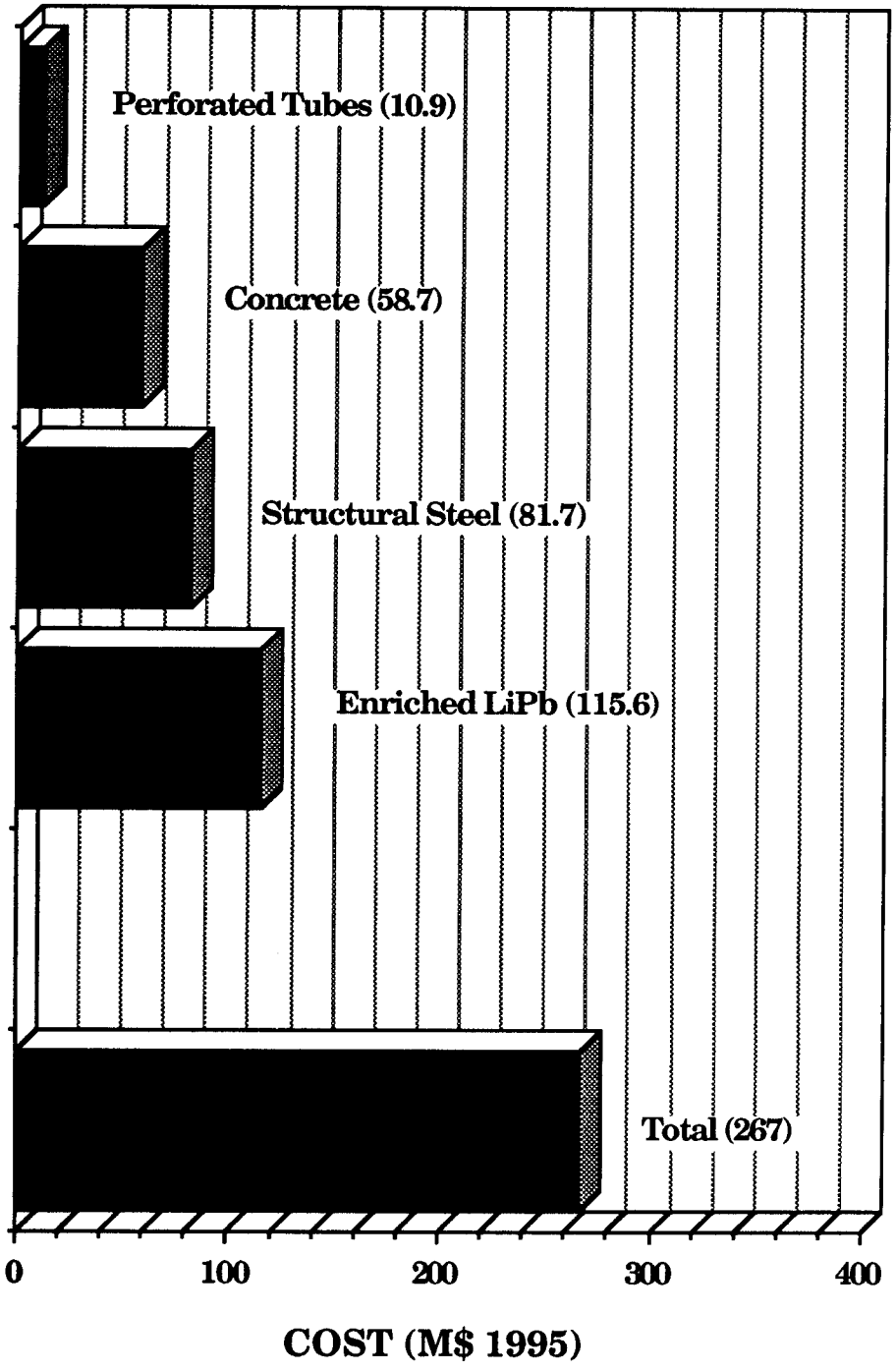

Figure 8.2.1. Breakdown of chamber costs (M$ 1995).

Table 8.2.1. Comparison of LiPb and Li as Coolants

	LIBRA-LiTE	LIBRA-SP
Coolant	Nat. Li	Enr. LiPb
Volume of coolant in reactor (m^3)	527.1	461.5
Mass of coolant in reactor (tonnes)	263.6	4,292.3
Unit cost of coolant ($/kg 1986)	57	22
Cost of coolant (M$ 1986)	15.02	94.43
Cost of coolant (M$ 1995)	18.38	115.58

cooling using the same thermal power. This is due to the density of LiPb, which requires much more support for heat exchangers and particularly for coolant transport pipes.

8.4. Indirect and Time Related Costs

The indirect costs for LIBRA-SP add 1101 M$ to the direct costs, and the time related costs add another 354 M$ for a total capital cost of 3227 M$. Table 8.4.1 summarizes all the costs.

Table 8.4.1. Summary of LIBRA-SP Costs

	M$ (1995)
Total direct costs	1772
Total indirect costs	1101
Total time related costs	354
Total capital costs	3227
Annualized fuel costs	17
Annualized O&M costs	86
Annualized cost of capital	267
Total annualized costs	370

8.5. Cost of Electricity

The cost of electricity (COE) is based on fuel targets costing 18¢/unit, 8% interest on capital and an availability of 75%. Using the total annualized cost, we get

$$\mathrm{COE}\,(1995) = \frac{370 \times 10^9\,\mathrm{mills}}{10^6\,\mathrm{kW}\,8760\,\mathrm{hr}\,(0.75)} = 56.4\,\mathrm{mills/kWh}$$

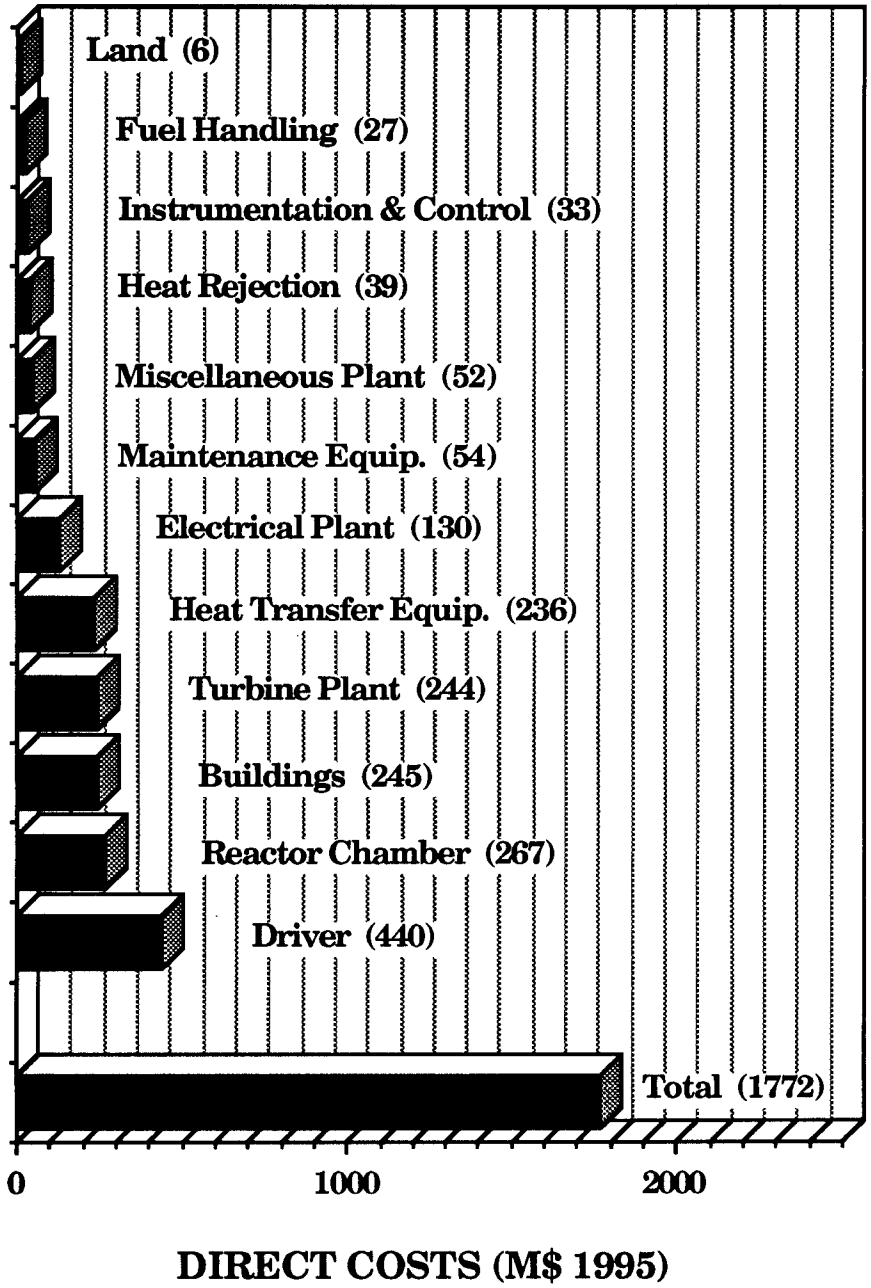

Figure 8.3.1. Breakdown of direct costs (M$ 1995).

The COE for LIBRA-LiTE in 1991$, under the same conditions was 42.6 mills/kWh using the original indirect costs and 48.6 mills/kWh using the new indirect costs. The difference of 16% between LIBRA-SP and LIBRA-LiTE is due to the higher cost of the reactor chamber, the heat transfer equipment, and due to inflation.

References for Section 8

1. Zoran Musicki, "FUSCOST: A PC-Based Menu Driven Program for Economic Analysis of Fusion Facilities," 12th Symposium on Fusion Engineering, Monterey, CA, 1987, University of Wisconsin Fusion Technology Institute Report UWFDM-743.
2. H. Thompson, UW School of Business, private communication.
3. B. Badger et al., "LIBRA-LiTE: A Commercial Light Ion Fusion Power Plant," University of Wisconsin Fusion Technology Institute Report UWFDM-880, Dec. 1991.
4. W. J. Schafer Associates et al., "OSIRIS and SOMBRERO Inertial Confinement Fusion Power Plant Designs," WJSA-92-01, DOE/ER/54100-1, March 1992.

9. LIBRA-SP System Parameters

The parameters for the LIBRA-SP conceptual design as of June 30, 1995 are presented in this chapter. The general power balance of LIBRA-SP is shown in Table 9.4. The same parameters are shown graphically in Figure 9.1. These general parameters are supported by more specific parameters for subsystems shown in Table 9.2 for the ion beams, Table 9.3 for the target, Table 9.4 for the target chamber, and Table 9.5 for activation and safety.

Table 9.1 shows the evolution of the LIBRA concept through three design concepts. The basic change for the three is the manner in which beams are transported. LIBRA used preformed plasma channels, LIBRA-LiTE used ballistic transport and LIBRA-SP uses self-pinched channels. As the designs progressed, improvements were made in analysis and subsystem concepts that led to better designs. One constant is that the HELIA inductive voltage adder technology for the drivers was used for all three designs. This technology has recently been shown to operate at high rep rate. The costs have been scaled from the LIBRA design, where a detailed costing study was performed. The thermal conversion efficiency of LIBRA-SP (43%) was obtained from the temperature of the target chamber coolant.

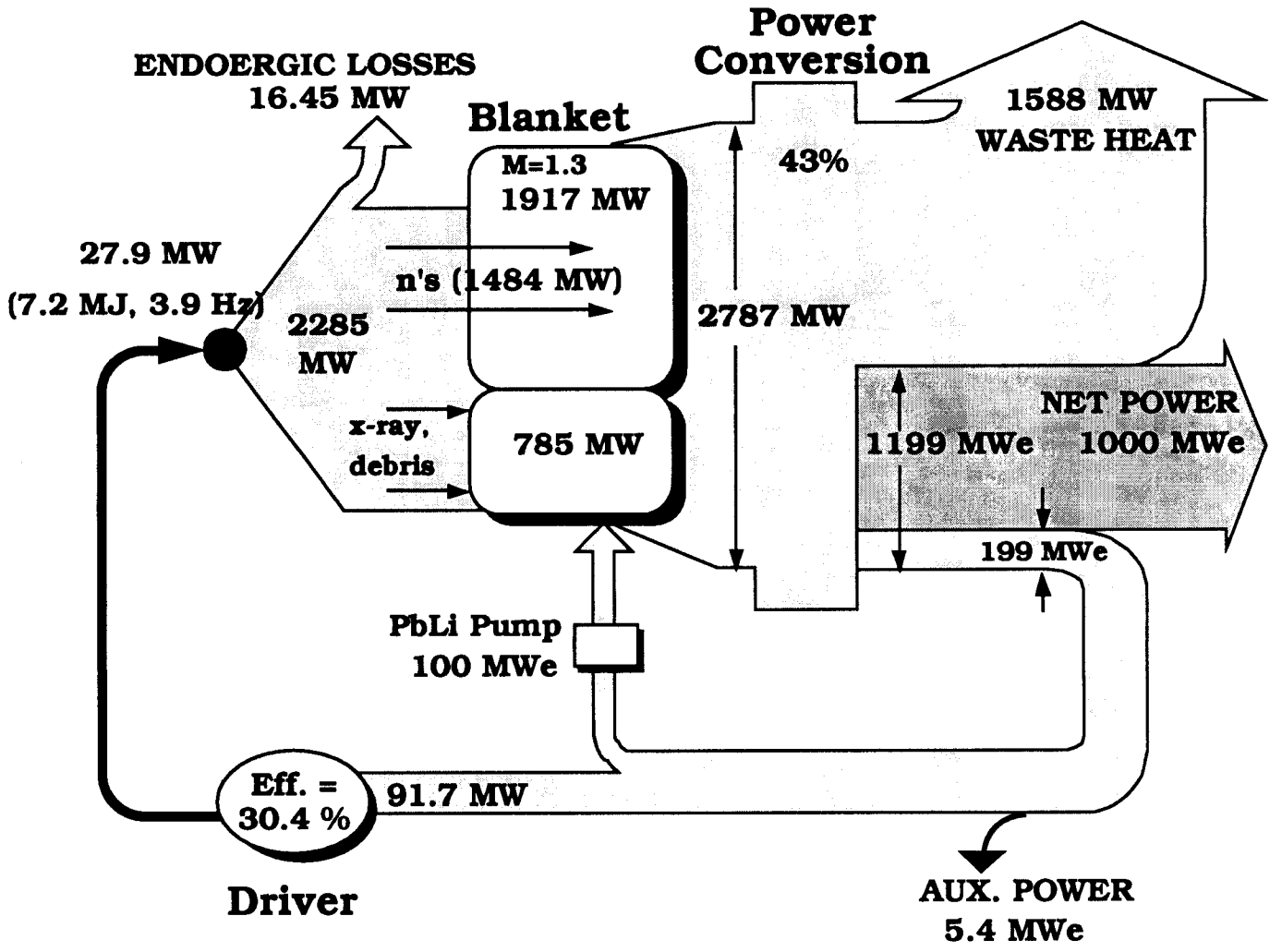

Figure 9.1. LIBRA-SP power balance.

Table 9.1. System Parameters for LIBRA, LIBRA-LiTE and LIBRA-SP

Parameter	Units	LIBRA	LIBRA-LiTE	LIBRA-SP
Net electrical power	MWe	331.96	1000.07	1001.45
Year published		1990	1991	1994
Accelerator technology		HELIA	HELIA	HELIA
Ion beam transport		Channel	Ballistic	Self-Pinched
Number of beams		18	30	24
Energy on target	MJ	4	6	7.2
Target gain		80	100	81.81
Target yield	MJ	320	600	589
Rep rate	Hz	3	3.99	3.88
Fusion power	MW	960	2394	2285
Target neutron fraction		0.6778	0.6778	0.6494
Target x-ray and ion fraction		0.2985	0.2985	0.3434
Target x-ray energy	MJ	63.68	119.40	168.08
Target debris energy	MJ	31.84	59.70	34.18
Target gamma fraction		0.0029	0.0029	0.00006
Target endoergic fraction		0.0209	0.0209	0.0072
Fusion neutron power	MW	653	1628	1484
Nuclear energy multiplication		1.28	1.211	1.288
Total neutron power	MW	836	1971	1912
X-ray and ion power	MW	287	715	785
Gamma power	MW	3.56	8.41	0.18
Endoergic power	MW	-20.06	-50.03	-16.45
Recirc. heat power	MW	37.40	83.10	85.00
Thermal power	MW	1163	2778	2781
Thermal efficiency		0.38	0.44	0.43
Gross electrical power	MWe	441.98	1222.11	1196.03

Table 9.1. (Continued)

Parameter	Units	LIBRA	LIBRA-LiTE	LIBRA-SP
Driver efficiency		0.49	0.376	0.376
Prime energy storage	MJ	17.01	33.24	23.64
Diode type		1 stage	1 stage	2 stage
Diode efficiency		0.8	0.8	0.9
Energy into diode	MJ	8.33	12.50	8.89
Transport efficiency		0.6	0.6	0.9
Energy into beam	MJ	6.67	10.00	8.00
Net driver efficiency		0.2352	0.18048	0.30456
Gain net driver efficiency		18.82	18.05	24.91
Net efficiency		0.0894	0.0794	0.1310
Gain efficiency		7.15	7.94	10.71
Driver power	MWe	51.02	132.65	91.73
Magnet power	MWe	27	75	0
Primary pump power	MWe	12	9	100
Secondary pump	MWe	15	0	0
Auxiliary power	MWe	5	5.4	5.4
Recirc. power	MWe	110.02	222.05	197.13
Recirc. power fraction		0.2489	0.1817	0.1645
Driver direct cost	M$ (1993)	304.38	426.06	440
Total direct cost	M$ (1993)	854.41	1739.56	1772
Unit direct cost	$(1993)/W	$2.57	$1.74	$1.77

Table 9.2. LIBRA-SP Ion Beam Parameters

Parameter	Unit	Main	Pre-Pulse
Ion species		Lithium	Lithium
Ion energy	MeV	30	30
Energy on target	MJ	6.0	1.2
Total transport efficiency	%	90	90
Energy leaving diodes	MJ	6.67	1.33
Number of beams		12	12
Pulse width at diodes	ns	40	40
Pulse width at target	ns	20	40
Power at diodes	TW	167	33
Power at target	TW	300	30
Particle current at diodes	MA	5.56	1.11
Particle current at target	MA	10	1
Diode			
Current/diode	kA	463	92.6
Voltage drop 1 V_1	MV	15	15
Voltage drop 2 V_2	MV	30	30
Physical gap 1 d_1	cm	2	2
Physical gap 1 d_2	cm	2	2
Enhancement factor K_e		5	5
Inner anode radius R_i	cm	10	10
Microdivergence θ_μ	mrad	4	4
Focal length F	cm	150	150
J_{scl}	kA/cm^2	0.3	0.3
J_d	kA/cm^2	1.5	1.5
Anode area A_a	cm^2	309	62
Outer anode radius R_o	cm	14.1	10.9
Focal spot radius r_f	cm	0.6	0.6
R/F		0.094	0.073
B_{crit} for gap 1	T	2.63	2.63
B_{crit} for gap 2	T	2.63	2.63
B_{appl} for gap 1	T	5.27	5.27
B_{appl} for gap 2	T	5.27	5.27

Table 9.2. (Continued)

Parameter	Unit	Main	Pre-Pulse
Self-Pinched Transport			
Transport length L	cm	550	550
γ		1.005	1.005
β		0.096	0.096
Charge state		3	3
Alfvén current	kA	6958	6958
I_{net}	kA	30.7	18.5
f_m		0.978	0.933
Energy loss ϵ	kJ	14.9	1.8
Efficiency	%	97.3	98.4
Neutronics			
Diode casing	dpa/FPY	0.06	0.06
End-of-life diode casing	dpa	1.8	1.8
Fast n fluence per FPY @ 5.7 m	n/cm^2	1.67×10^{20}	1.67×10^{20}
Lifetime of diode magnet out of direct-line-of-sight	FPY	240	240
Fast n fluence per FPY @ 5.7 m in direct line-of sight	n/cm^2	6.4×10^{21}	6.4×10^{21}
Lifetime of diode magnet in direct line-of-sight	FPY	6.25	6.25
Diode Vacuum System Parameters			
Initial He atom density in chamber	#/cm^3	7×10^{15}	
Initial chamber pressure in chamber	torr	0.52	
Pressure in chamber after a pulse	torr	260	
Volume of reaction chamber	m^3	2325	
Pressure required in diode enclosure	torr	10^{-4}	
Volume of diode enclosure	m^3	0.17	
Diode beam aperture diameter	cm	2.0	
Diameter of beam tube	cm	2.0	
Length of beam tube	cm	150	
Rotating disc diameter	m	0.5	
Hole in the disc is at a radius of	m	0.2	
Rep-rate of reactor	Hz	3.9	
Rep-rate of disc	Hz	3.9	
Pressure rise in diode enclosure	torr	4.3×10^{-2}	
Pump capacity for each diode (ℓ/s)		4500	

Table 9.3. Parameters for the LIBRA-SP Target

General Parameters	
Total absorbed beam energy (MJ)	7.2
Peak beam ion (TW)	330
Hohlraum radius (cm)	0.7
Yield (MJ)	589
Peak beam intensity (TW/cm^2)	54
Target mass (mg)	151.5
Burnup fraction (%)	35
Target gain	82
Debris Ion Kinetic Energies	
Species	Energy (MJ)
H	0.029
D	0.062
T	0.094
C	2.07
Pb	15.9
Target Burn Parameters	
Total yield	589 MJ
Neutron yield	383 MJ
X-ray yield	167 MJ
Debris ion yield	35 MJ
Energy lost in endoergic reactions	4 MJ
Target Data at Ignition	
	Material
Region 1	DT
Region 2	CH
Region 3	C
Region 4	Pb
	Density (g/cm^3)
Region 1	230
Region 2	0.013
Region 3	0.024
Region 4	11.4

Table 9.3. (Continued)

Target Data at Ignition (continued)	
	Radius Range (cm)
Region 1	0-0.0173
Region 2	0.0173-0.55
Region 3	0.55-0.6983
Region 4	0.6983-0.7
	Mass (mg)
Region 1	5.0
Region 2	9.1
Region 3	17.4
Region 4	120
Nuclear Energy Deposition in Target	
Region 1	2.53896 MeV/DT fusion
Region 2	0.00345 MeV/DT fusion
Region 3	0.00039 MeV/DT fusion
Region 4	0.00002 MeV/DT fusion
Total	2.54282 MeV/DT fusion
Energy Partitioning from LIBRA-SP Target	
Fusion energy	17.6 MeV/DT fusion
Energy carried by neutrons	11.429 MeV/DT fusion (64.94%)
Energy carried by gamma photons	0.001 MeV/DT fusion (0.006%)
Energy carried by x-rays and debris	6.043 MeV/DT fusion (34.34%)
Energy lost in endoergic reactions	0.127 MeV/DT fusion (0.72%)

Table 9.4. Parameters for the LIBRA-SP Target Chamber

First Surface (FS) Parameters	
Density of HT-9 (kg/m^3)	7625
Elastic modulus of HT-9 (GPa)	163.0
Density of LiPb (kg/m^3)	9440
Tube diameter (cm)	3
Tube thickness (mm)	3
Flow velocity (m/s)	4.0
Rep rate (Hz)	3.88
Number of the coolant tubes in the FS	362
Total surface area (m^2)	1910.6
Thickness of LiPb recondensed per second (μm)	1.35
Heat flux due to recondensation at FS (W/cm^2)	107
Maximum value of volumetric heating at FS (W/cm^3)	37
Temperature rise in the coolant tube wall (HT-9 wall thick = 3 mm) due to:	
1 - Surface heat flux only (condensation) (°C)	117.5
2 - Volumetric heating only (°C)	7.5
Total temperature rise in the FS coolant tube wall (°C)	125
Maximum FS coolant velocity (at inlet) (m/s)	4.0
Minimum FS coolant velocity (at exit) (m/s)	2.9
Inlet FS coolant bulk temperature (°C)	370
Exit FS coolant bulk temperature (°C)	430 (32.32×10^4 kg/s)
Average coolant bulk temperature of outside coolant (°C)	650 (12.26×10^4 kg/s)
Exit blanket coolant bulk temperature (°C) (V = 17.4 cm/s)	600 (5.23×10^4 kg/s)
Total mass flow rate (kg/s)	49.78×10^4
HX inlet coolant bulk temperature (°C)	502
Pumping power (inside cavity) (MW)	47.61
Thermal conversion efficiency (%)	43

Table 9.4. (Continued)

Chamber Neutronics Parameters	
Inner radius of blanket	4 m
Chamber wall radius	5.2 m
Neutron wall loading	7.4 MW/m^2
Local TBR	1.48
Nuclear energy multiplication, M_n	1.288
Overall energy multiplication, M_o	1.18
Peak dpa rate in PERIT tubes	94.2 dpa/FPY
Lifetime of front PERIT tubes	1.6 FPY
Peak helium production rate in PERIT tubes	436 He appm/FPY
Peak power density in PERIT tubes	18.3 W/cm^3
Peak dpa rate in chamber wall	4.2 dpa/FPY
Peak end-of-life damage in chamber wall	126 dpa
Peak helium production rate in chamber wall	0.9 He appm/FPY
Peak power density in chamber wall	0.52 W/cm^3

Table 9.5 (a). Tritium Inventory and LIBRA-SP Release Summary

Location	System	Inventory	Tritium Routine Release	Tritium Accidental Release
Target factory	–	g	Ci/d	g(T)
	In process	147	12	147
	Storage	1200	0	0
Reactor building	Targets Breeder alloy	49	12	49
	Breeder alloy	2	0	2
Fuel reprocessing	Equipment	106	13	106
	Cryo-still	193	13	0
Storage	Vault	1200	0	0
Steam generator	Water Coolant	0 Routine release Air 50 Ci/d Water 40 Ci/d	40	0 304

Table 9.5 (b). Radioactivity After Shutdown

Time After	Activity (MCi)		Decay Heat (MW)		BHP (km^3 air)	
Shutdown	Blanket	Reflector	Blanket	Reflector	Blanket	Reflector
0	721	924	2.99	3.34	3.7e+8	1.63e+9
1 hour	620	684	2.18	2.88	8.9e+7	8.02e+7
1 day	498	407	0.46	1.09	8.2e+7	5.54e+7
1 week	480	175	0.42	0.18	8.01e+7	3.2e+7
1 month	449	147	0.39	0.14	7.5e+7	2.7e+7
1 year	307	63	0.22	5.63e-2	3.7e+7	9.24e+6
10 years	29	6.5	1.23e-2	1.05e-2	1.05e+6	2.0e+6
100 years	2.78e-3	8.2e-3	1.39e-6	2.72e-6	1.02e+4	4.1e+4

Table 9.5 (c). Waste Disposal Ratings (WDR) of the Different Regions of LIBRA

WDR	Blanket	Reflector	LiPb	Shield
Class A (10CFR61 limits)	40.5 (1.62) (^{94}Nb, ^{3}H)	8.5 (7.66) (^{94}Nb, ^{60}Co)	0.2 (0.064) (^{63}Ni, ^{60}Co)	(0.125) (^{14}C, ^{94}Nb
Class C (10CFR61 limits)	2.57 (0.103) (^{94}Nb, ^{14}C)	0.68 (0.61) (^{94}Nb, ^{14}C)	9.6e-4 (3.2e-4) (^{63}Ni)	(8.64e-3) (^{14}C, ^{94}Nb
Class C (Fetter limits)	41.5 (1.66) (^{192m}Ir, ^{158}Tb)	28.4 (2.56) (^{192m}Ir, ^{108m}Ag)	40 (13.1) (^{108m}Ag, ^{208}Bi)	(2.78e-3) (^{94}Nb, ^{14}C)

• All WDR values are given after a one year cooling period.

Table 9.5 (d). Routine Atmospheric Release Parameters

• Site Information:	
Locations:	Albuquerque Boston Chicago Los Angeles
Temperature:	15 C
Rainfall:	75 cm/yr
• Emission Information:	
Year-Round Averaging	
Stack Height:	75 m
Stack Diameter:	30 cm
Momentum:	1 m/s
• Tritium Pathways:	
Reactor Building:	12 Ci/day
Steam Generator:	40 Ci/day
Fuel Reprocessing:	26 Ci/day
Target Factory:	12 Ci/day
Total (adjusted for 75% availability):	24,640 Ci/yr

10. Conclusions and Recommendations

Conclusions

- The self-pinched mode of beam propagation does not require magnets at the end of the beam tube, as in the case of LIBRA-LiTE. These focusing magnets were directly exposed to the target emanations and had a limited lifetime.
- The use of solid (as opposed to woven) perforated steel tubes called PERIT units has removed one major uncertainty of the woven tube configuration, namely the loss of preload. The preload on the woven tubes determined the natural frequency and the deflection of the tubes during pulsing. Thus, a loss of preload due to many different factors, would cause the frequency to change, also changing the deflection. This would have undesirable consequences for the reactor.
- Use of the BUCKY code has shown that the spray from the PERIT units remains intact after the explosion until it impinges on the tubes. This has allowed us to calculate more accurately the impulse on the tubes for use in determining their dynamic response.
- A preliminary design of the rotating shutters for the beam tubes has shown that it is possible to segregate the chamber vacuum from that of the diode vacuum, and to re-establish initial conditions at the proposed rep-rate.
- Recent target information declassification has allowed more realistic determination of target debris and x-rays, and consequently, a better understanding of their effect on the reactor chamber components.
- Continued economic analysis of the light ion beam mode of inertial confinement fusion has shown that it is competitive with other inertial and magnetic fusion concepts.

Recommendations

As more accurate information is obtained both from the target, the beam propagation and the chamber component responses, this information will be used to design the LIBRA-SP reactor with more confidence. During the next two years a more detailed reactor design study will be made integrating 3D neutronics calculations for the target chamber with the diodes and target injection. A full scale economic analysis will be performed at that time.

Appendices

A NOVEL FIRST WALL PROTECTION SCHEME FOR ION BEAM ICF REACTORS

E. Mogahed, P. Cousseau, R. Engelstad, R. Peterson,
H. Khater, G. Kulcinski, MacFarlane, P. Wang,
M. Sawan, I. Sviatoslavsky, L. Wittenberg
Fusion Technology Institute
University of Wisconsin- Madison

A novel scheme of first wall protection for ion beam driven inertial confinement fusion reactors is presented. This work is an outgrowth of a series of studies on light ion fusion reactors (LIBRA) performed at the University of Wisconsin. The current study called LIBRA-SP utilizes a self-pinched ion beam transport and is intended as a 1000 MWe power reactor. This paper will focus on the first wall protection which uses a liquid metal LiPb spray onto rigid steel tubes for absorbing X-ray and ion energy emanating from the target. Earlier versions of LIBRA reactors used flexible woven SiC or steel tubes. The current version uses rigid HT-9 ferritic steel tubes called PERIT (perforated rigid tubes) units. These tubes are equipped with tiny nozzles on either side which spray vertical fans of liquid metal, overlapping each other such that the first two rows of tubes are completely shadowed from the target emanations. The target generated X rays accelerate the LiPb spray through the rapid vaporization of the surface facing the target. Simulations of the behavior of the spray with the BUCKY computer code show that the spray remains intact and is still at liquid density when it hits the PERIT units producing a peak pressure on the PERITS of several GPa, and a total impulsive loading of 72 Pa-s. The spray that is vaporized by the X rays blows into the center of the target chamber intercepting the target debris ions. The first row of tubes in the blanket carry the brunt of the radial impulsive load, which is applied at the reactor repetition rate. A code has been developed for determining the transient and steady state response of the tubes containing the liquid metal, driven by sequential pulses for specific boundary conditions. Maximum steady state deflections and bending stresses as a function of the rep-rate are calculated and used to optimize the length of the PERIT units for avoiding resonant conditions. The cylindrical portion of the chamber is covered by a blanket of rigid steel tubes at a packing fraction of 50%. Only the front two rows of tubes are equipped with the spray nozzles. These tubes are at a radius of 4 m and the radius of the reflector, which is the vacuum boundary is 5.2 m. The reflector is made of HT-9 ferritic steel, and is 50 cm thick with a 10% fraction of LiPb coolant. In the vertical direction the front tubes are divided into two banks, each 5.3 m long. Manifolds feed the tubes at the top and at the midplane. The rear tubes are continuous from the top to the bottom and are manifolded only at the top. All the liquid metal ends up in a pool on the bottom and is fed through a perforated plate to heat exchangers located in the base of the reactor.

ABSTRACT SUBMISSION FORM
16TH IEEE/NPSS Symposium on Fusion Engineering

September 30 - October 5, 1995
Champaign, Illinois, USA

Paper Title:
A Novel First Wall Protection Scheme for Ion Beam ICF Reactors

Technical Topic Number (see section on Technical Topic Areas): 7

Keywords:
(1) Inertial Confinement
(2) Perforated Tubes
(3) Spray Protection

☐ If an oral presentation is requested (rather than the standard poster presentation indicate here

☐ Enter my paper in the "Distinguished Paper" competition. (Requires August 30 submission of full paper)

Submitted by:

Signature

Typed Name
I. N. Sviatoslavsky

Institution/Company
Fusion Technology Institute
University of Wisconsin-Madison

Address
1500 Johnson Drive

City, Province, State/Postal Code
Madison, WI 53706-1687

Country USA
Phone 608-263-6974
Fax 608-263-4499
E-mail igor@neep.engr.wisc.edu

Send the original abstract and 2 copies to:

Laurie B. Wink
Conferences & Institutes
Suite 202
302 E. John Street
Champaign, IL 61820 USA

ABSTRACTS MUST BE RECEIVED NO LATER THAN MAY 12, 1995.

FACSIMILE COPIES WILL NOT BE ACCEPTED

Evolution of Light Ion Driven Fusion Power Plants Leading to the LIBRA-SP Design

G.L. Kulcinski, R.R. Peterson, G.A. Moses, D. Bruggink,
P. Cousseau, R.L. Engelstad, Y.-M. Lee, H.Y. Khater,
E.G. Lovell, J.J. MacFarlane, E.A. Mogahed, S. Rutledge,
M.E. Sawan, I.N. Sviatoslavsky, P. Wang, L.J. Wittenberg

June 1994

FPA-94-3

Prepared for the Eleventh Topical Meeting on the Technology of Fusion Energy, June 19–23, 1994, New Orleans LA.

EVOLUTION OF LIGHT ION DRIVEN FUSION POWER PLANTS LEADING TO THE LIBRA-SP DESIGN

G. L. Kulcinski, R. R. Peterson, G. A. Moses, D. Bruggink, P. Cousseau, R. L. Engelstad,
Y.-M. Lee, H. Y. Khater, E. G. Lovell, J. J. MacFarlane, E. A. Mogahed,
S. Rutledge, M. E. Sawan, I. N. Sviatoslavsky, P. Wang, L. J. Wittenberg
Fusion Technology Institute
University of Wisconsin- Madison
Madison, Wisconsin 53706 U.S.A.
(608) 263-2308

ABSTRACT

The use of light ion or electron beams to compress matter to the densities required for fusion has been proposed for more than 20 years. In the past ten years, a series of light ion beam power plant conceptual designs have been published under the generic name LIBRA. Considerable advances in both physics and technology have allowed major improvements from the design performance of the earliest LIBRA 330 MW_e power plant to the more recent 979 MW_e LIBRA-LiTE, and the 1000 MW_e LIBRA-SP reactors. The recent declassification of target designs allows more realistic target spectra, gains, and injection parameters to be analyzed. The pulsed power driver technology has matured to the point that Helia induction technology can be tested in the laboratory under single pulse conditions and confidently extrapolated to LIBRA repetition rates. New concepts for protecting the first structural wall of the reactor have been developed; the use of flexible INPORT (INhibited Flow in PORous Tube) and rigid PERIT (PErforated RIgid Tube) units allow the reflector and first wall to last the lifetime of the power plant. The use of PbLi eutectic alloy has greatly improved the safety features of these reactors and the economics of all three compare very favorably to the tokamak, laser, and heavy ion beam reactors.

I. INTRODUCTION

Since the first proposal, in the early 1970's, to use energetic electrons to implode targets in ICF reactors[1] there have been several advances in the field of particle beam fusion. The early reactors were relatively high rep rate, low yield systems (see Fig. 1) with little detail on the driver technologies to be used. There were efforts in both the US and USSR. Novel ideas, in this early period, to protect the first wall from the target debris included "moving belts"[2] and Li "rain".[3]

In the 1980's, the driver beam was changed to 6-8 MeV proton beams which were used to drive targets to higher yields and consequently required lower rep rates.[4] Channel transport schemes were then the most popular means of transporting the ions to the target. The use of porous "INPORT" units[5] was applied in that time period to protect the first wall as was the use of internal gas protection.[6] Both of these latter techniques were used to reduce the diameter of the reaction chamber to 4-5 m. The scope of the international effort was expanded to Europe (Germany) and Asia (Japan).

As the physics of beam propagation and target interactions improved in the 1990's, scientists[7] used higher atomic weight ions (Li, and suggested even higher elements such as F) at higher voltages (30-40 MV). The use of Helia inductive voltage adder technology became standard and there was a great deal of analysis for ballistic and self-pinched transport of ions.[8] Some of this work is to be verified on the SABRE facility at SNL in the US.

The LIBRA class of reactors, which represent a collaboration between the US and Germany, have embodied the most recent changes and currently serve as the "flagship" of the light ion beam (LIB) community's reactor design program. The goals of the LIBRA project are:

- To develop a *self-consistent* conceptual design of a light ion beam driven fusion power plant.
- To evaluate the potential of light ion fusion power plants for economically attractive *small* power plants.

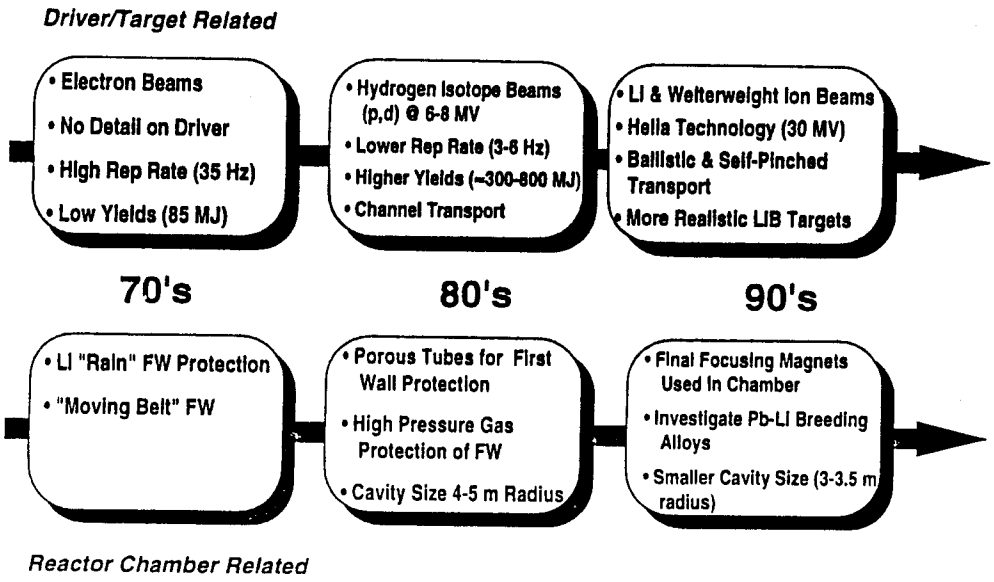

Fig. 1. The historical trends in light ion beam driven fusion power plant designs have reduced the size and increased their economic and safety attractiveness.

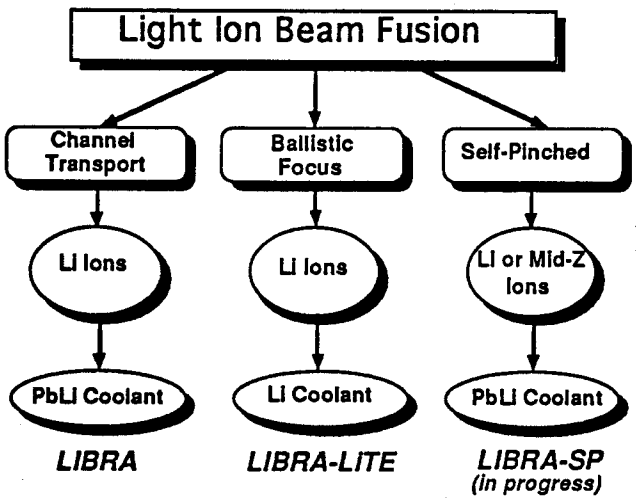

Fig. 2. The method of transferring the ion beam to the target has been the main difference in the LIBRA class of power plants. See Fig. 3 for a schematic for the various mechanisms.

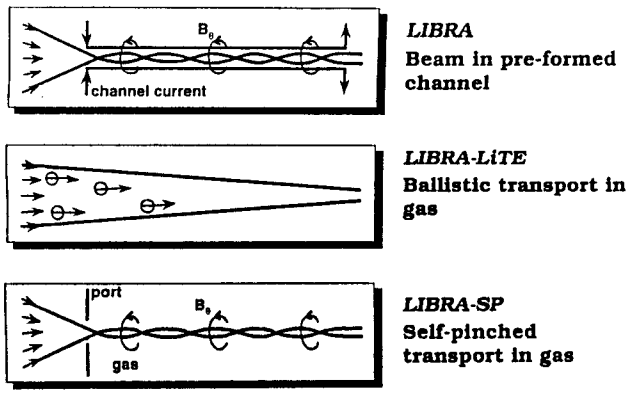

Fig. 3. Schematic of the various transport schemes used in the LIBRA class of light ion driven fusion power plants.

II. GENERAL FEATURES OF THE LIBRA CLASS OF FUSION POWER PLANTS

The main difference in the LIBRA class of reactors is the mode by which the high energy imploding ions are transferred from the diode to the target (see Fig. 2). In LIBRA,[9] completed in 1989, channel transport of the 30 MeV Li ions in preformed channels was utilized (see Fig. 3). The high background chamber gas pressure allowed the use of a PbLi eutectic alloy coolant inside the chamber.

The difficulty in forming a narrow plasma channel in LIBRA prompted the designers to investigate the ballistic transport mechanism in LIBRA-LiTE[10] completed in 1991. This transport mechanism required substantial final focusing magnets inside the reaction chamber which, in turn, had to be designed to withstand large neutron fluxes. In order to avoid excessive scattering of the ions, a low cavity gas pressure of low Z atoms (i.e., Li) is utilized requiring that the internal coolant be Li instead of the heavier PbLi.

While the focal spots could be kept small with ballistic focusing, the use of magnets in high radiation fields was not fully accepted and the safety considerations associated with liquid Li prompted another switch in 1994

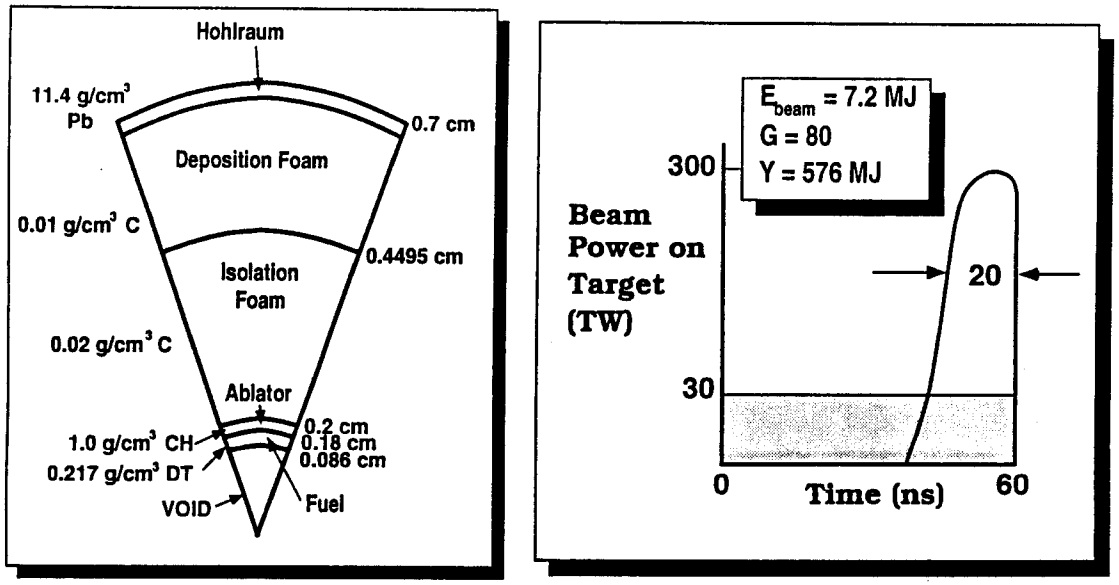

Fig. 4. Schematic of the target used for the LIBRA-SP power plant design along with the power profile used to drive the internally pulse shaped target to ignition and burn.

Table I

Key Parameters for the LIBRA Class of Light Ion Beam Driven Fusion Power Plants

Parameter	LIBRA	LIBRA-LITE	LIBRA-SP
Focus Mechanism	Channel Transport	Ballistic	Self-Pinched
Net Electric Power, MWe	331	979	1000
Li Ion Beam Energy to Target, MJ	4	6	7.2
Target Yield, MJ/Rep Rate, Hz	320/3	600/3.9	576/3.7
Coolant/Breeder	PbLi	Li	PbLi
INPORT/PERIT Material	SiC	Steel	Steel
Secondary Heat Transfer Fluid	He	Organic	He

*Use 25–35 MeV Li ions from Hella type driver

to the use of self-pinched beam transport, LIBRA-SP. The safety concerns with Li were solved by utilizing the PbLi alloy again.

The key parameters of the three designs are given in Table I. Aside from the coolant and beam transport differences, it can be seen that the ability of light ion beam (LIB) systems to operate at low power levels was demonstrated in the 330 MW_e LIBRA design. The other two designs were conducted at approximately the 1000 MWe level to be more consistent with current tokamak, laser and heavy ion beam conceptual designs.

Other differences apparent from Table I include increasingly higher ion beam energy on target (i.e., 4 vs. 6 vs. 7.2 MJ) and somewhat different yields depending on the evolving target physics that was used during each study. The method of protecting the first walls evolved from flexible SiC INPORT units (to be described later) in LIBRA, to flexible steel INPORT units in LIBRA-LiTE and more recently, perforated rigid steel (PERIT) units in LIBRA-SP. Finally, helium was used as a secondary heat transfer fluid in LIBRA and LIBRA-SP while a high operating temperature organic fluid was used with the Li in LIBRA-LiTE.

III. TARGET AND DRIVER PARAMETERS

The original LIBRA and LIBRA-LiTE designs were forced to use targets originally designed for heavy ion beam reactors because of classification in the US. The generic target chosen was that analyzed for HIBALL.[11] However, recent declassification[12] of light ion targets has allowed the use of more realistic configurations such as that shown in Fig. 4. If the target in Fig. 4 is illuminated with the beam power shown in that figure (from 12 prepulse beams and 12 full power beams), then the internal pulse shaping of the x-ray flux to the center capsule should be sufficient to achieve a gain of 80 (see Fig. 5 for the predicted comparison of the LIBRA targets compared to the targets from other ICF conceptual reactor designs.)

Table II

Summary of the Cavity Conditions in the LIBRA Designs

	LIBRA	*LIBRA-LiTE*	*LIBRA-SP (Preliminary)*
Initial Gas Conditions			
Temperature	500°C	500°C	550°C
Species	He	He	He
# Density	3.55×10^{18} cm^{-3}	3.55×10^{16} cm^{-3}	7.4×10^{16} cm^{-3}
Conditions at INPORTs or PERITs			
Peak Pressure	100 GPa	4.6 GPa	100 GPa
Pulse Width (FWHM)	1 ns	8 ns	1 ns
Total Impulse	125 Pa-s	100 Pa-s	TBD
Vaporization	7 μm PbLi	66 μm Li	21 μm PbLi

Table III

The Neutronic Properties of the LIBRA Designs are Quite Attractive

	LIBRA	*LIBRA-LiTE*	*LIBRA-SP (Preliminary)*
Neutron Wall Loading (MW/m^2)	6	10.6 (INPORT) 29 (Magnets)	7.2
Breeder	PbLi	Li	PbLi
% ^{6}Li	90	7.4	90
Tritium Breeding Ratio	1.36	1.41	1.48
Overall Energy Multiplication	1.17	1.12	1.18
Damage to INPORT/PERIT Units (dpa/FPY)	60	68	87
Damage to Steel Chamber Walls (dpa/FPY)	6.7	5	3.9

An example of how the pulsed power driver units are placed around the reaction chamber is shown in Fig. 6 for the LIBRA-LiTE reactor. The main difference for the LIBRA-SP design is that there would be fewer units (24 vs. 30 for LIBRA-LiTE).

The net driver efficiency (energy on target/prime energy storage) is very much a function of gross electrical conversion efficiency to the diode, the conversion of electrical energy in the diode to ions, and the transport efficiency of the ions to the target. Figure 7 shows how those factors are related for the LIBRA, LIBRA-LiTE, and LIBRA-SP designs. Note that the overall net efficiency of the self-pinched mode of ion transport is estimated to be ≈30%,[13] that of channel transport is 23.5%,[9] and only 18%[14] for the ballistic transport mode.

IV. CAVITY CONDITIONS

A cross section of the reaction vessel for the LIBRA-SP design is given in Fig. 8. Only 2 of the 24 beam lines are shown in the schematic along with a duct to the expansion chamber, the curved tubes which carry the PbLi coolant from the top header to the pool below, and the PbLi/He heat exchanger below the chamber. The roof is far enough away to be a lifetime component.

One of the unique engineering problems faced by all LIB reactor designers is that of containing the ≈600 MJ blast from the target if it is successfully ignited. In the past, the shock wave and neutron flux from the exploding target was absorbed by flexible, porous woven tubes of SiC (LIBRA) or steel (LIBRA-LiTE) such as those shown in Fig. 9.

In spite of the many advantages of the INPORT concept (see Refs. 9-11 for a fuller discussion), a considerable axial tension must be applied and maintained on the woven tubes to reduce radial deflection in response to the impulse from vaporized liquid and microexplosion. This is particularly difficult when the coolant is heavy like PbLi.

The solution to this problem in LIBRA-SP was to replace the flexible woven porous tubes with rigid, curved steel tubes that have small slits machined into them at appropriate angles. These slits, aimed at the inner chamber are designed to release a continuous sheet of coolant on the front tubes to intercept the blast wave (see Fig. 10).

The cavity conditions in each of the last 3 LIBRA designs are listed in Table II. Note that helium gas is used in all the designs but that the background pressure is 100 torr in LIBRA, 1 torr in LIBRA-LiTE, and 2 torr in LIBRA-SP. The pressure, impulse and vaporization conditions vary with pulse width and type of coolant.

V. NEUTRONIC PERFORMANCE

The simple geometric coverage inside the LIBRA chambers, in addition to the close proximity of an abundance of Li and PbLi alloys, allows a superior neutronic performance in the LIBRA reactors. The main parameters are listed in Table III for the three light ion beam reactors.

Note that the dpa damage is not proportional to the wall loading alone because the PbLi multiplies the number of neutrons more effectively than Li and the dpa cross sections of SiC are different than those of steel. It is also important to note that none of the designs has trouble breeding (e.g., TBR's range from 1.36 to 1.48) and the overall energy multiplication (total recoverable power

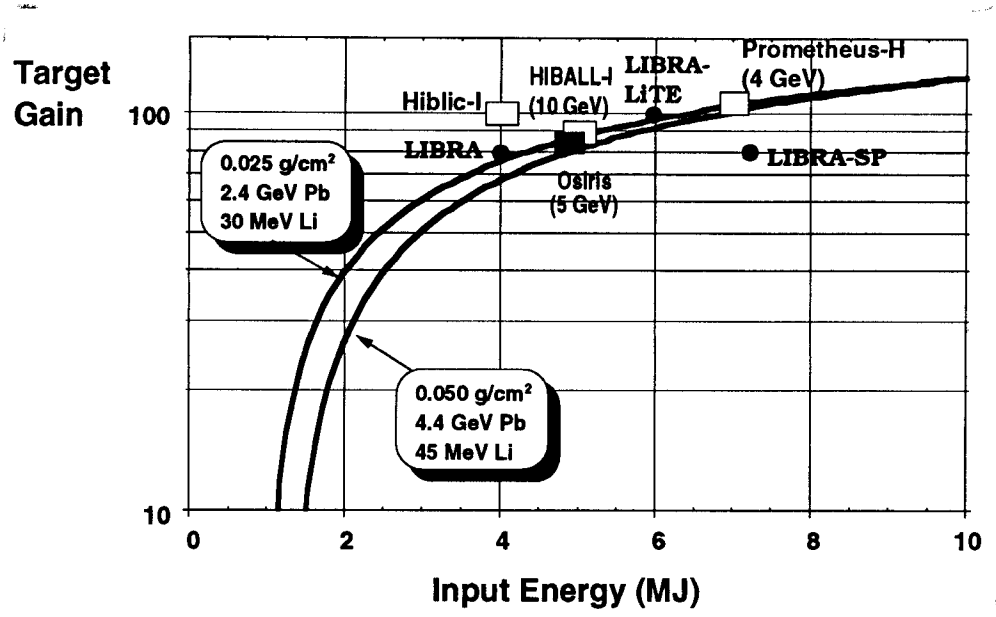

Fig. 5. The performance of targets that rely on internal pulse shaping is slightly degraded from the indirect drive ICF target designs.

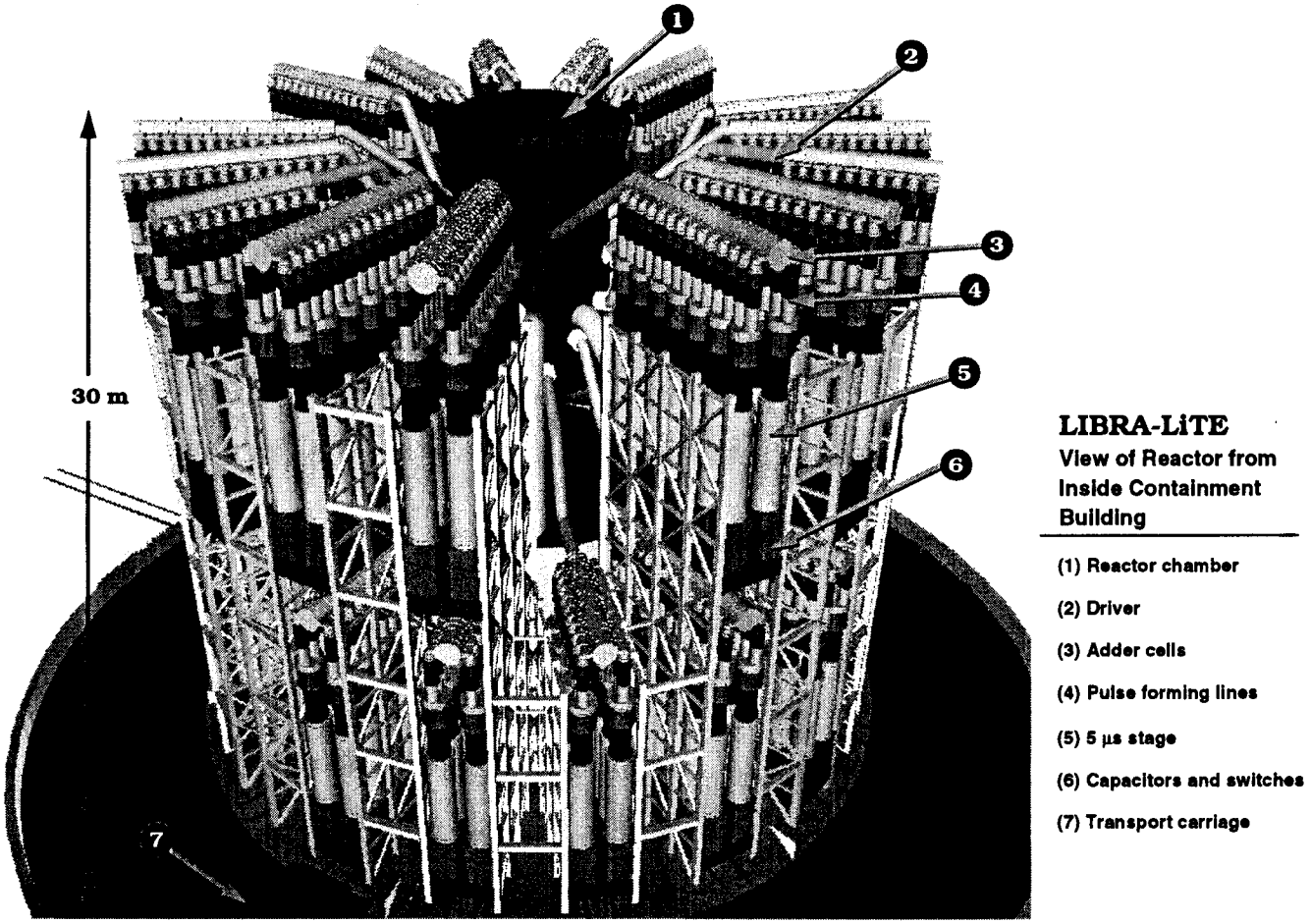

Fig. 6. Isometric view of the LIBRA-LiTE reaction chamber surrounded by 30 pulsed power units. Note the double stacking arrangement and the size of the reactor in the center (1).

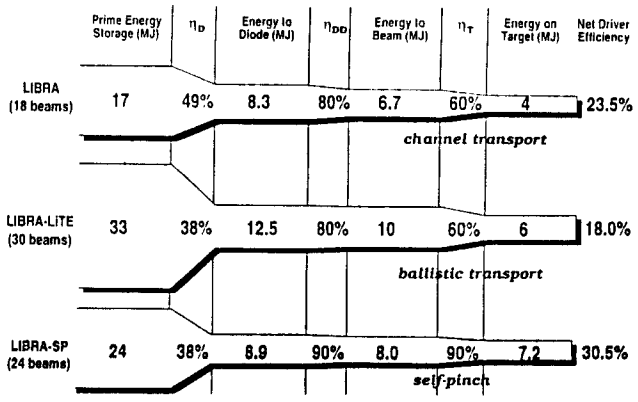

Fig. 7. The use of Helia driver technology and Li ion applied B diodes allows efficient energy transport to the target, especially in the self-pinched mode.

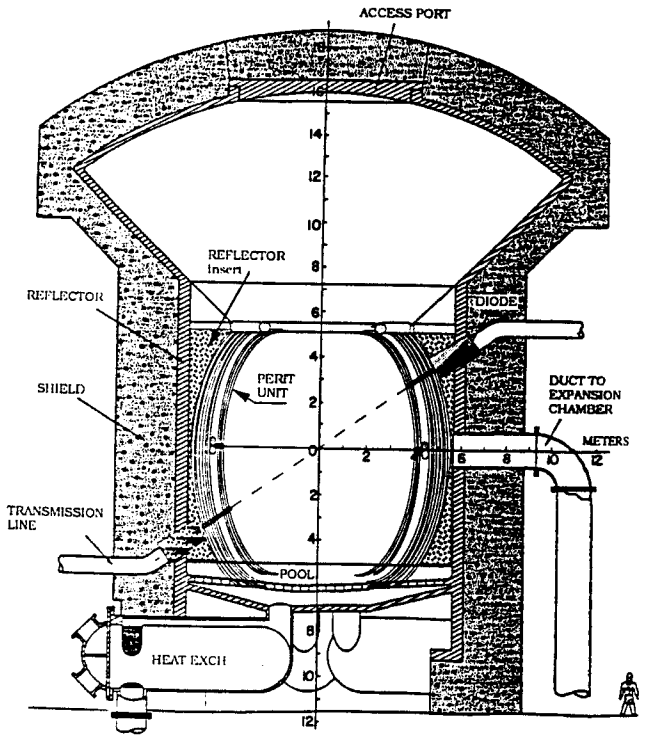

Fig. 8. The cross sectional view of the LIBRA-SP reaction chamber showing the placement of the Li diodes and the perforated rigid tubes (PERIT's) which absorb most of the target debris and neutrons emitted from the target.

from chamber/fusion power) is a respectable 1.12 to 1.18. The neutron wall loadings on the INPORT or PERIT units ranges from 6 to 11 MW/m^2 resulting in 60 to 90 dpa/FPY on those units. Such damage rates will require frequent replacement of the protective units (perhaps on a 2-3 year basis).

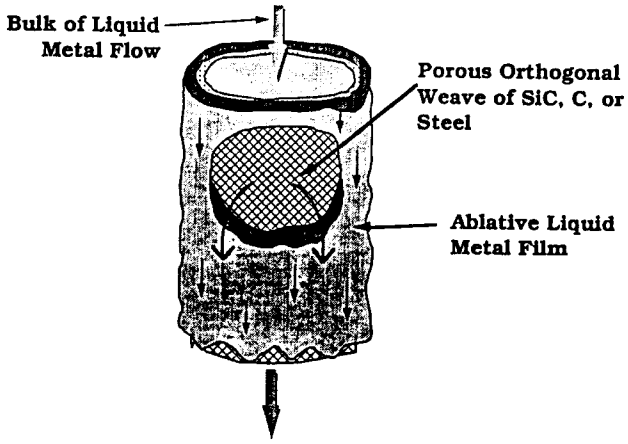

Fig. 9. A schematic of the flexible woven inhibited flow porous tube (INPORT) units displaying how the wetted surface of the tubes absorb the x-rays and target debris while the bulk of the liquid flowing through the tube absorbs the energy and mitigates the isochoric heating of the neutrons.

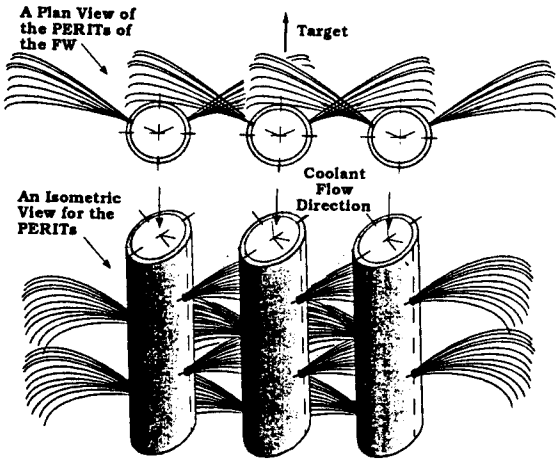

Fig. 10. Two views of the PErforated RIgid Tube (PERIT) units specially designed for the LIBRA-SP power plant. The small slits, pointing slightly forward, provide enough PbLi sheet in front of curved tubes to mitigate the shock wave and reduce the amount of x-ray induced vaporization from the tubes.

VI. TRITIUM INVENTORIES

The inventory of tritium in any ICF power plant can be conveniently divided into:

- The target fabrication facility
- Reactor hall
- Fuel processing.

The quantitative numbers for each of the LIBRA reactors are listed in Table IV.

Table IV
The Active Tritium Inventories in the LIBRA Reactors are Relatively Low

Location	LIBRA (PbLi)	LIBRA-LiTE (Li)	LIBRA-SP (PbLi)
	grams		
Target Fabrication Facility	134	193	198
Reactor Hall			
Targets (1 hr)	21	50	53
Breeder	0.4	230	2
INPORT/PERIT Units	150	~0	~0
Exhaust	1.3	7	4
	173	287	59
Fuel Processing			
Purification	1.3	4	2
Isotope Separation	45	35	35
	46	39	37
Total Active	353	519	294
Max. Exposure at fence if all T_2 were released-WB early dose	0.7 Rem (7 mSv)	1 Rem (10 mSv)	0.6 Rem (6 mSv)

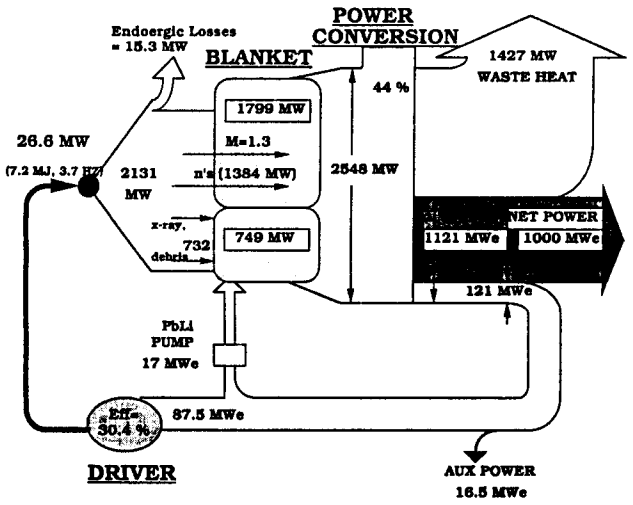

Fig. 11. The power flow diagram for the LIBRA-SP power plant.

Note that even though the power level of the LIBRA reactor was only 330 MW_e vs. LIBRA-SP at 1000 MW_e, the total active inventory is actually less in the LIBRA-SP design. This seeming contradiction can be explained by the fact that the target fabrication scheme is more efficient in LIBRA-SP, and because tritium is far less soluble in steel than in SiC. The end result is that the maximum whole body early exposure at the fence if all the T_2 were released is in the range of 0.6 to 1 Rem.

VII. POWER CYCLE CONSIDERATIONS

The 1000 MWe of net power is produced from 2131 MW of fusion power (see Fig. 11). The gross conversion of the energy in 550°C PbLi to electricity is ≈44%. With a net recirculating fraction of ≈11% there is enough

Table V
The Direct Capital Costs of the LIBRA Series of Reactor Designs

	M$ (1993) LIBRA	LIBRA-LiTE	LIBRA-SP (prelim.)
Driver	524	514	343
Total (incl. driver)	1157	1786	1528
Unit Direct Capital Costs ($/kWe)	3495	1835	1528
Net Power (MWe)	331	973	1000

auxiliary power to pump the heavy PbLi coolant and drive the pulsed power units to 7.2 MJ at a 3.7 Hz rate.

VIII. ECONOMIC PERFORMANCE

Because of the much higher efficiency of wall plug energy to ions on the target in LIBRA-SP, smaller pulsed power units can be purchased. This allows the driver costs to be reduced by 33% from those needed in LIBRA-LiTE for approximately the same net power output (see Table V). The total direct capital cost of LIBRA-SP is less than half that of the earlier 330 MWe LIBRA design and 17% less expensive compared to LIBRA-LiTE at about the same power level.

A comparison of the cost of light ion reactor studies to previous tokamak, laser, and heavy ion designs also shows that light ions retain their attractive economic performance (see Fig. 12). For example, the LIB designs are a full 30% lower than recent tokamak designs, 20% lower than laser power plants and ≈10% lower than the recent HIB designs.

IX. CONCLUSIONS

The LIBRA class of ICF power plants display (compared to heavy ion beam and laser designs):

- Comparable technological readiness
- Adaptability to lower power levels.
- Simplicity of design
- Attractive safety features
- Potentially the lowest COE.

However, there are two major concerns related to this form of inertial confinement fusion (in addition to the normal target fabrication, injection, and tracking concerns of all ICF concepts):

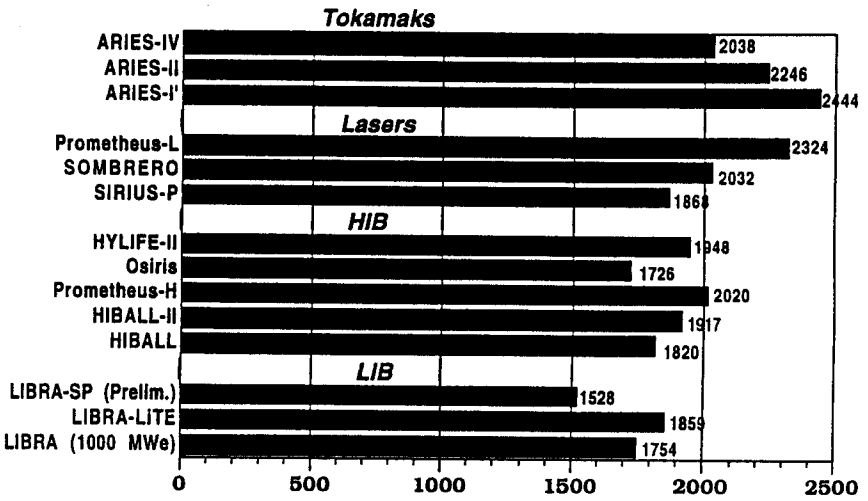

Fig. 12. The direct unit cost of the LIBRA reactors compares very favorably with other ICF and MCF DT power plants at the 1000 MWe level.

1. The transport of ions in a narrow beam to the target on a repeatable basis must be demonstrated experimentally. At the present time propagation in the self-pinched mode seems promising.
2. The light ion beam plants depend on the successful performance of internal pulse shaping in spherical targets. Experimental verification of this mechanism is vital.

If these two problems can be solved in the next 10-15 years, then electricity from DT fuels could be available from light ion driven fusion power plants in the second decade of the 21st century.

ACKNOWLEDGMENTS

Funding for this work was provided by Sandia National Laboratory and Kernforschungszentrum Karlsruhe.

REFERENCES

1. G. Yonas, et al., *Nuclear Fusion*, **14**, 732 (1979).
2. S. G. Varado and G. A. Carlson, *Nuclear. Tech.*, **29**, 415 (1976).
3. R. J. Burke, Argonne National Laboratory Report ENG/CTR/TM-31, 1974.
4. M. J. Clauser, "Ion Beam Implosion of Fusion Targets," *Phys. Rev. Letters*, **35**, 3, 848 (1975).
5. G. L. Kulcinski, G. A. Moses, J. Sapp, M. Sawan, I. N. Sviatoslavsky, D. K. Sze, and W. F. Vogelsang, "The INPORT Concept - An Improved Method to Protect ICF Reactor First Walls," *J. Nucl. Matls.*, 102 & 104, 103-108 (1981).
6. R. R. Peterson, G. W. Cooper, and G. Moses, "Cavity Gas Analysis for Light Ion Beam Fusion Reactors," *Nucl. Tech./Fusion*, **1**, 377 (1981).
7. D. L. Johnson, W. L. Nean and B. N. Turman, "PBFA-II Conceptual Design," Proc. 4th IEEE Pulsed Power Conf., Albuquerque, NM, p. 54 (1983).
8. D. L. Cook, to be published, *J. Fusion Energy*.
9. B. Badger, et al., "LIBRA - A Light Ion Beam Fusion Conceptual Reactor Design," University of Wisconsin Fusion Technology Institute Report UWFDM-800 (revised February 1990).
10. B. Badger, et al., "LIBRA-LiTE: A Commercial Light Ion Fusion Power Plant," University of Wisconsin Fusion Technology Institute Report UWFDM-880 and FPA-91-4, 1991.
11. B. Badger, et al., "HIBALL - A Conceptual Heavy Ion Beam Driven Fusion Reactor Study, Preliminary Report," University of Wisconsin Fusion Technology Institute Report UWFDM-450 and KfK-3202.
12. R. Olson, this conference.
13. C. L. Olson, et al., "LIF Standoff Research," 10th International Conf. on High Power Particle Beams, June 20-24, 1994, San Diego, CA, to be published.
14. P. F. Ottinger, et al., "Ballistic Transport and Solenoidal Focusing of Intense Ion Beams for Inertial Confinement Fusion," *J. Appl. Phys.*, **72**(2), 395 (1992).